Dissertation

submitted to the
Combined Faculties for the Natural Sciences and for Mathematics
of the Ruperto-Carola University of Heidelberg, Germany
for the degree of
Doctor of Natural Sciences

Put forward by

Josefina Michea
Born in: Santiago, Chile

Oral examination: 2 November 2021

Brought to Light: Disk and Clump Substructures in Dwarf Early-Type Galaxies

Josefina Michea

Referees: Prof. Dr. Eva K. Grebel
Prof. Dr. Jochen Heidt

Abstract

Dwarf early-type galaxies (ETGs) display a rich diversity in their photometric, structural, and dynamical properties. In this work, we address their structural complexity by studying with deep imaging two data sets of dwarf ETGs that are members of the Virgo and Fornax galaxy clusters. These dwarf ETGs are characterized by having disk-like or clump-like substructure features that lie mostly hidden within the bright diffuse light of the galaxies. We present a newly developed method that aims to robustly identify and extract the substructure features embedded in these dwarf ETGs. The method consists in an iterative procedure that gradually separates a galaxy image into two components: the bright, dominant, diffuse component, and the much fainter, underlying substructure component. By applying it to the two dwarf ETG data sets, we quantify their substructure features, and find that they contribute only between 2% to 10% of the total galaxy light within two effective radii. We test the reliability of the method, and prove that it is accurate in recovering the substructures we introduce in mock galaxy images, even at low substructure-to-total light fractions of a few percent. To showcase potential applications of the method, we subject the extracted substructure components of the Virgo and Fornax data sets to a Fourier analysis and to a color analysis, respectively. Our results indicate that the Virgo cluster has a larger fraction of dwarf ETGs with disk substructures compared to the Fornax cluster, and that embedded spiral arm features are common in disky dwarf ETGs in Virgo but completely absent in Fornax. We propose that these differences are a reflection of the particular characteristics of each distinct cluster environment. We also find that disk substructures tend to be fainter and redder than clump substructures, possibly indicating that disky and clumpy dwarf ETGs may have had different origins and/or evolutionary histories. However, both sub-classes are consistent with being transition-type dwarf galaxies, where environmentally-driven processes are transforming them from late-types to early-types. Through this work, we conclude that the cluster environment must play a major role in shaping and transforming the dwarf galaxy populations in galaxy clusters.

Zusammenfassung

Zwerggalaxien vom frühen Typ (ETGs) weisen eine große Vielfalt an photometrischen, strukturellen und dynamischen Eigenschaften auf. In dieser Arbeit befassen wir uns mit ihrer strukturellen Komplexität, indem wir zwei Datensätze von Zwerg-ETGs, die zu den Virgo- und Fornax-Galaxienhaufen gehören, mit tiefen Aufnahmen untersuchen. Diese Zwerg-ETGs zeichnen sich durch eine scheiben- oder klumpenartige Substruktur aus, die meist im hellen, diffusen Licht der Galaxien verborgen liegt. Wir stellen eine neu entwickelte Methode vor, die darauf abzielt, die in diesen Zwerg-ETGs eingebetteten Substruktureigenschaften robust zu identifizieren und zu extrahieren. Die Methode besteht aus einem iterativen Verfahren, das ein Galaxienbild schrittweise in zwei Komponenten aufteilt: die helle, dominante, diffuse Komponente und die viel schwächere, darunter liegende Substrukturkomponente. Indem wir die Methode auf zwei ETG-Zwergdatensätze anwenden, quantifizieren wir deren Substrukturmerkmale und stellen fest, dass sie nur zwischen 2% und 10% des gesamten Galaxienlichts innerhalb von zwei effektiven Radien beitragen. Wir testen die Zuverlässigkeit der Methode und beweisen, dass sie bei der Wiederherstellung der Substrukturen, die wir in die Bilder von Scheingalaxien einführen, genau ist, sogar bei niedrigen Substruktur-zu-Gesamtlicht-Anteilen von einigen Prozent. Um mögliche Anwendungen der Methode aufzuzeigen, unterziehen wir die extrahierten Substrukturkomponenten der Virgo- und Fornax-Datensätze jeweils einer Fourier-Analyse und einer Farbanalyse. Unsere Ergebnisse zeigen, dass der Virgo-Haufen einen größeren Anteil an Zwerg-ETGs mit Scheiben-Substrukturen aufweist als der Fornax-Haufen, und dass eingebettete Spiralarm-Merkmale in scheibenförmigen Zwerg-ETGs in Virgo häufig sind, in Fornax jedoch völlig fehlen. Wir vermuten, dass diese Unterschiede die Eigenschaften der jeweiligen Haufenumgebung widerspiegeln. Wir stellen auch fest, dass Scheiben-Substrukturen tendenziell schwächer und röter sind als Klumpen-Substrukturen, was möglicherweise darauf hindeutet, dass scheibenförmige und klumpige Zwerg-ETGs unterschiedliche Ursprünge und/oder Entwicklungsgeschichten haben könnten. Beide Unterklassen sind jedoch übereinstimmend Zwerggalaxien des Übergangstyps, die sich durch umweltbedingte Prozesse von einem späten Typ in einen frühen Typ verwandeln. Aus dieser Arbeit schließen wir, dass die Umgebung des Haufens eine wichtige Rolle bei der Formung und Veränderung der Zwerggalaxienpopulationen in Galaxienhaufen spielen muss.

Contents

List of Figures

List of Tables

1

Introduction: Dwarf Early-Type Galaxies

In this Chapter, we introduce our objects of study: dwarf early-type galaxies (ETGs). To begin with, in Section 1.1, we present their main characteristics, including their photometric, structural, and dynamical properties. Then, in Section 1.2, we describe the variety of environments they can be found in, and the different environmentally-driven processes that can affect them during their lifetime. In Section 1.3, we address their possible formation scenarios. To follow, in Section 1.4, we focus on the fact that faint substructure features can sometimes be found embedded in dwarf ETGs. As such, we identify the different types of substructure features that have been observed, and the attempts that have been done to detect and quantify them. Finally, in Section 1.5, we provide an outline of the contents of this work.

1.1 Properties

In general terms, the dwarf galaxy population is comprised by small-sized, low-mass, low-luminosity galaxies. Typically, dwarf galaxies are classified into early-types and late-types.

On the one hand, dwarf early-type galaxies (ETGs) tend to be red in color, are mostly quenched (i.e., not forming stars), are devoid of gas and dust, display an overall smooth and featureless appearance, and are frequently found in high-density environments (like in galaxy clusters). The dwarf ETG population encompasses dwarf elliptical (dE; Ferguson & Binggeli 1994; Graham & Guzmán 2003), dwarf lenticular or S0 (dS0; Sandage & Binggeli 1984; Binggeli & Cameron 1991), and dwarf spheroidal (dSph; Harbeck et al. 2001; Grebel et al. 2003) galaxies. While dE galaxies are usually recognized as the archetypes of the dwarf ETG population, dS0 galaxies are similar to them, but with hints of a (featureless) disk-like component. In contrast, dSph galaxies tend to be the smallest and faintest of the bunch (Ann

et al. 2015). It could be argued that ultra-compact dwarf galaxies (UCDs; Hilker et al. 1999; Drinkwater et al. 2000) and ultra-diffuse galaxies (UDGs, sometimes also referred to as low surface brightness galaxies, LSBs; Impey et al. 1988; van Dokkum et al. 2015) should also be considered part of the dwarf ETG population, given that they have some properties in common. Compared to dEs and dS0s, UCDs have comparatively smaller sizes and a brighter surface brightness, while UDGs have comparatively larger sizes with a similar surface brightness (Muñoz et al. 2015). However, for purposes of this work, when referring to "dwarf ETGs" we will specifically mean the combined population of dEs and dS0s, and will exclude the population of dSphs, UCDs, and UDGs. Under this definition, in Figure 1.1, we show some representative examples of galaxies that belong to the dwarf ETG population (i.e., dEs and dS0s), while also showing dSphs to serve as a comparison.

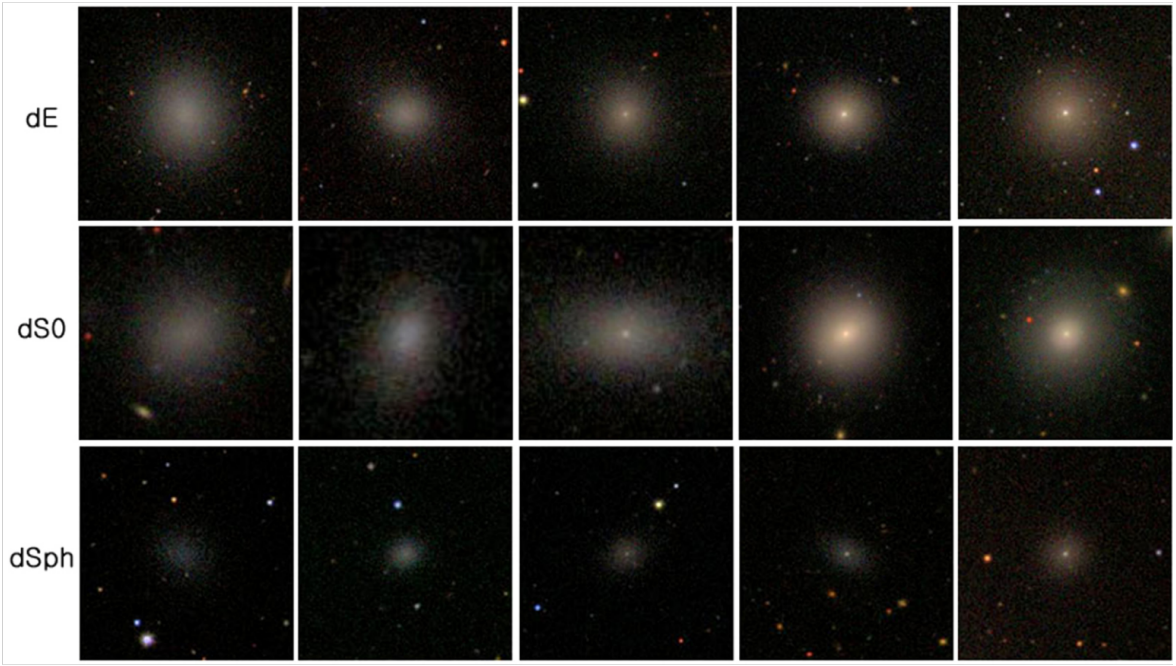

Figure 1.1: Representative galaxy images of the dwarf ETG population. From top to bottom, we show examples of dwarf elliptical (dE), dwarf S0 (dS0), and dwarf spheroidal (dSph) galaxies. From left to right, the galaxies are arranged from non-nucleated cases to nucleated cases that display increasingly brighter nuclei. These images are part of the study by Ann et al. (2015), and correspond to g, r, and i-band composite images from the Sloan Digital Sky Survey (SDSS) Data Release 7 (DR7; Abazajian et al. 2009). Image credit: this Figure is adapted from Figure 5 of Ann et al. (2015).

On the other hand, dwarf late-type galaxies (LTGs) tend to be blue in color, are actively forming stars, have a rich content of gas and dust, display an ample variety of structural features, and are frequently found in low-density environments (like in galaxy groups or in the field). The dwarf LTG population encompasses dwarf irregular (dIrr; Skillman et al. 1989; Carignan & Beaulieu 1989) and dwarf spiral (dSp; Swaters et al. 2002, 2009) galaxies. While dIrr galaxies are characterized by having clump structures and an amorphous appearance (Conselice 2003; Ann et al. 2015), dSp galaxies have disk structures, such as bars and spiral arms, similar to their normal-sized spiral galaxy counterparts (Grebel 2001).

While the aforementioned depictions of the dwarf ETG and LTG populations constitute a

very generalized view, they can still serve as a basic guideline to distinguish the two populations. As in this work we focus on the study of dwarf ETGs, we now provide a more in-depth look into their properties, which can be quite heterogeneous. Their main photometric, structural, and dynamical properties are as follows.

1.1.1 Photometric Properties

Due to being dwarf systems, dwarf ETGs are characterized by having a faint luminosity and a low surface brightness. The traditional definition of dwarf ETGs establishes the bright end at a magnitude of $M_B \gtrsim -18$ mag and at a surface brightness of $\mu_B \gtrsim 22$ mag arcsec^{-2} (Ferguson & Binggeli 1994). However, modern studies claim that this may be considered an artificial divide, as dwarf ETGs and normal-sized ETGs appear to constitute a continuous sequence of early-type galaxies (Graham 2019). Therefore, while dwarf ETGs do indeed have fainter magnitudes and a lower surface brightness compared to their normal-sized counterparts, we should not think that one population strictly "starts" where the other "ends", but instead that they share a common region in parameter space.

Due to their general lack of star formation in combination with their low gas and dust content (Grebel 2001), dwarf ETGs commonly adopt a red global optical color (van Zee et al. 2004a; Lisker et al. 2008). As such, the great majority of dwarf ETGs belong to the faint end of the red sequence of galaxies (Janz & Lisker 2009), constituted by red-colored and non-star-forming systems; as opposed to the blue cloud of galaxies, constituted instead by blue-colored and star-forming systems. Although many dwarf ETGs present flat radial color gradients (i.e., their color stays the same at all galactocentric radii), they can also present significant color gradients (Lisker et al. 2006b; Urich et al. 2017). Usually, their color tends to become redder with larger galactocentric radii (i.e., reddening outwards). This observed trend may be an indication that a population gradient exists: the central regions may contain younger stellar populations, while conversely the outer regions may contain comparatively older stellar populations (Jerjen et al. 2000a). In terms of the environmental context of dwarf ETGs, their global colors tend to become redder towards high-density regions (such as the core of galaxy clusters), and comparatively bluer (i.e., "less red") towards low-density regions (such as the outskirts of galaxy clusters or galaxy groups; Lisker et al. 2008).

It has long been observed that some dwarf ETGs can have significantly bluer colors at their central regions (Hodge 1973; Vigroux et al. 1984; Peletier 1993). These blue-cored dwarf ETGs are consistent with having either ongoing or recent ($\lesssim 1$ Gyr) central star formation episodes (Lisker et al. 2006b; Pak et al. 2014; Urich et al. 2017; Hamraz et al. 2019), which serve as an indication that they contain a non-negligible amount of gas (Conselice et al. 2003; Gu et al. 2006; De Rijcke et al. 2013). Their blue cores tend to be younger and more metal-rich compared to the rest of the galaxy (Urich et al. 2017). However, estimations suggest that within less than 1 Gyr from the cessation of star formation, their central blue colors will fade, causing these blue-cored dwarf ETGs to transition into ordinary "red and dead" dwarf ETGs, thus becoming indistinguishable from them (Lisker et al. 2006b). Blue-cored dwarf ETGs tend to be located in low-density environments, such as the outskirts of galaxy clusters, therefore

constituting an unrelaxed population (Conselice et al. 2003; Lisker et al. 2006b).

The stellar populations of dwarf ETGs can be quite heterogeneous, spanning a wide range of ages and metallicities (Jerjen et al. 2004; Toloba et al. 2014). First, we clarify that galaxies do not have a single age or metallicity, as they are constituted by a multitude of different stellar populations, each with their own particular characteristics. As such, we highlight the importance of deriving luminosity-weighted (or mass-weighted) ages and metallicities, as they can provide a better estimation of the properties of the dominant stellar population of a galaxy. In general terms, dwarf ETGs tend to be younger and more metal poor than their normal-sized counterparts (Schneider 2006; Michielsen et al. 2008), as the age and metallicity increases with the stellar mass of a galaxy (Gallazzi et al. 2005; Koleva et al. 2011).

On the one hand, the average luminosity-weighted ages of dwarf ETGs tend to be dominated by an intermediate-aged stellar population, grouping around values between $5-7$ Gyr (Michielsen et al. 2008; Toloba et al. 2014). However, the dwarf ETG population actually shows a wide spread of ages, which can range from as young as ~ 2 Gyr to as old as the estimated age of the Universe, ~ 14 Gyr (Michielsen et al. 2008; Chilingarian 2009; Paudel et al. 2010; Toloba et al. 2014). This serves as an indication that the dwarf ETG population can have complex star formation histories: while in some cases their star formation must have ceased long ago, in other cases their star formation must have extended to more recent epochs (Ryś et al. 2015).

On the other hand, the average luminosity-weighted metallicities of dwarf ETGs tend to be sub-solar, typically in the order of $\log_{10}(Z/Z_{\odot}) \approx -0.6$ (Gallazzi et al. 2005; Michielsen et al. 2008; Toloba et al. 2014). While this may serve as a representative value, the dwarf ETG population also shows a wide spread of metallicities, which can range from solar ($\log_{10}(Z/Z_{\odot}) \approx 0$) to even less than a tenth of solar ($\log_{10}(Z/Z_{\odot}) \lesssim -1$; Michielsen et al. 2008; Chilingarian 2009; Paudel et al. 2010; Toloba et al. 2014). The luminosity-weighted ages and metallicities of dwarf ETGs appear to correlate with their environmental context: older and more metal poor dwarf ETGs tend to be found in regions of higher local density (e.g., in the core region of galaxy clusters; Paudel et al. 2010; Sybilska et al. 2017). We provide a more in-depth look into the interrelation between the environment and the properties of dwarf ETGs in the upcoming Section 1.2.

1.1.2 Structural Properties

Dwarf ETGs have small intrinsic sizes. We can use the effective (or half-light) radius as a proxy for galaxy size, which is defined as the galactocentric radius that encloses half of the total flux of the galaxy. Typically, dwarf ETGs span effective radii that that can be as small $0.1-0.2$ kpc in length, and as large as $1-2$ kpc (Eigenthaler et al. 2018; Ordenes-Briceño et al. 2018a; Venhola et al. 2019). As a means to visualize the size distribution of the dwarf ETG population, in Figure 1.2 we show the size-luminosity relation followed by the dwarf ETGs belonging to the Fornax galaxy cluster (Ordenes-Briceño et al. 2018a).

As illustrated in both Figures 1.1 and 1.2, it is not rare for dwarf ETGs to host nuclei,

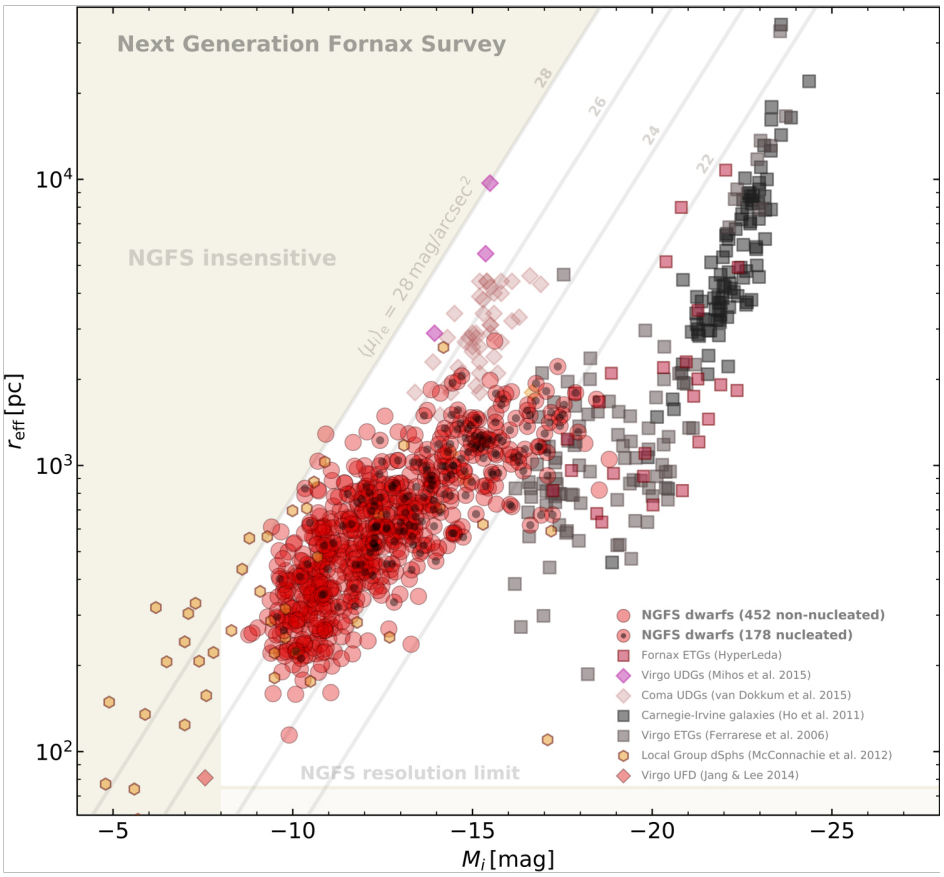

Figure 1.2: Size-luminosity relation of the dwarf ETG population. The effective radius is plotted against the total i-band absolute magnitude of the galaxies. The dwarf ETGs from the Next Generation Fornax Survey (NGFS; Muñoz et al. 2015) are plotted as red filled circles. In addition, nucleated dwarf ETGs have been marked with a central black dot. For comparison, dSphs from the Local Group are plotted as yellow hexagons. UDGs from the Virgo and Coma galaxy clusters are plotted as dark pink and light pink rhombuses, respectively. Normal-sized ETGs from the Virgo and Fornax galaxy clusters are plotted as light gray and red squares, respectively. Normal-sized ETGs from the Carnegie-Irvine catalog are plotted as dark gray squares. The sources of these comparison samples are indicated in the legend of the Figure. The diagonal lines in the background delimit regions of constant surface brightness, with the surface brightness increasing from left to right. Image credit: this Figure corresponds to Figure 2 of Ordenes-Briceño et al. (2018a).

which consist in compact light overdensities located at their central regions. Nucleated dwarf ETGs tend to have brighter luminosities and larger sizes than their non-nucleated counterparts (Muñoz et al. 2015; Eigenthaler et al. 2018; Ordenes-Briceño et al. 2018a,b; Venhola et al. 2019). The nucleation fraction ($f_{\rm nuc}$) of galaxies has been found to be strongly correlated with galaxy brightness (Côté et al. 2006; Sánchez-Janssen et al. 2019). In the particular case of dwarf ETGs, the nucleation fraction can be as high as $f_{\rm nuc} \gtrsim 0.9$ on the bright end, proceeding to steeply decrease towards fainter luminosities (Ordenes-Briceño et al. 2018b).

Apart from often hosting nuclei, dwarf ETGs are mostly featureless in appearance, with a light distribution that is, at least on first sight, predominantly smooth (Binggeli & Cameron 1991). Generally, their diffuse surface brightness profiles can be described well by a Sérsic (Sérsic 1968) function (Jerjen et al. 2000a; Grebel 2001). The Sérsic function is characterized

by a Sérsic index n, which acts like a concentration parameter: a small n represents a shallow inner profile with a truncated outer profile, while conversely a large n represents a steep inner profile with extended wings in the outer profile. While an $n = 1$ represents an exponential profile, typical for giant spiral galaxies; an $n = 4$ represents a de Vaucouleurs profile (de Vaucouleurs 1948), typical for giant elliptical galaxies. The surface brightness profiles of dwarf ETGs are characterized by Sérsic indices in the range $0 < n < 2$ (Venhola et al. 2018), with typical values in the order of $n \approx 0.7 - 0.8$ (Muñoz et al. 2015; Eigenthaler et al. 2018). In the dwarf ETG regime, the Sérsic index correlates with galaxy brightness, with brighter galaxies tending to have larger Sérsic indices (Venhola et al. 2019). We note that, in the case of nucleated dwarf ETGs, an additional component is usually required in order to properly model the innermost region (e.g., a point source function; Venhola et al. 2018; Su et al. 2021). Furthermore, while it is true that a large fraction of dwarf ETGs can be characterized by a single Sérsic profile, optionally with a nucleus, there are also cases that are structurally more complex, being best described by multiple components (Janz et al. 2012, 2014).

Within the dwarf ETG population, it is possible to identify a variety of morphologies, which allows to establish sub-classifications (see, e.g., studies by Lisker et al. 2006c,b, 2007, 2008). We have already seen that on the bright end, there is a predominance of nucleated dwarf ETGs ("dE(N)"), while their non-nucleated counterparts ("dE(nN)") dominate instead on the faint end. We have also seen that there are dwarf ETGs with blue cores ("dE(bc)"; Lisker et al. 2006b), indicating that a recent star formation episode has taken place in their central regions (see Section 1.1.1). We now introduce a new sub-class, which is constituted by dwarf ETGs with disk features ("dE(di)"; Lisker et al. 2006c). The dE(di) sub-class goes beyond being simple dS0s, which are restricted to having a featureless disk component. Instead, dE(di)s can also present embedded disk substructures, such as bars and spiral arms, akin to a dwarf spiral (dSp) galaxy. However, in stark contrast to dSps, the disk substructures of dE(di)s are very faint, and stay mostly hidden in the comparatively much brighter diffuse light that dominates the galaxy. In this work, we mainly focus on the study of faint embedded substructures such as these. More details are provided in the upcoming Section 1.4.

The study of Lisker et al. (2007) shows that the intrinsic shape of dwarf ETGs is dependent on their morphological sub-class. The axis ratio can be used as a proxy for the galaxy shape, and is defined as the ratio of the minor axis length to the major axis length of a galaxy. As such, an axis ratio of 1 indicates that the galaxy is perfectly spheroidal or round (i.e., circular in projection), and an axis ratio $\ll 1$ indicates that the galaxy is highly ellipsoidal or flat (i.e., highly elliptical in projection). According to Lisker et al. (2007), dwarf ETGs can span a wide range of axis ratios, ranging between $0.25 - 1.00$. On the one hand, they find that both the bright and faint dE(N) galaxies tend to be more spheroidal (or round) in shape. On the other hand, the dE(di), dE(bc), and bright dE(nN) galaxies display more ellipsoidal (or flattened) shapes, and could be understood to be shaped like thick disks. The faint dE(nN) galaxies appear to be somewhat in between these two categories. Interestingly, Lisker et al. (2007) also claim to observe a morphology-density relation within the dwarf ETG sub-classes. The bright and faint dE(N)s appear to be a relaxed population, concentrating towards the cluster

center; while dE(di)s, dE(bc)s, and bright dE(nN)s appear to be an unrelaxed population, showing no clustering. Consequently, the different environmental histories of dwarf ETGs seem to be playing a role in shaping their observable properties. The role of the environment is further addressed in the upcoming Section 1.2.

1.1.3 Dynamical Properties

Dwarf ETGs constitute low mass objects, with stellar masses that are typically smaller than $\log(M_*/M_\odot) = 9.0 - 9.5$. According to the traditional Tully-Fisher (Tully & Fisher 1977) and Faber-Jackson (Faber & Jackson 1976) relations, both the rotational support ($v_{\rm rot}$) and dispersion support (σ_v) of the stars of a galaxy correlate with the overall luminosity, and thus with the stellar mass of the host system (Schneider 2006). More modern approaches propose a unified dynamical scaling relation (Zaritsky et al. 2008; Cortese et al. 2014), where a combination of the rotational and dispersion support ($\sqrt{0.5\,v_{\rm rot}^2 + \sigma_v^2}$) has been found to strongly correlate with the baryonic content of a galaxy. As such, due to their small stellar masses, dwarf ETGs are among the galaxies with the smallest stellar velocities that can be observed.

The majority of normal-sized, luminous ETGs tend to be dispersion supported, with the relative contribution of the rotational component being significantly smaller (i.e., $v_{\rm rot} \ll \sigma_v$; Schneider 2006). If dwarf ETGs were to be simply interpreted as downsized versions of normal ETGs, then we would also expect them to be predominantly dispersion supported. However, several studies find that dwarf ETGs are instead a dynamically-complex population, presenting various degrees of rotational support (Toloba et al. 2011, 2015; Ryś et al. 2013; Janz et al. 2017; Bidaran et al. 2020). While some dwarf ETGs are clearly dispersion supported ($v_{\rm rot}/\sigma_v \lesssim 0.1$, measured within the effective radius), there are others that are unquestionably rotationally supported ($v_{\rm rot}/\sigma_v \lesssim 1.5$, measured within the effective radius), with a wide range spanning in between (values according to the study by Toloba et al. 2015). The internal dynamics of dwarf ETGs appear to be strongly dictated by their environmental context. On the one hand, slow-rotating dwarf ETGs tend to be commonly found in high-density environments, such as near the core of galaxy clusters. On the other hand, fast-rotating dwarf ETGs are instead more common in low-density environments, such as the cluster outskirts (Toloba et al. 2015). Refer to the upcoming Section 1.2 for a deeper look into the role that the environment can play.

Based on the internal velocity distribution of dwarf ETGs, it is possible to estimate their dynamical mass (Schneider 2006). The dynamical mass serves as a proxy of the total mass of the galaxy, as it includes the gravitational influence of both baryonic (i.e., stars, gas, and dust) and non-baryonic matter (i.e., dark matter). Therefore, by comparing the dynamical mass estimate with the stellar mass estimate, it is possible to derive the dark matter content of a galaxy. In the case of the dwarf ETG population, it is estimated that about half of their total mass is constituted by dark matter (Toloba et al. 2011, 2012), with a median dark-to-total mass ratio ($f_{\rm DM}$) measured within the effective radius of $f_{\rm DM} = 0.46 \pm 0.18$ (Toloba et al. 2014). To put things into perspective, the dark matter fraction of normal ETGs is considerably

smaller, with estimates indicating that only about a tenth of the total mass is constituted by dark matter ($f_{\rm DM} = 0.13$; Cappellari et al. 2013). In conclusion, dwarf ETGs are more dark matter dominated than their normal-sized counterparts (Ryś et al. 2014).

1.2 Environments

It is possible to find dwarf ETGs in a variety of environments, which can potentially induce different environmentally-driven processes. To begin with, in Section 1.2.1, we describe the three main environments that host galaxies: the field, galaxy groups, and galaxy clusters. We also address how common dwarf ETGs are in each environment compared to other galaxy types. Then, in Section 1.2.2, we describe the different environmental processes that a galaxy can experience during its lifetime, and the overall efficiency of each process in a given environment. We particularly focus on the effect that each process can have on dwarf ETGs.

1.2.1 Types of Environments

As follows, we define and describe the field, galaxy group, and galaxy cluster environments. As we will see, the presence of dwarf ETGs is strongly dependent on the environmental density: dwarf ETGs are extremely rare in low-density environments, such as the field, while in contrast they are the most common type of galaxy in high-density environments, such as galaxy clusters.

► Field environment.

First, we consider the field, the lowest density environment in which galaxies can be found in. The field can be understood as an existence in isolation. Field galaxies, therefore, can be defined as galaxies that are located more than 1.5 Mpc away from the nearest massive galaxy, as it has been observed that galaxies that are closer than this distance begin to be affected by each other's presence (Geha et al. 2012). With no galaxies in the immediate vicinity, a field galaxy is not exposed to external influences, such as the environmental processes described in the next Section 1.2.2. Instead, its evolution is fundamentally driven by its own internal processes, which are in charge of regulating the stellar feedback (i.e., the persistence versus the cease of star formation). The great majority of field galaxies are star-forming LTGs, like spiral galaxies or irregular galaxies, with non-star-forming ETGs being significantly more rare.

Only a handful of isolated, quenched dwarf galaxies have been found up to date. Some have been observed in our Local Group (e.g., KKR 25 and KKs 3, Makarov et al. 2012; Karachentsev et al. 2015), while there are others that have been found farther away (e.g., APPLES 1 and COSMOS-dw1, Pasquali et al. 2005; Polzin et al. 2021). Consequently, the detection of dwarf ETGs belonging to the field, seemingly in isolation with no close neighbors, constitutes an extremely rare event. What is more, field galaxies in the dwarf regime, with stellar masses $< 10^9$ $M_\odot$, are usually believed to be unable to permanently quench their star formation solely through internal processes. As such, the quenched fraction of field dwarf galaxies is estimated to be as low as 0.06% (Geha et al. 2012).

► Galaxy group environment.

We now consider galaxy groups, an environment that is comparatively denser than the field. Galaxy groups can contain as low as a few galaxies up to hundreds of galaxies that are gravitationally bound. According to Schneider (2006), galaxy groups are typically constituted by $\lesssim 50$ members, distributed within a sphere of diameter $\lesssim 1.5h^{-1} \approx 2.2$ Mpc[1], and with a total mass ranging between $10^{12} - 10^{13}$ $M_\odot$. The majority of the mass in a galaxy group is not in the form of visible stars and gas, but in the form of non-baryonic, dark matter. Depending on the size of the group, the velocity dispersion of its members can reach up to 300 km s^{-1}. Additionally, group members are usually immersed in a hot diffuse gas, named the intergalactic medium (IGM), which emits at high frequencies (X-ray radiation).

An example of such galaxy associations are compact galaxy groups, like the Hickson Compact Groups (HCGs; Hickson 1982), consisting in dense accumulations of galaxies conformed by four or more bright members (Schneider 2006). However, the closest example of a galaxy group is our own Local Group, centered around our own Galaxy, the Milky Way, and the Andromeda galaxy (M31). The Milky Way and Andromeda are both big spiral galaxies. This duet is accompanied by the Triangulum galaxy (M33), which is a smaller spiral galaxy, the Small and Large Magellanic Clouds (SMC and LMC, respectively), which are both dwarf irregular galaxies, plus a multitude of other dwarf galaxies (~ 100 dwarfs, McConnachie 2012).

Compared to the field environment, the fraction of dwarf ETGs drastically increases in a group environment (see, e.g., group dwarf ETGs in Jerjen et al. 1998, 2000a). The opposite is true for dwarf LTGs, which are comparatively more common in the field. Moreover, the larger the velocity dispersion of a group (which acts as a tracer of its total mass), the larger the relative fraction of ETGs in respect to LTGs (Schneider 2006). Overall, this contrast between the field and group environments is an indication that environmentally-driven processes are fundamental in building up the dwarf ETG population.

► Galaxy cluster environment.

Galaxy clusters are, in essence, bigger galaxy groups in all possible aspects. They constitute some of the highest density environments in the Universe, and can contain from hundreds to thousands of gravitationally-bound galaxies. According to Schneider (2006), galaxy clusters are typically conformed by $\gtrsim 50$ members, distributed within a sphere of diameter $\gtrsim 1.5h^{-1} \approx 2.2$ Mpc[1], and with a total mass ranging between 10^{13}–10^{15} $M_\odot$. They are estimated to contain even a larger amount of dark matter than the amount contained in groups. Cluster members can reach velocity dispersions well above 300 km s^{-1}, sometimes in the order of 1000 km s^{-1}. Additionally, the IGM of a galaxy cluster is comparatively hotter and metal-richer than a group IGM, reaching temperatures above 10^7 K.

The two closest and most massive aggregations of galaxies are the Virgo and Fornax galaxy clusters, located at about 16.5 Mpc and 20.0 Mpc away from us, respectively (Blakeslee et al.

[1]The value of h is intertwined with the Hubble constant, which can be defined as $H_0 = 100h$ km s^{-1} Mpc^{-1}. We adopt a value of $h = 0.674$, assuming that $H_0 = (67.4 \pm 0.5)$ km s^{-1} Mpc^{-1} (Planck Collaboration et al. 2020).

2009). The Virgo cluster is very massive ($\sim 10^{14}$ $M_\odot$), loosely concentrated, and conformed by several galaxy subclumps, giving it an irregular appearance. In comparison, the Fornax cluster is less massive ($\sim 10^{13}$ $M_\odot$), but much more compact and dense, thus adopting a more regular distribution. As such, the Virgo cluster can be understood as a dynamically young cluster, caught in the process of assembly, while in contrast the Fornax cluster is a dynamically old cluster, being close to virial equilibrium or relaxation. Therefore, they fundamentally constitute two different cluster environments. In this work, we analyze and compare two samples of dwarf ETGs, one belonging to the Virgo cluster (see Chapter 3) and the other belonging to the Fornax cluster (see Chapter 4). We provide a detailed description and an in-depth comparison between the two clusters in the future discussion Section 5.1.

Dwarf ETGs are by far the most common type of galaxy in cluster environments. For example, estimates indicate that they constitute approximately $3/4$ of the overall galaxy population in both the Virgo and Fornax clusters (76% and 77%, respectively; Ferguson 1989a). In addition, galaxies in the dwarf regime also follow the morphology-density relation (Dressler 1980) that is observed in normal-sized galaxies, as the fraction of dwarf ETGs steadily increases towards the center of clusters, with dwarf LTGs showing the opposite trend (Venhola et al. 2019).

Overall, it appears that the presence (or absence) of dwarf ETGs, and the relative fraction they represent of the total galaxy population, is strongly dependent on the environment. As we will see in the next Section 1.2.2, this is mainly due to the fact that dwarf ETGs are extremely susceptible to environmentally-induced processes, which can effectively shape their appearance and dictate their properties.

1.2.2 Environmental Processes

Throughout their lifetime, dwarf ETGs can be affected and thus shaped by a variety of environmental processes. For simplicity, we can classify environmental effects into two main categories. On the one hand, we have gravitational processes, which involve the gravitational interaction between a galaxy and its surrounding environment. These processes include tidal harassment and galaxy mergers. On the other hand, we have hydrodynamical processses, which involve the interaction between the interstellar medium (ISM) of a galaxy and its surrounding intergalactic medium (IGM). These processes include ram-pressure stripping, turbulent viscous stripping, thermal evaporation, and starvation. In the following Sections, we define and describe each process, state their main driving parameters, and explain how relevant (and thus how efficient) they are in a given environment —in the field, in galaxy groups, and in galaxy clusters. Finally, we address our objects of study, dwarf ETGs, and the potential effect that each environmental process can have on them.

► Tidal harassment.

The physical process of "tidal harassment" (Moore et al. 1996, 1998, 1999) involves the gravitational interaction of a galaxy with the potential well of an external system. Tidal harassment

is usually classified into two categories: gravitational interactions between galaxy systems ("galaxy-galaxy" harassment), and gravitational interactions between a galaxy system and the potential well of their host group or cluster ("galaxy-cluster" harassment).

On the one hand, we have galaxy-galaxy harassment, in which a galaxy becomes perturbed by the close fly-by encounter with another galaxy. The strength of this gravitational interaction is mainly dictated by the relative distance between the two galaxy systems, in relation to the radial extension of the galaxies. The closer they are and the larger they are, the stronger the tidal force they will experience. The relative mass of the galaxies also plays a role, with more massive galaxies exerting larger tidal forces. Galaxy-galaxy harassment is more likely to happen in high number density regions, such as the core of galaxy clusters. However, due to the high relative velocities between cluster members, the duration of the tidal interaction is short. Consequently, although galaxy-galaxy interactions are more infrequent in low number density regions (such as galaxy groups and the field), they are also longer-lived, thus causing larger perturbations overall (Boselli & Gavazzi 2006).

On the other hand, we have galaxy-cluster (or group) harassment, in which a galaxy becomes perturbed by the interaction with the tidal field of their host cluster (or group). The more massive the galaxy cluster (or group) is, then the bigger its potential well. As a result, galaxies are more susceptible of experiencing this type of tidal harassment in cluster environments than in group environments. The mass of the galaxy is also important, with low-mass, dwarf galaxies being particularly susceptible to the tidal force of their host system. Additionally, the efficiency of galaxy-cluster harassment is strongly dependent on the orbit of the galaxy. Galaxies in plunging orbits passing through the cluster core experience strong harassment; conversely, recent infalls still on the cluster outskirts barely experience any harassment (Smith et al. 2010, 2015, 2021).

Tidal harassment can induce in a galaxy a variety of transformations. First, the galaxy can suffer from mass stripping, and lose dark matter, stars, gas, and dust, depending on the gravitational bounding of each component (see Boselli & Gavazzi 2006, and references therein). The galaxy can also undergo morphological transformations, due to this externally-induced perturbation on their internal dynamics. These transformations can be mild; inducing small asymmetries on the galaxies, or more significant; like warping disks and producing tidal tails. In the most extreme case, rotation-supported disks can be transformed into dispersion-supported spheroids; i.e., late-type galaxies becoming early-types (Bialas et al. 2015). Thus, the galaxy-cluster harassment scenario helps to support the gradual build-up of the morphology-density relation (Dressler 1980). Alternatively, tidal harassment can also cause the formation of structural features, instead of erasing them. For example, disk features (such as spiral arms or bars) can be tidally triggered by the group or cluster potential on a featureless galaxy that has a rotation-supported component, according to numerical simulations (Smith et al. 2021).

Let us now address our object of study. Dwarf ETGs, due to their low masses and small sizes, are unlikely to experience strong effects from galaxy-galaxy harassment, unless it consists in a very close fly-by encounter. However, due to their shallow potential wells and their ubiquitous presence in high density environments, they are the prime candidates for experi-

encing galaxy-cluster harassment. Therefore, if a dwarf ETG is a member of a galaxy cluster for a long enough time, it is highly probable that it will eventually suffer from some level of perturbations caused by the tidal field of the cluster potential.

► **Galaxy mergers.**

Under the hierarchical structure formation scenario (addressed in the upcoming Section 1.3), large, massive systems are formed from the gradual accretion and merging of small, low-mass systems (White & Rees 1978; Davis et al. 1985; Cole et al. 2000). Consequently, galaxies are expected to experience merger events as a normal part of their formation and evolution. "Galaxy mergers" can be understood as a more extreme case of galaxy-galaxy harassment (see previous Section), in which instead of a close fly-by encounter, the galaxies collide and merge into one. The outcome of a merger event depends on several parameters, such as: the orientation and trajectory of the collision, the dynamical support of the systems, their relative velocities, and most importantly, their mass ratio (Schneider 2006). Based on the relative masses, galaxy mergers are usually classified into two types: "minor mergers" and "major mergers".

On the one hand, minor merger events occur when there is a big mass ratio, with the source galaxy being significantly more massive than the galaxy being accreted. In this case, the properties of the source galaxy remain mostly the same. In contrast, the accreted galaxy is completely torn apart by the tidal field of the source galaxy, with the stars and dark matter of the former being incorporated into the massive halo of the latter (Schneider 2006).

On the other hand, major merger events occur when there is a small mass ratio, with both galaxies having comparable masses. This time, both galaxies will experience strong transformations, altering their properties and appearance. For example, rotation-supported disks that collide will likely change into dispersion-supported spheroids. They can also suffer from significant mass loss, producing tidal tails and ejecting stars and most of their gas into the intracluster or intragroup medium. The shock of the collision can also heat up their remaining gas content, effectively suppressing any further star formation. Conversely, perturbations on the gas may trigger massive star formation episodes (Schneider 2006). Due to these different outcomes, merger events can also be classified based on the gas content of the galaxies. Collisions between gas-rich galaxies are denominated as "wet mergers", collisions of gas-poor galaxies are "dry mergers", and collisions between gas-rich and a gas-poor galaxies are "mixed mergers".

In a first instance, it would appear that the frequency of merger events should increase with the galaxy number density. However, high density regions also have high velocity dispersions, meaning that any encounter between galaxies is short-lived, and thus is less likely to lead to a merger of two systems into one (Fujita 2004; Mihos 2004). Therefore, just as with the physical process of galaxy-galaxy harassment, the probability of a galaxy merger is significantly higher in lower density environments, such as in galaxy groups, where the relative velocity between galaxies is lower and the duration of the interaction is longer (Makino & Hut 1997; Boselli & Gavazzi 2006).

Our objects of study, dwarf ETGs, are also expected to experience a higher merger rate in low density regions, such as in groups. As dwarf systems are the most common type of galaxy in the Universe, it is highly probable that they stumble upon other low-mass galaxies like themselves. Dwarf-dwarf interactions would constitute major merger events, in which a dwarf ETG serves as a precursor for more massive galaxies, such as giant elliptical galaxies. In this case, the properties of the dwarf ETG would be drastically transformed, probably ceasing to be a dwarf altogether by becoming a more massive system. However, it has been found that mergers between dwarf LTGs (i.e., wet mergers) are considerably more common than major mergers involving dwarf ETGs (i.e., dry or mixed mergers; Paudel et al. 2018). Conversely, dwarf-giant interactions would constitute minor merger events, in which a dwarf ETG adopts the role of the galaxy being accreted by its more massive counterpart. In this situation, the dwarf ETG would eventually be destroyed, becoming part of the source galaxy. Due to the intrinsically low masses of dwarf ETGs, it is improbable for them to act instead as the source galaxy that is accreting an even smaller galaxy. In conclusion, both major and minor mergers are strongly disruptive events for a dwarf ETG, completely transforming their properties.

► **Ram-pressure stripping.**

The physical process of "ram-pressure stripping" (Gunn & Gott 1972) involves the interaction between the interstellar medium (ISM) of a galaxy and the surrounding intergalactic medium (IGM). The strength of the ram pressure depends on two main parameters: the density of the IGM, and the velocity of the galaxy passing through the IGM. If this external pressure exceeds the gravitational force that binds together the gas of the galaxy, then its ISM is effectively stripped away and becomes part of the IGM (Boselli & Gavazzi 2006). As the surface density of both the gaseous and stellar components of a galaxy increases with the galaxy mass, ram-pressure stripping is more effective in low-mass, dwarf systems as they have a lower binding energy (Mori & Burkert 2000; Marcolini et al. 2003). Therefore, dwarf gas-rich galaxies (such as dwarf spirals and dwarf irregulars) are more susceptible to the effects of ram pressure than giant gas-rich galaxies (such as giant spirals).

This effect on the gaseous component of the galaxy affects its ability to form stars. If the gas content is partially removed, then the star formation rate of the galaxy decreases. If the gas content instead is completely removed, then any any further star formation in the galaxy is efficiently suppressed. As a consequence, from the dwarf galaxy range to the giant galaxy range, ram-pressure stripping can induce the transformation of late-type, star-forming systems into early-type, non-star-forming systems (van Zee et al. 2004b; Haines et al. 2007; Boselli et al. 2008; De Rijcke et al. 2010). However, ram-pressure stripping can also lead to a momentary burst of star formation, by compressing the cold gas of the galaxy in the direction of its infall (Steyrleithner et al. 2020). As ram pressure is not instantaneous, it is sometimes possible to observe long gaseous tails drifting away from the galaxies that are being stripped, giving them the appearance of jellyfish galaxies (Roediger et al. 2014). In some cases, tidal dwarf galaxies can form from the stripped material (Smith et al. 2013).

Ram-pressure stripping is more likely to occur in high density environments with a rich

IGM, such as the core of galaxy clusters. As a consequence, this physical process contributes to the build-up of the morphology-density relation (Dressler 1980), which states that ETGs tend to reside in high density regions (such as the cluster core), while conversely LTGs tend to reside in low density regions (such as the cluster outskirts).

Our objects of study, dwarf ETGs, traditionally fall under the classification of passive systems that do not contain gas. However, they could still contain small-enough gas fractions that are not easily detectable, and consequently do not affect the overall morphology and the measurable properties of the galaxy. In other cases, such as the case of blue-cored dwarf ETGs, their innermost regions show signatures of recent star formation, from which the presence of gas can be inferred (Urich et al. 2017; Hamraz et al. 2019). Due to the shallow potential wells of dwarf ETGs, any remainder gas content could be potentially stripped in an efficient way by the ram pressure exerted by the IGM they are immersed in.

► **Turbulent viscous stripping.**

Similar to ram-pressure stripping (see previous Section), the physical process of "turbulent viscous stripping" (Nulsen 1982) involves the interaction between the gaseous component of a galaxy and the gas of its surroundings. Fundamentally, viscous stripping is dependent on the relative differences in velocity, temperature, and density of the ISM and IGM. On the one hand, we have the ISM of a galaxy, which is usually slow-moving, cool, and dense. On the other hand, we have the surrounding IGM, which is comparatively fast-moving, hot, and diffuse. These differences in the gas properties can induce instabilities in the gas of the galaxy, such as a Kelvin–Helmholtz instability due to the difference in relative velocities at the ISM-IGM interface. If the induced perturbations manage to overcome the gravitational force that binds the gas to its galaxy, then the outer layers of its ISM will be inevitably stripped away. If the opposite is true, then the gravitational force will be able to eventually stabilize the outer layers of the ISM, incurring in no gas loss for the galaxy (Fillingham et al. 2016).

The effects of turbulent viscous stripping on a galaxy are expected to be similar to the ones caused by ram-pressure stripping (Boselli & Gavazzi 2006). Overall, the partial removal of gas leads to a reduction in the star formation capability, and a total cease of star formation if all of the gas is eventually lost. As the gravitational binding energy increases with the mass of a galaxy, more massive systems (like spiral galaxies) are more likely to retain their gas than low-mass systems (like dwarf spiral or dwarf irregular galaxies). Similarly, as in the case of ram-pressure stripping, the efficiency of turbulent viscous stripping increases with the environmental density. Therefore, the high density, high temperature IGM at the core of galaxy clusters constitutes the ideal environment for gas-stripping processes to take place.

In regards to our objects of study, dwarf ETGs, the possible occurrence of turbulent viscous stripping depends both on their remaining gas content and their surrounding environment. If a dwarf ETG with some gas is on an infall trajectory through a dense IGM, then it is very likely that it will experience gas stripping. In general, due to the low mass and shallow potential wells of dwarf ETGs, gas-stripping processes such as ram-pressure stripping and turbulent viscous stripping are expected to be very efficient in removing any gas that is still present.

► Thermal evaporation.

The physical process of "thermal evaporation" (Cowie & Songaila 1977; Cowie & McKee 1977) also concerns the interaction between the ISM of a galaxy and the surrounding IGM. As its name indicates, the main parameter driving this process is the temperature; in particular, the relative temperature between the ISM and IGM. However, several other parameters such as the density of the IGM also play a role, although to a lesser extent (Boselli & Gavazzi 2006). Due to the difference in temperature between the hot IGM and the cold ISM, a steep temperature gradient is produced at the IGM-ISM interface. At this interface, heat transfer from the IGM to the ISM can effectively increase the thermal energy of the latter. If the overall increase in energy surpasses the gravitational binding energy of the gas, then it "evaporates" and becomes part of the IGM. This process acts from the outside in; first affecting the outer layers of the ISM, and lastly its innermost regions.

In common with the previously addressed gas-stripping processes, thermal evaporation also leads to the loss of cold gas from a galaxy, reducing its star formation rate. In the case that all of its ISM is evaporated, then the star formation would cease altogether. The process of thermal evaporation is more efficient and more likely to happen in high density regions, such as in massive galaxy clusters and their core regions, as their IGM can potentially reach very high temperatures.

Once again, the level of influence of this hydrodynamical process on our objects of study, dwarf ETGs, depends on their gas content and surrounding environment. Any remaining gas in a dwarf ETG can be expected to be easily evaporated by a hot IGM, due to the low gravitational binding energy of the dwarf system.

► Starvation or strangulation.

The last physical process corresponds to "starvation" (sometimes also called "strangulation"), originally proposed as an environmental mechanism to explain the origin of lenticular (S0) galaxies (Larson et al. 1980). The hydrodynamical interaction between the cold ISM and the comparatively hot surrounding IGM can cause the removal of the extended gaseous halo that envelops a galaxy. As a result, there is a decline or truncation in the gradual infall of halo gas into the more internal star-forming regions of the galaxy. With no more gas becoming available, the galaxy will continue forming stars until its gas reservoir is depleted. At this point, the galaxy ceases its star formation, and transitions into a passive, quenched system (Boselli & Gavazzi 2006; Boselli et al. 2008). Consequently, the gas starvation process can be used to explain the sequential transformation of star-forming spiral galaxies into non-star-forming S0 galaxies. With the decrease (and eventual halt) in star formation, the spiral features become progressively less pronounced, eventually fading altogether. This way, spiral galaxies transition into passive spirals, which later transition into S0 galaxies (Bekki et al. 2002).

In sharp contrast with other gas-stripping processes (such as ram-pressure stripping, turbulent viscous stripping, and thermal evaporation), gas starvation acts on long timescales, in the order of several gigayears. This timescale is linked to the gas consumption rate of a

galaxy due to star formation (Balogh et al. 2000; Treu et al. 2003). Field galaxies with a gaseous component are expected to begin experiencing gas starvation as soon as they become part of a comparatively denser environment, like a galaxy group or cluster. However, unlike the aforementioned gas-stripping processes, there is no need for the galaxies to be in very high density regions, such as the cluster core. It has been found that the starvation process is already effective in low density regions, such as in small groups and the far outskirts of clusters. Therefore, it can help explain why galaxies located at large clustercentric distances show a systematic decline of their star formation relative to field galaxies (Balogh et al. 2000; Treu et al. 2003). Gravitational processes predominant in low density regions, such as galaxy-galaxy harassment, are also expected to contribute to gas starvation. In conclusion, starvation is a slow, gradual, and common process, which most galaxies (with the exception of isolated field galaxies) will experience during their lifetime.

Finally, our objects of study, dwarf ETGs, are prime candidates to have suffered from starvation in the past, due to their current lack of significant star formation. Additionally, dwarf ETGs are commonly found in either group or cluster environments, which is where the starvation mechanism begins to take place. As such, it is highly probable that any gas remaining in the halo of a group or cluster dwarf ETG will be (or is being) affected by starvation.

1.3 Formation

In order to understand the formation and evolution of dwarf ETGs, there are two main scenarios to be considered. First, in Section 1.3.1, we address the hierarchical structure formation scenario. Then, in Section 1.3.2, we address the environmental transformation scenario. We would like to highlight that these two formation channels are not mutually exclusive; on the contrary, it is very likely that both played an important role in building and shaping the dwarf ETG population as we know it. In particular, we address how each formation scenario can be used to explain the presence of faint substructure features that can sometimes be found embedded in dwarf ETGs.

1.3.1 Hierarchical Formation

To begin with, we consider the hierarchical structure formation scenario (see, e.g., White & Rees 1978; Davis et al. 1985; Cole et al. 2000). This scenario assumes a ΛCDM cosmology (Planck Collaboration et al. 2020) as the concordance model; i.e., a Universe governed by the cosmological constant ("Λ") that represents the dominance of dark energy[2], and that is filled not only with baryonic matter[3] but also with non-baryonic matter (dark matter; "DM"), which is both collisionless and dissipationless[4] (cold; "C"). As a natural outcome of the ΛCDM model,

[2]Dark energy drives the accelerated expansion of the Universe, and constitutes a constant, homogeneous energy density with negative pressure.

[3]Baryons are composite subatomic particles constituted by quarks, such as protons and neutrons. Thus, the ordinary, visible matter of the Universe (such as stars, gas, and dust) is mainly composed by baryons.

[4]Collissionless means that DM only interacts with other particles through the gravitational force. Dissipationless means that DM does not emit photons, and thus cannot cool down through radiative processes.

the formation of structures arises from primordial fluctuations in the Universe. From these perturbations, the first gravitationally-bound structures that form are small in size and low in mass. As the Universe evolves, progressively larger (both in size and mass) gravitationally-bound structures are able to assemble from the gradual accretion of smaller structures. In other words, there is a hierarchical order that governs the process of structure formation: small structures collapse first, while bigger structures collapse later.

The hierarchical formation of structures applies at all scales. At large scales, galaxy groups merge to become galaxy clusters, which eventually merge to become galaxy superclusters. Similarly, at comparatively smaller scales, massive galaxies are steadily growing through the accretion of less massive galaxies, which in turn form through mergers of primeval (or proto-) galaxies. As a consequence, small low-mass galaxies should be notoriously more common and abundant than big massive galaxies. This is precisely what we observe in the Universe: there is a prevalence of dwarf systems, such as dwarf ETGs. As such, the formation of dwarf ETGs is a necessary step in the hierarchical structure formation ladder, as they constitute the building blocks of more massive galaxies.

An alternative theory is that the formation of galaxies is not driven by a hierarchical collapse, but instead by a monolithic or primordial collapse (Eggen et al. 1962). In this scenario, a galaxy forms from the gravitational collapse of a single cloud of gas in the early Universe. In other words, all parts of a galaxy are formed at the same time, with no further accretion during their lifetime. This scenario can be quickly ruled out, since it is clearly observed that galaxies do not have a single but instead several stellar populations, each with their own characteristic ages and metallicities. Additionally, ample evidence of galaxy mergers and accretion events can be found both in the distant and local Universe. It is as simple as looking through our front door: our Galaxy, the Milky Way, is surrounded by satellite galaxies that are currently infalling (McConnachie 2012; Bechtol et al. 2015), and presents a multitude of stellar streams formed from dwarf galaxies or globular clusters that already have been torn apart (Shipp et al. 2018).

The appearance and dynamical properties of dwarf ETGs can also be explained through the hierarchical structure formation scenario. If they are gradually formed through the accretion and mergers of smaller systems, then the orbits of its own stars and of the newly accreted stars become perturbed and mixed up, in time giving dwarf ETGs a predominantly smooth spheroidal appearance. Similarly, if the progenitor system was rotationally supported (i.e., its stellar orbits had a preferential order), multiple accretion events can cause it to gradually become dispersion supported instead (i.e., its stellar orbits become more randomly distributed).

In this scenario, the presence of faint embedded substructure features in dwarf ETGs, such as disk substructures and clump substructures, can be understood as follows. One option is that the substructure features in dwarf ETGs are remnant features of the progenitor system, and have managed to at least partially survive even after the galaxy has experienced multiple accretion and merger events. Possibly, these events may not have been impactful enough as to completely erase these substructures. As another option, the substructure features in dwarf ETGs may be an indication that an accretion or merger event took place relatively recently. During this event, the galaxy may have acquired some substructures from the accreted or

merging system; e.g., clump substructures such as star-forming clumps or dust lanes. Alternatively, the formation of some substructures may have been triggered during the interaction; e.g., disk substructures such as bars or spiral arms.

1.3.2 Environmental Formation

To follow, we now consider the environmental transformation scenario (see, e.g., Kormendy 1985; Moore et al. 1996; Boselli & Gavazzi 2006, 2014). In Section 1.2.2, we extensively addressed the different environmental processes that can affect a galaxy during its lifetime. We classified the environmental processes into two main categories: gravitational processes and hydrodynamical processes. What is more, each type of process can be further divided into two subcategories.

On the one hand, there are "small-scale" gravitational processes, such as galaxy-galaxy harassment and galaxy mergers, which concern the gravitational interaction between galaxies. There also are "large-scale" gravitational processes, such as galaxy-cluster harassment, which concern the gravitational interaction between a galaxy and the potential well of the group or cluster they inhabit. On the other hand, there are "short-timescale" hydrodynamical processes, such as ram-pressure stripping, turbulent viscous stripping, and thermal evaporation, which concern the interaction between the cold interstellar medium (ISM) of a galaxy and its surrounding hot intergalactic medium (IGM). There also are "long-timescale" hydrodynamical processes, such as starvation or strangulation, in which the ISM of a galaxy is slowly but steadily depleted by its surrounding IGM. For details on each process, refer to Section 1.2.2.

In the environmental transformation scenario, one (or more) of these environmentally-induced processes shape and transform the properties of a galaxy. This way, it is possible to explain the transition of rotation-supported, star-forming galaxies into dispersion-supported, non-star-forming galaxies. In theory, if given a long enough time, all galaxies in isolation should naturally and slowly transition from the blue cloud to the red sequence due to internal processes (i.e., the eventual depletion of gas and thus the cease of star formation). However, the existence of external, environmental processes can accelerate this transition. In part, this contributes to the morphological segregation observed in different environments (Dressler 1980), where high-density regions such as galaxy clusters predominantly contain non-star-forming elliptical galaxies, while low-density regions such as the field mainly contain star-forming spiral galaxies.

In particular, the formation of dwarf ETGs can be explained through this transformative scenario. They could have been dwarf LTGs (such as dwarf spirals or dwarf irregulars) in the past, which experienced a series of environmental processes that stripped them from their gas, altered the orbits of their stars, and left them mostly "red and dead" as we observe them today. The importance that environmental processes have in shaping the dwarf ETG population can also help to explain the prevalence of dwarf ETGs in high-density environments, such as galaxy clusters, while in contrast they are extremely rare in low-density environments, such as the field (see Section 1.2.1).

This scenario can also seamlessly explain the existence of dwarf ETG with faint embedded substructure features, such as disk substructures or clump substructures, that are found immersed in high-density environments. One option is that the substructure features in dwarf ETGs are remnant features of the progenitor galaxy, which may have likely been a dwarf spiral galaxy if disk substructures are still present, or a dwarf irregular galaxy if clump substructures are still present. In this case, the environmental processes may still not have been able to completely transform these LTGs into ETGs. In this case, dwarf ETGs with disk substructures would constitute transition-type dwarf galaxies. As another option, the environment may be triggering these features in dwarf ETGs, instead of acting by gradually erasing them. For example, disk substructures, such as spiral arms or bars, may be tidally triggered in seemingly featureless dwarf ETGs if they still contain a rotation-supported component (Smith et al. 2021).

1.4 Substructure Features

In this work, we are interested in studying the various types of faint substructure features that can be found embedded in dwarf ETGs. To begin with, in Section 1.4.1, we describe the different types of substructure features that have been observed, which include disk and clump substructures. Then, in Section 1.4.2, we address the different attempts that have previously been made in order to detect and quantify them, which include the unsharp masking, galaxy modeling, and Fourier analysis techniques.

1.4.1 Types of Substructures

For purposes of clarity, we can categorize the substructure features of dwarf ETGs into two sub-classes: disk substructures and clump substructures.

► Disk substructures.

The sub-class of "disky" dwarf ETGs can present embedded "disk substructures", such as bars, spiral arms, rings, dumbbells, inclined disks, and edge-on disks. Thus, this category includes the dS0 population, which has a featureless disk component, and the dE(di) population, which can have disk features.

The presence of embedded disk substructures in dwarf ETGs has been known for a long time (Binggeli & Cameron 1991), and has been widely reported in the literature. The majority of the dwarf ETGs with disk substructures that have been found and studied belong to the Virgo galaxy cluster, owing to its close proximity (e.g., Jerjen et al. 2000b, 2001; Barazza et al. 2002; Geha et al. 2003; Ferrarese et al. 2006; Lisker et al. 2006c, 2007, 2008, 2009; Lisker & Fuchs 2009; Lisker et al. 2018; Janz et al. 2012, 2016). Faint disk features have also been observed in dwarf ETGs belonging to several other galaxy cluster environments, such as in the Fornax cluster (De Rijcke et al. 2003; Venhola et al. 2018; Hamraz et al. 2019), the Coma cluster (Graham et al. 2003; Graham & Guzmán 2003), the Perseus cluster (Penny et al. 2014), and the Ursa Major cluster (Pak et al. 2014). However, on the other side of the spectrum, such

features have also been observed in dwarf ETGs in the field environment, laying in apparent isolation (Graham et al. 2017).

As a consequence, probably more than one formation scenario is needed to explain the origin of these galaxies and their substructure features (Graham et al. 2017). While the environmental transformation scenario may serve as an explanation for their presence in cluster environments, it is not applicable in the field environment (see Section 1.3.2). Therefore, even though they are not commonly found in isolation, their presence in the field environment implies that an additional formation channel must exist, such as through accretion events in the hierarchical merging scenario (see Section 1.3.1).

In Figure 1.3, we present some illustrative examples of disky dwarf ETGs. The galaxy images have been subjected to an imaging analysis technique (unsharp masking, explained in the upcoming Section 1.4.2) that reveals any faint underlying substructures that lie hidden in the bright diffuse light. Their embedded disk features encompass a rich variety of structures, ranging from spiral arms, bars, edge-on disks, inclined disks, and warped or distorted disks.

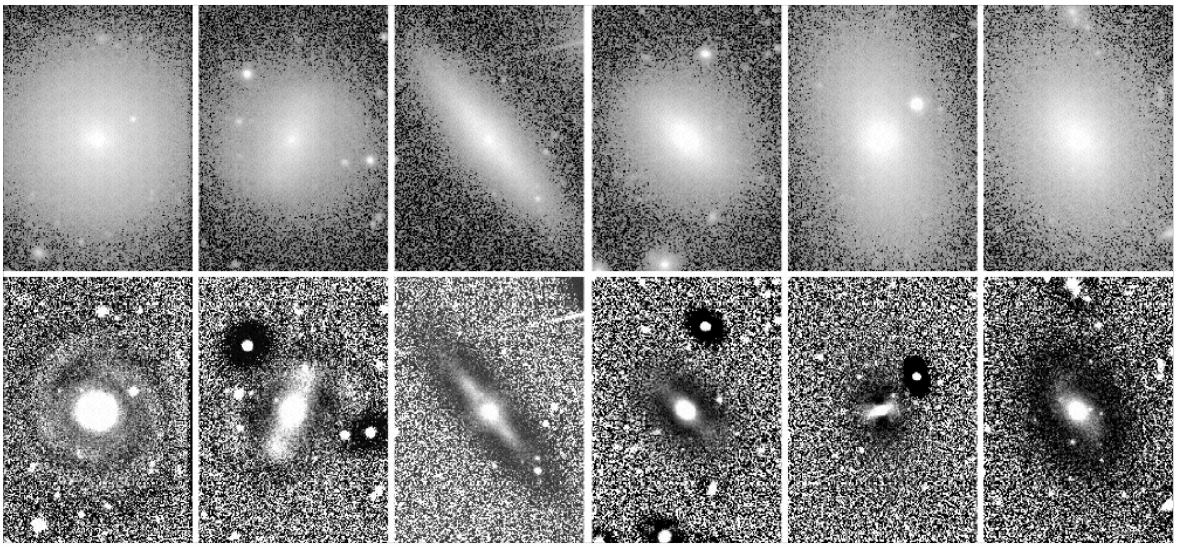

Figure 1.3: Examples of dwarf ETGs with disk substructures. *Top panels:* g, r, and i-band composite images from the SDSS DR4 (Adelman-McCarthy et al. 2006) of six dwarf ETGs from the Virgo cluster. From left to right: dwarf galaxies VCC0308, VCC1896, VCC1304, VCC0990, VCC1183, and VCC2019. *Bottom panels:* unsharp mask images (refer to Section 1.4.2) of the dwarf ETGs. The unsharp masks images were created by convolving (i.e., smoothing) the galaxy image with an elliptical Gaussian kernel that matches the overall shape and orientation of the galaxy, and then dividing the original galaxy image by this smoothed-out image. The size of the Gaussian standard deviation that was used was different for each galaxy. A rich variety of disk substructures are observed in their unsharp mask images: VCC0308 shows spiral arms, VCC1896 shows a bar and weak spiral arms, VCC1304 shows an edge-on disk, VCC0990 shows an inclined disk, VCC1183 shows a bar, and VCC2019 shows an inclined disk that appears to be warped or distorted. Each panel has a vertical scale of 98 arcsec. Image credit: this Figure is adapted from Figure 5 of Lisker et al. (2006c).

► Clump substructures.

The sub-class of "clumpy" dwarf ETGs can present embedded "clump substructures" that adopt the appearance of irregular light overdensities, such as star forming regions, dust lanes, and

off-center nuclei. Thus, this category includes, but is not restricted to, the dE(bc) population, which can have central clump features.

From the beginning, the presence of embedded clump substructures in dwarf ETGs has been interpreted as a signature of either ongoing or recent star formation (Binggeli & Cameron 1991). As such, these irregular features are believed to be constituted by gas and/or dust. Several studies report the existence of clumpy dwarf ETGs in cluster environments, such as in the Virgo cluster (Binggeli & Cameron 1991; Lisker et al. 2006c,b), and in the Fornax cluster (Hamraz et al. 2019). However, they can also be found in group environments, like the case of NGC 205, located in our Local Group (Hodge 1973). As these clump substructures are usually observed in the central region of dwarf ETGs, they have often been associated with the subclass of blue-cored dwarf ETGs (dE(bc)s; Lisker et al. 2006b, refer to Section 1.1.1 for more details and references). However, as we will find out through this work, it is also possible to find clump substructures beyond the central region of dwarf ETGs, extending to more outer regions of the galaxies (refer to Section 4.2).

As with the population of disky dwarf ETGs, multiple formation scenarios may be needed to explain the whole population of clumpy dwarf ETGs (refer to Section 1.3). It is plausible that environmentally-induced processes could play an important role in shaping the properties of the clumpy dwarf ETGs located in high-density environments, such as galaxy clusters. However, their blue and clumpy central regions could also be explained through secular evolution, with the star formation of the galaxies gradually ceasing from the outside-in. As such, some clumpy dwarf ETGs may have even lived a relatively tranquil life: the last drops of star formation could be happening at their centers, before completely fading to red. In this case, being immersed in a high-density environment would have contributed to accelerate this evolution process.

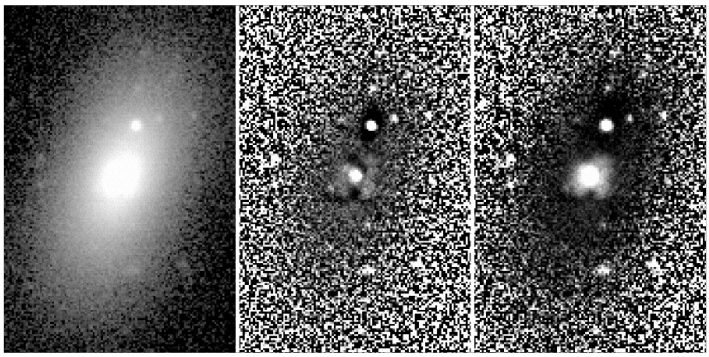

Figure 1.4: Example of a dwarf ETG with clump substructures. *Left panel:* g, r, and i-band composite image from the SDSS DR4 (Adelman-McCarthy et al. 2006) of a dwarf ETG from the Virgo cluster, VCC0781. *Middle panel:* unsharp mask image (refer to the caption of Figure 1.3) of the dwarf ETG. This particular unsharp mask image was created by using a small Gaussian standard deviation when smoothing. *Right panel:* another unsharp mask image of the dwarf ETG, created by using a comparatively larger Gaussian standard deviation when smoothing. The unsharp masks images of VCC0781 reveal clump substructures, which appear as irregular light overdensities in the central region, likely caused by the presence of gas and dust. Each panel has a vertical scale of 98 arcsec. Image credit: this Figure corresponds to Figure 6 of Lisker et al. (2006c).

In Figure 1.4, we present an illustrative example of a clumpy dwarf ETG. The galaxy image has been subjected to the unsharp masking technique (see Section 1.4.2), which reveals clump substructures embedded in the central region of the galaxy, possibly constituted by gas and dust.

1.4.2 Detection and Quantification

Compared to the bright and diffuse main body of dwarf ETGs, any embedded substructure features are much fainter, and thus lie mostly hidden from visual inspection. Therefore, image analysis techniques are necessary in order to be able to first detect and then analyze these features. We proceed to address three distinct techniques that would allow us to do so: the unsharp masking approach, the galaxy modeling approach, and the Fourier analysis approach.

► Unsharp masking technique.

The simplest and most efficient way of revealing underlying substructures in any kind of galaxy image is through "unsharp masking" (Malin 1977). In the unsharp masking technique, the galaxy image is first smoothed through convolution with a kernel function. Then, the galaxy image is either divided by this smoothed-out version of itself, or this smoothed-out version is subtracted from the galaxy image. Both approaches result in the removal of most of the dominant diffuse light, leaving behind the remaining substructures in a so-called "unsharp mask image". In other words, unsharp masking aims to isolate the non-diffuse light from the diffuse light of a galaxy. There are a multitude of studies that have used unsharp masking on different types of galaxies to reveal different types of structures (e.g., McGaugh & Bothun 1990; Erwin 2004; Lisker et al. 2006a; Laurikainen et al. 2014), with some using unsharp masking to specifically study dwarf ETGs with substructure features (e.g., Barazza et al. 2002; Lisker et al. 2006c; Hamraz et al. 2019). In Figures 1.3 and 1.4, we illustrate the potential of the unsharp masking technique, and how it can be used to reveal a rich variety of disky and clumpy substructures in dwarf ETGs.

The success of unsharp masking in revealing what is hidden, however, is tightly dependent on several parameters. On the one hand, there is the choice of the kernel function that is used to smooth the image (i.e., with what to smooth). Typically, a Gaussian function is a good choice for the convolution kernel, as it can smoothly redistribute the light, and has no sharp edges that could potentially introduce artifacts (like in the cases of a box kernel or a top-hat kernel). On the other hand, there is the choice of the size and the geometry (shape and orientation) of the kernel function (i.e., how much to smooth). As a rule of thumb, the kernel size should match the average size of the substructure features present in the galaxy image. Therefore, small kernel sizes reveal small-sized substructures, and large kernel sizes reveal large-sized substructures. In Figure 1.4, it is possible to appreciate how the kernel size affects the appearance of the substructures in the unsharp mask images. Additionally, the geometry of the kernel is also relevant. For a good result, it is recommended for it to match the average shape and orientation of the galaxy. Using the wrong kernel geometry can introduce artificial features in the unsharp mask images, which can be confused with real features (see Lisker

et al. 2006c, in particular their Figure 3). In the case of using a Gaussian function for the convolution kernel, the size of the standard deviation dictates the amount of smoothing, and its shape and orientation dictates the geometry.

More elaborate techniques involving unsharp masking have also been developed; for example, for the purpose of quantifying clumps typically associated with galaxy star-forming regions (Conselice 2003). However, in general, unsharp masking can only be recommended for detection purposes, and not for quantification purposes. This is because the smoothing process inevitably redistributes the light of the galaxy, and thus alters both the actual light content and the resolution of the substructure features that are present in the galaxy image.

In this work, we use the unsharp masking technique as a way to efficiently detect embedded substructure features in dwarf ETGs. Refer to Chapters 3 and 4, in particular to Sections 3.1, 3.3, and 4.2.

► Galaxy modeling technique.

A different possibility is to adopt a modeling approach, and attempt to model the axisymmetric component of the galaxy (i.e., the diffuse light). By subtracting the axisymmetric model from the galaxy image, the non-axisymmetric component containing the substructure features would remain (i.e., the non-diffuse light, constituted by irregular features such as bars, spiral arms, and clumps). Several attempts at the characterization and quantification of the substructure features in dwarf ETGs have followed this approach (e.g., Barazza et al. 2002; Lisker et al. 2006c). However, the modeling of the diffuse component tends to be simplistic, for example, by assuming a single shape and orientation throughout all galactocentric radii (like in Lisker et al. 2006c). This can be a source of problems, as the quality of the model of the diffuse component will directly affect the accuracy with which the true underlying substructure component is represented.

It has been observed that the radial light profiles of dwarf ETGs can be geometrically complex. In other words, their radial light profiles can present twists and turns, with the shape and orientation of their isophotes progressively changing with galactocentric radii (Lisker et al. 2009). In such cases, we cannot expect a simple model, with a single shape and orientation, to provide an adequate and sufficient representation of the diffuse component. Therefore, to be able to perform an accurate analysis and quantification of the substructure component of dwarf ETGs, being first able to properly model the geometrical complexity of their diffuse component is a necessity.

In this work, we develop a new method that, by robustly modeling the diffuse component of the galaxy, aims to accurately identify and extract the substructure features that can be embedded in dwarf ETGs. Refer to Chapter 2, in particular to Sections 2.1, 2.2, and 2.5.

► Fourier analysis technique.

Finally, another possibility is to perform a Fourier analysis. By using this approach, the surface brightness distribution of a galaxy image is decomposed into a Fourier series, which decon-

structs the galaxy into an alternate representation constituted by sine and cosine functions. Such a series is characterized by multiple Fourier modes (m), where each mode contributes a certain amount to the surface brightness distribution of the galaxy. Typically, even-numbered Fourier modes, in particular $m = 2$, are often associated with disk-like features, such as bars and spiral arms (Aguerri et al. 1998; Kraljic et al. 2012). Therefore, if a dwarf ETG with embedded disk substructure features was subjected to a Fourier decomposition, we would expect the features to prominently appear in the 2D Fourier amplitude map of mode $m = 2$. For more details on using Fourier analyses to study the substructure features in dwarf ETGs, refer to Section 3.4.1.

In general, the Fourier analysis of galaxy images can be used to both identify and characterize the different structural components that constitute a galaxy. It has been widely used to study real, observed galaxies (e.g., Elmegreen et al. 1989; Rix & Zaritsky 1995; Aguerri et al. 1998; Aguerri & González-García 2009) as well as simulated galaxies (e.g., Athanassoula & Misiriotis 2002; Kraljic et al. 2012). In particular, its application can also be extended to the dwarf regime, and has already been carried out on dwarf ETGs as an attempt to quantify their faint embedded disk substructure features (Jerjen et al. 2000b; Barazza et al. 2002).

In this work, we explore how the Fourier analysis technique can be used to detect and quantify embedded substructure features in dwarf ETGs. Refer to Chapter 3, in particular to Section 3.4.

1.5 Thesis Outline

In this Thesis work, we study the population of dwarf early-type galaxies (ETGs) with embedded substructure features. We consider two different environments, the Virgo and Fornax galaxy clusters; and two types of substructures features, disk-like and clump-like substructures. We develop a new method that aims to accurately identify and extract these substructure features, allowing us to quantify them (Chapter 2). The method is then applied to dwarf ETGs with substructure features from the Virgo (Chapter 3) and Fornax (Chapter 4) galaxy clusters. The results obtained are then critically compared (Chapter 5) and then summarized (Chapter 6). As follows, we provide a more detailed outline of the contents of this work.

► Chapter 1: "Introduction: Dwarf Early-Type Galaxies".

In the (current) introductory Chapter, we introduce our objects of study, dwarf ETGs. To characterize them, we present their main photometric, structural, and dynamical properties. We then describe the variety of environments they can be found in, including the field, galaxy groups, and galaxy clusters. Galaxies can experience a wide range of environmentally-driven processes, such as tidal harassment, galaxy mergers, ram-pressure stripping, turbulent viscous stripping, thermal evaporation, and starvation or strangulation. We explain these processes and the potential effect they can have on dwarf ETGs. We proceed to address their possible formation scenarios, which include the hierarchical structure formation scenario and the environmental transformation scenario. We then focus on the sub-population of dwarf ETGs with

embedded substructure features. We categorize their substructures into two types: disk-like features and clump-like features. Finally, we report the findings in the literature, and the approaches that have been taken in order to detect and quantify these substructures, including the unsharp masking, galaxy modeling, and Fourier analysis techniques.

► **Chapter 2: "Residual Method for the Extraction of Substructures".**
This Chapter describes the "residual method", a newly developed, iterative procedure that aims to robustly identify and extract the substructure features embedded in a galaxy image. We begin by introducing the concept behind it, followed with a detailed step-by-step description of the method. We then explain the parameter configuration of the method, beginning with the basic parameters, and then addressing the more complex parameters, such as the smoothing kernel size and the sampling step size, and the parameter configuration grid conformed by them. Next, as a means to quantify the substructure features extracted by the method, we introduce the concept of a "residual light fraction", which measures the relative contribution of the substructures to the total light of the galaxy. We proceed by describing the main strengths of the method and its improvements on previous approaches, which are mainly related to the factors of accuracy and adaptability. Finally, we discuss the potential of the method, and the kind of analyses that could be carried out on the extracted substructure features.

► **Chapter 3: "Substructures in Dwarf ETGs of the Virgo Cluster".**
In this Chapter, we analyze a white-band imaging sample of 9 dwarf ETGs with disk substructure features that are part of the Virgo galaxy cluster. We begin by describing the observations and the data reduction, and how we process the data to prepare it for analysis. To characterize the dwarf ETGs of the sample, we derive and present their main photometric and structural properties. The residual method is then applied to the sample, so we specify the adopted parameter configuration and show the results that were obtained. As a means of assessing the robustness of the residual method, we construct a mock galaxy sample and subject it to a variety of tests. We compare the residual method to alternative approaches, such as a simplified version of the method where there is no iterative procedure, and to the unsharp masking and galaxy modeling techniques. Then, to showcase a potential application of the method, we perform a Fourier analysis on the extracted substructure features in order to identify and quantify them. We explain the concept behind the Fourier decomposition, demonstrate the advantages of directly processing the extracted substructures instead of the original galaxy images, and finally present the results obtained.

► **Chapter 4: "Substructures in Dwarf ETGs of the Fornax Cluster".**
In this Chapter, we analyze a g and r-band imaging sample of 23 dwarf ETGs with disk and clump substructure features that are part of the Fornax galaxy cluster. To begin with, we introduce the data, which consists in a multi-band imaging survey and a dwarf galaxy catalog of the Fornax cluster. Next, we describe how we process and prepare the g and r-band imaging data of all the dwarf galaxies in the catalog, which includes: creating image cutouts,

matching point spread functions (PSFs), coadding images, and constructing unsharp mask images. From these processed images, we identify based on several criteria the dwarf ETGs that present substructure features and construct our sample. We then derive and present their main photometric and structural properties. The residual method is then applied to the sample, so we specify the adopted parameter configuration and show the results that were obtained, highlighting the different behavior of the disk and clump substructures. Then, to showcase a potential application of the method, we perform a color analysis on the dwarf ETG sample, in which we consider their diffuse and substructure components separately. We compare the colors of their diffuse and substructure components, addressing the observed differences between the disky and clumpy dwarf ETG subsamples. Finally, we describe the stellar population analysis we carry out based on the computed colors.

► **Chapter 5: "Discussion: From Virgo to Fornax".**

In this Chapter, we provide an in-depth discussion of our results and their implications. We begin by addressing the multiple factors that may be influencing and/or biasing the Virgo and Fornax dwarf ETG samples. First, the two samples are in different cluster environments, so we describe and compare the properties of the Virgo and Fornax galaxy clusters. Then, we evaluate the relative efficiency of various environmentally-driven processes in each cluster environment, and how they could have shaped the properties of their dwarf galaxy populations. Second, the two samples have different data sources, so we describe and compare the properties of the imaging data. In particular, we address the differences in data quality, such as the imaging resolution and imaging depth. Taking these factors into account, we proceed to describe and compare the photometric properties, structural properties, and the results obtained through the residual method for the two samples. We also make a brief link to simulations, and evaluate if tidal harassment by the cluster environment can serve as a possible explanation for the presence of disk substructures in dwarf galaxies. Finally, we attempt to constrain the possible formation and evolution scenarios of the dwarf ETG population with embedded substructure features. For this purpose, we critically consider the results obtained given the differences in cluster environment (Virgo vs. Fornax) and the differences in substructure types (disky vs. clumpy).

► **Chapter 6: "Conclusions".**

In the last Chapter, we wrap up all that we have learned through this Thesis work. First, we summarize the main findings and results of each Chapter. Then, by considering everything together, we draw our main conclusions.

2

Residual Method for the Extraction of Substructures

This Chapter addresses the "residual method", a newly developed procedure for the extraction of the substructure features of a galaxy. This Chapter is organized as follows. First, we introduce the concept in Section 2.1, followed by a detailed step-by-step description of the method in Section 2.2, while the configuration parameters of the method are explained and specified in Section 2.3. As a means of quantifying the extracted substructures, we introduce the concept of a "residual light fraction" in Section 2.4. Finally, the main strengths of the method and its improvements on previous approaches are described in Section 2.5, with some of its potential applications being discussed in Section 2.6.

2.1 The Concept

In general terms, the "residual method" consists in a newly developed procedure that aims to accurately identify, isolate, and extract the substructure features present in a galaxy image. Its development, subsequent testing, and fine tuning were carried out based on its application to a sample of dwarf ETGs that have underlying substructure features. This dwarf ETG sample is later described and analyzed in Chapter 3. Therefore, when testing the intended functionality of the method, we found it to work reliably in this particular science case, where faint substructures are embedded in the more homogeneous, and much brighter, main body of a galaxy.

The residual method is a robust iterative procedure that gradually separates a galaxy image into two distinct components, as illustrated in Figure 2.1. On the one hand, it produces a

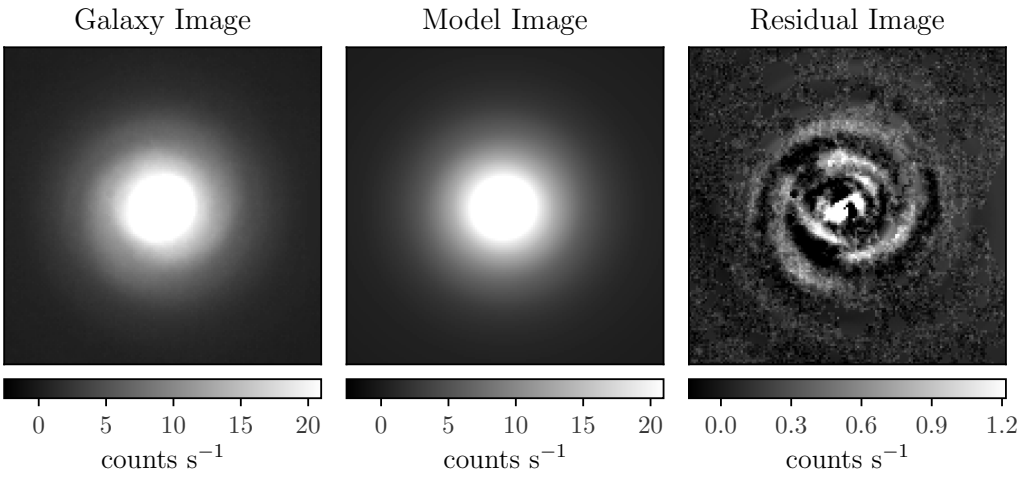

Figure 2.1: Image products of the residual method. As an example, the case of Virgo dwarf galaxy VCC0308 is shown. This galaxy is part of the dwarf ETG sample presented in Chapter 3, and is used as an example throughout this current Chapter. *Left panel:* original galaxy image. *Middle panel:* galaxy model image, containing the diffuse component of the galaxy. *Right panel:* galaxy residual image, containing the substructure component of the galaxy. These images relate to one another according to Equation 2.1. The images have their own gray-scale bar in units of counts s^{-1}, and are 100×100 arcsec^2 in size. North is up, east is to the left.

galaxy model image that contains the dominant, diffuse component of the galaxy. On the other hand, it produces a galaxy residual image that contains the secondary, substructure component of the galaxy. Conceptually,

$$\text{Galaxy image} = \underset{\text{(Diffuse component)}}{\text{Model image}} + \underset{\text{(Substructure component)}}{\text{Residual image}} \quad . \tag{2.1}$$

Initially, the galaxy model image is partially contaminated by light coming from the galaxy's underlying substructure features. Through an iterative loop, this extra light is progressively shifted to the galaxy residual image. The iterations end once the level of pollution in the model is minimized, and the majority of the substructure light is contained in the residual map. Thus, the galaxy residual image can then be used to identify the substructure features and quantify their relative contribution to the total light of the galaxy.

Throughout this work, we study substructure features that can be classified into two subtypes (refer to Section 1.4). First, we have disk substructures, which encompass features such as bars, spiral arms, rings, dumbbells, inclined disks, and edge-on disks. Second, we have clump substructures, which include irregular light overdensities, such as star forming regions, dust lanes, and off-center nuclei.

Additionally, it is important to note that the substructure component is defined as the non-smooth, excess light contained in the substructure features of a galaxy. Therefore, in the case that disk features are present, the substructure component does not correspond to the total amount of light that may be contained in a physically thin embedded disk, which may also have an additional thin smooth component of its own. The residual method separates smooth (axisymmetric) light from non-smooth (non-axisymmetric) light, and thus cannot distinguish

between different sources of smooth light (e.g., the diffuse light of a thin disk from that of a thick disk).

The residual method is built around the Image Reduction and Analysis Facility (IRAF; Tody 1986, 1993), an astronomical software system developed by the National Optical Astronomy Observatory (NOAO). The method makes use of IRAF built-in tasks, and also of the isophotal analysis and construction tools available in an external package of IRAF, the Space Telescope Science Data Analysis System (STSDAS; STSDAS Group 1994) package. For visualization of the image products, we use the SAOImage DS9 (Joye & Mandel 2003; Joye 2019) visualization tool for astronomical data.

2.2 Steps

We now provide a step-by-step description of the residual method, given as a recipe to follow. First, each step provides an explanation on what it aims to achieve, and why it is necessary. This is followed by a description of the specific IRAF tasks and parameter settings that are utilized for this purpose. The adopted parameter configuration is further discussed in Section 2.3. As a helpful reference, we provide a flowchart that illustrates the steps of the residual method in Figure 2.2.

▶ Step 1: Smooth out the galaxy image.

First, the objective is to smooth out the features of the substructure component of the galaxy while at the same time preserving the main geometry of the diffuse component. By smoothing the galaxy image by a specifically tuned amount, the substructure features embedded in the galaxy become washed out and less defined in appearance. Thus, there is a reduction in the relative contribution of these features to the brightness, shape, and orientation of the radial light profile of the galaxy.

Using the IRAF `gauss` task, the galaxy image is smoothed out by convolving it with an elliptical Gaussian kernel. The smoothing kernel has a shape and orientation that matches the ellipticity and position angle of the original galaxy image at two effective radii. From visual inspection of the unsharp mask images of the dwarf ETG samples of Chapters 3 and 4, the substructure features appear faint and not dominant at this particular galactocentric distance. For this reason, the two effective radii isophote is chosen to represent the geometry of the main body of the galaxy and is the geometry adopted for the smoothing kernel. Additionally, for the choice of kernel size, the observed thickness or width of the substructure features of the galaxy is taken into account. In order to smooth-out the galaxy image by just the necessary amount, the standard deviation of the Gaussian kernel is then tuned to match half of the average width of the substructure features. The parameter configuration of the IRAF `gauss` task is provided in Table 2.1.

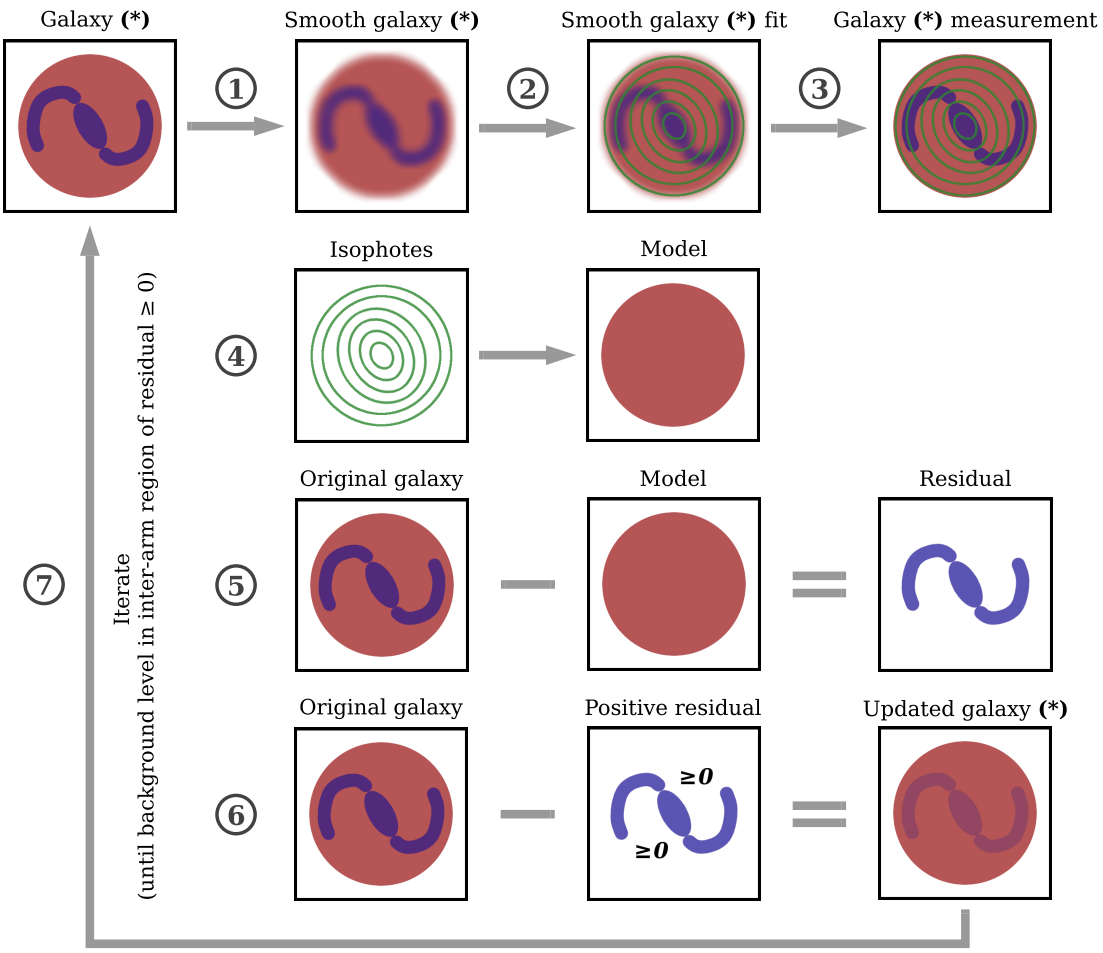

Figure 2.2: Flowchart of the residual method. Steps 1 through 7 are indicated, as described in the text. The diffuse component of the galaxy is illustrated in red and the substructure component in blue. The isophotal fit to the galaxy is illustrated by green ellipses. The updated, positive-residual-subtracted galaxy image resulting from the procedure is marked with an asterisk (*), and replaces the galaxy images that are similarly marked during the iterative loop.

► Step 2: Fit the smoothed-out galaxy image.

By fitting the radial light profile of the smoothed-out galaxy image, we construct a representation of the galaxy that is less affected by the radial changes in brightness, shape, and orientation that may be driven by the underlying substructure features. In an ideal case, the influence of these features would be removed completely in Step 1, so the radial fit of the smoothed-out galaxy image would solely describe the geometry of the diffuse component. However, in reality, the substructure features are still partially contaminating the light of the smoothed-out galaxy. Therefore, the resulting fit describes a diffuse component that is still slightly influenced by the geometry of the substructure component.

Using the IRAF `ellipse` task, the smoothed-out galaxy image is fit with concentric elliptical isophotes. The fit performed allows both the ellipticity and position angle of the isophotes to change freely with galactocentric radius, while their central coordinates are kept fixed. By adopting this configuration, the smoothed-out galaxy image is described as accurately as

possible, as the fit accounts for any radial changes in the shape and orientation of the light profile. The central coordinates, however, are kept fixed to ensure the convergence of the `ellipse` task even in the regions of the galaxy that have a highly flattened radial light gradient, which can arise as a result of the smoothing procedure in Step 1. The adopted galaxy center is extracted from a completely free fit (i.e., free central coordinates, ellipticity, and position angle) that must be previously performed on the original galaxy image. It corresponds to the central coordinates of the isophote that has a semi-major axis equal to 1.5 times the full width at half maximum (FWHM) of the point spread function (PSF), chosen in order to avoid any effects of the PSF in the determination of the center. The parameter configuration of the IRAF `ellipse` task ran in this "free mode" is provided in Table 2.2.

► Step 3: Measure the galaxy image by imposing the isophotes of the smoothed-out galaxy image.

Inherent to the process of smoothing out the galaxy image in Step 1, light from the galaxy is redistributed throughout the image. Therefore, when fitting the smoothed-out galaxy image in Step 2, the extracted isophotes do not reflect the actual intensity profile of the galaxy. To obtain the true average intensity at each isophote, we return to the galaxy image itself and superimpose these isophotal contours on the galaxy to measure the true average underlying brightness. This way, we obtain a representation of the radial light profile of the galaxy that reflects the actual brightness of the galaxy image, while at the same time following the shape and orientation of the smoothed-out galaxy image.

Using the IRAF `ellipse` task in no-fit, photometry-only mode, we measure the average radial brightness of the galaxy image by imposing the geometry of the isophotes of the smoothed-out galaxy image. This is achieved by setting the `inellip` parameter of the task, and providing the `ellipse` output table obtained from fitting the smoothed-out galaxy in Step 2. The parameter configuration of the IRAF `ellipse` task ran in this "fixed mode" is provided in Table 2.2.

► Step 4: Construct the galaxy model image, containing the diffuse component.

From the previous step, we now have a description of the light profile of the galaxy in which the impact of the underlying substructure features has been minimized. In other words, the extracted light profile aims at describing the diffuse component of the galaxy. In order to construct a 2D representation of the diffuse component, we use the information we have extracted of the radial changes in shape, orientation, and brightness of the light profile to build a model image.

Using the IRAF `bmodel` task, we create a galaxy model image that represents the diffuse component of the galaxy. This is achieved by providing the task with the `ellipse` output table obtained in Step 3. The parameter configuration of the IRAF `bmodel` task is provided in Table 2.1.

► Step 5: Construct the galaxy residual image, containing the substructure component.

If we remove the contribution of the diffuse component from the galaxy image, then what is left behind constitutes the substructure component. That is, any substructure features embedded in the galaxy, be it either disk or clump substructures, emerge as residual light when subtracting out the diffuse light of the galaxy.

Using the IRAF `imarith` task, the galaxy model image from Step 4 is subtracted from the original galaxy image. As a result, we obtain a galaxy residual image that represents the substructure component of the galaxy.

► Step 6: Construct the updated, positive-residual-subtracted version of the galaxy image.

Conceptually, the galaxy model image (Step 4) should only contain the diffuse light of the galaxy, in order for the galaxy residual image (Step 5) to contain the remaining light coming from substructure features. However, the separation into these two distinct components is not achieved in one go. Inevitably, the galaxy model image will be partially contaminated with light coming from the substructure features, as it is not possible to completely remove their influence when smoothing out the galaxy image in Step 1 and then fitting it in Step 2. Consequently, the galaxy model tends to be slightly brighter than it should be, resulting in a galaxy residual that is slightly fainter and that suffers from over-subtraction by the galaxy model. In other words, the inter-arm (or inter-substructure) region in the galaxy residual, by being devoid of substructure features, is dominated by negative values.

Therefore, the extra light that is coming from substructure features and that is currently contaminating the galaxy model has to be shifted instead to the galaxy residual, which is where we actually want it to be placed. To achieve this, we construct an updated version of the galaxy image in which all of the positive light coming from the galaxy residual image has been subtracted out. This new galaxy image, which is less driven by the influence of the substructure features, can be afterwards once again subjected to Steps 1 through 5.

First, using the IRAF `imreplace` task, the negative values in the inter-substructure region of the galaxy residual image are set to zero. This way, we get rid of the effects of over-subtraction and obtain a galaxy residual image that has only positive values along its substructure features. Next, using the IRAF `imarith` task, this positive-only galaxy residual image is subtracted from the original galaxy image. As a result, we obtain an updated, positive-residual-subtracted version of the galaxy image that can then be used again in Step 1.

► Step 7: Iterate until the inter-substructure region in the galaxy residual image reaches a level of zero.

By entering an iterative loop of Steps 1 through 6, the galaxy becomes gradually separated into a diffuse and a substructure component, contained in the galaxy model (Step 4) and galaxy residual (Step 5) images, respectively. This iterative procedure is carried on until the galaxy decomposition is complete. To know when we have reached this point in the loop, we con-

struct a stopping criterion for the iterations by monitoring the inter-arm (or inter-substructure) region of the galaxy residual image. We define the "inter-substructure region" as all the pixels that are negative in the initial version of the residual image (i.e., in the first residual image that is created before initiating the iterative loop), and that lie within the two effective radii isophote of the galaxy.

Initially dominated by negative values, the inter-substructure region becomes each time less negative with successive iterations, gradually alleviating the effects of over-subtraction. As our aim is to measure the excess light contained in substructure features, the iterations should continue until the inter-substructure region reaches a typical statistical value that is on par with the background level. While the images that constitute our dwarf ETG samples (see Chapters 3 and 4) have been background subtracted, they also contain noise, so their background consists in positive and negative values that fluctuate around zero. We have chosen the median as the statistical function to estimate the central value of the inter-substructure region, as it is robust against possible outliers. Thus, the final, stopping iteration is reached once the inter-substructure region of the galaxy residual first reaches a median value equal or bigger than zero. We note that, if the iterations were to continue after this point is reached, the galaxy residual would start suffering instead from under-subtraction. That is, too much light would begin to be displaced from the galaxy model to the galaxy residual, making the latter artificially brighter. Consequently, the stopping criterion for the iterations is designed to prevent both over- and under-subtraction in the galaxy residual image.

With its background at a zero level, the final, optimized version of the galaxy residual image can be then used to accurately quantify the amount of light contained in the substructure features. For reference, a schematic representation of the iterative procedure and the stopping criterion is provided in Figure 2.3.

2.3 Parameter Configuration

In order to successfully run the residual method on a given data set, it is first necessary to repeatedly test and accordingly modify several configuration parameters. In particular, the configuration setup described in this Section has been tuned to the application of two imaging samples of dwarf ETGs with embedded substructures (later analyzed in Chapters 3 and 4). Therefore, this configuration needs to be adjusted on a case-by-case basis, in accordance to the properties of the particular data set that the method is going to be applied to. This includes properties both of the imaging data and of the galaxies themselves. On the one hand, regarding the data properties, factors such as the signal-to-noise ratio (S/N), the seeing and PSF, and the resolution of the images should be taken into account. On the other hand, regarding the galaxy properties, the average width and relative strength of their substructure features will also influence the parameter configuration. For this reason, the parameter values that are described in this Section are tuned to the current science case and should only be used as a guideline.

We will now address the overall configuration of the IRAF tasks used in the residual

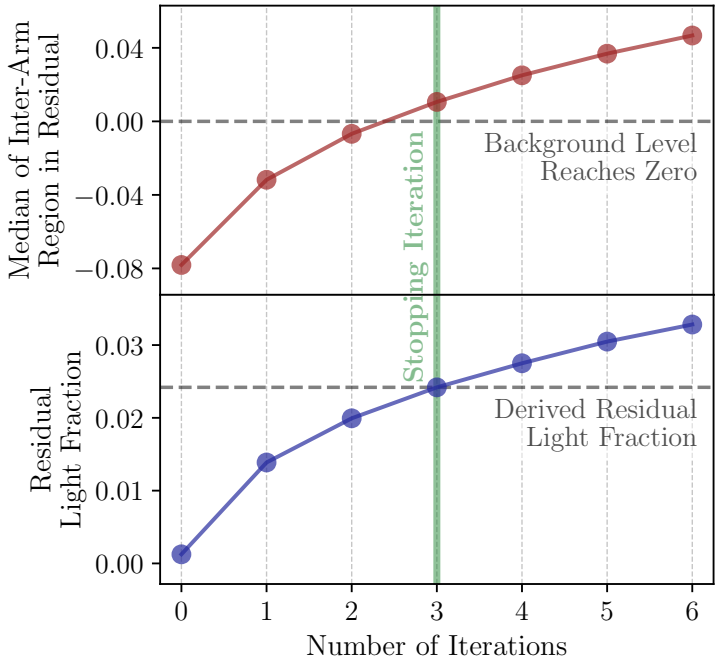

Figure 2.3: Schematic representation of the iterative procedure and stopping criterion implemented in the residual method. The data points correspond to empirical values obtained when applying the residual method to Virgo dwarf galaxy VCC0308. *Top panel:* the median value of the inter-arm (or inter-substructure) region in the galaxy residual image vs. the number of iterations, represented by a red curve. The specific iteration at which the background level in this region becomes equal or bigger than zero is marked with a vertical green line, and corresponds to the stopping iteration. *Bottom panel:* the measured residual light fraction of the galaxy vs. the number of iterations, represented by a blue curve. The accepted value for the residual light fraction is derived from the galaxy residual image at the stopping iteration, as shown by a horizontal dashed line.

method. In Table 2.1, we provide the setup of the IRAF `gauss` and `bmodel` tasks. Then, in Table 2.2, we provide the setup of the IRAF `ellipse` task.

First, the `gauss` task is used to smooth out the galaxy image in Step 1 of the method. For the convolution kernel, we adopt an elliptical Gaussian kernel that matches the ellipticity and position angle of the galaxy isophote at two effective radii (`ratio` and `theta` parameters). The total extension of the kernel is set to be 8 times the standard deviation of the Gaussian function (`nsigma` parameter). We do not use a bilinear approximation of the Gaussian function under any circumstance (`bilinear` parameter). In the case of encountering out-of-bounds pixels, we adopt an algorithm that takes the value of the nearest boundary pixel (`boundary` parameter). The size of the standard deviation of the Gaussian kernel (`sigma`) is a special case as it is a variable parameter, and is thus further addressed in Section 2.3.1.

Second, the `bmodel` task is used to create the galaxy model image in Step 4 of the method. When constructing the 2D model, we use the full range of semi-major axis lengths given by the input `ellipse` table (`fulltab` parameter). Any pixels that lie beyond the last isophote are assigned a value of zero (`backgr` parameter). To interpolate between successive isophotes, we use a spline function (`interp` parameter). Only the 1st and 2nd Fourier harmonic amplitudes are used when constructing each galaxy isophote (`highar` parameter).

Table 2.1: Parameter setup of the IRAF `gauss` and `bmodel` tasks.

Task (1)	Parameter (2)	Value (3)
`gauss`	`sigma`	variable (*)
	`ratio`	b/a (SMA $= 2\,R_e$)
	`theta`	θ (SMA $= 2\,R_e$)
	`nsigma`	8.0
	`bilinear`	no
	`boundary`	nearest
`bmodel`	`fulltab`	yes
	`backgr`	0.0
	`interp`	spline
	`highar`	no

Note. — Col. (1): IRAF task name. Col. (2): parameter name. A description of each parameter is provided in Table B.1. Col. (3): adopted parameter values. The smoothing kernel size, marked with an asterisk (*), adopts a series of values that depend on the specific properties of the data set.

Third, the `ellipse` task fits elliptical isophotes to a 2D light distribution. Each isophote is modeled by an ellipse that is described by a Fourier series decomposition into harmonics (i.e., sine and cosine functions), where each harmonic adds different perturbations (Jedrzejewski 1987). We use this task to fit the smoothed-out galaxy image in Step 2 ("free fit" mode), and then to measure the galaxy image using the smoothed-out galaxy isophotes in Step 3 ("fixed fit" mode).

We will first address the parameter values that are in common between these two modes. The `ellipse` task is provided with a data quality file in the form of a bad pixel mask (BPM) image, where interloping sources such as foreground stars and background galaxies are flagged as bad pixels and should be rejected by the fitting algorithm (`dqf` parameter). Next, all of the imaging sampling parameters are shared between the two modes. Each elliptical path that defines an isophote is sampled using the median of the pixel values (`integrmode` parameter). To filter out outlier points along an isophote, we adopt a three-sigma clipping algorithm (`usclip` and `lsclip` parameters) that iterates five times (`nclip` parameter). For an isophote to be valid, up to a maximum of 50% of its pixels are allowed to be flagged as bad (`fflag` parameter). Only the 1st and 2nd Fourier harmonic amplitudes are considered during the fit (`harmonics` parameter). Most of the algorithm control parameters are also shared. We adopt the same convergency criterion for stopping the iterations in the fitting algorithm (`conver` parameter). The algorithm iterates a minimum of 10 times up to a maximum of 50 times (`minit` and `maxit` parameters). The central coordinates are held fixed (`hcenter` parameter) and are not allowed to wander between successive isophotes (`wander` parameter), so the algorithm just accepts the central coordinates that are given (`olthresh` parameter). The semi-major axis length of the

Table 2.2: Parameter setup of the IRAF `ellipse` task.

Configuration Task	Parameter	Mode	
		Free	Fixed
(1)	(2)	(3)	(4)
Ellipse	`dqf`	BPM w/ interlopers	BPM w/ interlopers
	`inellip`	no	yes, from free mode run
Sampling	`integrmode`	median	median
	`usclip`	3.0	3.0
	`lsclip`	3.0	3.0
	`nclip`	5	5
	`fflag`	0.5	0.5
	`harmonics`	none	none
Control	`conver`	0.1	0.1
	`minit`	10	10
	`maxit`	50	50
	`hcenter`	yes	yes
	`hellip`	no	yes
	`hpa`	no	yes
	`wander`	0.0	0.0
	`maxgerr`	1.0	1.0
	`olthresh`	0.0	0.0
	`soft`	no	no
Geometrical	`x0`	x_c (SMA $= 1.5 \times$ PSF FWHM)	`inellip`
	`y0`	y_c (SMA $= 1.5 \times$ PSF FWHM)	`inellip`
	`ellip0`	e (SMA $= 1\,\mathrm{R}_e$)	`inellip`
	`pa0`	PA (SMA $= 1\,\mathrm{R}_e$)	`inellip`
	`sma0`	SMA (SMA $= 1\,\mathrm{R}_e$)	`inellip`
	`minsma`	0.0	`inellip`
	`maxsma`	SMA (SMA $=$ last valid iso.)	`inellip`
	`step`	variable (*)	variable (*)
	`linear`	no	no
	`maxrit`	INDEF	INDEF
	`recenter`	no	no
	`xylearn`	no	no
	`physical`	yes	yes

Note. — Col. (1): IRAF `ellipse` configuration tasks: ellipse parameters, image sampling parameters, algorithm control parameters, and geometrical parameters. Col. (2): parameter name. A description of each parameter is provided in Table B.2. Cols. (3) and (4): adopted parameter values when running `ellipse` in free and fixed mode, respectively. The sampling step size, marked with an asterisk (*), adopts a series of values that depend on the specific properties of the data set.

isophotes is allowed to grow until it exceeds a certain maximum relative error in the local intensity gradient (`maxgerr` parameter), which brings the fitting algorithm to an abrupt halt (`soft` parameter). The two modes also share some geometrical parameters. They both adopt the same step sizes in the semi-major axis length of successive isophotes (`step` parameter), which have a geometric growth as opposed to linear (`linear` parameter). As a special case, the sampling step size is a variable parameter and is thus further addressed in Section 2.3.2. We do not restrict the iterative mode of the fitting algorithm, so it is allowed to iterate at all semi-major axis lengths (`maxrit` parameter). As the central coordinates are held fixed, we do not allow the algorithm to re-center the isophotes nor to update the coordinates (`recenter` and `xylearn` parameters). Finally, all inputs are given in the physical coordinate system of the image (`physical` parameter).

The free fit and fixed fit modes differ in the following parameters. The `ellipse` task is first run in free mode, and the output table containing the information of the isophotal geometry is then given to the task to run it in fixed (no-fit, photometry-only) mode (`inellip` parameter). In regards to the algorithm control parameters, in free mode both the ellipticity and position angle of successive isophotes are allowed to change freely, while instead in fixed mode they are not allowed to change and are forced to adopt the geometry given by the input `ellipse` table given through the `inellip` parameter (`hellip` and `hpa` parameters). Regarding the geometrical parameters, the free mode is provided with initial guesses for the first isophote to be fit based on a previous completely-free `ellipse` run (free central coordinates, ellipticity, and position angle) that must be carried out on the original galaxy image. From this previous run, we set the the guess of central coordinates (`x0`,`y0`) from the isophote with semi-major axis equal to 1.5 times the PSF FWHM, and the guess of ellipticity (`ellip0`), position angle (`pa0`), and semi-major axis length (`sma0`) from the isophote at one effective radius. The fitting algorithm should start at a minimum semi-major axis length of zero (i.e., the center of the galaxy), and stop at a maximum semi-major axis length corresponding to the last valid isophote (i.e., the last isophote 2σ above the background level) according to the previous run (`minsma` and `maxsma` parameters). The setup of all these geometrical parameters is ignored during fixed mode, as then they simply follow the isophotal geometry of the `ellipse` table being fed through the `inellip` parameter.

As mentioned before, there are two parameters that are variable in the residual method: the smoothing kernel size (`sigma`), and the sampling step size (`step`). We explain the importance of these parameters and specify the range of values adopted when applying the method to each of our dwarf ETG samples in the following Sections 2.3.1 and 2.3.2.

2.3.1 Smoothing Kernel Size

In Step 1 of the residual method, the galaxy image is smoothed-out by convolving it with an elliptical Gaussian kernel. The "smoothing kernel size" then refers to the extension of the standard deviation of this Gaussian function along its semi-major axis.

As the objective is to blur out the substructure light while at the same time preserving the overall geometry of the diffuse light, the standard deviation of the Gaussian smoothing kernel

is adjusted to match half of the average width (i.e., the radius) of the substructure features. This choice can be understood as follows. On the one hand, if the kernel size is much smaller than the average thickness of the substructure features, then their brightness and appearance will not be significantly altered during the smoothing process. On the other hand, if the kernel size is instead much bigger, then not only the substructure features will be blurred out, but also the main body of the galaxy will become strongly affected. Consequently, there is a lower and an upper limit on the optimal kernel sizes that can be used in the smoothing procedure.

Both the data and the galaxy properties dictate the average half-width of the substructure features. While the Virgo dwarf ETG sample (see Chapter 3) presents average substructure half-widths in the range of $2.4-6.0$ arcsec, the Fornax dwarf ETG sample (see Chapter 4) has instead average values in the range of $1.2-4.7$ arcsec. These ranges can be re-defined in terms of the PSF FWHM of the data transformed into a Gaussian standard deviation, $\sigma_{\rm PSF}$. Thus, the average substructure half-widths of the Virgo sample lie in the range of $5-10\times\sigma_{\rm PSF}$, while for the Fornax sample they lie in the range of $3-8\times\sigma_{\rm PSF}$. In order to be consistent in the treatment of each data set, the same range of smoothing kernel sizes is applied to all of the galaxies in a given sample: $5,6,7,8,9,10\times\sigma_{\rm PSF}$ for the Virgo sample, and $3,4,5,6,7,8\times\sigma_{\rm PSF}$ for the Fornax sample.

Additionally, through testing, we found that once the galaxy is smoothed one time, the majority of the substructure features already become successfully blurred out, so it is not necessary to continue smoothing them by the same amount in subsequent iterations. Therefore, to reduce the amount of smoothing to the minimum required, and thus to help preserve the geometry of the diffuse component, the choice of the kernel size is decreased to a half once the galaxy image enters the iterative loop of the method. In other words, if the galaxy image is being initially smoothed out by a kernel of size X arcsec, this size is reduced to just $X/2$ arcsec from the first iteration onwards.

2.3.2 Sampling Step Size

In Step 2 of the residual method, the smoothed-out galaxy image is fit with concentric elliptical isophotes. The "sampling step size" then refers to the increase in semi-major axis length between two successive isophotes.

By adjusting the separation between successive isophotes, it is possible to sample the image at a greater or a lower frequency, corresponding to smaller or larger step sizes, respectively. Their difference can be understood as follows. On the one hand, if the step sizes are too small, the fitting algorithm will not have enough data points to sample the image and construct the isophotes. On the other hand, if the step sizes are instead too big, the resulting isophotes will be unable to accurately capture any of the more subtle radial changes in the brightness and geometry of the galaxy. Therefore, once again depending on the properties of the data set, there is a lower and an upper limit on the optimal sampling step sizes that can be used when fitting a galaxy image.

For both of our dwarf ETG samples, we opt for a geometric growth of the step size instead

of a linear growth, as it provides the fitting algorithm with more data points to construct the isophotes towards the fainter, lower S/N regions in the galaxy outskirts. In the case of the Virgo sample (see Chapter 3), we determine that a growth rate of the step size length in the range of $5 - 10\%$ is optimal, while for the Fornax sample (see Chapter 4) a growth rate of $18 - 23\%$ is optimal. Replicating the approach we took regarding the smoothing kernel sizes, we apply the same range of sampling step sizes to all of the galaxies in a given sample: a growth rate of $5, 6, 7, 8, 9, 10\%$ for the Virgo sample, and of $18, 19, 20, 21, 22, 23\%$ for the Fornax sample.

2.3.3 Configuration Grid

The aforementioned ranges of smoothing kernel sizes and sampling step sizes create a discrete 6×6 configuration grid, which translates into 36 possible parameter pair combinations. Each one of the two dwarf ETG samples has its own individually-tuned configuration grid. To implement it, the residual method is run several times on the same galaxy image, where each run is set up with a specific pair of smoothing and sampling parameter values. By exploring these parameter spaces while at the same time applying the criterion to stop the iterations of the method, we obtain as a result a set of residual images for each galaxy that only vary slightly with respect to one another. These residual images can then be used to quantify the contribution of the substructure light to the total galaxy light and its related uncertainties, as explained in the next Section 2.4.

2.4 Residual Light Fraction

To quantify the brightness of the substructure component of a galaxy, we measure the amount of light contained in the galaxy residual image compared to the amount of light contained in the original galaxy image. The quantity we are interested in corresponds to the ratio of the residual-to-total light, which we define as the "residual light fraction". To compute it, the light contained in each image, residual and original, is integrated up to the same given elliptical isophote. These sums include all enclosed pixel values, regardless of their sign. The ratio of these two sums is then calculated. As the parameter setup of the residual method provides us with several residual images for each galaxy (see previous Section 2.3.3), we compute the residual light fraction by taking the median value of all measurements and, as their distribution is not necessarily symmetric, derive their uncertainties from the 16th and 84th percentiles.

For both our Virgo and Fornax dwarf ETG samples (see Chapters 3 and 4), the measurements of the residual light fraction are computed within the one and two effective radii isophotes of the galaxies. On the one hand, these measurements omit the outermost region of the galaxy images for two main reasons. First, the noise level of the images starts dominating towards the lower S/N regions at the galaxy outskirts, so measurements at large galactocentric radii can become unreliable due to their big uncertainties. Second, the substructure features observed in both samples do not extend beyond two effective radii, lifting the necessity of computing a residual light fraction in the outer regions. On the other hand, these measurements also omit the innermost region of the galaxy images, as the pixels that lie just at the center

are affected by the PSF and usually contain some artifacts resulting from the IRAF `ellipse` fitting procedure. Thus, the central region is masked out by a circle of radius equal to 1.5 times the PSF FWHM of the data. We clarify that this constitutes a negligible fraction of the effective radius, so no important information is being masked out, even in cases where substructure features are present at small galactocentric radii. Nonetheless, we would also like to note that central overdensities, such as nuclei, become masked by this approach, and are thus excluded from the quantification of the substructrure light. Additionally, any foreground and background sources, such as interloping stars or galaxies, are also masked out and omitted from the measurements.

As stated in Section 2.1, the residual image contains the excess, non-axisymmetric light that deviates from the smooth, axisymmetric light of a galaxy. As such, it is important to note that all residual light fraction measurements constitute lower limits, as the real, physical substructure component of a galaxy could also contain smooth light of its own.

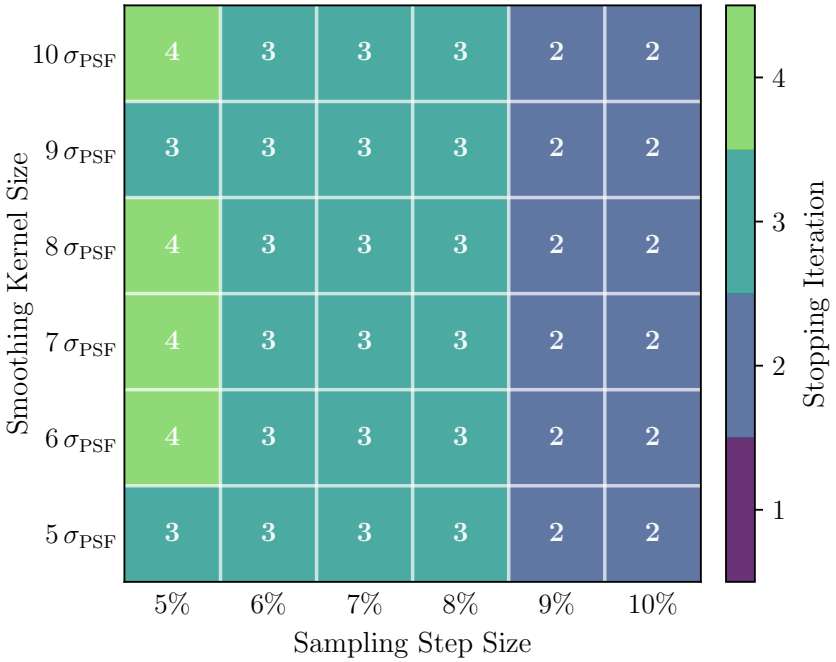

Figure 2.4: Heatmap showing the number of iterations of the residual method and their dependence on the configuration of the smoothing and sampling parameters. As an example, we consider the case of Virgo dwarf galaxy VCC0308, and thus show the configuration setup used when applying the the residual method to the Virgo dwarf ETG sample. The smoothing kernel size adopts a Gaussian standard deviation that ranges between a multiple of 5 to 10 times the Gaussian standard deviation of the PSF. The sampling step size adopts a growth rate between successive isophotes that ranges between 5 to 10%. The total number of iterations that are required by each parameter setup pair are labeled and color coded.

The accuracy with which we are able to isolate and quantify the embedded substructure features of a galaxy is closely linked to the iterative aspect and stopping criterion of the residual method (refer to Step 7 in Section 2.2). As the stopping criterion for the iterations is implemented on a case-by-case basis, different parameter configuration pairs can have a different number of iterations being needed, even when the method is being applied to the same

galaxy image. This is illustrated in Figure 2.4, which shows the case of VCC0308, one of the galaxies in our Virgo dwarf ETG sample (see Chapter 3). The Figure shows how the required number of iterations varies throughout the parameter configuration grid. The stopping iteration appears to be mostly insensitive to the smoothing kernel size, while it tends to decrease with increasing sampling step size. We can confirm that the same behavior is observed when applying the method to both of our dwarf ETG samples, and can be understood as follows. Larger step sizes sample with less definition an image, thus making it easier to shift light from the model to the residual with successive iterations. As a result, the inter-substructure regions in the residual image are able to reach a median background level of zero in a smaller amount of iterations, causing the stopping iteration to gradually decrease in number.

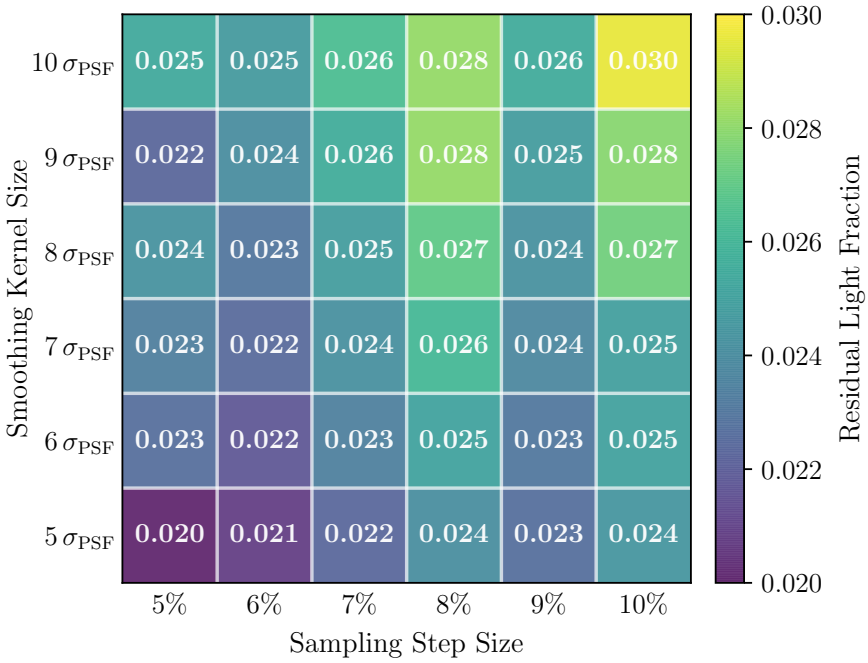

Figure 2.5: Heatmap showing the residual light fraction measurements and their dependence on the configuration of the smoothing and sampling parameters. As an example, we consider the case of Virgo dwarf galaxy VCC0308, and adopt the parameter setup described in Figure 2.4. The residual light fraction measured within two effective radii for each parameter setup pair is labeled and color coded.

The flexibility with which the residual method adapts to different parameter configurations is what ensures that the residual light fraction is quantified accurately. Each parameter configuration pair has its own independent stopping iteration, from which we obtain its associated residual image, which is then used to measure the residual light fraction. This is illustrated in Figure 2.5, which shows once again the case of dwarf galaxy VCC0308, and how the derived residual light fraction varies throughout the parameter configuration grid. We observe that the residual light fraction tends to increase with increasing smoothing kernel size and sampling step size. This overall trend is also displayed by the other dwarf ETGs that constitute our samples, and can be understood as follows. If the image is smoothed-out more and is sampled with coarser steps, the constructed model of the diffuse component becomes less affected by the underlying substructure component, thus resulting in a residual that is slightly brighter.

However, at the same time, the depiction of the diffuse component by the model will progressively become less accurate, which is why we establish clear lower and upper bounds on the allowed smoothing kernel and sampling step sizes. These gradual variations in the residual light fraction, albeit small, end up translating into the uncertainty range of the median of the measurements.

Visually, the residual images across the configuration grid look very similar to each other, as illustrated in Figure 2.6 for dwarf galaxy VCC0308. This is to be expected, given the very small differences in their residual light fractions. While the brightness and appearance of the residual images look almost identical, a closer look reveals the expected behavior: the substructure features become brighter and more well defined with increasing smoothing kernel size and sampling step size. This makes sense, as this is the same trend displayed by the residual light fraction. Thus, we have both quantitative and qualitative confirmations that the outputs of the residual method are reasonable and robust, as long as its configuration parameters have been carefully tested and accordingly chosen to fit the science case at hand.

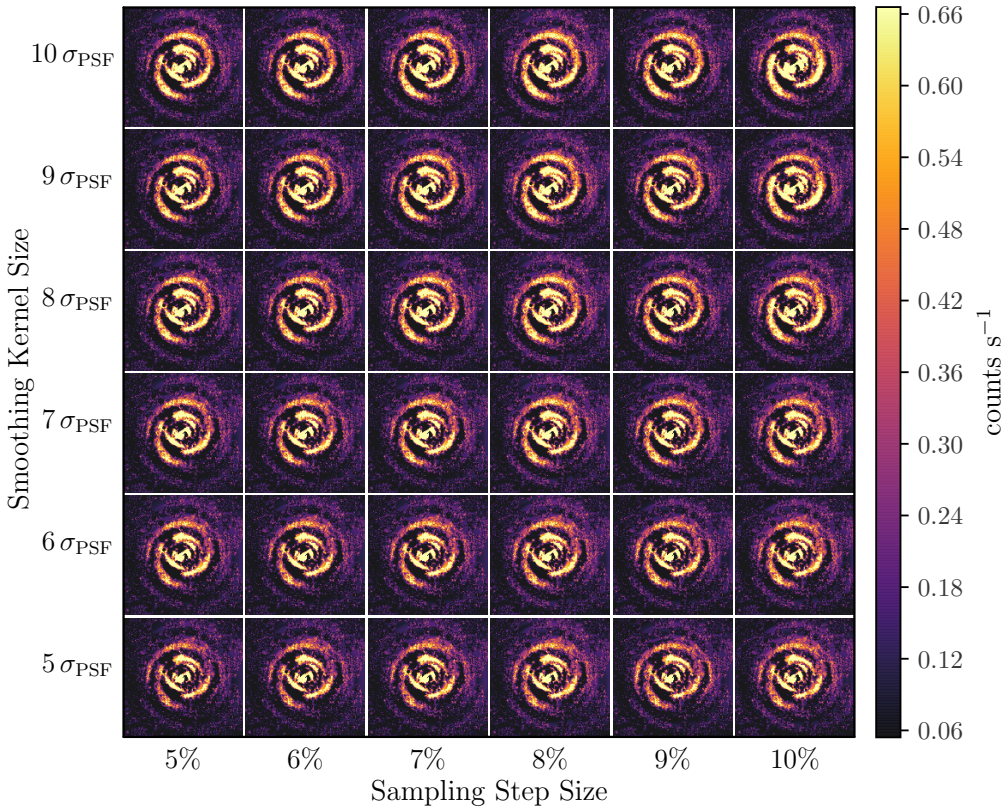

Figure 2.6: Heatmap showing the brightness and appearance of the residual images and their dependence on the configuration of the smoothing and sampling parameters. As an example, we consider the case of Virgo dwarf galaxy VCC0308, and adopt the parameter setup described in Figure 2.4. All images share the same color bar in units of counts s^{-1}, and are 100×100 arcsec^2 in size. North is up, east is to the left.

2.5 Strengths and Improvements

The residual method is based on and inspired by the residual image optimization procedure originally presented in Appendix A of Lisker et al. (2006c). In comparison, our residual method introduces several improvements on the weaknesses of this procedure, and its main strengths can be summarized into two attributes: accuracy and adaptability. In order to properly explain these attributes, we will address some of the results obtained when applying the residual method to the Virgo and Fornax dwarf ETG samples, which are presented in the upcoming Chapters 3 and 4.

2.5.1 Accuracy

The residual method is accurate, as it is able to reliably extract both the actual geometry (a qualitative measure) and the light content (a quantitative measure) of the substructure features that are underlying in a galaxy image.

First, a qualitative assessment can be given based on the appearance of the substructure features. By comparing the unsharp mask images (Figure 3.2 for the Virgo sample, Figure 4.6 for the Fornax sample) with the residual images obtained with the residual method (Figure 3.4 for the Virgo sample, Figure 4.12 for the Fornax sample), we observe that the geometry of the disk and clump features is preserved. The main difference lies in the innermost galaxy region: the unsharp mask images appear artificially bright in the center; an unavoidable, unwanted effect that arises from the light being redistributed when smoothing (as it is further explained in Section 3.3). In contrast, the galaxy residual images do not suffer from this central light excess. However, existing bar substructures adopt an hourglass-shape in the residuals. This effect has also been observed in other works (e.g., Barazza et al. 2002; Lisker et al. 2006c), and is understood as a highly probable indicator of the presence of a bar. Despite this effect, the residual method does a good job in capturing the shape and orientation of any substructure features originally revealed through unsharp masking, in preserving their pixel-by-pixel resolution, and in not introducing any artificial features. We acknowledge that all of this is possible thanks to Steps 1 and 2 of the residual method (see Section 2.2), in which the galaxy image is smoothed out and then subjected to a free fitting procedure. By first smoothing the galaxy image, the impact that the substructure features have in driving the galaxy geometry is reduced significantly. Then, by freely fitting the smoothed-out galaxy image, we are able to capture the overall geometry of its diffuse main body that is later used to construct a model. As a direct consequence, when subtracting the diffuse model from the galaxy itself, we obtain a residual that contains a geometrically-accurate representation of the remainder substructures. As real galaxies in clusters often present isophotal twists in their light distribution, being able to properly model the geometrical complexity of their diffuse light is a necessity that is satisfied by the residual method.

Second, a quantitative assessment can be given based on the brightness of the substructure features. While the diffuse light of the galaxy is modeled based on the geometry of the isophotes of the smoothed-out image, these isophotes are then superimposed on the galaxy

image itself in order to measure its actual brightness in Step 3 of the method. After the iterative procedure, the actual amount of diffuse light is correctly represented in the model image, consequently leaving the remainder amount of substructure light contained in the residual image. In order to test the accuracy of this separation process, we demonstrate in Section 3.3 that the residual method succeeds in recovering the residual light that is manually introduced into mock galaxy images. The method also proves to be sensitive to very faint substructure features, as we report contributions to the total light that go as low as 2% in both dwarf ETG samples (see Tables 3.4 and 4.5). The robustness of the method opens the possibility of reliably using the galaxy residual images for additional applications, as we discuss in the following Section 2.6. However, we note that in order to reach a good level of accuracy deep images are required, as the accuracy of any measurement depends on their uncertainties, and hence on the S/N of the data.

In comparison, the residual image optimization procedure of Lisker et al. (2006c) adopts a fixed fit instead of a free fit approach, by keeping both the ellipticity and position angle fixed to a single value during the isophotal fitting of the galaxy image. When testing the residual method and other alternative methods in Section 3.3, we show how a fixed fit approach fails to properly describe the light distribution of a galaxy when it is geometrically more complex. Furthermore, the approach of Lisker et al. (2006c) does not include a smoothing procedure, which is a new additional step introduced by our own residual method. All of these improvements we have incorporated are what ensures that both the geometry and the brightness of the galaxy components are captured faithfully. It should also be taken into consideration that the study of Lisker et al. (2006c) makes use of much shallower images from the Sloan Digital Sky Survey (SDSS) Data Release 4 (DR4; Adelman-McCarthy et al. 2006), meaning that the accuracy of their measurements has intrinsically higher uncertainties when compared to our deeper Virgo and Fornax dwarf ETG data.

2.5.2 Adaptability

The residual method is adaptable, as its iterative aspect and the setup of its configuration parameters allows it to be tuned on a case-by-case basis.

First, we refer to the iterative procedure, which is described in Step 7 of the residual method (see Section 2.2). The required number of iterations is directly dependent on the characteristics of the particular galaxy being processed. This is achieved thanks to the introduction of a stopping iteration, which dynamically adjusts the number of iterations based on the case at hand. This case-by-case adaptation is what ultimately allows an accurate determination of the amount of light contained in substructure features. As the iterative procedure gradually separates the diffuse and substructure components into a model and a residual image, respectively, it is of utmost importance that the iterations stop once the decomposition is complete (as illustrated in Figure 2.3). If the iterations were to continue arbitrarily longer, additional light would begin to be shifted from the diffuse to the substructure component, thus resulting in artificially brighter substructure features and consequently in an inaccurate estimation of their light content. For this reason, we iterate only as long as the stopping criterion

deems it necessary.

Similarly, the parameter configuration of the residual method is also tightly linked to the characteristics of the data. As extensively addressed in Section 2.3, factors such as the S/N, the seeing and PSF, the resolution, and the average width and relative strength of the substructure features are to be taken into account. Additionally, there are two important parameters that must be set: the smoothing kernel size and the sampling step size. To incorporate variations throughout the data set, the parameter configuration adopts a range of possible smoothing and sampling sizes, specifically tuned to the data properties. This whole range is then applied to each galaxy image. This way, when quantifying their substructure light, any case-by-case variations are translated into an uncertainty range, allowing a consistent measurement throughout the sample.

In comparison, even though the residual image optimization procedure of Lisker et al. (2006c) introduces the concept of iterations, the number of iterations they adopt is arbitrary. They do not implement a stopping criterion, and instead they iterate a fixed total of ten times for all the galaxies in their sample. Our residual method improves on this: by establishing a clear stopping criterion, we are required to iterate between two to five times for our Virgo dwarf ETG sample (see Chapter 3), and between one to three times for our Fornax dwarf ETG sample (see Chapter 4). This is less than half the number of iterations used in Lisker et al. (2006c). In the case of our galaxies, iterating ten times would have caused the residuals to suffer significant under-subtraction from the diffuse model, thus causing the substructure features to become artificially brighter. For this reason, it is possible that the measurements of Lisker et al. (2006c) are systematically biased towards higher values. For the three Virgo dwarf ETGs that we have in common (VCC0308, VCC0490, and VCC0856), they report residual light fractions that are on average three times brighter than the ones we measure (comparing their Table 2 to our Table 3.4). However, we also have to take into account that their measurements are based on images that have a different depth, seeing, and S/N compared to ours, so there may be other potential reasons contributing to this discrepancy. Nonetheless, thanks to the flexibility of our iterative procedure, we believe that we carry out a robust quantification of the actual amount of substructure light present in the analyzed galaxies.

2.6 Further Applications

In summary, the main objective of the residual method is to reliably separate the diffuse and substructure components of a galaxy image. Once the substructure features are extracted and isolated in a residual image, we can then quantify their relative contribution to the total galaxy light by defining a residual light fraction. However, there is also the possibility of subjecting the residual images to a variety of other analyses. For example, in Section 3.4, we perform a Fourier analysis of the residual images of the Virgo dwarf ETG sample. This allows us to mathematically identify and characterize in detail the bar and spiral arm features that are embedded in the galaxies. As another example, in Section 4.4, we carry out color analyses of the model and residual images of the Fornax dwarf ETG sample. Thus, we are able to derive

the integrated colors, color profiles, and stellar population information of both the diffuse and substructure components of the galaxies. Consequently, the residual method holds the potential of having further applications, which can help advance our understanding of the nature of the substructure features present in dwarf ETGs.

In order to take maximum advantage of the residual method, the data set being analyzed should ideally be a large-enough sample consisting in deep multi-band imaging. On the one hand, a big sample size would facilitate the ability of drawing meaningful correlations between derived quantities and galaxy properties. On the other hand, the deeper the data, the fainter the substructures that would be able to be revealed in the residual image. Additionally, as more depth means higher S/N, the measurements of the substructure light would become increasingly accurate. Multi-band imaging would allow to perform color (and thus stellar-population) analyses of the diffuse and substructure components separately. Suitable large and rich data sets can be provided by modern surveys of nearby galaxy clusters, such as NGVS (Ferrarese et al. 2012) in Virgo, or NGFS (Muñoz et al. 2015) and FDS (Iodice et al. 2016, see Chapter 4) in Fornax, and also by future large-scale sky surveys, such as LSST (Ivezić et al. 2019).

Last but not least, the residual method is not limited to the particular application we have given it in this work, in which we analyzed dwarf ETGs with substructure features. In theory, it should be possible to apply it to any galaxy image that can be separated into two components; a bright, smooth, axisymmetric component, and a faint, non-smooth, non-axisymmetric component. Thus, from the high-mass end of giant elliptical galaxies with dust lanes, to the low-mass end of dwarf spheroidal galaxies with underlying substructures or even dwarf irregular galaxies, the residual method should constitute a valid approach for decomposing and analyzing their structural features. However, the inherent limitations of the method should always be kept in mind, as it was designed to work properly in the case that faint substructures are embedded in a comparatively much brighter diffuse body. This means that it is not originally intended to be used, for example, for quantifying the substructure light in giant spiral galaxies, where the spiral arm light is dominant. Caution and careful testing are advised if the intention is to adapt the residual method to the application of science cases that go beyond its original scope.

3

Substructures in Dwarf ETGs of the Virgo Cluster

This Chapter focuses on the analysis of a sample of dwarf ETGs with substructure features that belong to the Virgo galaxy cluster. This Chapter is organized as follows. First, we introduce the data sample, process it in order to prepare it for analysis, and derive the main properties of the galaxies in Section 3.1. The application of the residual method, its configuration parameters, and the results obtained are then described in Section 3.2. As a means of assessing the robustness of the method and how it compares to alternative approaches, we construct a mock galaxy sample that is subjected to a variety of tests in Section 3.3. Finally, in order to showcase a potential application of the method, we perform a Fourier analysis on the residual images of the dwarf ETG sample in Section 3.4.

3.1 The Data Sample

The data sample analyzed in this Chapter is constituted by nine dwarf ETGs of the Virgo galaxy cluster. These galaxies are certain cluster members according to the Virgo Cluster Catalog (VCC; Binggeli et al. 1985), and correspond to VCC0216, VCC0308, VCC0490, VCC0523, VCC0856, VCC0940, VCC1010, VCC1695, and VCC1896. Lisker et al. (2006c) detected unambiguous substructures in the form of disk features in these galaxies, based on unsharp masking of images from the Sloan Digital Sky Survey (SDSS) Data Release 4 (DR4; Adelman-McCarthy et al. 2006).

3.1.1 Observations and Data Reduction

In order to obtain deep optical imaging, eight of these dwarf ETGs were targeted with the MPG/ESO 2.2m telescope at the European Southern Observatory (ESO), La Silla, using the

Table 3.1: Central coordinates of the Virgo dwarf ETG sample and data properties.

Dwarf Galaxy	Central Coordinates		N° Exp.	ZP_r	$Depth_r$	PSF FWHM
	R.A. (J2000.0)	Decl. (J2000.0)		(mag)	(mag arcsec^{-2})	(arcsec)
(1)	(2)	(3)	(4)	(5)	(6)	(7)
VCC0216	$12^h17^m01.10^s$	$+09°24'27.11''$	30	25.65	27.94	1.13
VCC0308	$12^h18^m50.91^s$	$+07°51'42.91''$	26	25.60	27.75	1.23
VCC0490	$12^h21^m38.81^s$	$+15°44'42.30''$	27	25.65	27.91	1.27
VCC0523	$12^h22^m04.13^s$	$+12°47'14.82''$	13	25.56	27.21	1.41
VCC0856	$12^h25^m57.94^s$	$+10°03'13.55''$	29	25.65	27.89	1.29
VCC0940	$12^h26^m47.07^s$	$+12°27'14.34''$	29	25.64	27.59	1.24
VCC1010	$12^h27^m27.39^s$	$+12°17'25.08''$	29	25.64	27.66	1.21
VCC1695	$12^h36^m54.86^s$	$+12°31'12.42''$	25	25.56	27.86	1.38
VCC1896	$12^h41^m54.62^s$	$+09°35'04.58''$	23	25.65	27.79	1.27

Note. — Col. (1): name of the dwarf galaxy. Cols. (2) and (3): right ascension and declination of the central coordinates in the International Celestial Reference System (ICRS). Col. (4): number of exposures taken during the observations, with each exposure lasting five minutes. Col. (5): magnitude zeropoint in the r band, allowing the transformation from instrumental to calibrated AB magnitudes. Col. (6): surface brightness depth in the r band, at a S/N $= 1$ and a scale of 0.71 arcsec pixel^{-1}. Col. (7): median PSF FWHM of the final, binned galaxy image cutouts, which have a scale of 0.71 arcsec pixel^{-1}.

Wide Field Imager (WFI; Baade et al. 1999) instrument (observation program 077.B-0785, P.I. T. Lisker). The field of view centered on the dwarf galaxy VCC1010 also contained VCC0940, which also displayed embedded disk features and was thus subsequently added to the sample. We provide the equatorial coordinates of our sample of nine dwarf ETGs in columns 2 and 3 of Table 3.1.

With the purpose of maximizing the signal, the observations were taken using the white filter. The net exposure time aimed for each target was 2.5 hours, although for some targets this was not achieved due to bad weather. The observations were split into individual dithered exposures of 5 minutes, in order to minimize the saturation of bright stars and to allow the construction of a good superflat image during the data reduction. The data reduction was carried out by T.L. with the THELI image data reduction pipeline (Erben et al. 2005; Schirmer 2013), which was specifically designed for the MPG/ESO 2.2m WFI. Nonetheless, some of its standard procedures were modified by T.L., in order to ensure that: *(a)* the masks of extended sources were clearly covering all source pixels, and *(b)* the image scaling for the superflat calculation correctly took into account these masks when computing mean or median image values. The latter required several iterations, first by constructing new object masks from a first iteration, and then by applying these in a second run.

Additionally, the THELI pipeline handled the registration of the individual images by using publicly available star catalogs, and performed the shifting and rebinning by using a Lanczos kernel. It also carried out the relative flux calibration of the images before finally coadding

them. The final, coadded, background-subtracted images reach a surface brightness that lies in the range of $27.2 - 27.9$ mag arcsec^{-2} in the SDSS r-band equivalent, with a median depth across the sample of $\mu_r = 27.8$ mag arcsec^{-2}, which corresponds to $\mu_B = 29.0$ mag arcsec^{-2} assuming typical dwarf ETG colors. The images were created using 3×3 pixel binning in order to reach the aforementioned depths at a S/N of 1 per binned pixel, with a scale equal to 0.71 arcsec per binned pixel. For the working sample, we constructed cutouts of the 3×3 binned images centered on each galaxy. We note that this data reduction and final, binned galaxy cutouts have also been used in the works of Lisker & Fuchs (2009), Lisker et al. (2009), and Lisker (2009, 2012). However, while these works present the galaxy sample and their unsharp mask images, no attempt at quantifying and characterizing their substructure features is made.

Some of the aforementioned data properties are provided in Table 3.1. In columns 4 through 6, we specify the number of exposures taken during the observations, the magnitude zeropoint, and the surface brightness depth of the galaxy images.

3.1.2 Sample Preparation

Before beginning to work with the dwarf ETG sample, we carried out some additional analyses and pre-processing of the data. For this purpose, we made use of the IRAF astronomical software system and the SAOImage DS9 visualization tool for astronomical data. We utilize them to independently analyze each galaxy image.

First, we measured the noise level of the background-subtracted images using the DS9 statistics tool by targeting regions that are devoid of any objects. We afterwards confirmed each of the measurements with the IRAF `imstat` task. The background noise of the sample is characterized by a standard deviation $\sigma_{\rm noise}$ that ranges between $0.06 - 0.11$ counts s^{-1} with a median value of $\sigma_{\rm noise} = 0.07$ counts s^{-1}. Another important quantity to constrain is the point spread function (PSF) of the galaxy images, which describes the response of the whole imaging system (telescope and instrument) to a point source. We visualized the images through DS9 to identify unsaturated foreground stars, and overlaid the IRAF `imexamine` task to measure their full width at half maximum (FWHM). Thus, we obtain that the PSF FWHM of the sample ranges between $1.13 - 1.41$ arcsec, with a median value of 1.27 arcsec. The median PSF FWHM of each galaxy image is provided in column 7 of Table 3.1. Both the background noise level and PSF FWHM of each galaxy image are relevant parameters that are used during later analyses.

The images were also pre-processed in order to identify and mask any foreground and background sources, such as stars and other galaxies, that lie in the projected vicinity of our objects. This way, subsequent analyses and measurements on the galaxy images are not contaminated by the light of interloping sources. Taking into consideration the small size of the data sample, we decided to individually inspect the images with DS9 and manually identify the position and extent of the interlopers. With this information, we then created a bad pixel mask (BPM) image for each galaxy image. In it, bad pixels that are to be rejected during later analyses are flagged with a number one, while good pixels are instead assigned the number

zero.

3.1.3 Sample Properties

With the aforementioned preparations complete, the next step consists in determining the basic photometric and structural properties of the dwarf ETG sample. For this purpose, we make use of the isophotal analysis and construction tools available in the external STSDAS package of IRAF. To construct an accurate representation of the light profile, we use the IRAF `ellipse` task to fit each galaxy image with elliptical isophotes, while allowing their central coordinates, shape (ellipticity), and orientation (position angle) to change freely with galactocentric radius. This way, any radial changes in the geometry of the galaxies are taken into account by the fitting algorithm.

With the information provided by the fit, the first step is to constrain the total area encompassed by the galaxies. We derive the total galaxy area from the area enclosed by the last valid isophote, which we define as the isophote whose intensity is 2σ above the background noise level. Then, from the flux enclosed by the last valid isophote, we compute the total flux of the galaxies and derive the effective radius, which we define as the semi-major axis length of the isophote that encloses half of the total galaxy light. For the galaxy center, provided previously in Table 3.1, we adopt the central coordinates of the isophote that has a semi-major axis length equal to 1.5 times the PSF FWHM. This particular isophote is chosen in order to avoid any effects of the PSF in the determination of the center. With knowledge of the position of the center, and of the lengths of the effective radius and the total radius, we are then able to derive several basic properties of the galaxies.

The photometric properties of the dwarf ETG sample are provided in Table 3.2. From the total flux of the galaxies, we derive their total apparent and absolute magnitude (in the AB system). The galaxies are intrinsically faint, with an absolute magnitude in the SDSS r-band equivalent that lies in the range $-16.6 > \mathrm{M}_r > -18.4$ mag; thus spanning almost two magnitudes. By knowing their central coordinates and effective radius, we are also able to compute their central and effective surface brightness. Additionally, although we only have imaging data in the white filter to work with, and thus lack color information, we provide the $g-r$ colors of the galaxies as a reference. These color measurements were performed by Janz & Lisker (2008, 2009) based on calibrated images of Lisker et al. (2007, 2008) from the SDSS Data Release 5 (DR5; Adelman-McCarthy et al. 2007). The $g-r$ color of the galaxies, integrated up to two effective radii, is predominantly red and very uniform across the sample, spanning the range $0.58 \leq g-r \leq 0.69$ mag. In summary, the data sample is characterized by having a low intrinsic brightness and an overall red color.

The structural properties of the dwarf ETG sample are provided in Table 3.3. By knowing the length of the effective radius, we measure both the ellipticity and position angle of the one and two effective radii isophotes of the galaxies. As detailed in Chapter 2, knowledge of these geometrical parameters is necessary during the application of the residual method and during the subsequent quantification of the substructure features through a residual light fraction. We observe that, in contrast to the homogeneity of their photometric properties, the structural

Table 3.2: Photometric properties of the Virgo dwarf ETG sample.

Dwarf Galaxy	$\mu_{r,0}$ (mag arcsec^{-2})	$\mu_{r,e}$ (mag arcsec^{-2})	m_r (mag)	M_r (mag)	$g-r$ (mag)
(1)	(2)	(3)	(4)	(5)	(6)
VCC0216	19.25	22.18	14.42	-16.67 ± 0.15	0.603
VCC0308	19.02	22.16	13.30	-17.79 ± 0.15	0.595
VCC0490	19.28	23.09	13.06	-18.03 ± 0.15	0.648
VCC0523	19.29	22.36	12.75	-18.34 ± 0.15	0.622
VCC0856	18.88	22.28	13.47	-17.62 ± 0.15	0.636
VCC0940	19.82	22.90	13.97	-17.12 ± 0.15	0.655
VCC1010	18.77	21.81	12.87	-18.22 ± 0.15	0.693
VCC1695	19.59	23.22	13.61	-17.48 ± 0.15	0.575
VCC1896	19.85	22.61	14.25	-16.84 ± 0.15	0.618

Note. — Col. (1): name of the dwarf galaxy. Col. (2): central surface brightness in the r band. Col. (3): effective surface brightness in the r band. Col. (4): total apparent magnitude in the r band. Col. (5): total absolute magnitude in the r band, assuming a Virgo cluster distance modulus of 31.09 ± 0.15 mag (Blakeslee et al. 2009). Col. (6): $g-r$ color integrated within two effective radii (Janz & Lisker 2008, 2009). All magnitudes are in the AB magnitude system.

Table 3.3: Structural properties of the Virgo dwarf ETG sample.

Dwarf Galaxy	Effective Radius	Ellipticity		Position Angle	
		At 1 R_e	At 2 R_e	At 1 R_e	At 2 R_e
	(arcsec)			(deg)	(deg)
(1)	(2)	(3)	(4)	(5)	(6)
VCC0216	12.93	0.324 ± 0.002	0.333 ± 0.002	28.3 ± 0.1	27.4 ± 0.2
VCC0308	18.41	0.068 ± 0.004	0.060 ± 0.003	59.9 ± 1.9	83.0 ± 1.4
VCC0490	30.13	0.188 ± 0.003	0.122 ± 0.006	122.3 ± 0.5	118.0 ± 1.6
VCC0523	26.11	0.298 ± 0.001	0.252 ± 0.004	138.4 ± 0.1	139.6 ± 0.5
VCC0856	17.24	0.122 ± 0.002	0.063 ± 0.005	85.6 ± 0.4	86.3 ± 2.2
VCC0940	20.99	0.236 ± 0.003	0.077 ± 0.009	17.6 ± 0.4	8.5 ± 3.5
VCC1010	21.41	0.407 ± 0.002	0.392 ± 0.002	176.3 ± 0.2	0.5 ± 0.2
VCC1695	23.00	0.188 ± 0.002	0.191 ± 0.008	83.8 ± 0.4	83.5 ± 1.2
VCC1896	16.90	0.358 ± 0.005	0.062 ± 0.006	22.5 ± 0.5	106.8 ± 3.0

Note. — Col. (1): name of the dwarf galaxy. Col. (2): effective semi-major axis radius. Cols. (3) and (4): ellipticity at one and two effective radii, respectively. The ellipticity is defined as $e = 1 - ba^{-1}$, where a and b are the semi-major and semi-minor axis lengths of the elliptical isophote, respectively. Cols. (5) and (6): position angle at one and two effective radii, respectively. The position angle is measured counterclockwise from the $+y$-axis (north towards east of the images).

properties of the galaxies are much more diverse. While there are some cases in which the ellipticity and position angle of the galaxy isophotes are similar at one and two effective radii, there are also cases in which their values are distinctly different. Due to this diversity, the residual method has been adapted to work properly in the cases of both geometrically simple and geometrically complex radial light profiles.

To further characterize the galaxies, we construct radial profiles of their surface brightness, ellipticity, and position angle parameters, and overlay the isophotes on the galaxy images. As an example, we present the case of dwarf galaxy VCC0308 in Figure 3.1, with the rest of the sample being shown in Appendix A.1. Through the radial parameter profiles, it is possible to observe in more detail the varied levels of geometrical complexity displayed by our sample of dwarf ETGs.

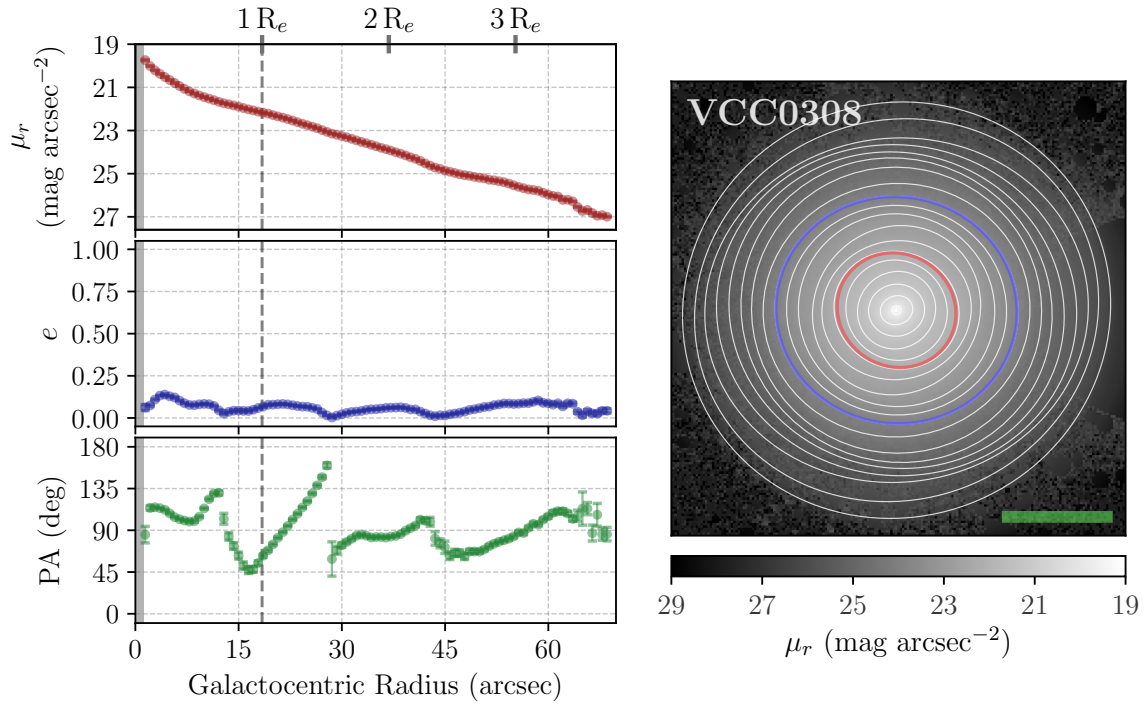

Figure 3.1: Radial parameter profiles and isophote overlays of Virgo dwarf galaxy VCC0308. *Left panels:* from top to bottom, radial profiles of the surface brightness in the r band, the ellipticity, and the position angle. The position angle is measured counterclockwise from the $+y$-axis (north towards east of the images). The gray-shaded area indicates the extension of the PSF FWHM. The vertical dashed line marks the position of the one effective radius. The radial profiles are shown out to the last valid isophote, whose intensity is 2σ above the background noise level. *Right panel*: galaxy image with isophote overlays. The isophotes at one and two effective radii are shown as red and blue ellipses, respectively. The last ellipse shown corresponds to the last valid galaxy isophote. The image scale is shown as a green line, and corresponds to 30 arcsec. North is up, east is to the left. For Figures of the complete sample, see Appendix A.1.

Additionally, we also use the IRAF `bmodel` task to translate the fit parameters into a galaxy model image. We then take the original galaxy image, locate the positions of the bad pixels according to the BPM image, and replace each bad pixel with the corresponding value given by the galaxy model. Consequently, by masking out all interloping sources, we obtain as a result a galaxy image that has a much cleaner and regular appearance. This is mainly for

visualization purposes, as the regions marked on the BPM image are still omitted during any kind of measurement or analysis. However, in the case that the galaxy image is subjected to smoothing, this prevents it from becoming contaminated by the blurred halos of bright interloping sources. Thus, as an example, the unsharp mask of this masked galaxy image would then be able to provide a clearer picture of any faint substructures that are present.

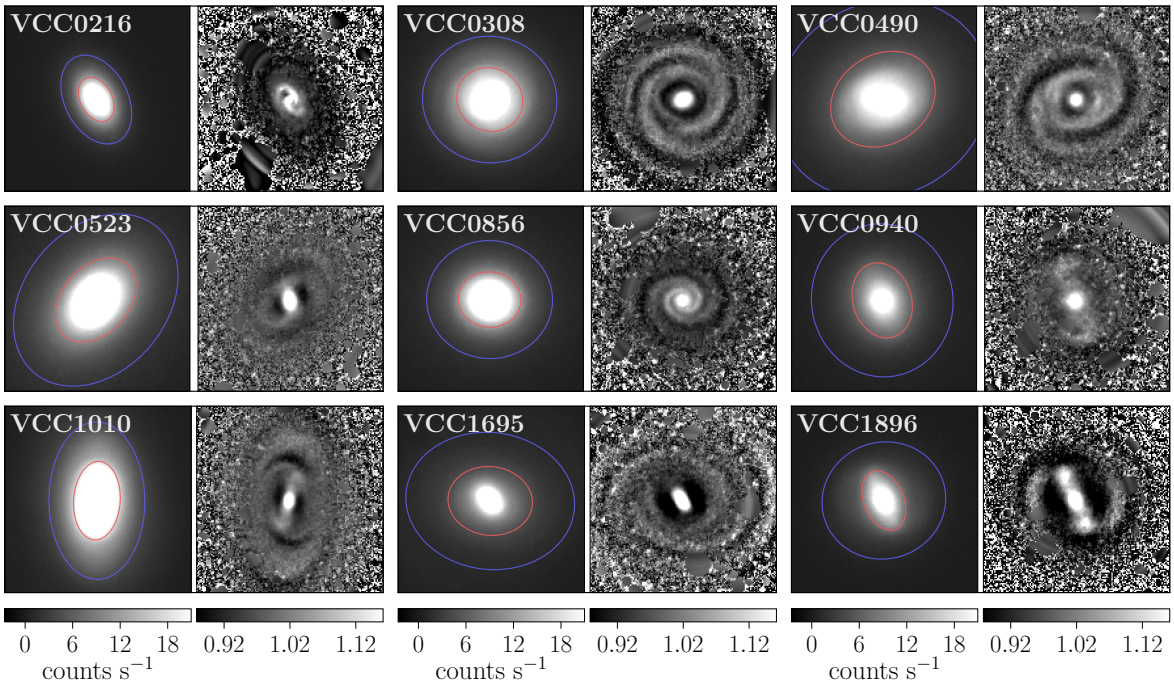

Figure 3.2: Original galaxy images and unsharp mask images of the Virgo dwarf ETG sample. Each original galaxy image is labeled with the name of the corresponding dwarf galaxy, with its unsharp mask image displayed to its right. The galaxy isophotes at one and two effective radii are overlaid on the original image as red and blue ellipses, respectively. Interloping sources have been masked out. The columns share the same gray-scale bar; the original images are in units of counts s^{-1}, while the unsharp masks are unitless due to being image ratios. The images are 100×100 arcsec^2 in size. North is up, east is to the left.

In order to visualize the data sample, we present the original galaxy images and their unsharp mask images in Figure 3.2. For the creation of the unsharp masks, we divide the galaxy image by a smoothed-out version of itself. The galaxy image is smoothed out by using the IRAF `gauss` task to convolve it with an elliptical Gaussian kernel that matches the geometry (ellipticity and position angle) of the isophote at two effective radii, and whose standard deviation along its semi-major axis is 4 arcsec. On the one hand, we choose the isophote at two effective radii to serve as a representation of the overall geometry of the main body of the galaxies, as at these radii they do not appear to be dominated by substructures. On the other hand, the choice of a standard deviation of 4 arcsec is tuned to match half of the average width of the substructure features observed throughout the sample, in order for them to be smoothed out by just the necessary amount. As previously explained in Section 2.3.1, this way the smoothing process efficiently blurs out the disk substructures, while at the same time mostly preserving and not heavily altering the overall geometry of the galaxies.

In Figure 3.2, we observe that the original galaxy images are predominantly smooth in

appearance, although in some cases it is already possible to discern the presence of faint substructure features towards the galaxy outskirts. Albeit smooth, the galaxy light can have at the same time a complex radial geometry, as illustrated by some of the isophotes at one and two effective radii that have been overlaid on the galaxy images. In contrast, by removing most of the smooth light, the unsharp mask images reveal a rich variety of disk features —such as bars, spiral arms, rings, and dumbbells— that normally lie hidden in the dominant diffuse component of the galaxies. These disk features constitute the galaxy substructures that we are interested in quantifying and characterizing in this Chapter.

To understand the context of the dwarf ETGs that constitute our sample, we provide a view into their color-magnitude, spatial, and phase-space distributions compared to other Virgo cluster galaxies in Figure 3.3. Our sample is represented by red points, which are crossed by a vertical blue line in the case that they have identified bar substructures, according to the Fourier analysis performed in Section 3.4. No significant differences are observed between the distributions of our galaxies with and without bars. Overall, the whole sample is consistent with being part of the red sequence that is defined by the other dwarf ETGs of the Virgo cluster. The galaxies of the sample also lie within the projected outer radius of the cluster. In phase-space, the sample lies within one standard deviation of the cluster mean velocity, while being in agreement with having passed the cluster pericenter at least once. Together, this draws a picture in which our sample of dwarf ETGs are not recent infalls and have thus been members of the Virgo cluster for some time, possibly constituting part of the virialized galaxy population of the cluster.

3.2 Application of the Residual Method

We now proceed to apply the residual method, described in Chapter 2, to our sample of nine dwarf ETGs of the Virgo cluster. We closely follow the steps outlined in Section 2.2 and adopt the general parameter configuration specified in Section 2.3.

3.2.1 Parameter Configuration

As explained in detail in Section 2.3, there are two important parameters that have to be set when applying the residual method to a particular data set: the smoothing kernel size and the sampling step size. On the one hand, the smoothing kernel size (see Section 2.3.1) dictates the amount of smoothing the galaxy image is subjected to. As the objective is to blur out the substructure features while at the same time preserving the overall geometry of the diffuse light, the standard deviation of the Gaussian smoothing kernel is tuned to match the average half-width of the substructure features of the galaxies. On the other hand, the sampling step size (see Section 2.3.2) controls the frequency with which the galaxy image is sampled. The length of the step size between successive isophotes is adjusted based on the image resolution of the data, and adopts a geometric growth in order to adequately sample the lower S/N regions at the galaxy outskirts.

In the case of our Virgo dwarf ETG sample, the average half-widths of their substructures

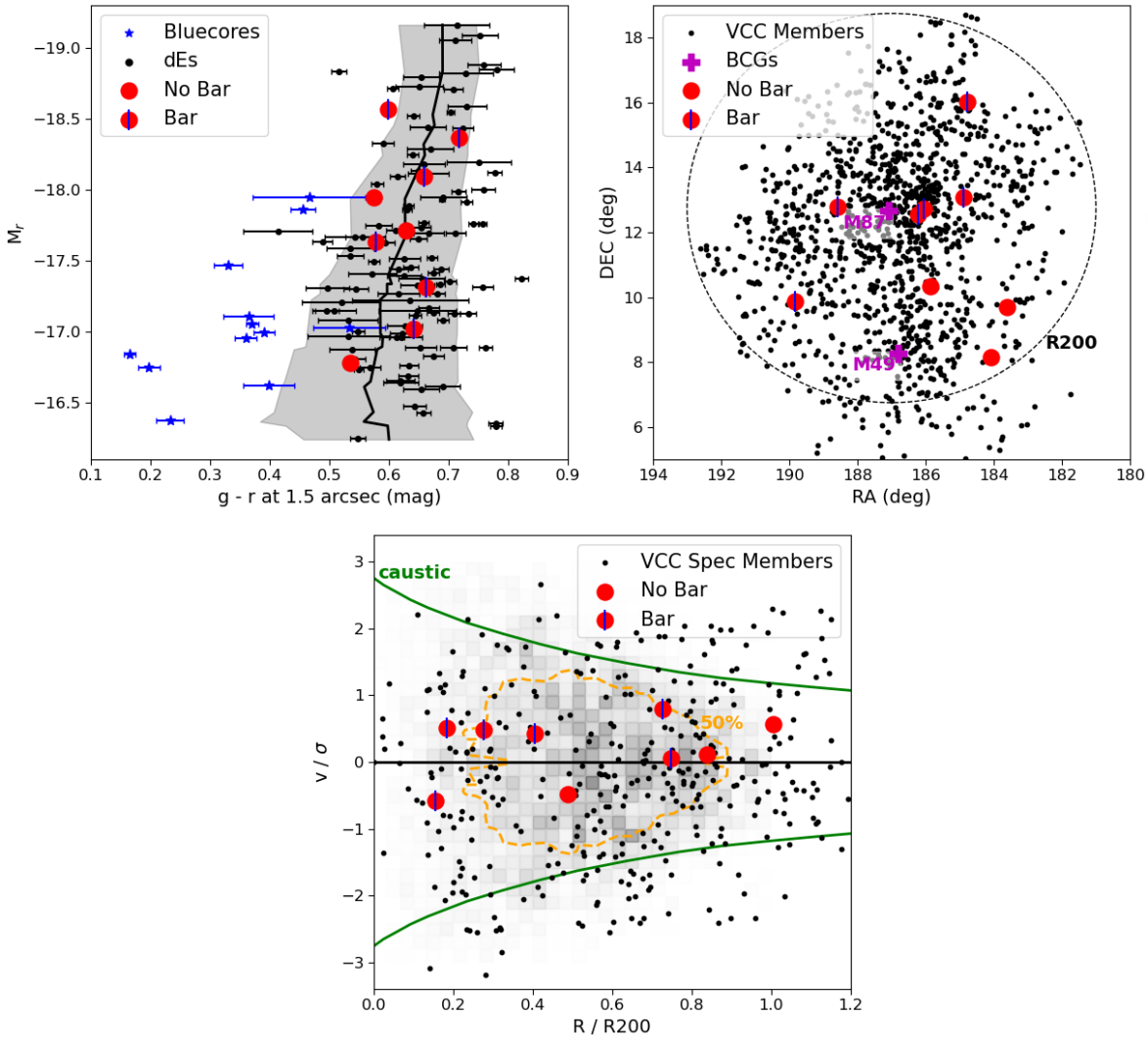

Figure 3.3: Color-magnitude, spatial, and phase-space distribution of the Virgo dwarf ETG sample. Our objects are shown as red points, and are crossed by a vertical blue line if they have an identified bar substructure according to the Fourier analysis of Section 3.4. *Top left panel:* Optical color-magnitude diagram. The $g - r$ color is measured at a radius of 1.5 arcsec from the galaxy center (Urich et al. 2017). Black points are typical dwarf ETGs from the Virgo cluster, while blue points correspond to a sample of blue-cored Virgo dwarf ETGs from Urich et al. (2017). The location of the red sequence is shown as a black line, with its spread shaded in gray. *Top right panel:* Projected spatial distribution. Black points correspond to all VCC members (Binggeli et al. 1985), while the pink crosses correspond to the two Brightest Cluster Galaxies (BCGs) of the Virgo cluster (M87 and M49). The dotted circle represents the outer cluster radius ($R_{200} = 1.55$ Mpc; McLaughlin 1999), defined as the radius at which the mean interior density is 200 times the critical density of the Universe. *Bottom panel:* Phase-space diagram, consisting in the line-of-sight velocity of Virgo galaxies (v) normalized by the cluster velocity dispersion (σ) vs. the clustocentric radius. Black points correspond to all VCC members with radial velocity measurements. The green lines trace out a caustic profile that separates different galaxy infall times (Pasquali et al. 2019), with galaxies within the caustic having fallen in earlier. Gray-scale pixels indicate the relative probability of finding galaxies that have passed the cluster pericenter at least once, derived from cosmological simulations (for more details, refer to Smith et al. 2021). The orange contour encompasses half of the simulated satellite sample. Image credit: this Figure and its caption are adapted from Figure 11 of Smith et al. (2021).

lie in the range of $2.4 - 6.0$ arcsec, which expressed in terms of the PSF FWHM of the data transformed into a Gaussian standard deviation corresponds to $5 - 10 \times \sigma_{\rm PSF}$. Thus, we adopt smoothing kernel sizes equal to $5, 6, 7, 8, 9, 10 \times \sigma_{\rm PSF}$. Similarly, we determine that the optimal separation between successive isophotes is given by a growth rate of the step size length in the range of $5 - 10\%$, so we adopt sampling step sizes with a growth rate equal to $5, 6, 7, 8, 9, 10\%$. As explained in Section 2.3.3, this setup creates a 6×6 configuration grid, with a total of 36 possible combinations of smoothing-sampling parameter pairs. For a consistent application of the residual method across the sample, we run it several times on each galaxy image, where each run adopts a specific parameter configuration pair. Due to the inherent variability of the parameter configuration, any case-by-case variations are taken into account by translating them into the uncertainty range of the median measurement of the residual-to-total light; the residual light fraction. For details on this calculation, refer to Section 2.4. Finally, depending on the configuration, we find that the number of iterations needed in the method ranges between $2 - 5$ iterations, with a median of 3 iterations.

3.2.2 Residual Method Results

We now present the results obtained from the application of the residual method to the dwarf ETG sample. The method allows us to isolate the substructure component of the galaxies in a galaxy residual image, as shown in Figure 3.4. We observe a wide diversity of disk features that, based on a purely qualitative assessment, include bars (e.g., VCC1695, VCC1896), spiral arms (e.g., VCC0308, VCC0856), rings (e.g., VCC0490, VCC1010), and dumbbells (e.g., VCC1010). These features also appear to have different brightness distributions, being in some cases brighter and in others fainter. From a direct comparison with the unsharp mask images presented in Figure 3.2, it is possible to confirm that all the disk features visible in the unsharp masks are captured successfully by the residual method in the residual images.

To quantify the contribution of the substructure component to the total light of the galaxies, the residual light fraction measurements within the one and two effective radii isophotes are summarized in Table 3.4. Overall, we find that, throughout our sample, the disk substructures contribute less than 7% of the total galaxy light, supporting the notion that that these features are indeed faint and lie hidden in a much brighter diffuse component. In particular, we find that the residual light fraction ranges between $1.7 - 6.8\%$ within one effective radius, and between $2.2 - 6.4\%$ within two effective radii. The differences between the one and two effective radii measurements for each galaxy are not significant, making either or both of them good candidates to represent their residual light fraction. These results can be visualized in Figure 3.5, which shows the residual light fraction as a function of the total r-band absolute magnitude of the galaxies. Even though the dwarf ETG sample spans a range of almost two magnitudes, we find no conclusive trend between the residual light fraction and the galaxy brightness. However, given that this is a small data set comprised of only nine dwarf galaxies, we are cautious about drawing any conclusions.

As the diffuse and substructure components of the galaxies have been separated into a model and a residual image, respectively, we can use these images to extract the surface bright-

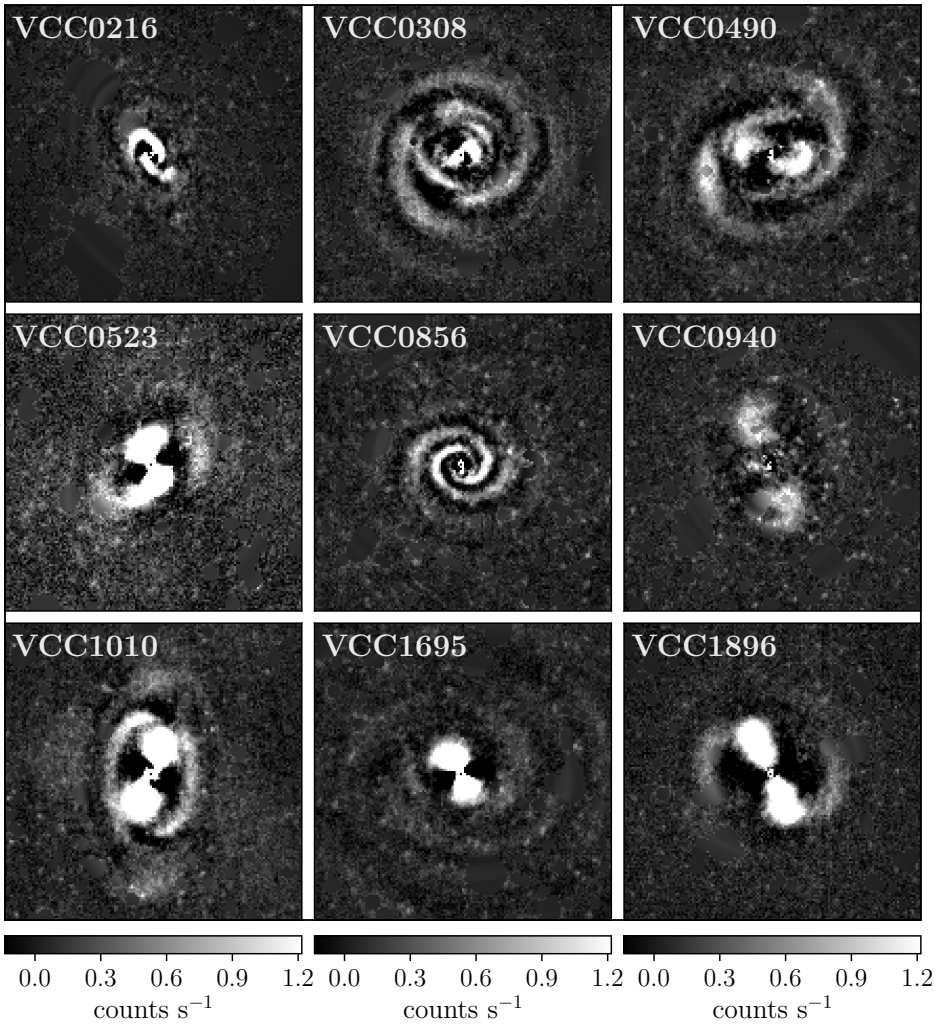

Figure 3.4: Galaxy residual images obtained when applying the residual method to the Virgo dwarf ETG sample. The parameter setup used to obtain these particular residual images corresponds to a smoothing kernel size equal to 7 times the Gaussian standard deviation of the PSF, and a sampling step size with a growth rate of 7% between successive isophotes. Each residual image is labeled with the name of the corresponding dwarf galaxy. All images share the same gray-scale bar in units of counts s^{-1}, and are 100×100 arcsec^2 in size. North is up, east is to the left.

ness profile of each component. For this purpose, we construct concentric elliptical annuli that follow the ellipticity and position angle of the isophotes of the diffuse component of the galaxy, in order to minimize the effect that the substructure features may have in driving the galaxy geometry. These elliptical annuli, which are of a constant 2 pixels (~ 1.4 arcsec) in width, are then used to sample the galaxy model and galaxy residual images out to two effective radii. As a result, in Figure 3.6 we show the surface brightness profiles of the diffuse and substructure components of the dwarf ETG sample, which present some clear differences.

On the one hand, the surface brightness profile of the diffuse component has a smooth appearance, and its brightness declines steadily with increasing galactocentric radius. For a more quantitative assessment, we run the 2D fitting algorithm GALFIT (Peng et al. 2002) on the galaxy model images. We fit them with a Sérsic function (Sérsic 1968), which takes the

Table 3.4: Residual light fractions of the Virgo dwarf ETG sample.

Dwarf Galaxy	Residual Light Fraction	
	Within 1 R_e	Within 2 R_e
(1)	(2)	(3)
VCC0216	$0.033^{+0.002}_{-0.003}$	$0.029^{+0.004}_{-0.002}$
VCC0308	$0.017^{+0.002}_{-0.001}$	$0.024^{+0.002}_{-0.002}$
VCC0490	$0.029^{+0.004}_{-0.004}$	$0.036^{+0.004}_{-0.003}$
VCC0523	$0.040^{+0.005}_{-0.006}$	$0.042^{+0.003}_{-0.004}$
VCC0856	$0.017^{+0.001}_{-0.001}$	$0.022^{+0.004}_{-0.002}$
VCC0940	$0.024^{+0.003}_{-0.003}$	$0.035^{+0.003}_{-0.003}$
VCC1010	$0.031^{+0.005}_{-0.006}$	$0.030^{+0.004}_{-0.005}$
VCC1695	$0.058^{+0.008}_{-0.010}$	$0.054^{+0.005}_{-0.007}$
VCC1896	$0.068^{+0.016}_{-0.017}$	$0.064^{+0.011}_{-0.013}$

Note. — Col. (1): name of the dwarf galaxy. Cols. (2) and (3): residual light fraction measurements within the one and two effective radii isophotes, respectively.

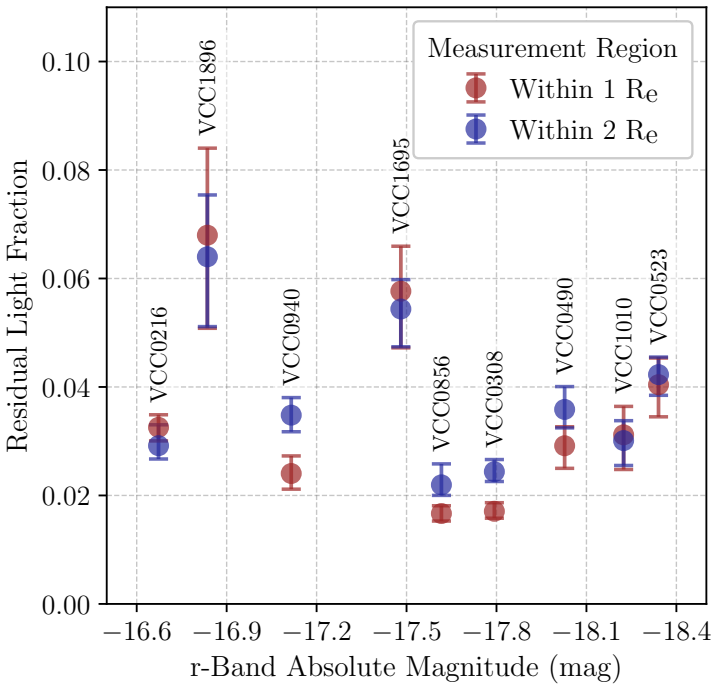

Figure 3.5: Residual light fractions of the Virgo dwarf ETG sample, as a function of the total absolute magnitude of the galaxy in the r band. The measurements are performed within the one and two effective radii isophotes of the galaxies, which are shown as red and blue points, respectively. The error bars are given by the 16th and 84th percentiles of the distributions. Each pair of data points is labeled with the name of the corresponding dwarf galaxy.

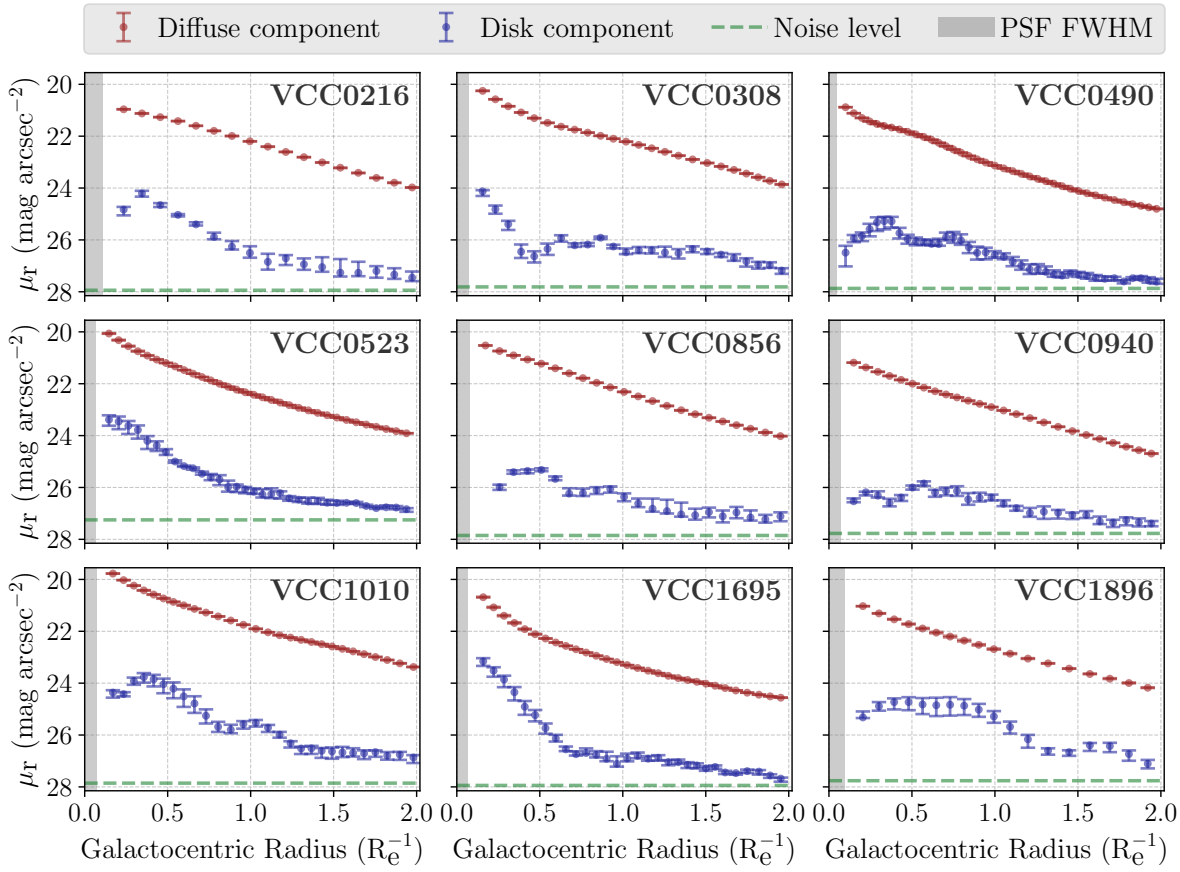

Figure 3.6: Surface brightness profiles in the r band of the diffuse and substructure components of the Virgo dwarf ETG sample. The profile of the diffuse component is shown as red points, while the profile of the substructure component is shown as blue points. The measurements are performed in concentric elliptical annuli of constant width that match the geometry of the isophotes of the diffuse component of the galaxy. The radial profiles are computed out to two effective radii. The central region is excluded due to the effects of the PSF, disregarding an amount equal to 1.5 times the PSF FWHM. The PSF FWHM is indicated by a gray-shaded area. For reference, the background surface brightness level is shown as a green dashed line.

form:

$$\mu(r) = \mu_e \exp\left[-b_n\left(\left(\frac{r}{R_e}\right)^{1/n} - 1\right)\right], \tag{3.1}$$

where $\mu(r)$ is the radial surface brightness, μ_e is the effective surface brightness, R_e is the effective radius, n is the Sérsic index, and b_n is a parameter dependant on the Sérsic index. The Sérsic index acts like a concentration parameter: a small n represents a shallow inner profile with a truncated outer profile, while conversely a large n represents a steep inner profile with extended wings in the outer profile. In the case of our sample, we find that their diffuse components are described well by a single Sérsic profile with Sérsic indices ranging between $1.15 - 2.02$, with a median value of $n = 1.43$. Therefore, the diffuse component of our dwarf ETGs is more consistent with having an exponential disk profile ($n = 1$) than a de Vaucouleurs profile ($n = 4$; de Vaucouleurs 1948), the latter being typical for giant elliptical

galaxies.

On the other hand, the profile of the substructure component presents instead strong fluctuations that can be attributed to the irregularity of the underlying substructures, and its brightness tends to decline less steeply with galactocentric radius. While we do not attempt to fit the galaxy residual images with GALFIT, as the numerous fluctuations in their surface brightness profiles would make this task difficult, we note that there are some cases that would require at least two components to be properly described (see, e.g., VCC0308 and VCC1695). Overall, the surface brightness profile of the diffuse component is, on average, between three to four magnitudes brighter compared to the profile of the substructure component at all radii. Even though the substructure component is comparatively very faint, its surface brightness at the two effective radii isophote is still above the background noise level, so the measurements performed are valid.

Together, these results help build a picture in which the diffuse light and substructure light constitute two distinct galaxy components, as supported by their substantial quantitative and qualitative differences (i.e., their brightness and appearance). Despite this, the similarity of the residual light fraction measurements within one and two effective radii (see Table 3.4 and Figure 3.5) could be an indication that the total physical extension of the diffuse component may not be too different from that of the disk substructure component. In other words, it is possible that these galaxies do not have inner or nuclear disks, but instead their disks are extended all along the galaxy body (at least out to two effective radii, as can be appreciated in Figure 3.6). The analysis of deep images, such as the ones at our disposal, was an essential requirement in order to reveal this behavior. They allowed us to perform robust measurements towards the galaxy outskirts, which would not have been feasible with shallower imaging data.

3.3 Testing the Residual Method

In order to assess both the reliability and relevance of the residual method, we construct a series of diagnostic tests. First, to evaluate its reliability, we test the accuracy with which it is able to recover the light contained in the substructure features of a galaxy. Second, to evaluate its relevance, we compare its performance to the results obtained when other possible, alternative approaches are used to quantify the substructure light. We will show how these alternative approaches are not fundamentally designed to quantify substructures, thus justifying the creation of the residual method to fulfill that purpose. The aforementioned tests are carried out on a sample of mock galaxy images we build specifically for testing purposes.

We begin with a description of the sample of mock galaxy images in Section 3.3.1, followed by an explanation of the different methods to be tested in Section 3.3.2. Then, in Section 3.3.3, we present the results obtained when applying these methods to the mock galaxy sample.

3.3.1 Mock Galaxy Sample

We first address how the mock galaxy sample is constructed. The mock galaxy images have an observational and not a simulated origin, in the sense that they are based on actual images

from our dwarf ETG sample. In particular, we choose two dwarf galaxies, each of which features one of the main signatures of a disk substructure component: VCC0308, which has clear, wound-up spiral arms and no bar; and VCC1896, which has a bright, prominent bar and two faint, short spiral arms. In other words, we focus on the spiral arm and bar substructures.

To construct mock galaxy images from these two galaxies, we take their galaxy model and residual images obtained through the application of the residual method. Next, for each model-residual image pair, we measure the amount of light contained within the total galaxy area (i.e., the region enclosed by the last valid isophote of the original galaxy image, as defined in Section 3.1.3). Then, we proceed to scale each image pair and add them in different relative fractions, while keeping the total amount of light constant. As a result, we obtain a series of mock galaxy images that share the same brightness, but where some have fainter and some have brighter substructure features. In particular, we choose residual-to-total light fractions that encompass the range of empirical values measured across the dwarf ETG sample (refer to Table 3.4 and Figure 3.5). Consequently, for each of the two selected dwarf galaxies, we construct four mock galaxy images by introducing residual light fractions equal to 2.5%, 5.0%, 7.5%, and 10% of the total light. The mock galaxy sample then consists of a total of eight mock galaxy images, which are shown in Figure 3.7. It is possible to observe how the substructure features become brighter and more noticeable with increasing residual light fraction.

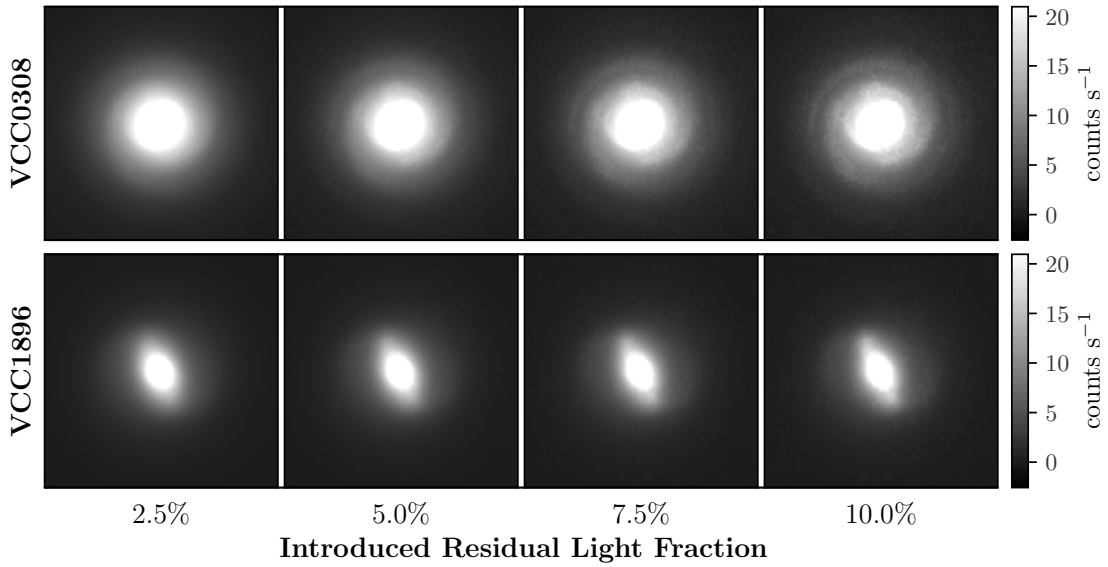

Figure 3.7: The mock galaxy sample, constituted by eight mock galaxy images. *Top row:* mock galaxy images based on Virgo dwarf galaxy VCC0308. *Bottom row:* mock galaxy images based on Virgo dwarf galaxy VCC1896. The residual light fraction that has been introduced increases from left to right, and ranges between 2.5% to 10% of the total galaxy light. All images share the same gray-scale bar in units of counts s^{-1}, and are 100×100 arcsec^2 in size. North is up, east is to the left.

3.3.2 Tested Methods

Because we control the amount of substructure light introduced, we know the exact amount we should expect to recover when subjecting the mock galaxy images to a particular method.

As part of the diagnostic test on the recovery efficiency of the residual light fraction, there are five different methods we want to compare, which are outlined below.

► 1. Residual method.

The objective of the residual method, developed in this work and presented in Chapter 2, is to isolate the substructure component of a galaxy in order to quantify the amount of light it contains. By applying it to the mock galaxy sample, we want to assess the accuracy with which the method is able to recover the introduced amount of residual light. For this test, we apply the complete procedure as described in Section 2.2, and adopt the same parameter configuration we used for our Virgo dwarf ETG sample, described in Section 2.3.

► 2. Residual method, no iterations.

The residual method includes an iterative procedure that allows the gradual separation of the diffuse and substructure components of a galaxy into two separate images. To evaluate how important this iterative aspect is to the success of the residual method, we apply an incomplete, simplified version of the method to the mock galaxy images, in which there are no iterations. For this purpose, we follow only Steps 1 through 5 described in Section 2.2, and keep the first residual image that we obtain, thus omitting the iterative loop altogether. We once again adopt the same parameter configuration we used for our Virgo dwarf ETG sample, described in Section 2.3.

► 3. Unsharp mask method.

The unsharp masking technique aims to bring forward any kind of faint, underlying substructures that could be hiding in the bright, diffuse light of a galaxy image. An unsharp mask image is obtained by smoothing out the galaxy image, and then either dividing or subtracting the smoothed-out image from the original image. Both types of unsharp masking provide comparable results. As the process of smoothing spatially redistributes the light of the galaxy, thus altering the true radial light profile, this technique is originally intended only for visualization purposes, and not for quantification. However, in order to perform a comparison with the residual method, we test the performance of unsharp masking as a means of quantifying substructure features. First, using the IRAF `gauss` task, the mock galaxy images are smoothed out by following the same approach and adopting the same parameter configuration employed in Step 1 of the residual method (see Sections 2.2 and 2.3). Then, for the creation of the unsharp mask images, the IRAF `imarith` task is used to subtract the smoothed-out images from the original mock images. We note that subtraction and not division is used to create these unsharp mask images, as we obtain a measurable flux through subtraction, while division provides instead a flux ratio. Finally, the resulting unsharp mask images are then treated as residual images and are used to quantify the substructure light.

► 4. Fixed fit method.

When fitting a galaxy image, the most common objective is to model the brightness and geometry of the radial light profile as accurately as possible. In the ideal case that a model image is the perfect representation of a galaxy, by subtracting the model from the original image we obtain a residual image filled with zero values. Consequently, the intended purpose of such a residual image is to assess the goodness of the isophotal fit, and not to quantify the substructure features of the galaxy. However, we want to test what happens when the geometry of the galaxy is kept fixed by the fitting algorithm (as in Lisker et al. 2006c), meaning that a single value for the ellipticity and position angle is imposed at all galactocentric radii. Such a geometrically simple fit does not take into account any radial twists and turns of the light profile, and thus it will not be able to capture effectively the complex geometry of the underlying substructure features. As a result, at least part of the substructure light will appear in the residual image created when subtracting this lackluster model. To evaluate how this setup compares to the residual method, the mock galaxy images are fit with concentric isophotes using the IRAF `ellipse` task in fixed mode, by imposing at all galactocentric radii the geometry of the galaxy isophote at two effective radii. We adopt the same parameter configuration used for sampling in the residual method, described in Section 2.3. Finally, we construct the model images using the IRAF `bmodel` task, and subtract the model from the original mock images with the IRAF `imarith` task to create the residual images.

► 5. Free fit method.

This approach follows the explanation of the previous fixed fit method, with one fundamental difference. In this case, we perform an isophotal fit that allows the ellipticity and position angle to change freely at all galactocentric radii. Therefore, the purpose of this method is to model the light profile of the galaxy as accurately as possible, in order for the resulting residual image to contain little to no remaining substructure light. To test how accurate such a free fitting procedure is and to assess how it compares to the residual method, we quantify any light that is left in the residual images of the mock galaxies. For this purpose, the mock galaxy images are fit with concentric isophotes using the IRAF `ellipse` task in free mode, by allowing the geometry of the galaxy isophotes to freely change radially. Apart from this difference, we adopt the same sampling configuration specified in the fixed fit method, and follow the same procedure to create the residual images.

3.3.3 Test Results

We now present the results obtained when applying these five different methods to the mock galaxy sample. We note that, during the creation of the mock galaxy images, the scaling and addition of the galaxy components was done in terms of the total galaxy light, and therefore all reported measurements are also performed in the total encompassing area of the galaxies.

To begin with, we assess the reliability of the residual method in recovering the introduced amount of substructure light. The recovered versus introduced residual light fractions are re-

Table 3.5: Residual light fractions from applying the residual method to mock galaxies.

Dwarf Galaxy	Residual Light Fraction	
	Introduced	Recovered
(1)	(2)	(3)
VCC0308	0.025	$0.026^{+0.003}_{-0.002}$
	0.050	$0.047^{+0.002}_{-0.002}$
	0.075	$0.070^{+0.002}_{-0.002}$
	0.100	$0.093^{+0.002}_{-0.002}$
VCC1896	0.025	$0.039^{+0.006}_{-0.007}$
	0.050	$0.058^{+0.006}_{-0.006}$
	0.075	$0.078^{+0.009}_{-0.006}$
	0.100	$0.100^{+0.005}_{-0.008}$

Note. — Col. (1): name of the dwarf galaxy used to construct the mock galaxy images. Col. (2): residual light fraction introduced into the mock galaxy. Col (3): residual light fraction recovered when applying the residual method.

ported in Table 3.5. The recovery efficiency of the residual method proves to be quite accurate, staying mostly within the uncertainty ranges. These results can be visualized in Figure 3.8, in which we notice an overall trend for the recovered fraction to slightly decrease with respect to its introduced fraction as the residual light increases (i.e., the filled circle data points start to go below the one-to-one expected relation). Therefore, it is reasonable to assume that the residual method only stays accurate when dealing with low amounts of substructure light, as it was specifically developed for that purpose. Its application is thus not advisable in cases with bright substructures (e.g., giant spiral galaxies). Additionally, the measurements present error bars of different sizes, which can be attributed to the different morphology of the substructures that dominate in each mock galaxy. The dwarf galaxy VCC0308, with strong spiral arms, shows small uncertainties; while VCC1896, with a strong bar, presents instead comparatively larger uncertainties. This is a possible indication that the residual method is better suited to capturing the light contained in spiral arms than in prominent bar substructures.

Figure 3.8 also provides a comparison of the performance of the residual method with and without its iterative procedure. This test shows that the iterative aspect is fundamental: without iterating, the residual method is unable to properly isolate the light of the substructure component from the light belonging to the diffuse component, resulting in a residual light fraction that is too low. In other words, the galaxy residual image only contains a small fraction of the substructure light, while the majority of it is still blended with the diffuse light in the galaxy model image. Consequently, the complete, iterative version of the residual method is needed in order to provide accurate measurements of the faint substructure features embedded in galaxies.

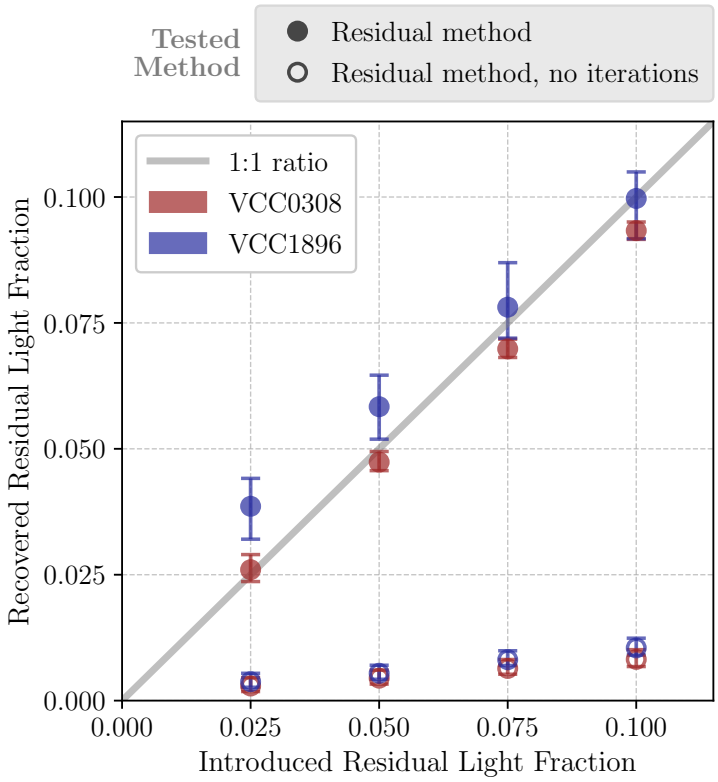

Figure 3.8: Recovered vs. introduced residual light fractions obtained when applying the residual method to the mock galaxy images based on Virgo dwarf galaxies VCC0308 (red points) and VCC1896 (blue points). The results of applying the complete residual method are shown by filled circles, while the results of applying an incomplete, simplified version of the residual method, in which there is no iterative procedure, are shown by empty circles. All measurements are performed within the total galaxy area, and their error bars are given by the 16th and 84th percentiles of their distributions. The one-to-one expected relation is shown as a gray line, representing the ideal case in which the introduced residual light fraction is recovered in its entirety.

Next, we evaluate the performance of alternative methods that are normally not used for quantification purposes. In Figure 3.9, we present the recovered versus introduced residual light fractions when applying the unsharp mask method, the fixed fit method, and the free fit method to the mock galaxy sample. The main result is that these methods are unable to successfully recover the introduced amount of substructure light. First, for the unsharp mask method, we find that it fails to recover a positive amount of residual light. It is also mostly insensitive to the introduced residual light fraction, presenting a relatively flat relation. Second, for the fixed fit method, we find that its performance varies depending on the dwarf galaxy on which the mock images are based. The mock galaxy images based on VCC0308 are in the positive recovery region of the plot, albeit with a very low recovery efficiency, while the mock galaxy images based on VCC1896 are in the negative recovery region of the plot. This discrepancy is a reflection of how the complexity level of the galaxy geometry affects the goodness of the fit. Third, for the free fit method, we find that, despite staying in the positive recovery region of the plot, it still does not recover enough light from the one that is introduced. In conclusion, these three methods cannot be used for quantification, and should instead be used for their intended purposes; namely, visualization of faint embedded substructures in

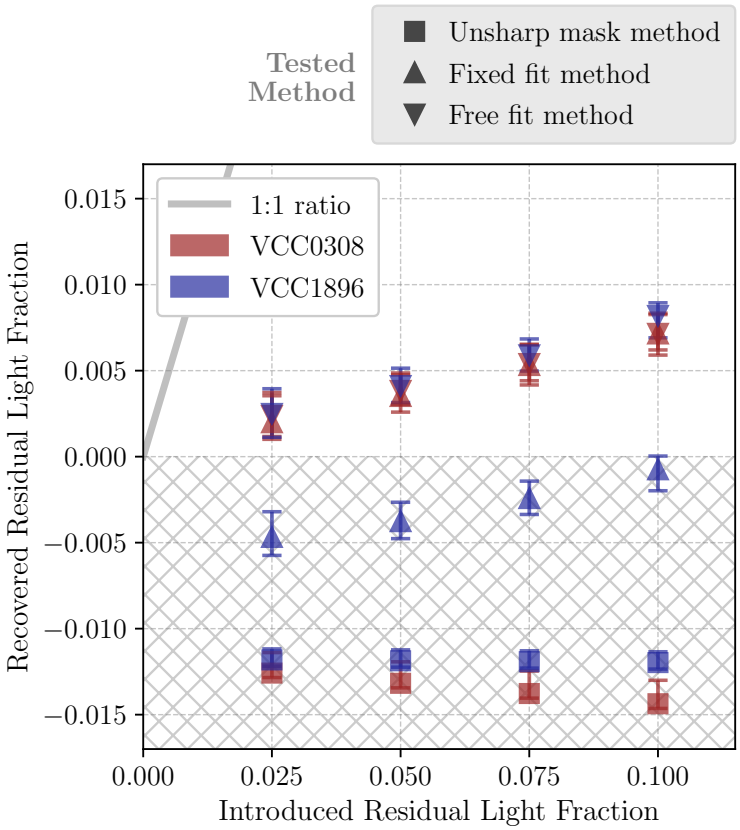

Figure 3.9: Recovered vs. introduced residual light fractions obtained when applying alternative methods to the mock galaxy images based on Virgo dwarf galaxies VCC0308 (red points) and VCC1896 (blue points). Different symbols represent the results of applying each method: the unsharp mask method (squares), the fixed fit method (up triangles), and the free fit method (down triangles). All measurements are performed within the total galaxy area, and their error bars are given by the 16th and 84th percentiles of their distributions. The hatched area delimits the negative recovery region of the plot, where the tested methods fail to recover a positive amount of residual light. The one-to-one expected relation is shown as a gray line, representing the ideal case in which the introduced residual light fraction is recovered in its entirety.

the case of the unsharp mask method, and modeling of the light distribution in the case of the fixed and free fit methods.

In order to visualize the results of these diagnostic tests, the residual images that are obtained by applying these five methods to the mock galaxy sample are displayed in Figure 3.10. For illustration purposes, we only show the residual images of the mock galaxies in which a residual-to-total light fraction of 10% has been introduced. However, we can confirm that the rest of the sample follows the same behavior that is observed on these residuals. At first glance, the residual images of each mock galaxy may appear quite similar in general morphology; however, they present particularities that strongly differentiate one method from the next.

In the case of the residual method, we observe that the disk substructure features appear bright and with the correct geometry in the residual images, and that the negative values in the inter-arm (or inter-substructure) galaxy regions have been minimized. In contrast, for the

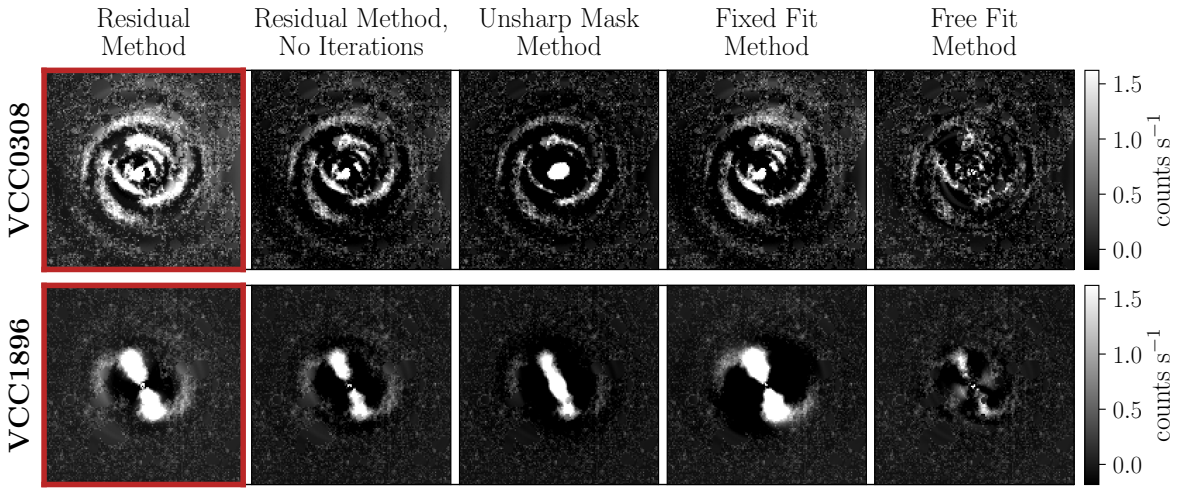

Figure 3.10: Galaxy residual images obtained when applying different methods to the mock galaxy images based on Virgo dwarf galaxies VCC0308 (top row) and VCC1896 (bottom row). From left to right, the columns represent the different methods that have been tested: the residual method (highlighted by a red frame), the residual method with no iterations, the unsharp mask method, the fixed fit method, and the free fit method. The particular residual images that are shown correspond to the mock galaxies in which a residual-to-total light fraction of 10% has been introduced. All images share the same gray-scale bar in units of counts s^{-1}, and are 100×100 arcsec^2 in size. North is up, east is to the left.

residual method with no iterations, the substructure features present the same geometry but appear much fainter, while the inter-substructure regions are dominated by negative values. As previously explained in Step 7 of the method (see Section 2.2), this is because the residual image is suffering from over-subtraction of the model image, which is something that can only be alleviated by the iterative aspect of the method.

We will now address the alternative methods. For the unsharp mask method, we observe that the disk substructure features present the correct geometry in the residual images, albeit being too faint, while the inter-substructure regions are dominated by negative values. Additionally, the bulge region appears artificially bright and prominent, which is an unwanted effect that is inherent to any smoothing procedure. When smoothing, light from the brighter central region is redistributed towards the fainter galaxy outskirts. As a consequence, when subtracting this smooth and flattened light profile from the original galaxy image, the resulting residual image is unavoidably brighter in the central region and fainter in the outskirts. Thus, whenever using unsharp masking for visualization purposes, the presence of this artificial effect should be kept in mind.

For the fixed fit method, the result we obtain is directly dependent on the complexity level of the galaxy geometry. On the one hand, dwarf galaxy VCC0308 is geometrically simple, as it has a face-on appearance that can be characterized by circular isophotes. Consequently, despite modeling the radial light profile with a single fixed value for the ellipticity and position angle, the disk substructures in the residual image have the correct geometry. On the other hand, VCC1896 is geometrically more complex, as its inner region is dominated by a bar with highly elliptical isophotes, while its outer region is dominated by spiral arms with more

circular isophotes. Therefore, a single fixed value for the ellipticity and position angle fails to properly characterize the galaxy as a whole, and thus artificially alters the appearance of the disk substructures in the residual image. We can clearly observe the flared-out appearance of the bar, while the spiral arms appear to be truncated. Additionally, and regardless of the specific galaxy geometry, the inter-substructure regions of the residual images of both mock galaxies are dominated by negative values. Given that a fixed fit approach has a high risk of underestimating and thus mischaracterizing the complex geometry of a galaxy, the user should be wary when using it for modeling purposes.

Finally, for the free fit method, we observe that the residual images contain only a very small fraction of the substructure light. The remaining disk substructures either appear very faint, or are not visible at all. This makes sense, as the objective of the free fit method is to model the light distribution of a galaxy as accurately as possible by allowing the ellipticity and position angle of the isophotes to change freely. We note that the fitting algorithm of the IRAF `ellipse` task has issues in fitting properly the bar of dwarf galaxy VCC1896, as an artificial feature appears perpendicular to the bar in the central region. In essence, these residual images reveal the inherent limitations of the particular fitting procedure that is being implemented (in our case, of the IRAF `ellipse` task), and can therefore play a useful role when assessing the quality of the modeling.

In conclusion, it is clear from these quantitative and qualitative assessments that the residual method constitutes the best option to both reliably identify and accurately quantify faint substructure features that are embedded in the bright diffuse body of a galaxy.

3.4 Fourier Analysis of Residual Images

As a means of showcasing the potential of the residual method, we subject the Virgo dwarf ETG sample to a Fourier analysis. The Fourier analysis of galaxy images can be used to both identify and characterize the different structural components that constitute a galaxy (Elmegreen et al. 1989; Rix & Zaritsky 1995). In particular, its application can also be extended to the dwarf regime, and has already been carried out on some of the dwarf galaxies belonging to our sample as an attempt to quantify their faint disk substructure features (see, e.g., Jerjen et al. 2000b; Barazza et al. 2002). In this work, we want to show that it is possible to go one step further, and perform a Fourier decomposition of the galaxy residual images obtained through the residual method. This way, by analyzing the residual images instead of the galaxy images themselves, we are able to deal directly with the disk substructures that have already been efficiently extracted and isolated by our method.

To begin with, we introduce the Fourier decomposition formalism in Section 3.4.1, and explain how it can be used to identify and characterize bar and spiral substructure features. Then, in Section 3.4.2, we evaluate the performance of this decomposition when being applied to the residual images, as compared to the traditional approach of applying it to the original galaxy images. Finally, in Section 3.4.3, we present the results obtained from carrying out a Fourier analysis on the residual images of the dwarf ETG sample. We would like to note that

the Fourier decomposition itself was carried out by a close collaborator, K. Kraljic; while all the posterior analyses and interpretations stemming from this decomposition were carried out by the author.

3.4.1 Fourier Formalism

Formally, the Fourier approach consists in the azimuthal spectral analysis of the surface brightness distribution of a galaxy image. The surface brightness profile is decomposed into a Fourier series, which takes the form

$$\Sigma(r,\theta) = \Sigma_0(r) + \sum_m A_m(r)\cos\left(m\theta - \Phi_m(r)\right) \ , \tag{3.2}$$

where $\Sigma(r,\theta)$ is the surface brightness of the galaxy expressed in polar coordinates, with r being the radial distance and θ being the azimuthal angle. The associated Fourier amplitude and phase are given by A_m and Φ_m, respectively, where m is the Fourier mode. Here, $\Sigma_0(r)$ stands for the azimuthally averaged surface brightness profile.

The advantage of this approach is that the presence of disk features, such as bars and spiral arms, can be ascertained based on the behavior of specific Fourier parameters. On the one hand, the signature of a bar is typically associated with a prominence of even components, in particular of the mode $m = 2$. Thus, a bar can be identified based on a constant phase $\Phi_2(r)$, which stays fixed with radius within a region of certain extent. On the other hand, the presence of spiral arms manifests itself through a linearly varying phase $\Phi_m(r)$ for an m-armed spiral mode. That is, a two-armed spiral feature would present a linear variation of $\Phi_2(r)$ with radius over an extended region.

► Bar substructure features.

First, we address the identification and characterization of bar-like substructures. When searching for a bar, we decide that a bar is present if the phase $\Phi_2(r)$ remains constant within ± 5 degrees around the median over a large enough region, which we denominate as the "bar region" (Kraljic et al. 2012). This definition is tuned to exclude spiral-like features, which typically vary by a few tens of degrees over several arcseconds. As an additional requirement, a bar region must present a peak in the normalized radial amplitude of mode $m = 2$; $A_2(r)/A_0(r)$. The bar region should also start at galactocentric radii between $2.1 - 5.0$ arcsec ($3 - 7$ pixels) and cover a radial extension of at least 3.6 arcsec (5 pixels). The minimum extent of the bar region is set such that it encompasses the bars that have already been identified in our sample. We avoid the innermost galaxy region (< 2.1 arcsec or 3 pixels), as central asymmetries can cause large variations in $\Phi_2(r)$ even for visually identified barred systems. We also estimate that the bar length measurements have an associated uncertainty of 0.71 arcsec (1 pixel), which corresponds to the resolution of the Fourier algorithm, as it operates in radial bins of one pixel in size.

When the aforementioned criteria are met, the galaxy is classified as having a bar. To

characterize the identified bar substructure, we proceed to quantify the bar strength, based on the definition proposed by Aguerri et al. (1998),

$$S_{\text{bar}} = \frac{1}{r_{\text{bar}}} \int_{r_{\text{start}}}^{r_{\text{end}}} \frac{A_2(r)}{A_0(r)} \, \mathrm{d}r \,, \tag{3.3}$$

where r_{start} and r_{end} are the inner and outer radius of the bar region, respectively; and r_{bar} is the overall bar length (thus, $r_{\text{bar}} = r_{\text{end}} - r_{\text{start}}$). Here, $A_0(r)$ and $A_2(r)$ correspond to the Fourier amplitudes of modes $m = 0$ and $m = 2$, respectively. However, as the computation of the bar strength is in practice a discrete measurement in pixel-sized steps, we use the following definition:

$$S_{\text{bar}} = \frac{1}{r_{\text{bar}}} \sum_{r=r_{\text{start}}}^{r_{\text{end}}} \frac{A_2(r)}{A_0(r)} \,. \tag{3.4}$$

This definition is implemented with a small adjustment: we always assign $A_0(r)$ as the amplitude of mode $m = 0$ of the original galaxy image. In other words, when analyzing either the original image or the residual image, $A_2(r)$ will always be normalized by the $A_0(r)$ of the original image. In order to assess the influence of the innermost galaxy region that is being excluded ($r < 2.1$ arcsec or 3 pixels), we additionally provide in each case an alternative bar strength measurement that starts instead at $r_{\text{start}} = 0$.

In addition, we also want to quantify the disk substructures of the whole sample of galaxies, independently of whether they are barred or non-barred systems. For this purpose, we consider the overall contribution of their mode $m = 2$ relative to their mode $m = 0$. By adapting Equation 3.4, we thus define the total strength of mode $m = 2$ as

$$S_2 = \frac{1}{\mathrm{R}_e} \sum_{r=0}^{\mathrm{R}_e} \frac{A_2(r)}{A_0(r)} \,, \tag{3.5}$$

where R_e is the effective radius of the galaxy, previously specified in Table 3.3 for our sample. Just as stated before, when either analyzing the original galaxy image or the residual image, $A_0(r)$ always corresponds to the amplitude of mode $m = 0$ of the original image.

► Spiral substructure features.

Next, we address the identification and characterization of spiral-like substructures. From the visual inspection of the galaxy residual images, we observe that only two-armed spiral features are present across the sample (refer to Figure 3.4). Consequently, we search for regions in which the phase $\Phi_2(r)$ varies linearly with galactocentric radius, which we then designate as "spiral arm regions". In order to characterize the identified spiral features, we proceed to compute their pitch angles. At any given radius, the pitch angle $\psi(r)$ is defined as the angle between the tangent of a spiral arm and the tangent of a circle, and is a measure of the tightness of the winding of the spiral (Binney & Tremaine 2008). Tightly wound spiral

arms have small pitch angles, while instead loosely wound spiral arms have big pitch angles. Formally, the pitch angle can vary between $-90 < \psi(r) < 90$ degrees, where the sign indicates the direction of rotation of the spiral arm: positive being clockwise winding, and negative being counterclockwise winding.

As our sample is constituted by real galaxies that do not have perfect logarithmic spiral features, their pitch angles are expected to vary with radius. Taking this into consideration, we first identify in the mode $m = 2$ phase plot the locations of the spiral arms. Then, we proceed to linearly fit each spiral arm segment separately, adopting the form $\Phi_2(r) = ar + b$; where a is the slope and b the intercept. From this linear fit, we can then derive an instantaneous pitch angle for any given radius r of the spiral, given by

$$\psi = \arctan\left(\frac{\mathrm{d}r}{r\,\mathrm{d}\Phi_2}\right) = \arctan\left(\frac{1}{ar}\right), \tag{3.6}$$

where $\mathrm{d}\Phi_2/\mathrm{d}r$ corresponds to the slope a of the linear relation. Following this approach, we obtain a series of pitch angles (one for each radial step) for the spiral arm regions. Finally, by taking the median of all pitch angle values, we compute a representative pitch angle for each galaxy, and derive their uncertainties from the 16th and 84th percentiles of the distribution.

As a final remark, the Fourier analysis we carry out does not make any assumptions on the possible inclination angles of the dwarf ETGs of our sample. Consequently, derived quantities such as the bar length and median spiral arm pitch angle correspond to projected measurements.

3.4.2 Galaxy Images vs. Residual Images

To prove how the aforementioned analyses of the bar and spiral substructures benefit from using the galaxy residual images instead of the original images themselves, we provide two examples from our sample: dwarf galaxies VCC1896 and VCC1010. These two galaxies are chosen because they present both similarities and differences, which makes them ideal for a comparison. They have a similar morphology, in the sense that a strong bar feature dominates their substructures. However, these substructures differ in their contribution to the total galaxy light, with VCC1896 having a residual light fraction more than two times larger than that of VCC1010 (refer to Table 3.4 and Figure 3.5).

On the one hand, dwarf galaxy VCC1896 has comparatively brighter substructures, and the Fourier analysis is successful when applied to both the original image (Figure 3.11) and the residual image (Figure 3.12). In both cases, the even modes dominate the surface brightness distribution, and the disk substructures of the galaxy are clearly visible in the mode $m = 2$ map. The amplitude plots also show a peak in the normalized A_2 amplitude, which is a signature of a bar-like feature, and the phase Φ_2 plots allow an unambiguous identification of both the bar and spiral arm regions. We would like to highlight that a bar of almost identical length is detected in both cases, and that the radial position of the normalized A_2 peak is preserved. This serves as a confirmation of the robustness of the residual method, proving that it is able

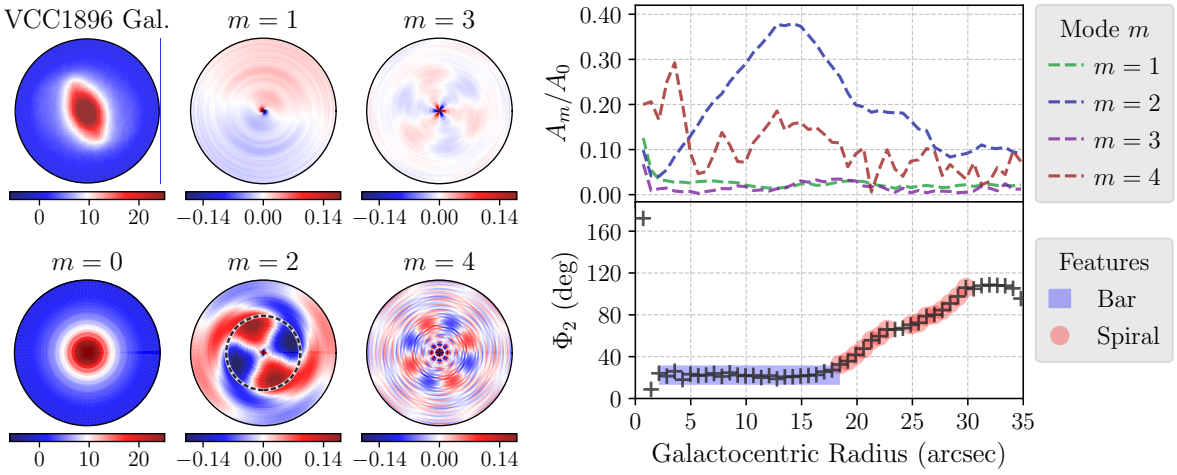

Figure 3.11: Fourier mode maps and Fourier parameters corresponding to the original galaxy image of Virgo dwarf galaxy VCC1896. *Left circular panels*: the original galaxy image and maps of Fourier modes $m = 0$ through $m = 4$ are shown. The Fourier maps of modes $m = 1$ through $m = 4$ have been normalized by the map of mode $m = 0$. Each image has its own color bar; the original galaxy image and the map of mode $m = 0$ are in units of counts s^{-1}, while the maps of modes $m = 1$ through $m = 4$ are unitless. The dashed circle in the $m = 2$ map marks the detected end radius of the bar. The images display a circular area of 35 arcsec in radius. North is up, east is to the left. *Right rectangular panels*: the Fourier parameters, amplitude and phase, are shown as a function of galactocentric radius. On the top panel, we show the amplitude of modes $m = 1$ through $m = 4$, which have been normalized by the amplitude of mode $m = 0$. On the bottom panel, we show the phase of mode $m = 2$, measured counterclockwise from the $+y$-axis. The detected bar-like substructure is highlighted by a blue rectangle, while the data points associated with spiral-like substructure are highlighted by red circles.

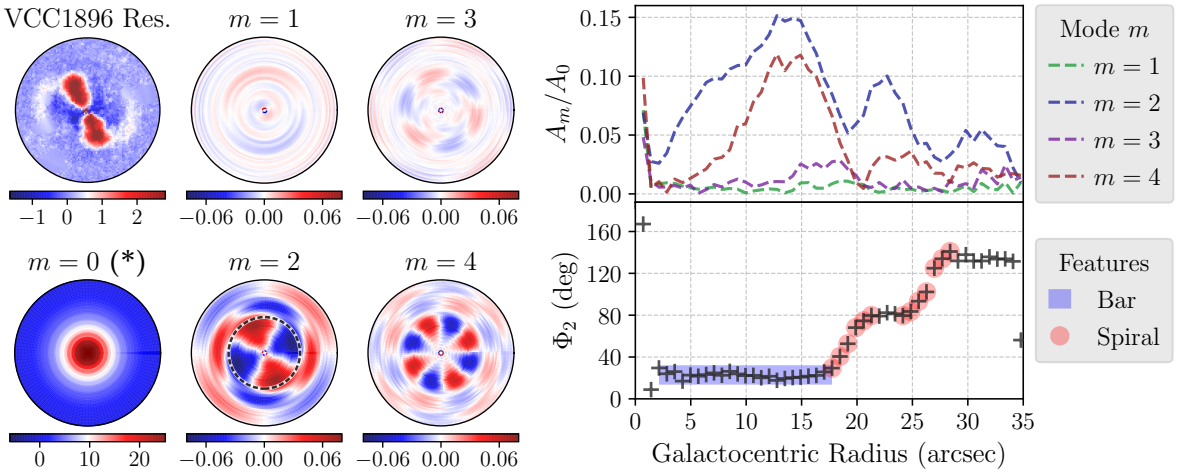

Figure 3.12: As in Figure 3.11, but for the galaxy residual image of Virgo dwarf galaxy VCC1896. We note that the Fourier maps of modes $m = 1$ through $m = 4$ have been normalized by the map of mode $m = 0$ of the original galaxy image, which is once again displayed here and marked with an asterisk (*). Likewise, the amplitude of modes $m = 1$ through $m = 4$ have been normalized by the amplitude of mode $m = 0$ of the original galaxy image. The galaxy residual image is in units of counts s^{-1}. Both bar-like and spiral-like substructures are detected. For Figures of the complete sample, see Appendix A.2.

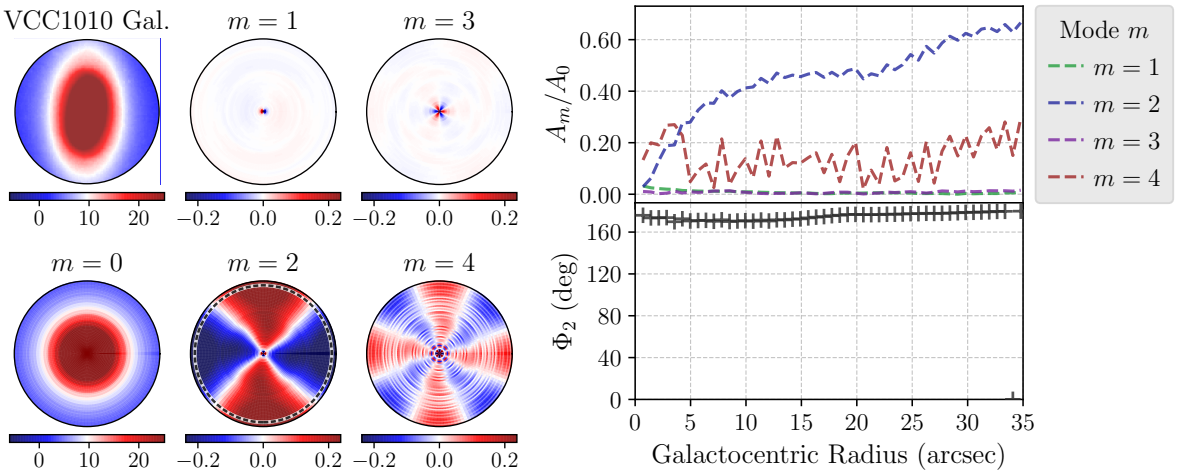

Figure 3.13: As in Figure 3.11, but for the original galaxy image of Virgo dwarf galaxy VCC1010. No bar-like or spiral-like substructures are detected; instead, we identify a strong triaxial feature.

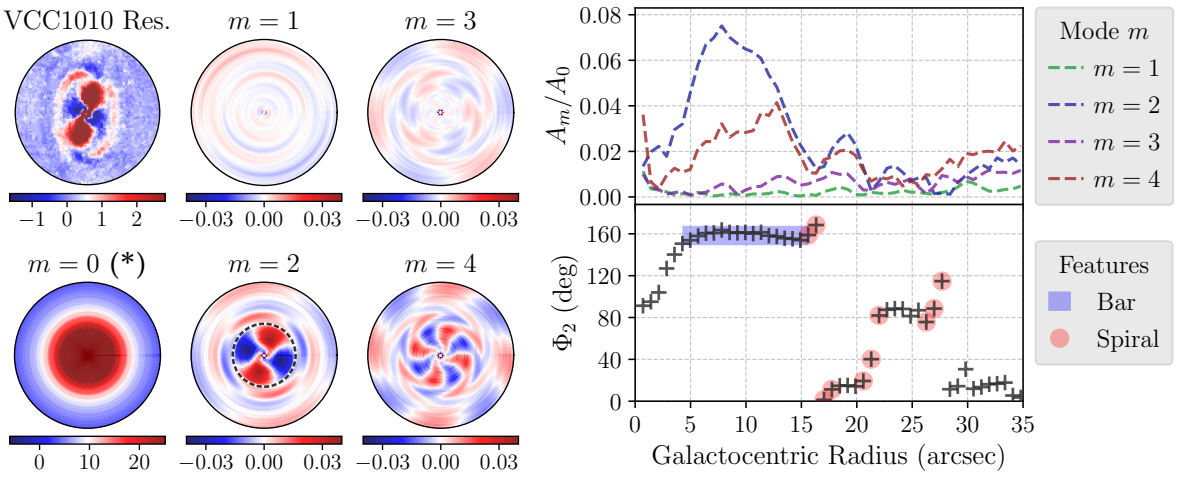

Figure 3.14: As in Figure 3.12, but for the galaxy residual image of Virgo dwarf galaxy VCC1010. Both bar-like and spiral-like substructures are detected. For Figures of the complete sample, see Appendix A.2.

to accurately extract any hidden substructure features and properly isolate them in a residual image.

On the other hand, dwarf galaxy VCC1010 has comparatively fainter substructures, and the Fourier analysis is unsuccessful in detecting any disk features when applied to the original image (Figure 3.13). However, it succeeds when applied to the residual image (Figure 3.14). For the original image, we observe no peak in the normalized A_2 amplitude, so the region of constant Φ_2 that we detect does not correspond to a bar, but instead to a strong triaxial feature. We are also unable to detect any spiral-like features. In contrast, in the case of the residual image, the disk substructures have already been extracted and isolated, so this time the Fourier decomposition succeeds in describing them. We can clearly identify the bar and spiral arm regions in the mode $m = 2$ map, recognize the expected behavior of their normalized A_2 amplitude in the amplitude plot, and constrain them based on the phase Φ_2 plot.

In conclusion, when the residual-to-total light is too low, as is the case of VCC1010, the Fourier decomposition will fail to detect the faint substructure features that lie hidden in the much brighter main body of the galaxy. For this reason, the Fourier analysis that we subsequently carry out does not make use of the original galaxy images, and instead it only considers the residual images of our dwarf ETG sample.

3.4.3 Fourier Analysis Results

The results obtained from the Fourier component analysis of the residual images of our dwarf ETG sample are summarized in Table 3.6. Their Fourier mode maps, amplitude plots, and phase plots are presented in Appendix A.2. Overall, we identify six galaxies that are barred (VCC0490, VCC0523, VCC0940, VCC1010, VCC1695, and VCC1896), and three galaxies that are non-barred (VCC0216, VCC0308, and VCC0856). For the barred systems, we characterize the bar substructures by deriving their extension —start radius ($r_{\rm start}$), end radius ($r_{\rm end}$), and length ($r_{\rm bar}$)— and orientation —phase ($\Phi_{\rm bar}$)— from the $\Phi_2(r)$ plot, and compute their strength ($S_{\rm bar}$) through Equation 3.4. Then, for the full sample, we compute the strength of mode $m = 2$ (S_2) through Equation 3.5. Additionally, we also derive the tightness of the winding —median pitch angle (ψ)— of their spiral arm substructures from the $\Phi_2(r)$ plot and by applying Equation 3.6. For details on these calculations, refer to the previous Section 3.4.1.

The Fourier analysis reveals that the identified bar features are between $5.7 - 15.6$ arcsec in projected angular length, with a median of 9.6 arcsec. Assuming a Virgo cluster distance of 16.5 ± 1.1 Mpc, derived from a Virgo distance modulus of 31.09 ± 0.15 mag (Blakeslee et al. 2009), these angular sizes are equivalent to a projected physical length ranging between $460-1250$ pc, with a median of 770 pc. We also find that the strength of the bar features ranges between $3.5 - 12.7\%$. The alternative measurements starting at $r_{\rm start} = 0$ alter the result by a few percent at most, serving as a confirmation of the robustness of this calculation.

For the identified spiral arm features, we find that the absolute value of their median projected pitch angles ranges between $4.5 - 25.4$ degrees. We note that Lisker et al. (2006c) reports pitch angles in agreement with ours for the four dwarf galaxies that we have in common (VCC0308, VCC0490, VCC0856, and VCC1896; refer to their Figure 8), despite having used a completely different approach. The majority of our sample presents small pitch angles, and thus tightly wound spiral arms, which are typically found in spiral galaxies of Hubble early-type (S0−Sb; Ma et al. 1999). However, we also have some galaxies with comparatively larger pitch angles, which are instead more consistent with spirals of the Hubble late-type (Sc−Sd). Therefore, even though our dwarf ETG sample tends towards small pitch angles, the broad range they cover could be a possible indication of their different origins and/or evolutionary histories.

Overall, the full sample presents a strength of their mode $m = 2$ that lies in the range between $2.0 - 8.3\%$. We can directly compare these Fourier strengths with the residual strengths (i.e., residual light fractions) obtained through the residual method, previously reported in Table 3.4 and Figure 3.5. Within the same measurement region of one effective radius, the residual method estimates a residual light fraction that ranges between $1.7 - 6.8\%$. There-

Table 3.6: Quantities from the Fourier component analysis of the residual images of the Virgo dwarf ETG sample.

Dwarf Galaxy	Bar Length			Bar Phase	Bar Strength	Mode 2 Strength	Pitch Angle
	Start (arcsec)	End (arcsec)	Length (arcsec)	(deg)			(deg)
(1)	(2)	(3)	(4)	(5)	(6)	(7)	(8)
VCC0216	—	—	—	—	—	0.046	$23.1^{+5.8}_{-4.0}$
VCC0308	—	—	—	—	—	0.020	$11.2^{+9.0}_{-2.3}$
VCC0490	7.10 ± 0.71	12.78 ± 0.71	5.68 ± 0.71	68.4	0.036 (0.032)	0.030	$17.5^{+21.2}_{-7.8}$
VCC0523	2.13 ± 0.71	8.52 ± 0.71	6.39 ± 0.71	19.9	0.083 (0.067)	0.045	$25.4^{+15.8}_{-9.2}$
VCC0856	—	—	—	—	—	0.022	$12.8^{+5.2}_{-5.2}$
VCC0940	7.81 ± 0.71	22.72 ± 0.71	14.91 ± 0.71	20.1	0.035 (0.028)	0.026	$13.0^{+0.5}_{-0.4}$
VCC1010	4.26 ± 0.71	15.62 ± 0.71	11.36 ± 0.71	158.4	0.052 (0.043)	0.043	$4.5^{+8.0}_{-0.9}$
VCC1695	2.13 ± 0.71	9.94 ± 0.71	7.81 ± 0.71	22.1	0.127 (0.109)	0.068	$15.6^{+3.2}_{-6.0}$
VCC1896	2.13 ± 0.71	17.75 ± 0.71	15.62 ± 0.71	22.8	0.103 (0.095)	0.083	$11.0^{+6.8}_{-1.2}$

Note. — Col. (1): name of the dwarf galaxy. Cols. (2) to (4): projected bar length quantities; the bar starting radius ($r_{\rm start}$), bar ending radius ($r_{\rm end}$), and overall bar length ($r_{\rm bar} = r_{\rm end} - r_{\rm start}$), respectively. Col. (5): bar phase ($\Phi_{\rm bar}$), measured counterclockwise from the $+y$-axis (north towards east of the images). Col. (6): bar strength ($S_{\rm bar}$), as defined in Equation 3.4. In parenthesis, an alternative bar strength measurement starting instead at $r_{\rm start} = 0$. Col. (7): strength of mode $m = 2$ (S_2), as defined in Equation 3.5. Col. (8): absolute value of the median projected spiral arm pitch angle ($|\psi|$), as defined in Equation 3.6.

Table 3.7: Bar and spiral light fractions of the Virgo dwarf ETG sample.

Dwarf Galaxy	Residual Light Fraction	
	Bar	Spiral
(1)	(2)	(3)
VCC0216	—	$0.029^{+0.004}_{-0.002}$
VCC0308	—	$0.024^{+0.002}_{-0.002}$
VCC0490	$0.028^{+0.005}_{-0.006}$ $(0.022^{+0.004}_{-0.004})$	$0.039^{+0.006}_{-0.003}$
VCC0523	$0.050^{+0.010}_{-0.012}$ $(0.050^{+0.010}_{-0.012})$	$0.039^{+0.003}_{-0.002}$
VCC0856	—	$0.022^{+0.004}_{-0.002}$
VCC0940	$0.032^{+0.003}_{-0.004}$ $(0.025^{+0.002}_{-0.003})$	$0.054^{+0.008}_{-0.006}$
VCC1010	$0.037^{+0.007}_{-0.008}$ $(0.032^{+0.006}_{-0.006})$	$0.026^{+0.003}_{-0.003}$
VCC1695	$0.081^{+0.011}_{-0.017}$ $(0.080^{+0.011}_{-0.017})$	$0.041^{+0.004}_{-0.003}$
VCC1896	$0.059^{+0.013}_{-0.014}$ $(0.059^{+0.013}_{-0.014})$	$0.076^{+0.009}_{-0.014}$

Note. — Col. (1): name of the dwarf galaxy. Col. (2): residual light fraction of the bar substructures, measured within the start ($r_{\rm start}$) and end ($r_{\rm end}$) radius of the bar. In parenthesis, an alternative measurement starting instead at $r_{\rm start} = 0$. Col. (3): residual light fraction of the spiral arm substructures, measured within the end of the bar ($r_{\rm end}$) out to two effective radii. If there is no bar detected, the measurement starts instead at $r = 0$.

fore, the Fourier and residual methods achieve similar results, even though their quantification techniques are fundamentally different. Together, they support a picture in which the underlying disk substructure light only constitutes a few percent of the much brighter and dominant diffuse light of these galaxies.

As a way to take further advantage of the identification of the bar and spiral arm substructure regions provided by the Fourier analysis, we proceed to compute the residual-to-total amount of light in each region separately. For this purpose, we make use of the multiple residual images obtained for each dwarf ETG of our sample (see Section 3.2.1), and derive the median residual light fraction and related uncertainties of their bar and spiral arms regions. On the one hand, for the bar region, we perform the measurement within the start ($r_{\rm start}$) and end ($r_{\rm end}$) radius of the bar. In addition, we also provide an alternative measurement starting at $r_{\rm start} = 0$. On the other hand, for the spiral arm region, the measurement is performed within the end of the bar ($r_{\rm end}$) out to two effective radii. For the galaxies that do not have a bar, no bar measurement is performed, and the spiral arm region measurement starts instead at $r = 0$.

The results of the residual light fractions of the bar and spiral arm regions of the dwarf ETG sample are summarized in Table 3.7. We find that these two types of disk substructures contribute a comparable fraction to the total galaxy light, with the bar light fraction ranging between $2.8-8.1\%$ ($2.2-8.0\%$ if measured from $r_{\rm start} = 0$), and the spiral light fraction ranging between $2.2 - 7.6\%$. The aforementioned bar light fractions (or residual bar strengths) are

roughly consistent with the Fourier bar strengths produced by the Fourier analysis (see column 6 of Table 3.6), as they present differences of a few percent at most. We also note that we do not find any conclusive correlation between the presence (or absence) of a bar and the relative brightness of the spiral arms of our galaxies.

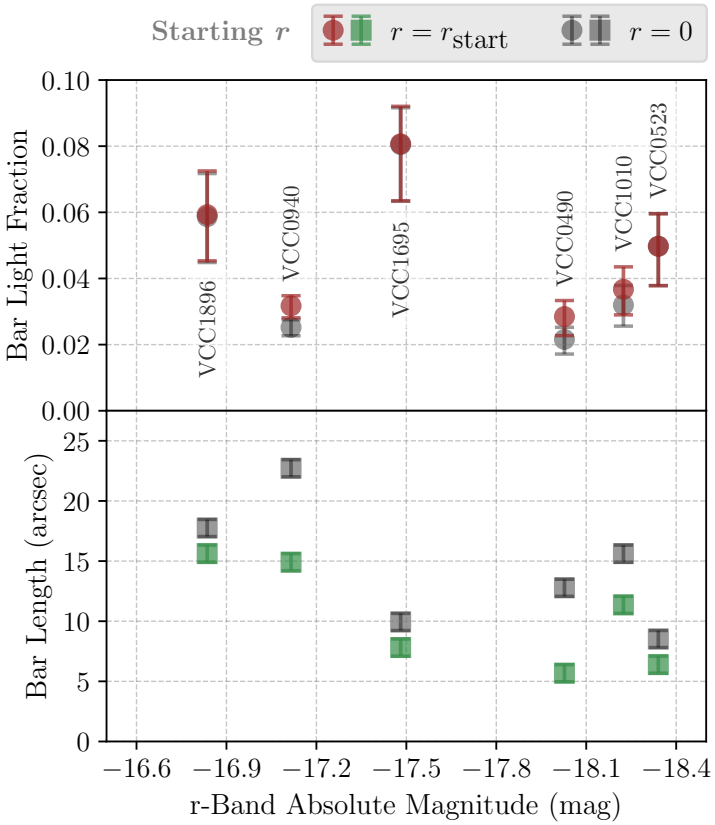

Figure 3.15: Bar residual light fractions (top panel, circles) and projected bar lengths (bottom panel, squares) of the Virgo dwarf ETG sample, as a function of the total r-band absolute magnitude of the galaxy. The measurements are performed within the bar's start ($r_{\rm start}$) and end ($r_{\rm end}$) radius and are shown as colored points. The alternative measurements starting instead at $r_{\rm start} = 0$ are shown as gray points. The error bars of the bar light fraction are given by the 16th and 84th percentiles of their distribution, while the error bars of the bar length are given by the resolution of the Fourier algorithm. Each set of data points is labeled with the name of the corresponding dwarf galaxy.

As the Fourier analysis has broadened our knowledge regarding the bar and spiral arm substructures separately, it is possible to search for correlations between the properties of these disk features and the properties of their host galaxies. Thus, in Figure 3.15, we present the bar properties, the bar residual light fraction and the projected bar length, as a function of the r-band absolute magnitude of the galaxies. Similarly, in Figure 3.16, we present the spiral arm properties, the spiral arm residual light fraction and the median projected spiral arm pitch angle. Overall, the dwarf ETG sample appears to be relatively homogeneous, in the sense that we find no definitive trends between the bar and spiral arm properties and the brightness of the galaxies. However, there could be a weak indication of the projected bar lengths getting smaller with increasing galaxy brightness. For the bar length measurements starting at $r_{\rm start}$ (green squares in Figure 3.15), we find a Pearson correlation coefficient $r = 0.76$ with a

p-value $= 0.08$. Nonetheless, to ascertain the existence of meaningful correlations in this low-luminosity, low-mass galaxy range, these results would greatly benefit from having a bigger sample of dwarf galaxies to analyze.

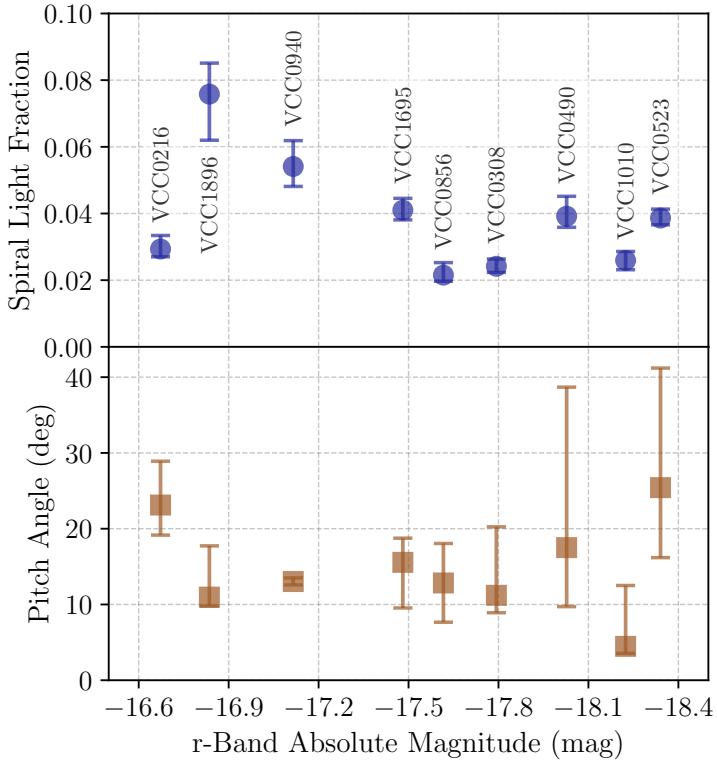

Figure 3.16: Spiral arm residual light fractions (top panel, circles) and absolute values of the median projected spiral arm pitch angles (bottom panel, squares) of the Virgo dwarf ETG sample, as a function of the total r-band absolute magnitude of the galaxy. The residual light measurements are performed within the bar's end radius ($r_{\rm end}$) out to two effective radii. If the galaxy has no identified bar substructure, the measurement starts instead at $r = 0$. The error bars are given by the 16th and 84th percentiles of the distributions. Each set of data points is labeled with the name of the corresponding dwarf galaxy.

In conclusion, the Fourier analysis has proven to be a very useful application of the residual method. By applying it directly to the residual images, it opened the possibility of carrying out a detailed quantitative analysis of the shape, extension, and light content of the bar and spiral arm substructures of the dwarf ETGs in our sample.

4

Substructures in Dwarf ETGs of the Fornax Cluster

This Chapter focuses on the analysis of a sample of dwarf ETGs with substructure features that belong to the Fornax galaxy cluster. This Chapter is organized as follows. We first introduce the data, which consists in an imaging survey and a dwarf galaxy catalog of the Fornax cluster in Section 4.1. Next, we process and prepare the imaging data, identify based on several criteria the dwarf ETGs that present substructure features, construct the sample, and characterize it by deriving the main properties of the galaxies in Section 4.2. The residual method is then applied to the sample, with its configuration parameters and the results obtained being described in Section 4.3. Finally, in order to showcase a potential application of the method, we perform color and stellar population analyses of the diffuse and substructure components of the dwarf ETG sample in Section 4.4.

4.1 Data Description

To begin with, we introduce the data that we will work with throughout this Chapter. In Section 4.1.1, we present the Fornax Deep Survey (FDS; Iodice et al. 2016), a deep, multi-band imaging survey of the Fornax cluster. Then, in Section 4.1.2, we present the Fornax Deep Survey Dwarf Catalog (FDSDC; Venhola et al. 2018), a catalog containing all of the dwarf galaxies falling on the FDS footprint.

4.1.1 FDS Images

The Fornax Deep Survey (FDS; Iodice et al. 2016) is a joint effort of the guaranteed-time observation surveys FOCUS (P.I. R. Peletier) and VEGAS (P.I. M. Capaccioli, Capaccioli et al. 2015), carried out with the Very Large Telescope (VLT) Survey Telescope (VST; Arnaboldi et al. 1998) located at the European Southern Observatory (ESO), Paranal. Using the OmegaCAM instrument (Kuijken et al. 2002; Kuijken 2011), the FDS targets the Fornax galaxy cluster centered on galaxy NGC 1399 out to the virial radius (0.7 Mpc; Drinkwater et al. 2001), and also the Fornax A infalling subgroup centered around galaxy NGC 1316. The FDS data consists in deep, multi-band imaging in the u, g, r, and i bands, although the Fornax A subgroup lacks u-band imaging. With OmegaCAM having a field-of-view of 1×1 deg^2, the FDS is constituted by a total of 32 fields of this size. In practice, we will only work with 25 fields, as these are the ones covered by the FDS dwarf galaxy catalog (see following Section 4.1.2). We provide a view of the FDS footprint and its constituting fields in Figure 4.1.

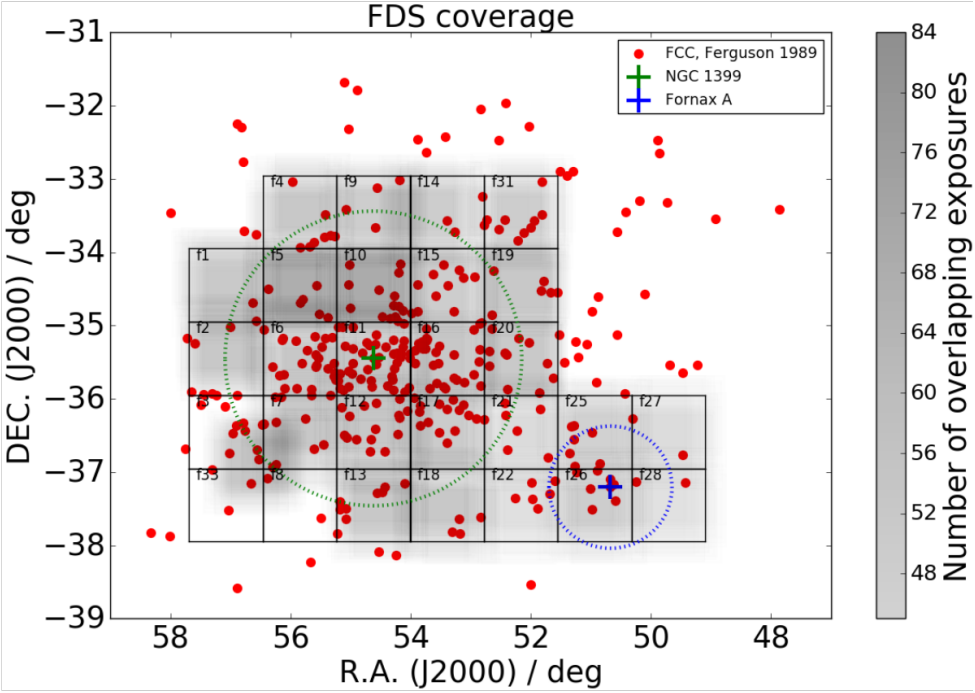

Figure 4.1: Footprint and fields of the FDS. Each field is outlined by a black square and labeled with its corresponding number. The gray-scale shading represents the number of exposures taken in the r band, with a darker shading corresponding to deeper observations. All of the galaxies that have been classified either as "definitive" or "likely" cluster members by the Fornax Cluster Catalog (FCC; Ferguson 1989b) are shown as red points. The location of the central galaxy of the Fornax cluster, NGC 1399, is shown as a green '+' sign. The virial radius of the cluster (0.7 Mpc; Drinkwater et al. 2001) is represented by a green dotted circle, and is equivalent to a radial extension of 2.0 deg assuming a Fornax cluster distance of 20.0 ± 1.4 Mpc (Blakeslee et al. 2009). The location of the central galaxy of the Fornax A subgroup, NGC 1316, is shown as a blue '+' sign. The 2σ galaxy overdensity around it is represented by a blue dotted circle. Image credit: this Figure corresponds to Figure 2 of Venhola et al. (2018).

As part of a collaboration with the FDS team, we have access to the final version of the FDS images. They have been reduced by performing the necessary instrumental corrections,

the masking of bad pixels, the background subtraction, the astrometric alignment and stacking, and the flux calibration. For a detailed description of the observation strategy and data reduction, refer to Venhola et al. (2018).

After assessing the available imaging data and associated metadata, we make the decision to discard the u and i-band imaging, and to work only with the g and r-band imaging. This can be understood as follows. On the one hand, the u-band imaging does not extend to the Fornax A subgroup, thus leaving out an interesting region of the cluster that is worth studying, as it is possible that there are differences in the main cluster and subgroup galaxy populations. Additionally, the median depth in the u-band is about one magnitude shallower compared to the depths reached by both the g and r bands. On the other hand, the i-band imaging does not provide the necessary information in order to properly model the PSF. In Section 4.2.2, we show how the FWHM is not enough information to build a good representation of the PSF, and instead a detailed characterization of the inner and outer regions of the PSF is needed if we want to model it accurately. The FDS data includes complete PSF models for each field in the g and r bands, but none for the u and i bands. In addition, the i-band imaging has a lackluster depth, which is comparable to the more shallow u-band imaging depth. For these aforementioned reasons, our analysis will solely focus on the g and r-band FDS data.

In Table 4.1, we provide the median depth and median PSF FWHM of the FDS fields in the g and r bands. After correcting for galactic extinction (addressed in detail in Section 4.2.6), the g-band depth lies in the range of $25.9 - 26.8$ mag arcsec^{-2}, with a median of $\mu_g = 26.6$ mag arcsec^{-2}, while the r-band depth lies in the range of $25.5 - 26.2$ mag arcsec^{-2}, with a median of $\mu_r = 26.0$ mag arcsec^{-2}. Therefore, the g-band imaging is on average about half a magnitude deeper. We note that these surface brightness depths correspond to a S/N of 1 at the scale of the FDS data, which corresponds to 0.2 arcsec pixel^{-1}. In regards to the FWHM of the PSF, the g band has a median FWHM$_g = 1.11$ arcsec, while the r band has slightly better seeing with a median FWHM$_r = 0.95$ arcsec.

4.1.2 FDS Dwarf Galaxy Catalog

The Fornax Deep Survey Dwarf Catalog (FDSDC; Venhola et al. 2018) contains a total of 564 dwarf galaxies spread throughout 26 FDS fields. Their membership to the cluster has been established based on the distribution and correlation of their properties (such as brightness, color, size, and concentration), which allows to distinguish them from background galaxies. The catalog considers all galaxies with an r-band absolute magnitude fainter than $M_r = -18.5$ mag to be dwarfs, and reaches a 50% completeness limit at $M_r = -10.5$ mag and at a limiting r-band surface brightness of $\mu_r = 26.0$ mag arcsec^{-2}. For more details on the construction and overall characteristics of the FDSDC, refer to Venhola et al. (2018).

The catalog provides a variety of relevant information for each dwarf galaxy. It includes their central coordinates in the ICRS, several structural and photometric parameters, and a morphological classification. To derive the galaxy parameters, the 2D fitting algorithm GALFIT (Peng et al. 2002) is used to model the light distribution of the galaxies with either a single Sérsic function (Sérsic 1968), or a combination of a Sérsic function and a PSF function if a nu-

Table 4.1: Data properties of the FDS fields.

FDS Field	Depth		PSF FWHM	
	g band (mag arcsec^{-2})	r band (mag arcsec^{-2})	g band (arcsec)	r band (arcsec)
(1)	(2)	(3)	(4)	(5)
1	26.76	26.05	1.35 ± 0.09	1.14 ± 0.15
2	26.60	26.03	1.11 ± 0.07	0.90 ± 0.07
4	26.70	26.01	1.39 ± 0.05	1.19 ± 0.12
5	26.79	26.10	1.15 ± 0.10	1.39 ± 0.14
6	26.72	25.98	0.84 ± 0.08	1.08 ± 0.08
7	26.81	26.06	0.83 ± 0.10	0.95 ± 0.09
9	26.83	26.15	1.20 ± 0.08	0.97 ± 0.09
10	26.77	26.16	1.15 ± 0.04	1.02 ± 0.12
11	26.51	26.02	1.06 ± 0.12	1.09 ± 0.11
12	26.74	26.09	0.83 ± 0.10	1.04 ± 0.10
13	26.83	26.14	0.91 ± 0.06	1.03 ± 0.06
14	26.70	26.00	1.18 ± 0.08	0.96 ± 0.09
15	26.60	26.14	1.13 ± 0.05	0.90 ± 0.07
16	26.68	26.09	1.26 ± 0.07	0.94 ± 0.08
17	26.54	26.21	1.11 ± 0.12	0.87 ± 0.08
18	26.79	26.17	0.95 ± 0.08	1.03 ± 0.09
19	26.70	26.14	1.14 ± 0.13	0.89 ± 0.07
20	26.46	26.06	1.22 ± 0.07	0.95 ± 0.09
21	26.51	25.84	1.12 ± 0.06	0.78 ± 0.05
22	26.52	25.90	1.04 ± 0.07	0.81 ± 0.05
25	26.63	25.84	1.11 ± 0.10	0.77 ± 0.06
26	25.89	25.96	0.93 ± 0.07	0.81 ± 0.05
27	26.39	25.63	1.07 ± 0.10	0.78 ± 0.06
28	26.31	25.57	1.08 ± 0.14	0.79 ± 0.09
31	26.58	25.86	1.22 ± 0.13	1.00 ± 0.08

Note. — Col. (1): FDS field number. Cols. (2) and (3): surface brightness depth in the g and r bands, respectively, at a S/N $= 1$ and a scale of 0.2 arcsec pixel^{-1}. These values are not corrected for galactic extinction. Cols. (4) and (5): Mean PSF FWHM its standard deviation in the g and r bands, respectively. Table credit: this Table is adapted from Table A.1 of Venhola et al. (2018).

cleus is present. The structural parameters are derived from a fit of the r-band galaxy image, and correspond to the position angle, axis ratio, Sérsic index, and effective radius. The photometric parameters are then derived by using the structural information provided by the r-band fit, and correspond to the apparent magnitude of the galaxy in the g and r bands, the apparent magnitude of its nucleus (if present) in the g and r bands, and the apparent magnitude within the effective radius in the u, g, r, and i bands. These photometric measurements are given in the SDSS u, g, r, and i filters calibrated to the AB magnitude system, and are not corrected for galactic extinction (see Section 4.2.6). Additionally, based on the appearance and overall color of the galaxies, they are classified into early-type and late-type morphological groups.

In practice, we will work with the FDSDC information of 560 dwarf galaxies located in 25 FDS fields. Our analysis excludes the four dwarf galaxies contained in field 33, as the inner and outer regions of the PSF were not modeled for this particular field. Nonetheless, a quick check reveals that no substructure features are embedded in these four galaxies, so no loss is incurred by excluding them.

4.2 Constructing the Data Sample

In order to construct the data sample, we first need to be able to identify which of the dwarf ETGs of the Fornax cluster have substructure features. For this purpose, we build g and r-band image cutouts of each dwarf galaxy in the FDSDC in Section 4.2.1. Then, we construct the PSF models of each FDS field, and match the PSFs of the g and r-band galaxy image cutouts in Section 4.2.2. Next, in order to increase the S/N and thus the depth of the images, we coadd the PSF-matched g and r-band galaxy cutouts in Section 4.2.3. Using different smoothing kernel sizes, we proceed to create several unsharp mask images of each $g+r$ galaxy cutout in Section 4.2.4. By jointly inspecting the $g+r$ galaxy images and their unsharp mask images, we select the galaxies that present an early-type morphology while also having underlying substructure features in Section 4.2.5.

Once we have clearly established our sample of dwarf ETGs with substructures, we prepare their g and r-band data for analysis, which includes masking any interloping sources and correcting for galactic extinction in Section 4.2.6. Finally, we characterize the sample by deriving the photometric and structural properties of the galaxies in Section 4.2.7.

4.2.1 Galaxy Cutouts

The first step is to construct cutouts of the g and r-band FDS images centered on each dwarf galaxy that has been catalogued by the FDSDC. For each galaxy, we extract the FDSDC information on their central coordinates (right ascension and declination) and their effective radius.

Using the `astropy` package (Astropy Collaboration et al. 2013, 2018) in Python, we are able to read the World Coordinate System (WCS) metadata associated to the FDS images, which are given in the image header. This way, by providing the central coordinates of the FDSDC galaxies in the ICRS, we can find their position on the FDS images. Additionally, this

package also allows the construction of image cutouts of arbitrary sizes centered on a given set of coordinates. We decide to make the size of each cutout a variable parameter that depends on the overall extension of the galaxy. If we consider the effective radius as a proxy for the galaxy size, the FDSDC galaxies then display a wide variety of sizes, so the most efficient approach is to make the cutout size variable. Consequently, for each of the 560 FDSDC galaxies, we construct cutouts of their g and r-band FDS images with dimensions $20\,\mathrm{R}_e \times 20\,\mathrm{R}_e$, where R_e is the effective radius. In other words, the cutouts cover a radial length out to $10\,\mathrm{R}_e$ from the galaxy center. These dimensions ensure that the galaxy is well contained within the cutout, and that part of the sky or background appears towards the exterior of the image.

4.2.2 PSF-Matching

To be able to perform reliable measurements in the g and r-band galaxy cutouts simultaneously, it is necessary to take into account the effect of the PSF. As the PSF of an image is dependent both on the imaging system (telescope and instrument) and the observing conditions, each particular FDS field and band has its own characteristic PSF. In order to describe the PSF, we consider two possible approaches.

► Option 1: Simple PSF model.

The first option is to use the FWHM of a point source, such as a star. The FWHM acts as a probe of the radial extension of a point source. Therefore, by measuring the FWHM of several unsaturated stars in a given FDS field and band, it is possible to derive a median FWHM that describes the image. If we assume the PSF is well represented by a Gaussian distribution, the FWHM can be transformed into a Gaussian standard deviation following the relation

$$\sigma = \frac{\mathrm{FWHM}}{2\sqrt{2\ln 2}}\,, \tag{4.1}$$

where σ is the standard deviation of the Gaussian function. In columns 4 and 5 of Table 4.1, we provide the PSF FWHM of each FDS field in the g and r bands.

► Option 2: Composite PSF model.

The second option is to use analytic functions to describe the inner and outer regions of the PSF separately. To do so, Venhola et al. (2018) constructs the inner PSF region by stacking the central regions of bright non-saturated stars, and the outer PSF region by stacking the outskirt regions of saturated stars. To represent the whole extension of the PSF, these inner and outer PSF regions are then combined into one before being modeled. As there is a limited number of saturated stars in the FDS data, the same outer PSF model is used for all FDS fields, while the inner PSF is modeled for each particular field and band.

Based on the approach of Venhola et al. (2018) (see their Section 5.1), the radial intensity profile of the PSF can be described by the following superposition:

$$I(r) = I_{\mathrm{inner}}(r) + I_{\mathrm{outer}}(r)\,, \tag{4.2}$$

where $I_{\rm inner}(r)$ is the inner PSF model and $I_{\rm outer}(r)$ is the outer PSF model. This composite PSF profile is normalized such that the peak of the PSF equals one.

On the one hand, the inner model describes the central 10 arcsec of the PSF, and is constituted by a Gaussian function and a Moffat function. The Gaussian function is used to model the peak of the PSF (< 2 arcsec), while the Moffat function is used to model the region beyond the peak ($2 - 10$ arcsec). Both functions are fit simultaneously, and take the form

$$\begin{aligned} I_{\rm inner}(r) &= I_{\rm Gau}(r) + I_{\rm Mof}(r)\,, \\ &= I_{\rm 0,Gau}\exp\left[-\left(\frac{r}{\sqrt{2}\sigma}\right)^2\right] + I_{\rm 0,Mof}\left[1+\left(\frac{r}{\alpha}\right)^2\right]^{-\beta}\,, \end{aligned} \tag{4.3}$$

where $I_{\rm Gau}(r)$ is the Gaussian function and $I_{\rm Mof}(r)$ is the Moffat function. The Gaussian function has a central intensity of $I_{\rm 0,Gau}$, and a standard deviation of σ. The Moffat function has a central intensity of $I_{\rm 0,Mof}$, while α and β are the slope and the extension of the profile, respectively. In Table 4.2, we provide the inner PSF parameters of each FDS field in the g and r bands. In some cases, a Gaussian function is not required in order to describe properly the innermost PSF region, so only a Moffat function is used.

On the other hand, the outer model describes the outskirts of the PSF, defined as the radial region beyond 40 arcsec. It is characterized by an exponential function, and takes the form

$$\begin{aligned} I_{\rm outer}(r) &= I_{\rm exp}(r) \\ &= I_{\rm 0,exp}\exp\left[-\frac{r}{h}\right]\,, \end{aligned} \tag{4.4}$$

where $I_{\rm 0,exp}$ is the central intensity, and h is the scale length. As mentioned before, the outer PSF parameters are the same for all the FDS fields. In the g band, $I_{\rm 0,exp,g} = 1.556 \times 10^{-6}$ and $h_g = 87.38$ arcsec. In the r band, $I_{\rm 0,exp,r} = 6.022 \times 10^{-6}$ and $h_r = 74.26$ arcsec. The central intensities are normalized such that the peak of the composite PSF profile (Equation 4.2) is equal to one; i.e., $I(r=0) = I_{\rm 0,Gau} + I_{\rm 0,Mof} + I_{\rm 0,exp} = 1$.

In Figure 4.2, we provide a detailed view of the composite PSF model, by showing the contribution of each constituting function. We observe that while the Moffat function does a good job in describing the overall radial profile of the PSF, it is necessary to include a Gaussian function to characterize properly the innermost PSF region (< 2 arcsec), and an exponential function to characterize properly the outermost PSF region (> 40 arcsec).

► Comparison: simple vs. composite PSF models.

We now assess the advantages and disadvantages of using a simple or composite approach when modeling the PSF. In Figure 4.3, we compare the radial intensity profile of the simple and composite PSF models for a particular FDS field in the g and r bands. Within the innermost region of 1 arcsec, the simple and composite PSF models have a comparable performance.

Table 4.2: Inner PSF parameters of the FDS fields.

FDS Field	$I_{0,\mathrm{Gau}}$		σ		$I_{0,\mathrm{Mof}}$		α		β	
	g band	r band	g band (arcsec)	r band (arcsec)	g band	r band	g band (arcsec)	r band (arcsec)	g band	r band
(1)	(2)	(3)	(4)	(5)	(6)	(7)	(8)	(9)	(10)	(11)
1	0.181	0.093	0.765	0.638	0.819	0.907	0.763	0.681	1.69	1.67
2	0.152	0.000	0.574	0.016	0.848	1.000	0.651	0.524	1.72	1.69
4	0.211	0.103	0.768	0.705	0.789	0.897	0.768	0.692	1.66	1.66
5	0.139	0.163	0.677	0.903	0.861	0.837	0.692	0.708	1.70	1.50
6	0.000	0.081	0.000	0.623	1.000	0.919	0.608	0.636	1.90	1.63
7	0.000	0.070	0.076	0.523	1.000	0.930	0.544	0.558	1.74	1.60
9	0.165	0.079	0.657	0.521	0.835	0.921	0.718	0.595	1.73	1.67
10	0.129	0.042	0.651	0.724	0.871	0.957	0.687	0.561	1.72	1.52
11	0.085	0.061	0.613	0.757	0.915	0.938	0.648	0.635	1.73	1.60
12	0.000	0.061	0.000	0.597	1.000	0.938	0.532	0.603	1.71	1.61
13	0.000	0.050	0.000	0.591	1.000	0.950	0.590	0.635	1.76	1.67
14	0.141	0.088	0.633	0.480	0.859	0.912	0.704	0.576	1.75	1.66
15	0.128	0.000	0.621	0.118	0.872	1.000	0.664	0.535	1.71	1.67
16	0.173	0.086	0.693	0.500	0.827	0.914	0.720	0.543	1.70	1.59
17	0.135	0.000	0.711	0.000	0.865	1.000	0.704	0.565	1.69	1.80
18	0.065	0.053	0.546	0.560	0.935	0.947	0.593	0.633	1.71	1.68
19	0.177	0.000	0.573	0.000	0.823	1.000	0.662	0.519	1.72	1.68
20	0.175	0.053	0.681	0.606	0.825	0.946	0.687	0.544	1.65	1.55
21	0.114	0.000	0.647	0.000	0.886	1.000	0.683	0.455	1.72	1.66
22	0.080	0.000	0.592	0.000	0.920	1.000	0.646	0.487	1.75	1.68
25	0.102	0.000	0.629	0.000	0.898	1.000	0.691	0.487	1.76	1.76
26	0.000	0.000	0.000	0.000	1.000	1.000	0.655	0.479	1.85	1.68
27	0.088	0.000	0.607	0.000	0.913	1.000	0.662	0.461	1.75	1.66
28	0.091	0.000	0.615	0.000	0.909	1.000	0.674	0.459	1.76	1.66
31	0.185	0.100	0.647	0.491	0.815	0.900	0.729	0.593	1.74	1.68

Note. — Col. (1): FDS field number. Cols. (2) and (3): central intensity $I_{0,\mathrm{Gau}}$ of the Gaussian profile in the g and r bands, respectively. Cols. (4) and (5): standard deviation σ of the Gaussian profile in the g and r bands, respectively. Cols. (6) and (7): central intensity $I_{0,\mathrm{Mof}}$ of the Moffat profile in the g and r bands, respectively. Cols. (8) and (9): extent α of the Moffat profile in the g and r bands, respectively. Cols. (10) and (11): slope β of the Moffat profile in the g and r bands, respectively. These parameters are used to construct the inner PSF profile as defined by Equation 4.3. Table credit: this Table is adapted from Table A.2 of Venhola et al. (2018).

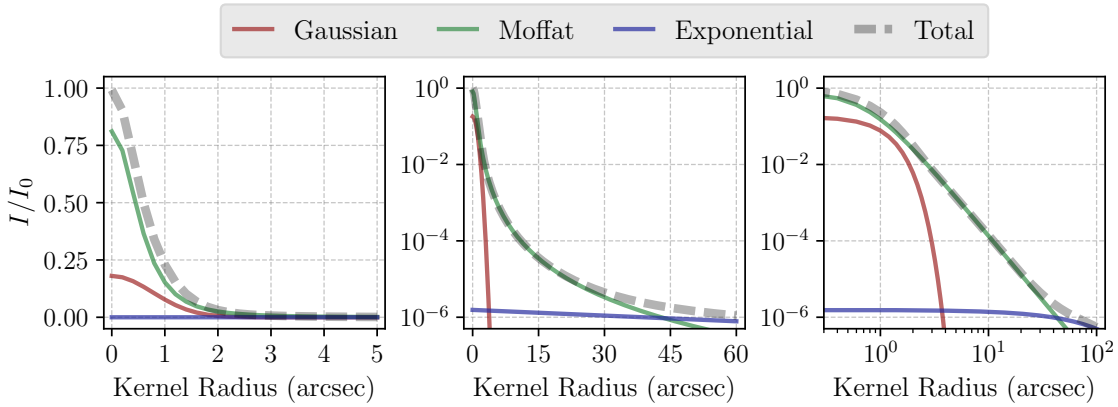

Figure 4.2: Decomposition of the radial intensity profile of the composite PSF model in the g band of FDS field 1. The composite PSF model (gray dashed line) is constituted by the superposition of Gaussian (red line), Moffat (green line), and exponential (blue line) functions. From left to right, the decomposition is shown in linear scale, logarithmic scale, and logarithmic-logarithmic scale. The composite model is normalized such that its central peak intensity equals 1. This Figure draws inspiration from Figure 7 of Venhola et al. (2018).

However, beyond a radial length of 2 arcsec, the difference between the two models becomes apparent. A single Gaussian function ceases to be a good representation of the PSF at large radii, as it is unable to describe the outer PSF region. We note this same behavior is observed in both the g and r bands.

A 2D view of this comparison is provided in Figure 4.4. Once again, it is evident that while the simple PSF model manages to characterize the core of the PSF, it completely fails to incorporate the wings of the PSF.

Both the simple and composite modeling of the PSF provide their own particular benefits. On the one hand, a simple PSF model is much easier to construct, as it only requires knowledge of the FWHM of a handful of point sources scattered throughout the image. This way, it is possible to compute a median FWHM, derive a median Gaussian standard deviation through Equation 4.1, and use it to construct a 2D Gaussian function to represent the PSF. As a matter of fact, an estimate of the PSF FWHM is provided for all the FDS fields in the four observed bands (u, g, r, and i bands).

On the other hand, despite being harder to construct, a composite PSF model provides a more complete characterization of the PSF, especially towards the outskirts of the profile. As in this work we are interested in analyzing substructure features that cover extended regions that are spread throughout the whole galaxy, it is of fundamental importance that the images in different bands have their PSFs properly matched at all radii. This way, all pixel-by-pixel measurements and comparisons between bands are guaranteed to be both valid and accurate. For this reason, we make the choice of working with the composite PSF models, and not with the simple PSF models. The only drawback is that the inner and outer regions of the PSF have only been characterized in the g and r bands of the FDS fields. As already mentioned in Section 4.1.1, this limits us to work exclusively with the g and r-band FDS imaging.

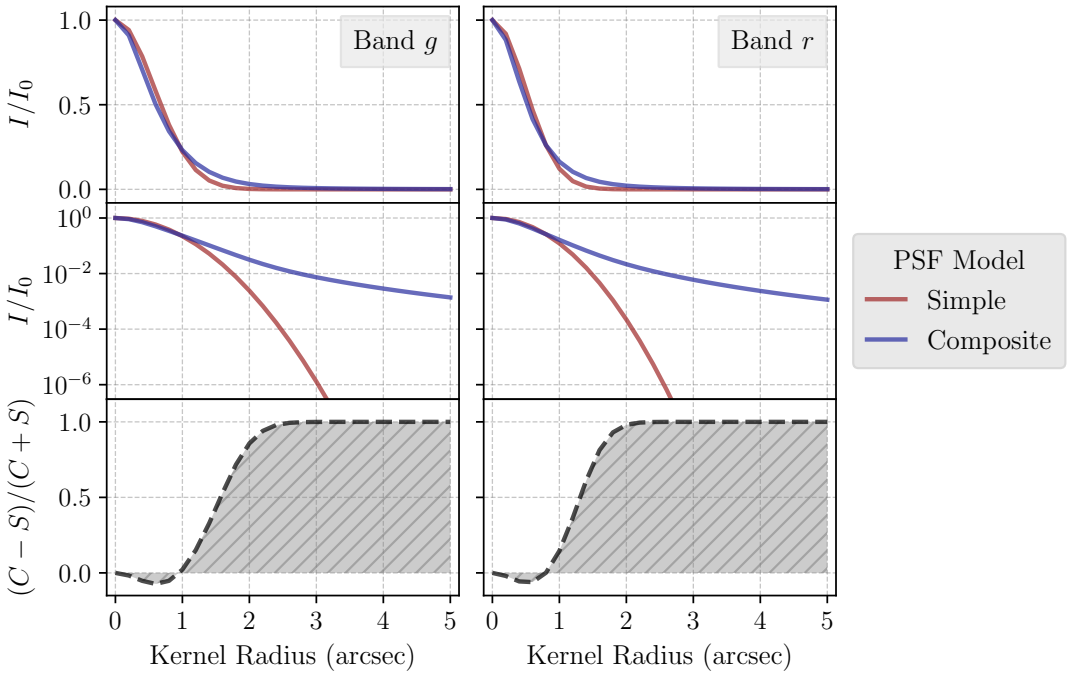

Figure 4.3: Comparison of the radial intensity profiles of the simple and composite PSF models in the g and r bands of FDS field 1. *Left panels:* simple (red line) and composite (blue line) PSF models in the g band. *Right panels:* simple and composite PSF models in the r band. The top row panels are in linear scale, while the central row panels are in logarithmic scale. The bottom row panels show the radial relative difference between the composite ('C') and simple ('S') PSFs. The models are normalized such that their central peak intensity equals 1. The PSF models are constructed with a total radial extension of 20 arcsec, but for illustration purposes only the innermost 5 arcsec are shown.

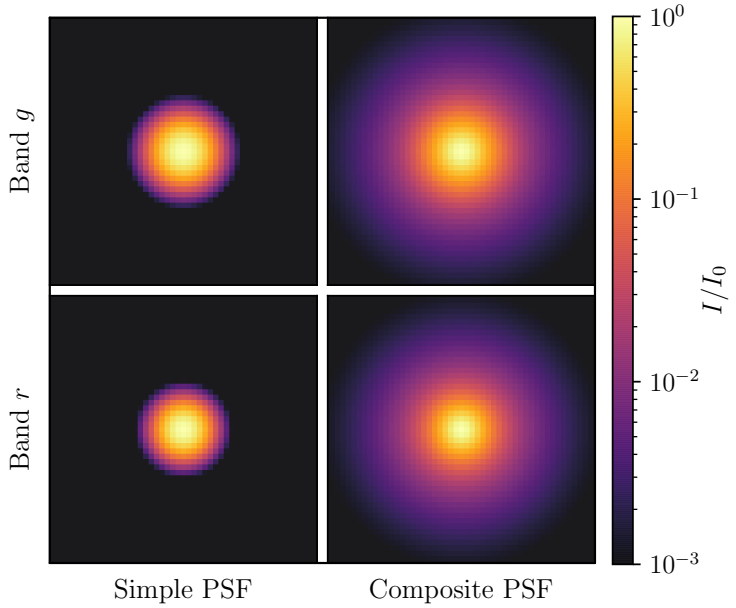

Figure 4.4: Simple and composite PSF model images in the g and r bands of FDS field 1. *Top row:* simple (left panel) and composite (right panel) PSF model images in the g band. *Bottom row:* simple and composite PSF model images in the r band. The models are normalized such that their central peak intensity equals 1, and are displayed in logarithmic scale. The PSF model images are constructed with total extension of 20×20 arcsec^2. For illustration purposes, the innermost region of the PSF encompassing 10×10 arcsec^2 in size is shown.

► **The convolution theorem.**

In Section 4.2.1, we described the process of creating FDS image cutouts in the g and r bands for all the FDSDC galaxies. The next step consists in understanding how to match the g and r-band PSFs of each galaxy image cutout. To understand how this is done, we first introduce the theory behind the convolution of images. The convolution theorem states that the convolution of two signals, S_1 and S_2, is equivalent to a point-wise multiplication in the Fourier domain. Conceptually, in Fourier space,

$$\mathcal{F}\{S_1 * S_2\} = \mathcal{F}\{S_1\} \cdot \mathcal{F}\{S_2\}\,, \tag{4.5}$$

where $*$ is the convolution operator, and $\mathcal{F}$ is the Fourier transform operator. A Fourier transform deconstructs a signal into an alternate representation constituted by sine and cosine functions. By applying the inverse Fourier transform $\mathcal{F}^{-1}$ on both sides of Equation 4.5, it follows that

$$S_1 * S_2 = \mathcal{F}^{-1}\{\mathcal{F}\{S_1\} \cdot \mathcal{F}\{S_2\}\}\,. \tag{4.6}$$

Thus, the convolution of two signals S_1 and S_2 is equivalent to taking the inverse Fourier transform of the point-wise multiplication of the Fourier transforms of S_1 and S_2.

We now consider the task at hand: how to match the PSF of one image to the PSF of another image. Broadly speaking, we need to convolve one of the images (the one with the narrower PSF, as we will see soon) with a kernel that matches the two PSFs. Following Equation 4.6, this can be written in Fourier space as

$$\begin{aligned} \text{PSF-matched image} &= \text{original image} * \text{matching kernel}\,, \\ &= \mathcal{F}^{-1}\left\{\mathcal{F}\{\text{original image}\} \cdot \mathcal{F}\{\text{matching kernel}\}\right\}\,. \end{aligned} \tag{4.7}$$

Therefore, to match the PSFs of two images, we need to construct a PSF-matching kernel. For this purpose, we first need to identify the image with the best (or narrow) PSF, and the image with the worst (or broad) PSF. By definition, the matching kernel worsens the narrow PSF to match the broad PSF. Once again using Equation 4.6, this can be written as

$$\begin{aligned} \text{broad PSF} &= \text{narrow PSF} * \text{matching kernel}\,, \\ &= \mathcal{F}^{-1}\left\{\mathcal{F}\{\text{narrow PSF}\} \cdot \mathcal{F}\{\text{matching kernel}\}\right\}\,. \end{aligned} \tag{4.8}$$

By rearranging the terms, we obtain the definition of the matching kernel:

$$\text{matching kernel} = \mathcal{F}^{-1}\left\{\frac{\mathcal{F}\{\text{broad PSF}\}}{\mathcal{F}\{\text{narrow PSF}\}}\right\}\,. \tag{4.9}$$

Finally, by replacing the definition of the matching kernel in Equation 4.7, we arrive at the following expression for the PSF-matched image:

$$\text{PSF-matched image} = \mathcal{F}^{-1}\left\{\mathcal{F}\{\text{original image}\} \cdot \frac{\mathcal{F}\{\text{broad PSF}\}}{\mathcal{F}\{\text{narrow PSF}\}}\right\} . \tag{4.10}$$

In other words, to match the PSFs of two images, the image with the narrow PSF needs to be convolved with the broad PSF, and then deconvolved with the narrow PSF. Essentially, this is like removing the own PSF of the image (the narrow PSF) and replacing it with the PSF of the other image (the broad PSF).

Following this approach, we do not need to convolve the g-band FDS image with the r-band PSF, and likewise the r-band FDS image with the g-band PSF. In this case, the PSFs of both images would become broader in order to match. Instead, we compute the matching kernel that matches the g and r-band PSFs, and then convolve the image that has the narrow PSF with the matching kernel, in order to worsen it to the broad PSF. This way, the image with the broad PSF remains untouched, so the resolution of the images is degraded only the minimum that is necessary. As an example, in Figure 4.5 we provide a 1D and 2D view of g and r-band composite PSF models and their matching PSF kernel.

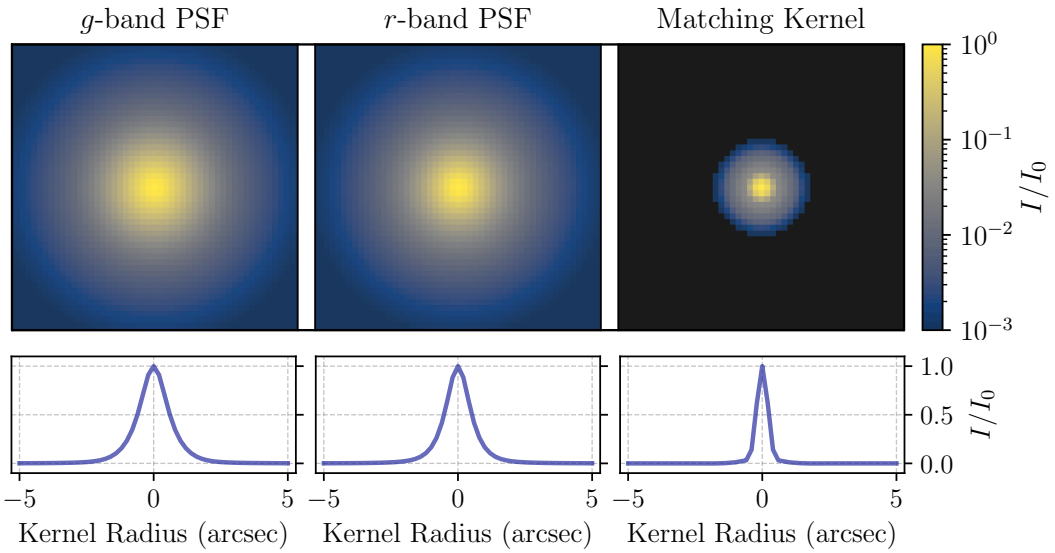

Figure 4.5: Matching kernel of the g- and r-band composite PSF models of FDS field 1. *Left panels:* composite PSF model image (top panel) and radial intensity profile (bottom panel) in the g band. *Central panels:* composite PSF model image and radial intensity profile in the r band. *Right panels:* matching kernel image and radial intensity profile that matches the PSF in the r band (narrower FWHM) to the PSF in the g band (broader FWHM), as defined by Equation 4.9. The models are normalized such that their central peak intensity equals 1. The images are displayed in logarithmic scale, and the radial profiles in linear scale. Negative values present in the matching kernel image are displayed in black. These example PSF model images are constructed with total extension of 20×20 arcsec^2. For illustration purposes, the innermost region of the PSF encompassing 10×10 arcsec^2 in size is shown.

► **Matching the PSF of the galaxy cutouts.**

In order to match the g and r-band PSFs of each galaxy image cutout, we make use of the utilities provided by the `astropy` package and its affiliated package `photutils` (Bradley et al. 2021) in Python.

To begin with, we create a model of the composite PSF for each FDS field and band following Equation 4.2 and the parameters provided in Table 4.2. Then, for each FDSDC galaxy, we translate their g and r-band composite PSF models into kernel images, where the kernel size is a variable parameter that depends on the observable galaxy size. As the process of convolution redistributes the galaxy light across the image, it is important that the size of the convolution kernel matches the overall observable extension of the galaxy, so that no light becomes unnecessarily dispersed and lost beyond the galaxy's boundaries. To get an estimation of the observable galaxy size, we consider the characteristics of our Virgo dwarf ETGs (see Chapter 3). The surface brightness limit of the Virgo data allows to reach out to $4-5\,\mathrm{R}_e$ of the galaxies, where R_e is their effective radius. However, the surface brightness limit of the FDS data, which is comparatively shallower, is instead reached at $3\,\mathrm{R}_e$ on average. Therefore, under the assumption that the Virgo and Fornax dwarf ETGs with substructures are comparable populations, we decide to create g and r-band PSF kernel images of dimensions $6\,\mathrm{R}_e \times 6\,\mathrm{R}_e$ (i.e., of $3\,\mathrm{R}_e$ in radial length) for each of the FDSDC galaxies. As a consequence, all measurements and analyses performed on the following Sections only consider the radial region out to a maximum of $3\,\mathrm{R}_e$ of the galaxies.

The next step consists in identifying for each FDSDC galaxy the band with the best (or narrow) PSF and the band with the worst (or broad) PSF. For this purpose, we use the information on the g and r-band PSF FWHMs provided in Table 4.1 as a measure of their extent. Once we have identified the narrow and broad PSFs, we create the matching kernel from the PSF kernel images by following Equation 4.9.

Finally, we can match the PSFs of the two bands. In accordance to Equation 4.7, we convolve the galaxy image cutout of the band that has the best (or narrow) PSF with the matching PSF kernel we have constructed, thus degrading its PSF to match the band that has the worst (or broad) PSF. As a result, we obtain PSF-matched g and r-band image cutouts for each of the FDSDC galaxies.

4.2.3 Coaddition

The PSF-matched g and r-band galaxy cutouts we created will allow us to make reliable photometric measurements in both bands simultaneously. However, we are also interested in stacking both bands in order to create a single $g+r$ galaxy image. This provides the following benefits. First, stacking increases the S/N and thus the depth of the resulting image. As we aim to analyze substructure features that are intrinsically faint, the increase in depth will aid us in being able to detect and identify them. Second, stacking ensures that both bands are taken into account during the substructure detection process. At this stage, we still have no knowledge about the brightness and color of the substructure features. This means that we do

not know in which band they are brighter, or if there is a band in which they are barely visible. The impact of these unknowns is minimized when we combine the contribution of both bands into one image.

For the aforementioned reasons, we construct a $g+r$ image for each of the FDSDC galaxies by coadding their PSF-matched g and r-band image cutouts. We adopt a simple approach when stacking: the g and r bands are assigned the same weights, so their contribution to the total flux of the final coadded image is the same.

4.2.4 Unsharp Masking

Unsharp masking constitutes an efficient way to assess if faint substructure features are embedded in the bright diffuse body of a galaxy. The creation of an unsharp mask image requires first to smooth the galaxy image, and then to divide the original galaxy image by the smoothed-out version of itself. This way, the majority of the smooth light is removed, thus revealing any non-smooth features that would normally lie hidden to the naked eye.

Using utilities from the `astropy` package in Python, we create a series of unsharp mask images from the $g + r$ coadded image of the FDSDC galaxies. As the size of the smoothing kernel dictates the width of the substructures that are revealed, we adopt a range of smoothing kernel sizes. For each FDS field and band, we transform their PSF FWHM (provided in Table 4.1) into a Gaussian standard deviation σ_{PSF} through Equation 4.1. Then, we create five different Gaussian smoothing kernels, with standard deviations corresponding to $1, 3, 5, 7, 9 \times \sigma_{\text{PSF}}$ of the PSF, respectively. In regards to the shape and orientation of the kernels, we adopt the axis ratio and position angle given by the FDSDC, in order to match the overall geometry of the galaxy when smoothing. As a result, we obtain five unsharp mask images for each FDSDC galaxy, where each unsharp mask is tuned to reveal potential substructure features of a particular width and extent.

4.2.5 Sample Selection

With the aforementioned preparations ready, we can now construct our sample of Fornax dwarf ETGs with substructure features. For each of the 560 FDSDC galaxies, we visually inspect their $g + r$ coadded image and their associated unsharp mask images. To become part of the sample, a dwarf galaxy must comply with the following three criteria:

1. **Early-type morphology.** In the $g+r$ coadded image, the galaxy must have in appearance an early-type morphology, such as of a dwarf elliptical (dE) or dwarf spheroidal (dS0).
2. **Disk or clump substructure features.** In the unsharp mask images, the galaxy must show either disk or clump substructure features. Disk substructures encompass bars, spiral arms, rings, and dumbbells; while clump substructures encompass irregular light overdensities such as star forming regions, dust lanes, and off-center nuclei.
3. **Red color ($\mathbf{g - r \geq 0.5}$ mag).** The galaxy must have a red overall color, which we define as $g - r \geq 0.5$ mag. The total $g - r$ color of the galaxy is derived from their g and r band apparent magnitudes reported by the FDSDC.

Based on these selection criteria, we end up with a sample constituted by 23 dwarf ETGs with embedded disk or clump substructure features.

4.2.6 Sample Preparation

Before beginning to work with the dwarf ETG sample, there are certain preparations that need to be made. Just as we did for our Virgo sample (see Section 3.1.2), the foreground and background sources that lie in the projected vicinity of our objects need to be masked out. This way, subsequent measurements and analyses of the galaxy images will not be contaminated by the light of interloping sources. Using the SAOImage DS9 visualization tool for astronomical data, we individually inspect the $g + r$ coadded images of our sample, and manually identify the position and extent of any interloping sources. Then, with this information, a bad pixel mask (BPM) image is constructed for each galaxy image. In it, bad pixels that are to be rejected during later analyses are flagged with a number one, while good pixels are instead assigned the number zero.

The next preparation consists in constructing clean versions of the galaxy images, in which the bad pixels have been masked out. The main purpose of these clean galaxy images is to prevent any unnecessary light contamination when subjecting the image to smoothing, as bright interloping sources can form blurred halos that leak their light beyond the boundaries established by the BPM. To avoid this effect, we use the isophotal analysis and construction tools available in the external STSDAS package of the IRAF astronomical system. Using the IRAF `ellipse` task, we independently fit the PSF-matched g and r-band galaxy images with elliptical isophotes, while allowing their central coordinates, shape (ellipticity), and orientation (position angle) to change freely with galactocentric radius. As a consequence, the radial light distribution of the galaxy is described as accurately as possible. With the information provided by the fit, we then use the IRAF `bmodel` task to translate the g and r-band fit parameters into g and r-band galaxy model images. The final step is to take the PSF-matched g and r-band galaxy images, locate the positions of the bad pixels according to their BPM image, and replace each bad pixel with the corresponding value given by the g and r-band galaxy models, respectively. By masking the interloping sources, we obtain PSF-matched g and r-band galaxy images that have a much cleaner and regular appearance. Nonetheless, we note that the regions marked on the BPM images are still omitted during any kind of measurement or analysis.

We also need to be able to correct for galactic extinction, as both the FDS images and the photometric measurements provided by the FDSDC do not take dust reddening into account. Even though the Fornax cluster is located at a high galactic latitude (its central galaxy NGC 1399 is located -53.6 deg from the galactic plane), dust from our Galaxy is still expected to contaminate the observations to a certain degree. The amount of light absorption that occurs at a a certain wavelength λ can be quantified by the dust extinction coefficient A_λ, defined as:

$$A_\lambda = m_\lambda - m_{\lambda,0}\,, \tag{4.11}$$

where m_λ is the observed magnitude of the source, while $m_{\lambda,0}$ is its true, intrinsic magnitude. To correct for galactic extinction, we make use of the NASA/IPAC Extragalactic Database (NED) Extinction Calculator. This calculator uses the galactic extinction maps of Schlafly & Finkbeiner (2011) to compute the dust extinction coefficient in a given direction in the sky and in a given passband. By inputting the equatorial coordinates and observation epoch for each of the dwarf ETGs in our sample, we obtain the dust extinction coefficients associated to the g and r bands. In the g band, the extinction coefficient lies in the range of $0.015 - 0.079$ mag, with a median value of $A_g = 0.040$ mag. In the r band, the extinction coefficient lies in the range of $0.010 - 0.055$ mag, with a median value of $A_r = 0.028$ mag. As expected, the dust extinction is bigger in the g band compared to the r band, as the former covers shorter wavelengths (or higher frequencies) of the light spectrum, and thus is more prone to light absorption. In the Sections that follow, all photometric measurements are corrected for galactic extinction.

4.2.7 Sample Properties

Having carefully selected and prepared our sample of 23 dwarf ETGs, we now proceed to characterize the galaxies by deriving their basic photometric and structural properties. We will make use of some of the properties already provided by the FDSDC, namely the total apparent magnitude in the g and r bands, and the effective radius in the r band. In what follows, the photometric properties of the galaxies are given in both the g and r bands, while the structural properties always correspond to measurements in the r-band images.

Using the IRAF `ellipse` task, we first fit with elliptical isophotes the PSF-matched r-band galaxy images, while allowing the central coordinates, ellipticity, and position angle to change freely with galactocentric radius. Then, by setting the `inellip` parameter of the `ellipse` task, we impose the geometry of the r-band isophotes to sample the PSF-matched g-band galaxy images in no-fit photometry-only mode. This way, the galaxy geometry stays the same in both bands, making all photometric measurements in the g and r bands comparable on an isophote-by-isophote basis.

To begin with, we define the galaxy center, for which we adopt the central coordinates of the isophote that has a semi-major axis length equal to 1.5 times the PSF FWHM in the r band. This particular isophote is chosen in order to avoid any effects of the PSF in the determination of the center. The central coordinates of the sample, expressed as right ascension and declination, are provided in columns 2 and 3 of Table 4.3.

The photometric properties of the dwarf ETG sample are also provided in Table 4.3. From the g and r-band total apparent magnitudes given by the FDSDC, we derive the total $g - r$ color and g and r-band total absolute magnitudes of the galaxies. By construction (see Section 4.2.5), the galaxies in our sample were selected based on their overall red colors, and thus span the range $0.51 \leq g - r \leq 0.76$ mag, with a median of $g - r = 0.61$ mag. Being dwarf systems, they are also characteristically faint. Their absolute magnitudes in the g band lie in the range between $-14.3 \geq \mathrm{M}_g \geq -18.0$ mag, with a median of $\mathrm{M}_g = -16.8$ mag; while in the r band they cover the range between $-14.9 \geq \mathrm{M}_r \geq -18.7$ mag, with a median of

Table 4.3: Central coordinates and photometric properties of the Fornax dwarf ETG sample.

Dwarf Galaxy	Central Coordinates (J2000.0)		μ_0 (mag arcsec^{-2})		μ_e (mag arcsec^{-2})		m (mag)		M (mag)		$g-r$ (mag)
	R.A.	Decl.	g band	r band	g band	r band	g band	r band	g band	r band	
(1)	(2)	(3)	(4)	(5)	(6)	(7)	(8)	(9)	(10)	(11)	(12)
F01D145	$03^h46^m33.38^s$	$-34°41'10.32''$	22.81	22.27	24.52	23.90	17.23 ± 0.24	16.66 ± 0.21	-14.28 ± 0.28	-14.85 ± 0.25	0.57 ± 0.31
F02D000	$03^h50^m36.72^s$	$-35°54'33.84''$	19.40	18.81	22.23	21.53	14.17 ± 0.11	13.51 ± 0.09	-17.34 ± 0.19	-18.00 ± 0.18	0.66 ± 0.15
F04D000	$03^h42^m45.55^s$	$-33°55'12.36''$	20.69	20.09	22.49	21.83	14.49 ± 0.11	13.84 ± 0.09	-17.02 ± 0.19	-17.67 ± 0.18	0.65 ± 0.14
F04D001	$03^h41^m3.60^s$	$-33°46'44.76''$	19.27	18.58	21.66	20.99	13.48 ± 0.10	12.83 ± 0.09	-18.03 ± 0.18	-18.68 ± 0.17	0.65 ± 0.13
F04D002	$03^h43^m22.66^s$	$-33°56'19.68''$	20.76	20.16	22.46	21.77	15.22 ± 0.15	14.55 ± 0.12	-16.29 ± 0.21	-16.96 ± 0.19	0.67 ± 0.19
F04D053	$03^h41^m45.41^s$	$-33°47'29.40''$	22.41	21.95	24.24	23.67	15.90 ± 0.16	15.35 ± 0.14	-15.61 ± 0.22	-16.16 ± 0.21	0.55 ± 0.21
F04D061	$03^h41^m21.19^s$	$-33°46'9.84''$	21.75	21.13	24.29	23.71	15.61 ± 0.17	15.03 ± 0.15	-15.90 ± 0.23	-16.48 ± 0.21	0.57 ± 0.22
F05D000	$03^h41^m32.54^s$	$-34°53'19.68''$	19.88	19.48	21.99	21.41	13.74 ± 0.11	13.20 ± 0.09	-17.77 ± 0.18	-18.31 ± 0.18	0.54 ± 0.14
F07D000	$03^h45^m3.58^s$	$-35°58'21.72''$	18.33	17.56	20.79	20.08	13.76 ± 0.07	13.15 ± 0.06	-17.75 ± 0.17	-18.36 ± 0.16	0.62 ± 0.09
F09D255	$03^h36^m49.73^s$	$-33°27'39.24''$	21.03	20.49	23.44	22.81	16.34 ± 0.16	15.74 ± 0.14	-15.17 ± 0.22	-15.77 ± 0.21	0.60 ± 0.22
F09D492	$03^h39^m55.03^s$	$-33°03'11.88''$	20.87	20.43	23.26	22.69	16.81 ± 0.14	16.26 ± 0.12	-14.70 ± 0.21	-15.25 ± 0.19	0.54 ± 0.19
F10D189	$03^h38^m9.17^s$	$-34°31'7.68''$	21.05	20.69	23.52	22.84	15.20 ± 0.15	14.58 ± 0.13	-16.31 ± 0.21	-16.93 ± 0.20	0.62 ± 0.20
F11D279	$03^h36^m54.31^s$	$-35°22'28.92''$	19.38	18.54	22.41	21.64	14.35 ± 0.09	13.59 ± 0.08	-17.16 ± 0.18	-17.92 ± 0.17	0.76 ± 0.12
F14D144	$03^h33^m34.06^s$	$-33°34'17.04''$	20.23	19.77	23.33	22.62	14.76 ± 0.13	14.10 ± 0.11	-16.75 ± 0.20	-17.41 ± 0.18	0.66 ± 0.17
F15D384	$03^h34^m30.82^s$	$-34°17'50.64''$	20.69	19.96	23.26	22.63	15.26 ± 0.15	14.66 ± 0.13	-16.25 ± 0.21	-16.85 ± 0.20	0.61 ± 0.19
F15D417	$03^h32^m47.69^s$	$-34°14'19.32''$	19.43	18.69	22.20	21.55	14.70 ± 0.11	14.06 ± 0.09	-16.81 ± 0.18	-17.45 ± 0.18	0.64 ± 0.14
F17D227	$03^h31^m8.28^s$	$-36°17'24.36''$	18.73	18.43	21.91	21.35	14.51 ± 0.09	13.97 ± 0.08	-17.00 ± 0.17	-17.54 ± 0.17	0.54 ± 0.12
F19D001	$03^h27^m18.02^s$	$-34°31'35.40''$	19.18	18.44	21.28	20.49	13.77 ± 0.10	13.02 ± 0.08	-17.74 ± 0.18	-18.49 ± 0.17	0.75 ± 0.13
F22D244	$03^h26^m25.03^s$	$-37°07'40.08''$	19.38	19.15	22.48	21.94	15.66 ± 0.12	15.15 ± 0.11	-15.85 ± 0.19	-16.36 ± 0.18	0.51 ± 0.16
F26D000	$03^h23^m54.41^s$	$-37°30'36.00''$	20.94	20.49	22.13	21.57	13.72 ± 0.11	13.16 ± 0.10	-17.79 ± 0.19	-18.35 ± 0.18	0.56 ± 0.15
F26D003	$03^h24^m58.37^s$	$-37°00'34.56''$	19.58	19.03	21.83	21.16	14.03 ± 0.12	13.39 ± 0.10	-17.48 ± 0.19	-18.12 ± 0.18	0.64 ± 0.15
F26D141	$03^h22^m22.70^s$	$-37°23'51.36''$	20.69	20.03	23.04	22.41	15.14 ± 0.15	14.53 ± 0.13	-16.37 ± 0.21	-16.98 ± 0.20	0.61 ± 0.20
F31D196	$03^h29^m43.25^s$	$-33°33'25.20''$	21.51	20.95	23.70	23.06	14.46 ± 0.16	13.86 ± 0.14	-17.05 ± 0.22	-17.65 ± 0.20	0.60 ± 0.21

Note. — Col. (1): name of the dwarf galaxy. Cols. (2) and (3): right ascension and declination of the central coordinates in the International Celestial Reference System (ICRS), according to the FDSDC (Venhola et al. 2018). Cols. (4) and (5): central surface brightness in the g and r bands, respectively. Cols. (6) and (7): effective surface brightness in the g and r bands, respectively. Cols. (8) and (9): total apparent magnitude in the g and r bands, respectively, according to the FDSDC. Cols. (10) and (11): total absolute magnitude in the g and r bands, respectively, assuming a Fornax cluster distance modulus of 31.51 ± 0.15 mag (Blakeslee et al. 2009). Col. (12): total $g-r$ color. All photometric measurements are in the AB magnitude system and have been corrected for galactic extinction.

Table 4.4: Structural properties of the Fornax dwarf ETG sample.

Dwarf Galaxy	Effective Radius	Ellipticity		Position Angle	
		At 1 R_e	At 2 R_e	At 1 R_e	At 2 R_e
	(arcsec)			(deg)	(deg)
(1)	(2)	(3)	(4)	(5)	(6)
F01D145	14.63 ± 2.76	0.705 ± 0.003	0.736 ± 0.003	91.9 ± 0.2	91.6 ± 0.2
F02D000	14.54 ± 1.23	0.413 ± 0.003	0.364 ± 0.003	49.7 ± 0.3	48.5 ± 0.3
F04D000	12.45 ± 1.05	0.114 ± 0.003	0.132 ± 0.003	160.1 ± 0.7	151.4 ± 0.7
F04D001	17.03 ± 1.31	0.571 ± 0.003	0.445 ± 0.003	172.2 ± 0.2	172.6 ± 0.2
F04D002	14.98 ± 1.67	0.706 ± 0.003	0.704 ± 0.002	4.5 ± 0.3	6.3 ± 0.1
F04D053	13.17 ± 1.68	0.135 ± 0.004	0.117 ± 0.008	137.3 ± 0.9	165.8 ± 2.0
F04D061	16.64 ± 2.23	0.190 ± 0.005	0.203 ± 0.013	139.3 ± 0.8	145.1 ± 1.7
F05D000	16.47 ± 1.38	0.492 ± 0.008	0.485 ± 0.002	7.0 ± 0.6	1.0 ± 0.2
F07D000	7.60 ± 0.41	0.414 ± 0.002	0.348 ± 0.002	156.8 ± 0.2	156.4 ± 0.1
F09D255	11.04 ± 1.41	0.612 ± 0.004	0.665 ± 0.003	124.7 ± 0.3	124.8 ± 0.2
F09D492	6.75 ± 0.75	0.317 ± 0.004	0.415 ± 0.005	71.4 ± 0.5	73.0 ± 0.4
F10D189	16.04 ± 1.88	0.445 ± 0.003	0.431 ± 0.004	140.3 ± 0.3	141.9 ± 0.3
F11D279	9.67 ± 0.66	0.058 ± 0.003	0.002 ± 0.003	0.9 ± 1.6	172.5 ± 8.5
F14D144	13.97 ± 1.34	0.131 ± 0.002	0.124 ± 0.003	47.8 ± 0.5	50.2 ± 0.8
F15D384	14.72 ± 1.68	0.476 ± 0.002	0.514 ± 0.003	152.4 ± 0.2	151.9 ± 0.2
F15D417	10.65 ± 0.87	0.466 ± 0.005	0.531 ± 0.001	120.0 ± 0.4	119.6 ± 0.1
F17D227	8.09 ± 0.55	0.213 ± 0.007	0.228 ± 0.004	134.8 ± 1.1	154.7 ± 0.5
F19D001	14.64 ± 1.09	0.592 ± 0.004	0.514 ± 0.001	29.1 ± 0.3	29.3 ± 0.1
F22D244	8.51 ± 0.82	0.381 ± 0.004	0.365 ± 0.004	82.9 ± 0.3	81.1 ± 0.4
F26D000	17.90 ± 1.56	0.197 ± 0.018	0.083 ± 0.003	32.2 ± 2.8	152.5 ± 1.3
F26D003	16.89 ± 1.51	0.625 ± 0.002	0.543 ± 0.001	82.6 ± 0.2	80.9 ± 0.1
F26D141	16.62 ± 1.97	0.579 ± 0.003	0.400 ± 0.004	56.0 ± 0.2	54.8 ± 0.4
F31D196	24.30 ± 2.98	0.433 ± 0.002	0.468 ± 0.003	58.0 ± 0.2	60.9 ± 0.2

Note. — Col. (1): name of the dwarf galaxy. Col. (2): Effective semi-major axis radius in the r band, according to the FDSDC (Venhola et al. 2018). Cols. (3) and (4): ellipticity in the r band at the one and two effective radii isophotes, respectively. Cols. (5) and (6): position angle in the r band at the one and two effective radii isophotes, respectively. The position angle is measured counterclockwise from the $+y$-axis (north towards east of the images).

$M_r = -17.5$ mag. Additionally, from the isophotal fits carried out with IRAF `ellipse`, we compute the g and r-band central and effective surface brightness, where knowledge of the length of the effective radius is given by the FDSDC. The central surface brightness of the sample has a median value of $\mu_{0,g} = 20.7$ mag arcsec^{-2} in the g band, and $\mu_{0,r} = 20.0$ mag arcsec^{-2} in the r band. Similarly, the effective surface brightness of the sample has a median value of $\mu_{e,g} = 22.5$ mag arcsec^{-2} in the g band, and $\mu_{e,r} = 21.8$ mag arcsec^{-2} in the r band. Therefore, both the absolute magnitude and surface brightness distributions of the sample indicate that the galaxies are brighter in the r band than in the g band.

The structural properties of the dwarf ETG sample are provided in Table 4.4. Using the r-band effective radius given by the FDSDC in conjunction with the r-band isophotal fit of the galaxies, we measure both the ellipticity and position angle of their one and two effective radii isophotes. As previously explained in Chapter 2, knowledge of these geometrical parameters is necessary during the application of the residual method. The sample features an ample variety of sizes and shapes. Their effective radii cover the range between $6.7 - 24.3$ arcsec, with a median of $R_e = 14.6$ arcsec. Their axis ratios at one effective radius lie in the range between $0.29 - 0.94$, with a median of $b/a = 0.57$. They show a similar distribution at two effective radii. Furthermore, various levels of geometrical complexity are observed throughout the sample. While for some galaxies the ellipticity and position angle stay approximately the same at one and two effective radii, there are also cases in which the galaxy geometry changes drastically with galactocentric radius. Consequently, the structural properties of the sample are quite heterogeneous, in contrast to its more homogeneous photometric properties.

In order to visualize the dwarf ETG sample, we present the PSF-matched r-band galaxy images and their unsharp mask images in Figure 4.6. In this Figure, we show the clean version of the images, in which the interloping sources have been masked out (see previous Section 4.2.6). In some unsharp masks, wavy patterns appear on extended masked regions, but we note that these are only artifacts and not real features. The unsharp mask images are created by following the approach described in Section 4.2.4. For the size of the Gaussian smoothing kernel, we adopt a Gaussian standard deviation of size $4 \times \sigma_{\rm PSF}$ along its semi-major axis, derived from the FWHM of the r-band PSF in accordance to Equation 4.1. For its geometry, we adopt the ellipticity and position angle of the two effective radii isophote of the galaxy, which are given in Table 4.4. We observe that the galaxy images have a predominantly smooth appearance, although in some cases it is already possible to discern some of their embedded substructure features. By removing the bright diffuse light of the galaxies, a rich variety of substructures are clearly revealed in their unsharp mask images. These include disk features, such as edge-on disks and rings; and clump features, such as irregular light overdensities and off-center nuclei.

We would like to highlight that, within the dwarf ETGs of the FDSDC, we do not find any cases that present well-defined spiral arm features. This strongly contrasts with our sample of Virgo dwarf ETGs, in which all of the galaxies have embedded spiral arms (compare Figures 3.2 and 4.6). However, as shown in Figure 4.7, subtle hints of very wide and faint spiral arms can be seen in the unsharp mask images of Fornax dwarf galaxies F04D053 and F26D000.

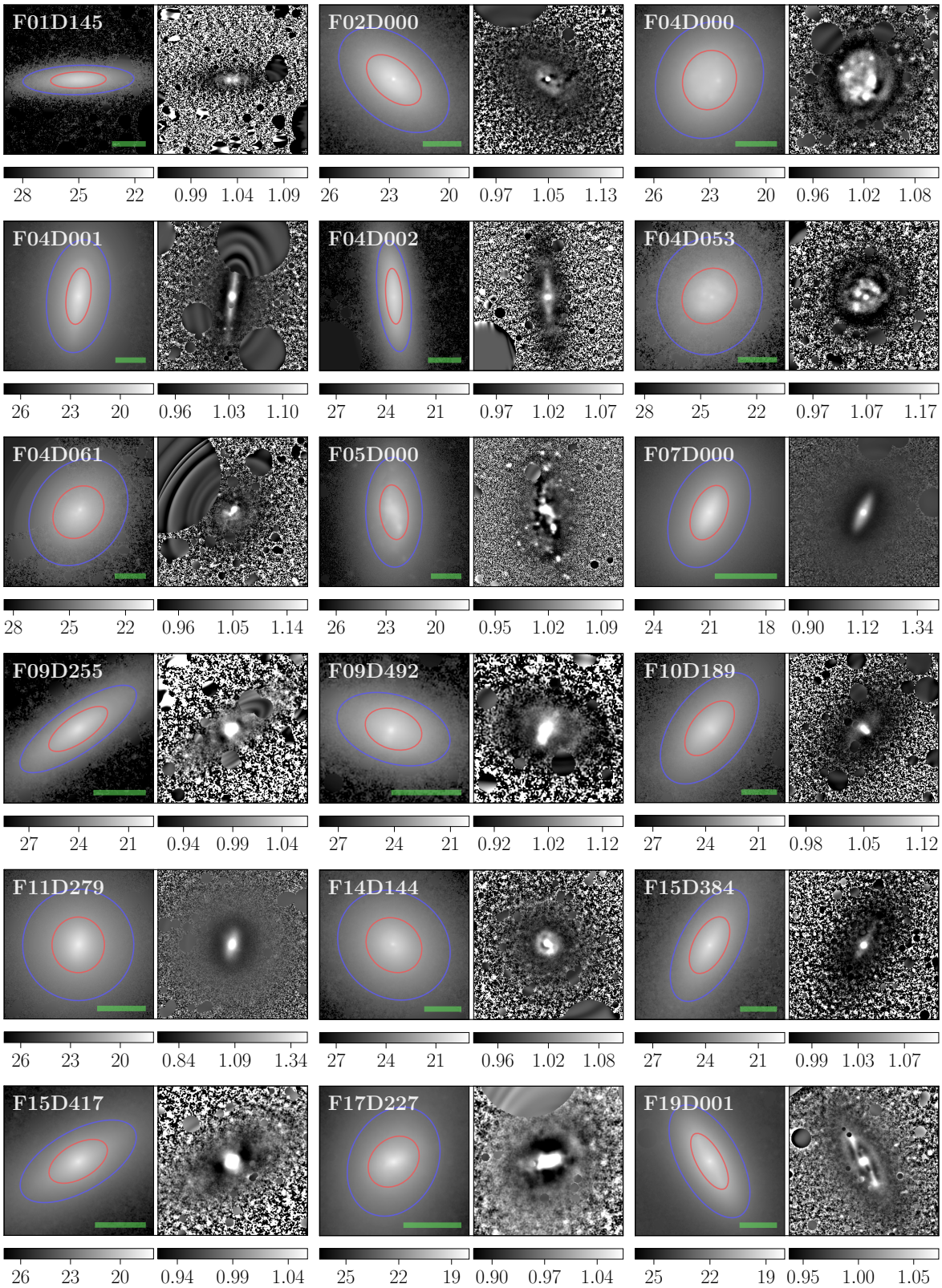

Figure 4.6: Original galaxy and unsharp mask images in the r band of the Fornax dwarf ETG sample. Each image is labeled with the name of the corresponding dwarf galaxy, with its unsharp mask image displayed to its right. The galaxy isophotes at one and two effective radii are overlaid on the original image as red and blue ellipses, respectively. Interloping sources have been masked out. The original images are in units of mag arcsec^{-2}, while the unsharp masks are unitless due to being image ratios. The image scale is shown as a green line, and corresponds to 15 arcsec. North is up, east is to the left.

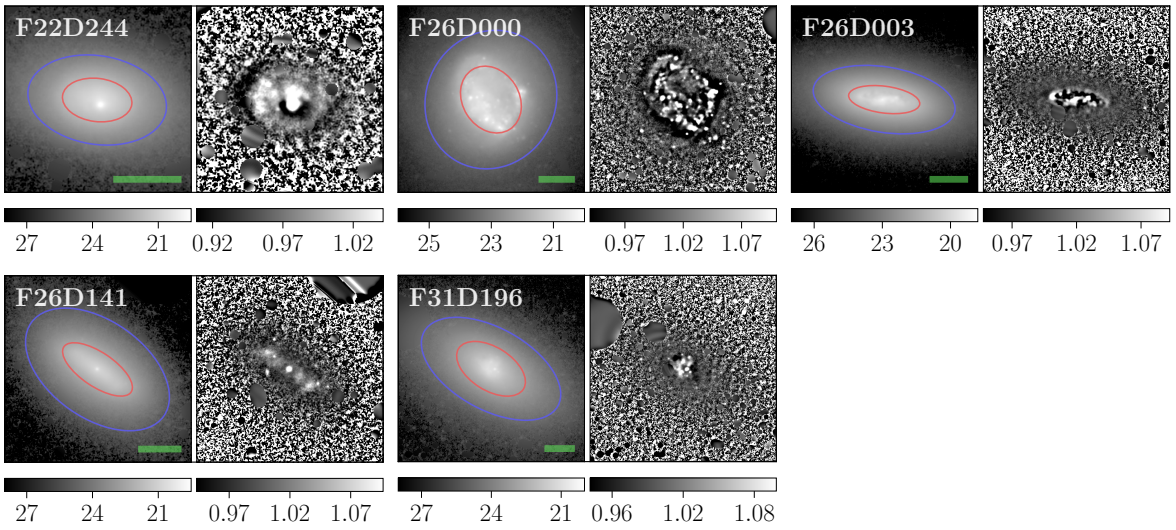

Figure 4.6: Original galaxy and unsharp mask images in the r band of the Fornax dwarf ETG sample *(cont.)*.

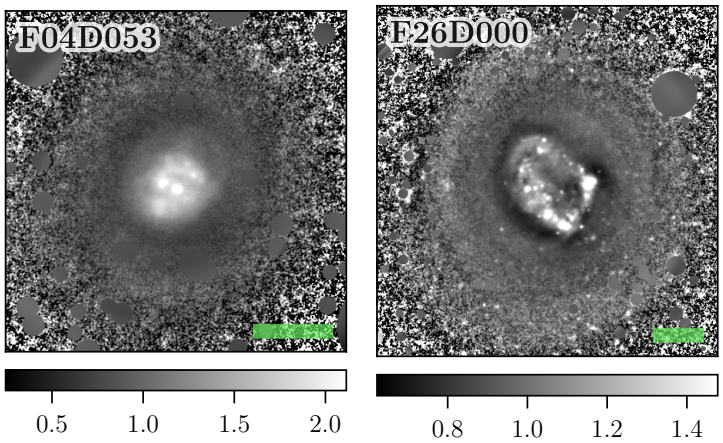

Figure 4.7: Unsharp mask images in the r band of the two galaxies from the Fornax dwarf ETG sample that show faint spiral arms. The creation of these unsharp mask images involve smoothing the original galaxy image with a very large kernel size, equal to 12 times the Gaussian standard deviation of the PSF. This causes the unsharp masks to reveal any wide, large-scale embedded substructures that are present. Each image has its own unitless gray-scale bar. The image scale is shown as a green line, and corresponds to 15 arcsec. North is up, east is to the left.

These unsharp masks were created by using a very large smoothing kernel in order to reveal any substructures of broad extension that could be present in the sample. Specifically, we used a Gaussian smoothing kernel of standard deviation $12 \times \sigma_{\rm PSF}$ of the PSF; i.e., three times the size used for the creation of the unsharp mask images of Figure 4.6. The width of these spiral features far exceed the average width of the substructure features observed throughout the sample. Consequently, as we will see in Section 4.3, they will not be captured by the residual method, as its configuration is tuned to capture substructure features of smaller average widths.

To further characterize the dwarf ETG sample, we construct radial parameter profiles of several quantities from the IRAF `ellipse` fits. These include: the g and r-band surface bright-

ness, the ellipticity, the position angle, and the $g-r$ color profiles. We note that, due to the PSF-matching process of the g and r bands described in Section 4.2.2, all radial measurements can be performed out to a maximum of three effective radii of the galaxies. As an example, we present the case of dwarf galaxy F02D000 in Figure 4.8, which shows the radial profiles of its surface brightness, ellipticity, and position angle, and also shows the isophotes overlaid on the PSF-matched r-band galaxy image. Corresponding Figures for the rest of the sample are provided in Appendix A.3. By comparing the g and r-band surface brightness profiles of the sample, it is evident that all the dwarf ETGs are brighter in the r band than in the g band, with their surface brightness profiles decreasing smoothly with galactocentric radius. Their ellipiticity and position angle profiles are instead more varied, displaying different levels of geometrical complexity on a case-by-case basis.

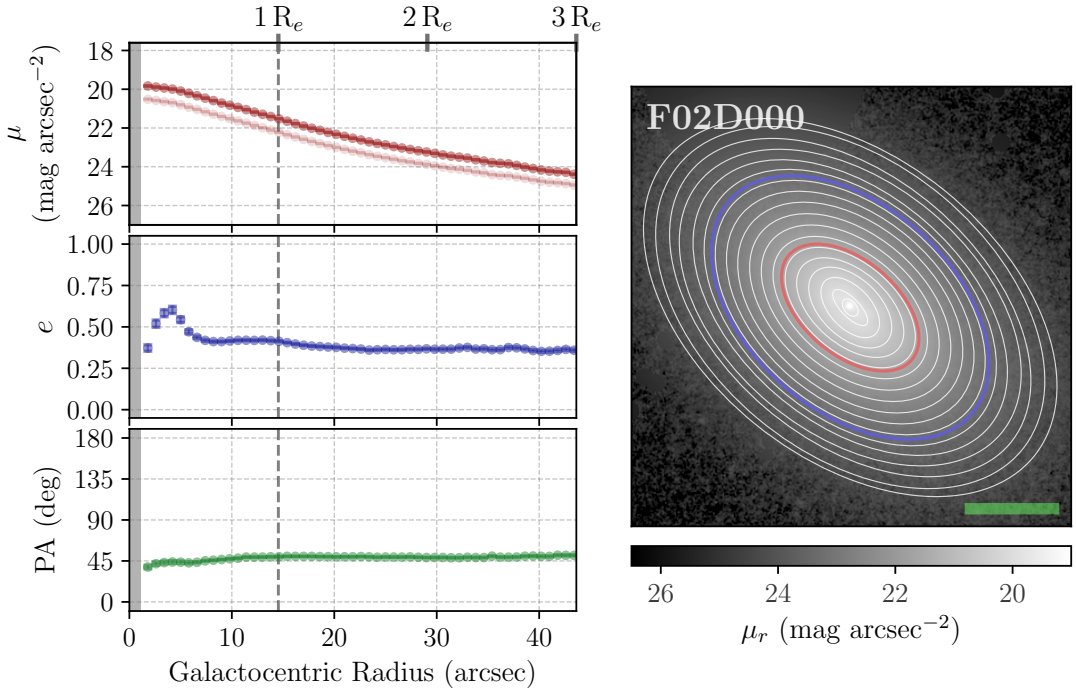

Figure 4.8: Radial parameter profiles and isophote overlays of Fornax dwarf galaxy F02D000. *Left panels:* from top to bottom, r-band radial profiles of the surface brightness, the ellipticity, and the position angle. On the top panel, the g-band surface brightness profile is also plotted in a fainter red color. The position angle is measured counterclockwise from the $+y$-axis (north towards east of the images). The gray-shaded area indicates the extension of the PSF FWHM. The vertical dashed line marks the position of the one effective radius. The radial profiles are shown out to three effective radii. *Right panel*: r-band galaxy image with isophote overlays. The isophotes at one and two effective radii are shown as red and blue ellipses, respectively. The last ellipse shown corresponds to the isophote at three effective radii. The image scale is shown as a green line, and corresponds to 15 arcsec. North is up, east is to the left. For Figures of the complete sample, see Appendix A.3.

The color profiles of the sample also display diverse behaviors. In Figure 4.9, we present the $g-r$ color profiles of three dwarf ETGs: F17D227, F15D384, and F04D001; with the rest of the sample being shown in Appendix A.4. While dwarf galaxy F17D227 has a blue core and red outskirts, F15D384 has a relatively flat color profile, and F04D001 has a red profile that becomes gradually bluer towards the outskirts. Such rich diversity can be appreciated in

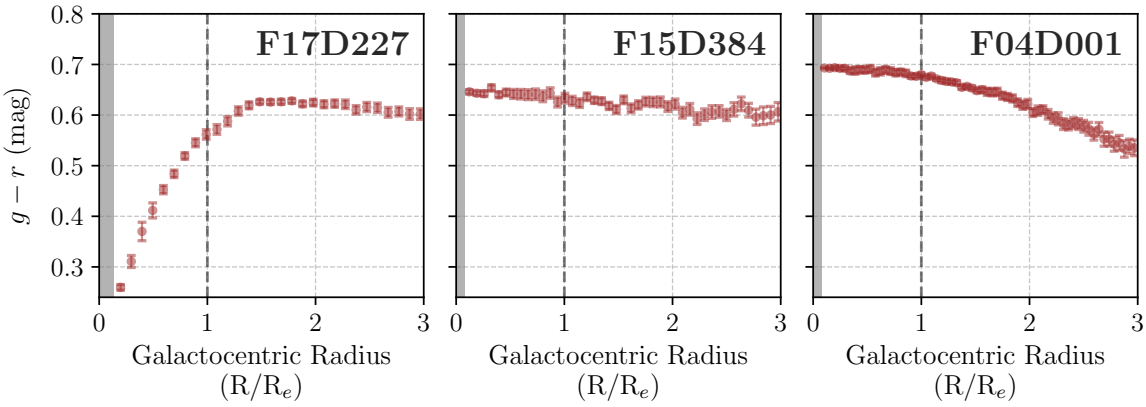

Figure 4.9: $g-r$ color profiles of three galaxies from the Fornax dwarf ETG sample. From left to right: F17D227, with a blue core and red outskirts; F15D384, with a relatively flat color profile; and F04D001, with slightly bluer outskirts. The gray-shaded area indicates the extension of the PSF FWHM. The vertical dashed line marks the position of the one effective radius. The color profiles are shown out to three effective radii. For Figures of the complete sample, see Appendix A.4.

Figure 4.10, in which we superpose the $g-r$ color profiles of the complete sample, color-coded based on the r-band absolute magnitude of the galaxies. The expected trend according to stellar evolution is observed: brighter ETGs are on average redder, as the age and metallicity increase with the stellar mass of the galaxy (Gallazzi et al. 2005). This assumes that the galaxy brightness is a proxy of the stellar mass content. As evidenced here by our sample, this trend clearly extends from the giant ETG regime to the dwarf ETG regime. Another expected trend is for the galaxies to be redder towards the outskirts, as star formation normally ceases from the outside towards the inside. However, while we observe this trend in some of our galaxies (e.g., the blue-cored ones), the great majority of the sample present other diverse color profiles. This may be a reflection of the different evolutionary histories of these galaxies, each having formed and evolved while being subjected to a unique arrangement of internal and external processes.

Finally, to understand the context of the dwarf ETGs that constitute our sample, we provide a view into their color-magnitude and projected spatial distributions compared to the other FDSDC galaxies in Figure 4.11. Our sample is represented by red and blue points, based on the classification of their substructures into the disky and clumpy categories, respectively; which we carry out in the upcoming Section 4.3.2. The dwarf ETG sample is consistent with being part of the red sequence defined by the dwarf galaxies of the Fornax cluster, with the disky subsample having in overall redder colors than the clumpy subsample. Additionally, the majority of the disky subsample lies inside the projected virial radius of the Fornax cluster, while the clumpy subsample tends to lie outside of it instead. Only galaxies belonging to the clumpy subsample are found in the projected vicinity of the Fornax A subgroup. When considered together, these differences could be an indication that dwarf ETGs with disk and clump substructures may constitute two different galaxy subpopulations. Or, alternatively, that the disk and clump subsamples are currently in different stages of their evolution. We will continue to address how the properties of the disk and clump subsamples differ from one

another in the upcoming Sections 4.3 and 4.4.

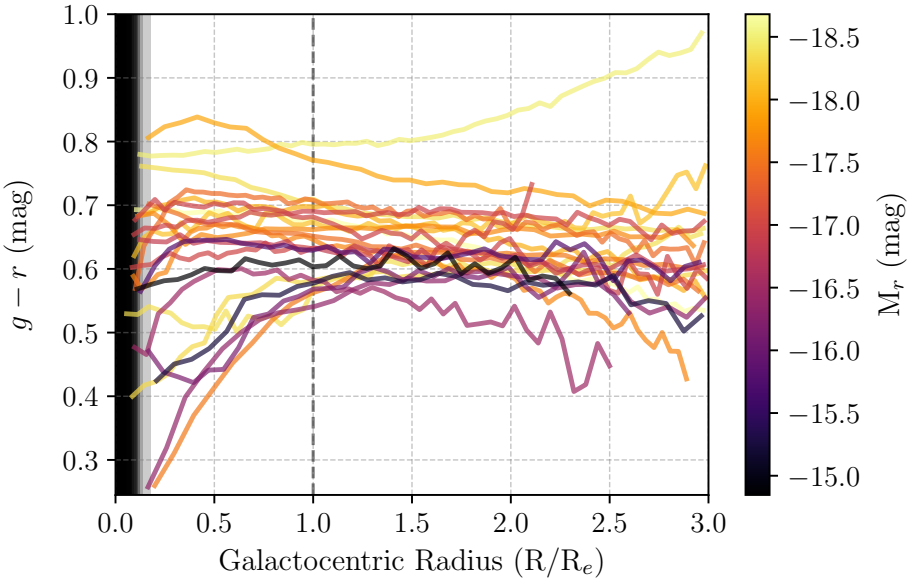

Figure 4.10: Superposition of the $g-r$ color profiles of the Fornax dwarf ETG sample. Each color profile is color coded based on the total r-band absolute magnitude of the galaxy, with lighter colors corresponding to brighter galaxies. The black-shaded area indicates the extension of the PSF FWHMs. The vertical dashed line marks the position of the one effective radius. The color profiles are shown out to a maximum of three effective radii. In cases where the background surface brightness level is reached before three effective radii, the profiles are instead shown out to the last valid galaxy isophote.

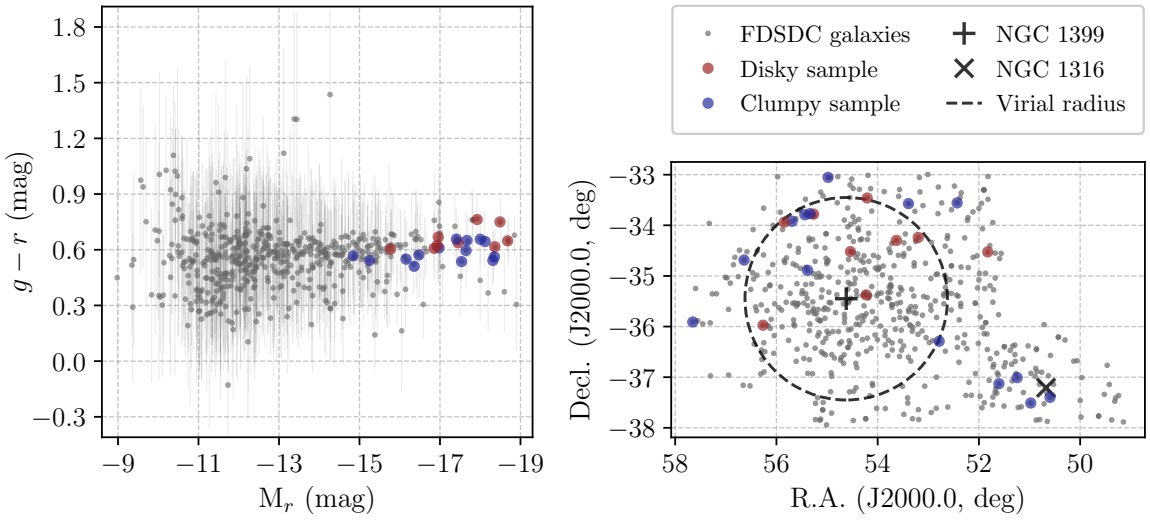

Figure 4.11: Color-magnitude diagram and projected spatial distribution of the FDSDC dwarf galaxies and of the Fornax dwarf ETG sample. *Left panel:* Total $g-r$ color vs. total r-band absolute magnitude of the galaxies. *Right panel:* Projected spatial distribution of the galaxies in the ICRS. On both panels, all the FDSDC galaxies are plotted as gray points, while the galaxies that belong to our sample are highlighted as red and blue points, depending on their classification into the disky or clumpy categories, respectively. On the right panel, the central galaxy of the Fornax cluster (NGC 1399) is marked with a '+' sign, while the central galaxy of the Fornax A subgroup (NGC 1316) is marked with a '×' sign. The dotted circle indicates the virial radius of the Fornax cluster ($R_{vir} = 0.7$ Mpc; Drinkwater et al. 2001) centered on NGC 1399, which is equivalent to a radius of 2.0 deg assuming a Fornax cluster distance of 20.0 ± 1.4 Mpc (Blakeslee et al. 2009).

4.3 Application of the Residual Method

We now proceed to apply the residual method, described in Chapter 2, to our sample of 23 dwarf ETGs of the Fornax cluster. First, in Section 4.3.1, we explain how we adapt the method to work in two different bands, and specify the configuration of the parameters. Then, in Section 4.3.2, we present the results obtained, such as the residual images and the residual light fractions of our sample.

4.3.1 Parameter Configuration

The application of the residual method closely follows the steps described in Section 2.2. However, there is a small change to consider: this time, we have imaging available in two bands (g and r bands) instead of only one. In order to incorporate the existence of two bands, we take the following approach. The residual method is first run as usual on the PSF-matched r-band images of the sample. This means that, for each galaxy, we obtain a series of r-band residual images, where each one corresponds to a particular configuration of the method's parameters. Next, to run the residual method on the g band, we make use of the geometry information of the galaxy obtained during the run in the r band. Specifically, for each parameter configuration set, we extract the radial shape and orientation of the diffuse component of the galaxy at the r-band stopping iteration. By using the `inellip` parameter of the IRAF `ellipse` task, this geometry is then imposed and kept fixed when running the method on the PSF-matched g-band images. The method is then allowed to iterate as usual, until a g-band stopping iteration is reached.

In summary, the residual method is first run freely on the r band, then the geometry of the r-band diffuse component is extracted, and finally the method is run with this constrained geometry on the g band. This way, the geometry of the diffuse component is kept fixed between the g and r bands, making any photometric measurements directly comparable. We note that a given parameter configuration set still has its own stopping iteration that is independent for each galaxy in each band. In the g band, the iterative aspect of the method requires between $1-3$ iterations, with a median of 2 iterations. In contrast, in the r band, it requires between $1-2$ iterations, with a median of 1 iteration.

In regards to the parameter configuration of the method, the same values are implemented in both the g and r-band runs. In Section 2.3, we specify the general parameters, as well as the specific parameters that must be tuned to the properties of the data set. These specific parameters correspond to the smoothing kernel size and the sampling step size, which are explained in detail in Sections 2.3.1 and 2.3.2.

On the one hand, the smoothing kernel size dictates the amount of smoothing the galaxy image is subjected to. It should be tuned to match the average half-width of the substructure features of the galaxies. By inspecting the unsharp mask images of our dwarf ETG sample (see Figure 4.6), we identify the substructure features and measure that their average half-widths lie in the range of $1.2-4.7$ arcsec, which expressed in terms of the PSF FWHM of the data transformed into a Gaussian standard deviation corresponds to $3-8\times\sigma_{\rm PSF}$. Consequently,

we adopt smoothing kernel sizes equal to $3, 4, 5, 6, 7, 8 \times \sigma_{\rm PSF}$.

On the other hand, the sampling step size dictates the frequency at which the radial light profile of the galaxy is sampled. It should be tuned based on the image resolution and provide the ability to sample the lower S/N regions at the galaxy outskirts. Taking into consideration that the resolution of the FDS data corresponds to 0.2 arcsec pixel^{-1}, we carry out some test runs, and determine that the optimal separation between successive isophotes is given by a growth rate of the step size length in the range of $18 - 23\%$. Therefore, we adopt sampling step sizes with a growth rate equal to $18, 19, 20, 21, 22, 23\%$.

As explained in Section 2.3.3, these parameter ranges create a 6×6 configuration grid. Consequently, the residual method is run a total of 36 times on the g and r-band images of a galaxy, with each run adopting a particular smoothing-sampling parameter pair. As a result, small variations will be present throughout the multiple residual images being obtained for a single galaxy. When quantifying the contribution of the residual light to the total galaxy light, these variations then translate into the uncertainty range of the median measurement.

4.3.2 Residual Method Results

By adopting the aforementioned parameter configuration, we proceed to apply the residual method to the Fornax dwarf ETG sample. This allows us to extract the light of the substructure features of the galaxies and isolate them in a galaxy residual image. In Figure 4.12, we show the r-band residual images of the sample. For illustration purposes, we do not show the g-band residual images, as the appearance of the substructure features is extremely similar (if not the same) in both bands. We observe that the rich variety of substructures that were originally revealed in the unsharp mask images (see Figure 4.6) have been faithfully captured in the residual images. Based on the appearance of the substructures in the residuals, and by using the unsharp masks as confirmation, we classify them into two categories: disk substructures, such as edge-on disks and rings; and clump substructures, such as irregular light overdensities and off-center nuclei. Out of the 23 dwarf ETGs in our sample, we classify 9 as disky, and 14 as clumpy. Therefore, about 40% $(2/5)$ of the sample is disky, and 60% $(3/5)$ is clumpy. and The substructure classification of each galaxy is provided in column 2 of Table 4.5.

We would like to note that some of our galaxies with embedded edge-on disks present artifacts in the central region of their residual images. These artifacts manifest as an hourglass-shaped light overdensity that is perpendicular to the major axis of the disk, and can be either very prominent (e.g., F04D002, F15D417) or quite small (e.g., F04D001, F07D000). This fake feature arises as a direct consequence of smoothing with a highly elliptical kernel something that is circular in shape, such as a prominent bulge or nucleus. In the residual method, the smoothing kernel adopts the shape and orientation of the galaxy isophote at two effective radii, as the objective is to match the overall geometry of the diffuse light, and not the geometry of the most central region. Consequently, this makes the presence of this artifact unavoidable in some cases. To address it, we carefully identify the affected regions in the residual images, and flag the pixels as bad in the corresponding BPM images. This way, all measurements and analyses we carry out consistently exclude these artificial features, whenever present.

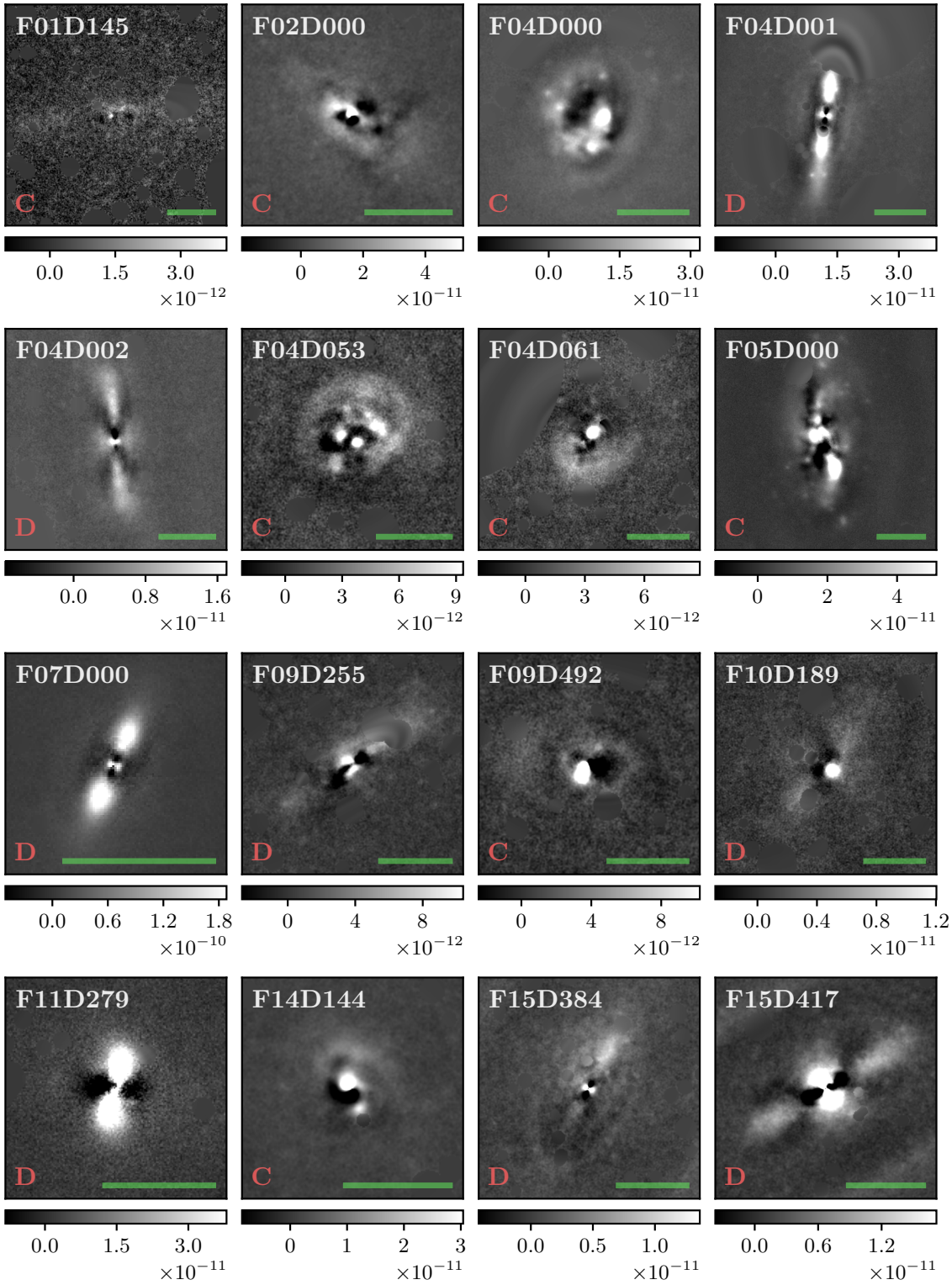

Figure 4.12: Galaxy residual images in the r band of the Fornax dwarf ETG sample. The parameter setup used to obtain these particular residual images corresponds to a smoothing kernel size equal to 5 times the Gaussian standard deviation of the PSF, and a sampling step size with a growth rate of 20% between successive isophotes. Each image is labeled with the name of the corresponding dwarf galaxy, and has its own gray-scale bar in units of erg cm^{-2} s^{-1} Hz^{-1}. The red letter indicates the classification of the galaxy as either disky ('D') or clumpy ('C'). The image scale is shown as a green line, and corresponds to 15 arcsec. North is up, east is to the left.

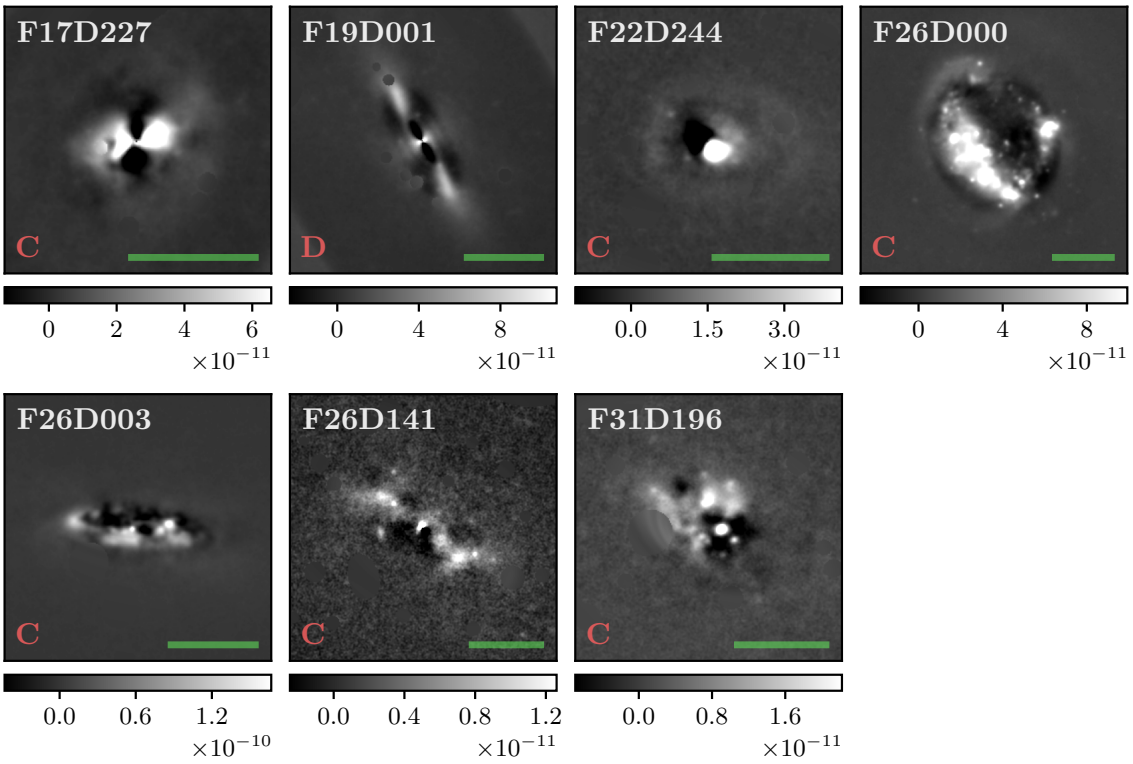

Figure 4.12: Galaxy residual images in the r band of the Fornax dwarf ETG sample *(cont.)*.

To quantify the contribution of the substructure features to the total galaxy light, we compute the residual light fraction (RLF; introduced in Section 2.4) within the one and two effective radii isophotes of the galaxies. The residual light fraction is always quantified in its respective band; that is, the g-band residual light fraction is derived from the g-band residual image and g-band galaxy image, and in the r band it is derived from the r-band residual image and r-band galaxy image. The results obtained are presented in Table 4.5. In the g band, we find that the residual light fraction ranges between $2.7 - 22.3\%$ within one effective radius, with a median value of 6.7%, and between $4.7 - 20.0\%$ within two effective radii, with a median value of 8.7%. Similarly, in the r band, it ranges between $2.9 - 20.8\%$ within one effective radius, with a median value of 4.6%, and between $4.5 - 16.9\%$ within two effective radii, with a median value of 5.3%. Overall, the residual light fraction tends to be larger at two effective radii than at one effective radius, and larger in the g band than in the r band.

To visualize these results, and to establish if there are any differences between the disky and clumpy subsamples, we plot the g-band versus the r-band residual light fractions in Figure 4.13. It is evident that there is a strong correlation between the measurements: if the substructures have a high relative brightness in g band (i.e., a large RLF), then they will also appear bright in the r band, and vice versa. To quantify this correlation, we compute the Pearson correlation coefficient r of the distributions and its associated p-value. This coefficient provides a measure of the linear correlation of a distribution, with $r = 0$ representing no correlation and $r = -1$ or 1 representing a strong negative or positive correlation, respectively. The p-value is an indication of the statistical significance of the correlation; the smaller the value, the more

Table 4.5: Substructure classifications and residual light fractions of the Fornax dwarf ETG sample.

Dwarf Galaxy	Classification	Residual Light Fraction			
		Within 1 R_e		Within 2 R_e	
		g band	r band	g band	r band
(1)	(2)	(3)	(4)	(5)	(6)
F01D145	Clumpy	$0.065^{+0.005}_{-0.006}$	$0.038^{+0.006}_{-0.005}$	$0.110^{+0.007}_{-0.008}$	$0.060^{+0.012}_{-0.006}$
F02D000	Clumpy	$0.067^{+0.006}_{-0.005}$	$0.039^{+0.005}_{-0.004}$	$0.085^{+0.008}_{-0.007}$	$0.046^{+0.006}_{-0.006}$
F04D000	Clumpy	$0.086^{+0.004}_{-0.019}$	$0.050^{+0.003}_{-0.003}$	$0.087^{+0.005}_{-0.016}$	$0.053^{+0.005}_{-0.005}$
F04D001	Disky	$0.051^{+0.009}_{-0.009}$	$0.050^{+0.009}_{-0.009}$	$0.050^{+0.006}_{-0.007}$	$0.051^{+0.006}_{-0.007}$
F04D002	Disky	$0.043^{+0.005}_{-0.006}$	$0.032^{+0.004}_{-0.006}$	$0.063^{+0.011}_{-0.006}$	$0.050^{+0.005}_{-0.006}$
F04D053	Clumpy	$0.101^{+0.007}_{-0.006}$	$0.077^{+0.006}_{-0.006}$	$0.129^{+0.013}_{-0.009}$	$0.095^{+0.009}_{-0.007}$
F04D061	Clumpy	$0.078^{+0.007}_{-0.007}$	$0.065^{+0.005}_{-0.006}$	$0.109^{+0.008}_{-0.008}$	$0.084^{+0.006}_{-0.007}$
F05D000	Clumpy	$0.107^{+0.009}_{-0.015}$	$0.087^{+0.005}_{-0.009}$	$0.103^{+0.009}_{-0.015}$	$0.092^{+0.008}_{-0.010}$
F07D000	Disky	$0.055^{+0.009}_{-0.009}$	$0.057^{+0.009}_{-0.010}$	$0.052^{+0.007}_{-0.006}$	$0.053^{+0.007}_{-0.007}$
F09D255	Disky	$0.050^{+0.010}_{-0.011}$	$0.033^{+0.008}_{-0.007}$	$0.091^{+0.010}_{-0.010}$	$0.063^{+0.010}_{-0.008}$
F09D492	Clumpy	$0.084^{+0.007}_{-0.005}$	$0.046^{+0.004}_{-0.004}$	$0.099^{+0.008}_{-0.006}$	$0.054^{+0.007}_{-0.004}$
F10D189	Disky	$0.062^{+0.004}_{-0.006}$	$0.037^{+0.005}_{-0.004}$	$0.079^{+0.012}_{-0.004}$	$0.045^{+0.011}_{-0.004}$
F11D279	Disky	$0.051^{+0.005}_{-0.006}$	$0.051^{+0.007}_{-0.006}$	$0.053^{+0.006}_{-0.006}$	$0.054^{+0.006}_{-0.006}$
F14D144	Clumpy	$0.051^{+0.007}_{-0.007}$	$0.037^{+0.004}_{-0.004}$	$0.067^{+0.010}_{-0.010}$	$0.045^{+0.006}_{-0.005}$
F15D384	Disky	$0.057^{+0.006}_{-0.005}$	$0.037^{+0.005}_{-0.003}$	$0.083^{+0.007}_{-0.007}$	$0.049^{+0.005}_{-0.004}$
F15D417	Disky	$0.027^{+0.010}_{-0.009}$	$0.029^{+0.011}_{-0.010}$	$0.055^{+0.009}_{-0.007}$	$0.052^{+0.008}_{-0.007}$
F17D227	Clumpy	$0.086^{+0.022}_{-0.018}$	$0.064^{+0.008}_{-0.008}$	$0.085^{+0.018}_{-0.015}$	$0.061^{+0.007}_{-0.007}$
F19D001	Disky	$0.032^{+0.004}_{-0.003}$	$0.034^{+0.004}_{-0.003}$	$0.047^{+0.007}_{-0.005}$	$0.048^{+0.006}_{-0.005}$
F22D244	Clumpy	$0.100^{+0.004}_{-0.023}$	$0.068^{+0.021}_{-0.003}$	$0.101^{+0.006}_{-0.021}$	$0.074^{+0.019}_{-0.004}$
F26D000	Clumpy	$0.223^{+0.009}_{-0.010}$	$0.208^{+0.005}_{-0.059}$	$0.201^{+0.005}_{-0.008}$	$0.169^{+0.008}_{-0.039}$
F26D003	Clumpy	$0.106^{+0.017}_{-0.013}$	$0.068^{+0.005}_{-0.004}$	$0.102^{+0.015}_{-0.011}$	$0.068^{+0.007}_{-0.006}$
F26D141	Clumpy	$0.070^{+0.006}_{-0.006}$	$0.040^{+0.006}_{-0.005}$	$0.123^{+0.010}_{-0.008}$	$0.053^{+0.008}_{-0.006}$
F31D196	Clumpy	$0.072^{+0.005}_{-0.005}$	$0.045^{+0.003}_{-0.004}$	$0.091^{+0.006}_{-0.006}$	$0.052^{+0.004}_{-0.006}$

Note. — Col. (1): name of the dwarf galaxy. Col. (2): classification of the substructure into the disky or clumpy categories. Cols. (3) and (4): residual light fraction measurements within the one effective radius isophote in the g and r bands, respectively. Cols. (5) and (6): residual light fraction measurements within the two effective radii isophote in the g and r bands, respectively.

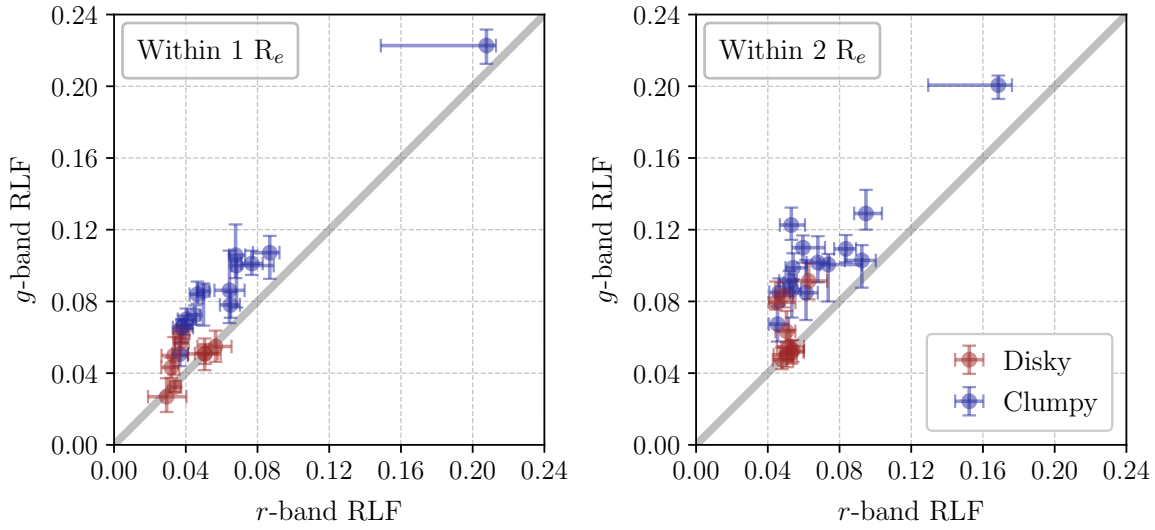

Figure 4.13: Residual light fractions in the g band vs. the r band of the Fornax dwarf ETG sample. *Left panel:* residual light fractions measured within one effective radius. *Right panel:* residual light fractions measured within two effective radii. Galaxies classified as disky are shown as red points, while galaxies classified as clumpy are shown as blue points. The error bars are given by the 16th and 84th percentiles of the distributions. The one-to-one relation is shown as a gray line.

significant. We find that the distribution within one effective radius (left plot) has a Pearson correlation coefficient of $r = 0.94$ and a p-value $= 1 \times 10^{-11}$. Similarly, the distribution within two effective radii (right plot) has an $r = 0.84$ and a p-value $= 5 \times 10^{-7}$. Thus, the g and r-band residual light fractions are strongly correlated within both the one and two effective radii of the galaxies. However, we also note that for a given r-band residual light fraction, the g-band residual light fraction tends to be comparatively larger (i.e., above the one-to-one relation). This difference is accentuated when dividing the dwarf ETGs into the disky and clumpy subsamples. Overall, the disky subsample presents smaller residual light fractions in both bands, and also smaller differences between its g and r-band measurements. In contrast, the clumpy subsample presents larger residual light fractions, with its g-band measurements being larger than the r-band measurements. This is a possible indication that the substructure features are comparatively bluer in the clumpy subsample than in the disky subsample.

In Figure 4.14, we plot the g and r-band residual light fractions versus the g and r-band total absolute magnitude of the galaxies, respectively. Two main things are noticeable. First, there appear to be no significant trends, which we corroborate by computing the Pearson correlation coefficient of the distributions and its associated p-value. However, if we exclude the outlier galaxy D26D000 (located on the upper right region of the plots, presenting a very large RLF), we find that there is one weak correlation: the g-band residual light fraction measured within two effective radii correlates with the total g-band absolute magnitude, with fainter galaxies having larger RLFs. This distribution has a Pearson correlation coefficient of $r = 0.55$ with a p-value $= 8 \times 10^{-3}$. The second noticeable thing is that the distributions have a larger scatter in the g band than in the r band. Overall, we recognize the same behavior we observed in Figure 4.13. That is, the clumpy subsample tends to have larger residual light

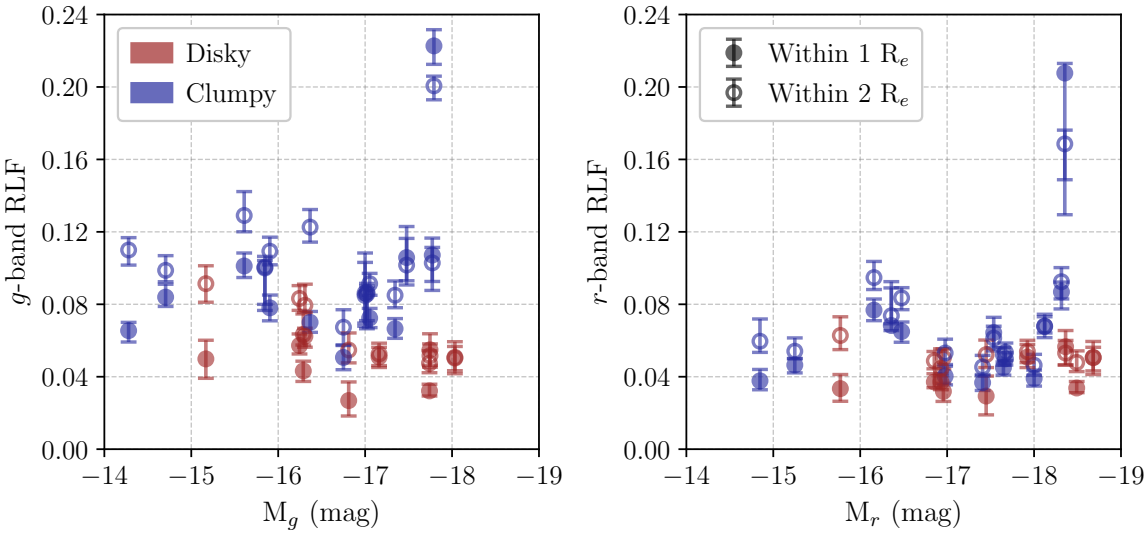

Figure 4.14: Residual light fractions of the Fornax dwarf ETG sample as a function of their total absolute magnitude. *Left panel:* g-band residual light fraction vs. total g-band absolute magnitude. *Right panel:* r-band residual light fraction vs. total r-band absolute magnitude. Galaxies classified as disky are shown as red points, while galaxies classified as clumpy are shown as blue points. The measurements are performed within one and two effective radii of the galaxies, shown as filled and empty circles, respectively. The error bars are given by the 16th and 84th percentiles of the distributions.

fractions than the disky subsample in both the g and r bands, albeit the difference is more substantial in the g band.

In Figure 4.15, we plot the g and r-band residual light fractions versus the total $g-r$ color of the galaxies. We can clearly appreciate how the residual light fraction in both bands increases with bluer galaxy colors, although the correlation is stronger in the g band than in the r band. In the g band, the distributions have a Pearson correlation coefficient of $r=-0.51$ ($r=-0.60$) and a p-value $=1\times10^{-2}$ (p-value $=2\times10^{-3}$) for the one and two effective radii measurements, respectively. The correlations are less significant in the r band, with a Pearson correlation coefficient of $r=-0.37$ ($r=-0.45$) and a p-value $=8\times10^{-2}$ (p-value $=3\times10^{-2}$) for the one and two effective radii measurements, respectively. The main result, however, is how the disky and clumpy subsamples become separated by the $g-r$ color of the galaxies. The disky subsample is comparatively redder ($g-r\geq0.6$ mag), being relegated to the right half of the plots; while the clumpy subsample is comparatively bluer ($g-r\leq0.65$ mag), and is thus relegated to the left half of the plots. In the upcoming Section 4.4, we provide a more in-depth view into these color differences, as we compute and analyze the $g-r$ colors of the diffuse and substructure components of the galaxies separately.

As a way to compare our sample of dwarf ETGs with substructures with the total dwarf ETG population of the Fornax cluster, in Figure 4.16 we plot the brightness distribution of the populations. For this purpose, we consider all of the dwarf galaxies that have been morphologically classified as early types by the FDSDC. There are six galaxies in our sample that were classified as late types by the FDSDC, so we re-classify them as early types to perform this comparison. While on the top panel we show the luminosity function of our complete

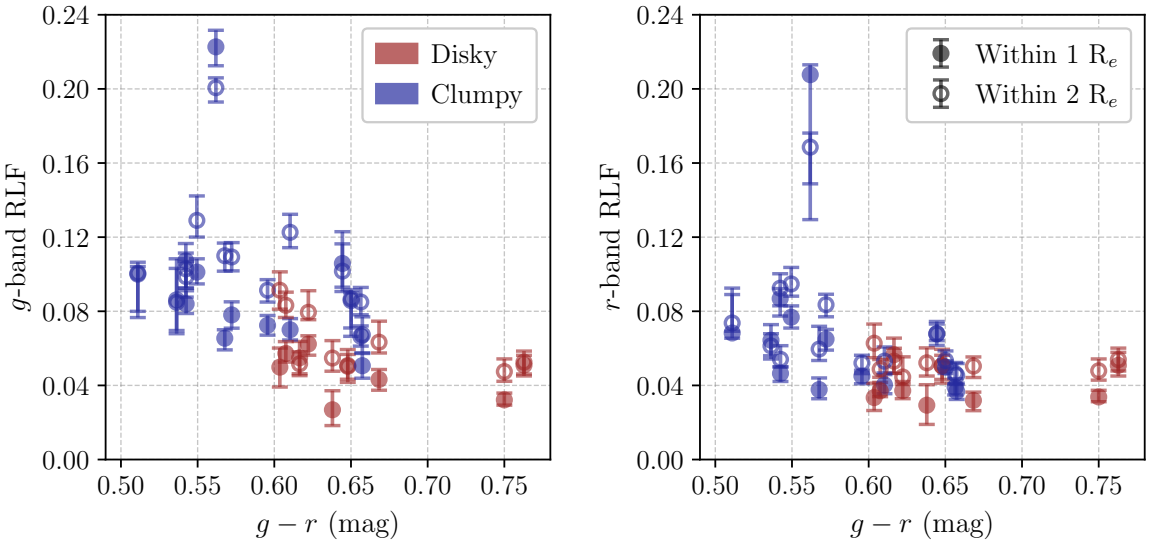

Figure 4.15: Residual light fractions of the Fornax dwarf ETG sample as a function of their total $g - r$ color. *Left panel:* g-band residual light fraction vs. total $g - r$ color. *Right panel:* r-band residual light fraction vs. total $g - r$ color. Galaxies classified as disky are shown as red points, while galaxies classified as clumpy are shown as blue points. The measurements are performed within one and two effective radii of the galaxies, shown as filled and empty circles, respectively. The error bars are given by the 16th and 84th percentiles of the distributions.

sample, on the bottom panel we show the luminosity function of the disky subsample. As the main result, we find that the brighter the dwarf ETG is, the higher the probability of it having embedded substructure features, be them either disky or clumpy. Thus, the dwarf ETG substructure fraction can be as high as 80% on the bright end ($M_r \approx -19$ mag), dropping to 5% on the faint end ($M_r \approx -15$ mag). If we only consider disk substructures, the dwarf ETG disk fraction can reach up to 40% on the bright end, dropping to 5% already by $M_r \approx -16$ mag. We provide a comparison with the dwarf ETG disk fraction of the Virgo cluster in the discussion Section 5.3. Overall, we highlight the fact that substructures, in either the form of disk features or clump features, are almost guaranteed to be present in a dwarf ETG if the galaxy is bright enough ($M_r \leq -18$ mag).

In conclusion, by applying the residual method to the PSF-matched g and r-band galaxy images of our dwarf ETG sample, we have been able to characterize their embedded substructure features both in a qualitative and a quantitative way. We have categorized the substructures into the disky and clumpy categories by inspecting the residual images, quantified their relative contribution to the total galaxy light in the g and r bands, and finally assessed the existence of possible correlations between the residual light fractions and some global galaxy properties.

4.4 Color Analysis of Model and Residual Images

As a means of showcasing the potential of the residual method, we subject the Fornax dwarf ETG sample to a series of color analyses, in which we consider their diffuse and substructure

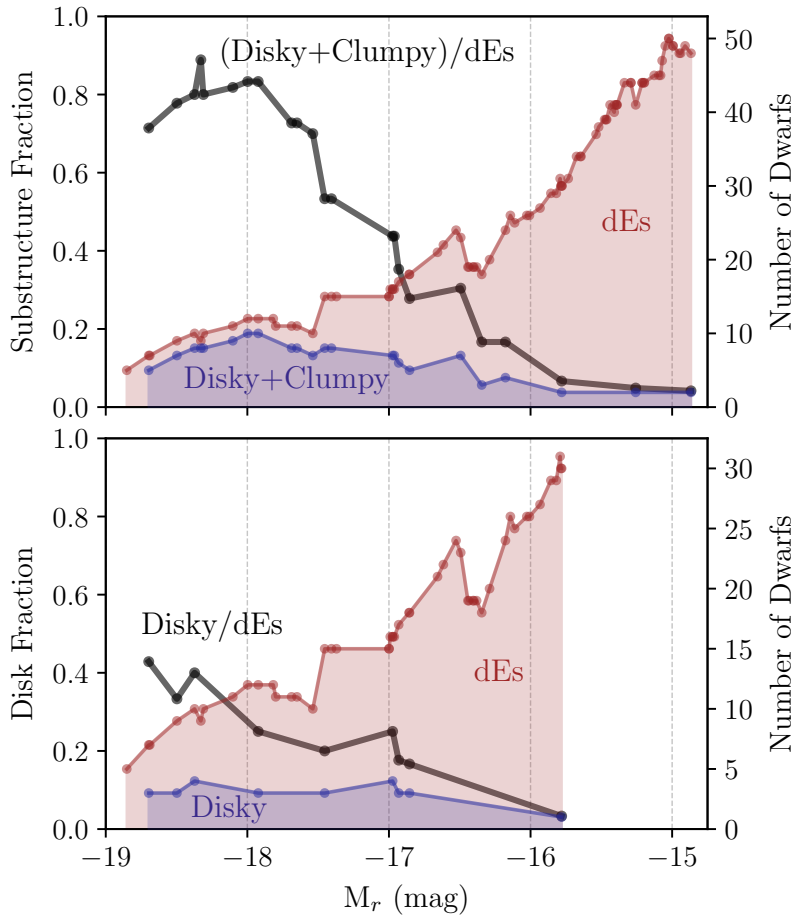

Figure 4.16: Substructure fraction, disk fraction, and luminosity functions of the Fornax dwarf ETGs. In red, the running histogram of all dwarf ETGs in the FDSDC as a function of their total r-band absolute magnitude (right y-axis). Similarly, in blue, the running histogram of the dwarf ETGs with substructure that constitute our sample (right y-axis). *Top panel:* dwarf ETGs with substructure classified as either disky or clumpy. The black line corresponds to the ratio of both histograms, and represents the substructure fraction of the dwarf ETGs (left y-axis). *Bottom panel:* dwarf ETGs with substructure classified as disky. The black line represents the disk fraction of the dwarf ETGs (left y-axis). In both panels, the bins are calculated at the position of each galaxy, with a width that is one magnitude in size. We plot the luminosity functions out to the faintest galaxy in our sample. The counts are complete, as the completeness limit of the FDSDC is several magnitudes deeper than the faintest galaxy in our sample.

components separately. First, in Section 4.4.1, we compute and compare the integrated $g-r$ colors and radial $g-r$ color profiles of the diffuse and substructure components of the sample. Then, in Section 4.4.2, we use the color information to provide some insight into the stellar populations of the galaxies and of their components.

4.4.1 Color of the Diffuse and Substructure Components

As explained in Section 4.3.1, the residual method provides us with a series of g and r-band image products for each galaxy in our sample. On the one hand, we have the model images, which contain the diffuse component of the galaxy; on the other hand, we have the residual images, which contain the substructure component. During the application of the method,

we imposed the r-band galaxy geometry on the g band, thus making any photometric measurements directly comparable in both bands on a pixel-by-pixel (and isophote-by-isophote) basis. Consequently, for each galaxy, we are able to robustly compute the $g-r$ color of its diffuse component out to three galactocentric radii (see Section 4.2.2) by comparing the g and r-band model images, and likewise the color of its substructure component by comparing the g and r-band residual images.

We would like to note that, while our method succeeds in isolating the excess light coming from substructure features in a residual image, the light contained in each pixel is still constituted by a mix of substructure and diffuse light. As the light coming from a galaxy is integrated along the line of sight, any information along the radial direction is lost. In other words, we have no depth information, only a projection on a 2D image. Consequently, the color analyses we carry out are based on these projected color values, as there is no way to know the actual, true color of each component by only using imaging photometry.

In Table 4.6, we provide the integrated $g-r$ colors of the diffuse and substructure components of our dwarf ETG sample. These color measurements are integrated within the one and two effective radii isophotes of the galaxies, for which we derive a median color value and its associated uncertainties from the 16th and 84th percentiles of the distributions. We find that the color of the diffuse component lies in the range between $0.47-0.82$ mag within one effective radius, with a median across the sample of $g-r=0.67$ mag; and in the range between $0.53-0.80$ mag within two effective radii, with a median of $g-r=0.68$ mag. In contrast, the substructure component covers a wider color range and is comparatively much bluer on average: its color lies in the range between -0.16 and 0.84 mag within one effective radius, with a median of $g-r=0.23$ mag; and in the range between -0.27 and 0.83 mag within two effective radii, with a median of $g-r=0.26$ mag. It would appear that, when considering the color of an individual component, the measurements within one and two effective radii are quite similar and thus comparable.

As a way to visualize these results, in Figure 4.17 we plot the integrated $g-r$ color of the diffuse and substructure components versus the total r-band absolute magnitude of the galaxies. We can clearly appreciate that while the diffuse component tends to have more consistently red colors, the substructure component displays a richer diversity, with the majority adopting bluer colors than their diffuse counterparts. Overall, there are weak correlations between the component color and the galaxy brightness. For the diffuse component, we compute a Pearson correlation coefficient of $r=-0.37$ ($r=-0.32$) and an associated p-value $=8\times10^{-2}$ (p-value $=1\times10^{-1}$) for the one and two effective radii measurements, respectively. In comparison, the correlations are slightly stronger for the substructure component, having an $r=-0.57$ and a p-value $=5\times10^{-3}$ for both the one and two effective radii measurements. As addressed in Section 4.2.7, this is the expected behavior according to galaxy evolution: brighter ETGs are on average redder, and we find here that this is also reflected on the colors of their two components separately. Additionally, we observe that both the diffuse and substructure components of the clumpy subsample tend to have comparatively bluer colors than the disky subsample. This color difference, however, is significantly more pronounced in the substructure compo-

Table 4.6: $g-r$ color of the diffuse and substructure components of the Fornax dwarf ETG sample.

Dwarf Galaxy	$g-r$ Color			
	Diffuse Component		Substructure Component	
	Within 1 R_e (mag)	Within 2 R_e (mag)	Within 1 R_e (mag)	Within 2 R_e (mag)
(1)	(2)	(3)	(4)	(5)
F01D145	$0.639^{+0.002}_{-0.020}$	$0.670^{+0.003}_{-0.031}$	$-0.105^{+0.362}_{-0.076}$	$-0.163^{+0.370}_{-0.038}$
F02D000	$0.732^{+0.002}_{-0.002}$	$0.734^{+0.003}_{-0.002}$	$0.115^{+0.038}_{-0.029}$	$0.032^{+0.041}_{-0.044}$
F04D000	$0.701^{+0.001}_{-0.030}$	$0.701^{+0.002}_{-0.031}$	$0.029^{+0.405}_{-0.012}$	$0.094^{+0.405}_{-0.030}$
F04D001	$0.685^{+0.002}_{-0.002}$	$0.675^{+0.001}_{-0.001}$	$0.695^{+0.031}_{-0.040}$	$0.688^{+0.018}_{-0.030}$
F04D002	$0.682^{+0.018}_{-0.001}$	$0.689^{+0.027}_{-0.001}$	$0.491^{+0.025}_{-0.456}$	$0.539^{+0.020}_{-0.428}$
F04D053	$0.500^{+0.022}_{-0.002}$	$0.552^{+0.034}_{-0.002}$	$0.250^{+0.016}_{-0.236}$	$0.263^{+0.013}_{-0.263}$
F04D061	$0.595^{+0.002}_{-0.002}$	$0.599^{+0.004}_{-0.001}$	$0.400^{+0.020}_{-0.017}$	$0.294^{+0.008}_{-0.013}$
F05D000	$0.543^{+0.006}_{-0.028}$	$0.560^{+0.004}_{-0.032}$	$0.226^{+0.275}_{-0.032}$	$0.373^{+0.314}_{-0.016}$
F07D000	$0.734^{+0.001}_{-0.001}$	$0.714^{+0.001}_{-0.001}$	$0.760^{+0.013}_{-0.015}$	$0.744^{+0.008}_{-0.012}$
F09D255	$0.661^{+0.005}_{-0.022}$	$0.672^{+0.005}_{-0.030}$	$0.090^{+0.441}_{-0.205}$	$0.090^{+0.382}_{-0.056}$
F09D492	$0.559^{+0.007}_{-0.006}$	$0.598^{+0.005}_{-0.004}$	$-0.164^{+0.079}_{-0.046}$	$-0.123^{+0.055}_{-0.046}$
F10D189	$0.721^{+0.001}_{-0.002}$	$0.720^{+0.002}_{-0.002}$	$0.125^{+0.052}_{-0.029}$	$0.031^{+0.084}_{-0.055}$
F11D279	$0.815^{+0.001}_{-0.001}$	$0.787^{+0.001}_{-0.001}$	$0.832^{+0.017}_{-0.022}$	$0.828^{+0.012}_{-0.019}$
F14D144	$0.724^{+0.011}_{-0.010}$	$0.728^{+0.015}_{-0.015}$	$0.358^{+0.229}_{-0.222}$	$0.288^{+0.252}_{-0.242}$
F15D384	$0.666^{+0.003}_{-0.003}$	$0.677^{+0.003}_{-0.003}$	$0.142^{+0.017}_{-0.035}$	$0.021^{+0.029}_{-0.017}$
F15D417	$0.660^{+0.002}_{-0.001}$	$0.646^{+0.001}_{-0.001}$	$0.816^{+0.082}_{-0.052}$	$0.642^{+0.025}_{-0.020}$
F17D227	$0.473^{+0.012}_{-0.026}$	$0.540^{+0.009}_{-0.029}$	$-0.028^{+0.361}_{-0.013}$	$-0.021^{+0.392}_{-0.015}$
F19D001	$0.784^{+0.001}_{-0.001}$	$0.796^{+0.001}_{-0.001}$	$0.845^{+0.025}_{-0.033}$	$0.806^{+0.013}_{-0.013}$
F22D244	$0.486^{+0.029}_{-0.005}$	$0.525^{+0.031}_{-0.005}$	$0.311^{+0.016}_{-0.338}$	$0.374^{+0.024}_{-0.345}$
F26D000	$0.546^{+0.067}_{-0.007}$	$0.588^{+0.054}_{-0.004}$	$0.427^{+0.027}_{-0.327}$	$0.369^{+0.029}_{-0.306}$
F26D003	$0.709^{+0.021}_{-0.018}$	$0.705^{+0.021}_{-0.019}$	$0.179^{+0.191}_{-0.185}$	$0.217^{+0.212}_{-0.210}$
F26D141	$0.661^{+0.002}_{-0.003}$	$0.712^{+0.003}_{-0.004}$	$0.032^{+0.070}_{-0.067}$	$-0.273^{+0.059}_{-0.063}$
F31D196	$0.667^{+0.002}_{-0.002}$	$0.675^{+0.002}_{-0.002}$	$0.118^{+0.014}_{-0.019}$	$0.025^{+0.020}_{-0.045}$

Note. — Col. (1): name of the dwarf galaxy. Cols. (2) and (3): $g-r$ color of the diffuse component measured within the one and two effective radii isophotes, respectively. Cols. (4) and (5): $g-r$ color of the substructure component measured within the one and two effective radii isophotes, respectively.

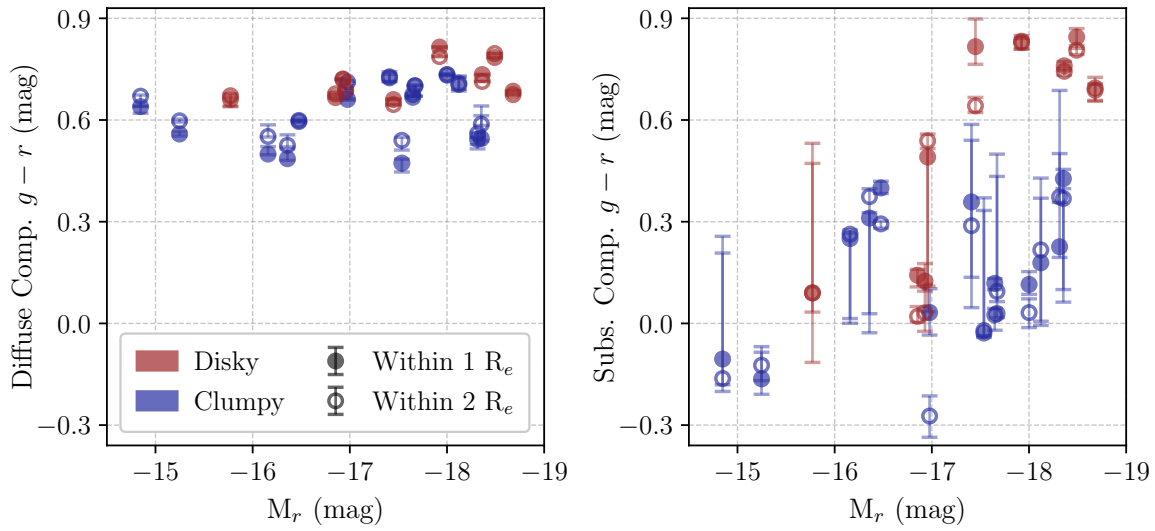

Figure 4.17: $g-r$ color of the diffuse and substructure components of the Fornax dwarf ETG sample as a function of the total r-band absolute magnitude of the galaxies. *Left panel:* $g-r$ color of the diffuse component vs. total r-band absolute magnitude. *Right panel:* $g-r$ color of the substructure component vs. total r-band absolute magnitude. Galaxies classified as disky are shown as red points, while galaxies classified as clumpy are shown as blue points. The measurements are performed within one and two effective radii of the galaxies, shown as filled and empty circles, respectively. The error bars are given by the 16th and 84th percentiles of the distributions.

nent than in the diffuse component. In other words, clump substructures are on average bluer than disk substructures.

To provide a different perspective, in Figure 4.18 we plot the integrated $g-r$ colors of the substructure component versus the diffuse component. The colors of the components appear to be weakly correlated. We compute a Pearson correlation coefficient of $r = 0.42$ with an associated p-value $= 4 \times 10^{-2}$ for the measurements within one effective radius, while no correlation of any significance is obtained for the measurements within two effective radii. In the upper panel, we can appreciate the striking difference between our two subsamples. On the one hand, the clumpy subsample has a substructure component that is always bluer than the diffuse component (i.e., below the one-to-one relation). The colors of both components also display a large scatter. On the other hand, the disky subsample is divided into two: while there are some cases similar to the clumpy subsample, in which the substructure component is bluer than its diffuse counterpart, there are also galaxies in which both components have approximately the same color (i.e., on top of the one-to-one relation). The colors of the components also present a smaller scatter, with comparatively redder colors than the clumpy subsample. When considering the dwarf ETG sample as a whole, it is clear that the substructure features are never redder than the diffuse light of a galaxy. Next, in the middle panel, we color-code the measurements based on the total r-band absolute magnitude of the galaxies. Corroborating with our findings of Figure 4.17, we can indeed observe that brighter galaxies tend to present redder colors in both of their components, albeit with a large scatter. Finally, the results shown on the lower panel are addressed in the next Section 4.4.2.

To further characterize the diffuse and substructure components, we construct their g

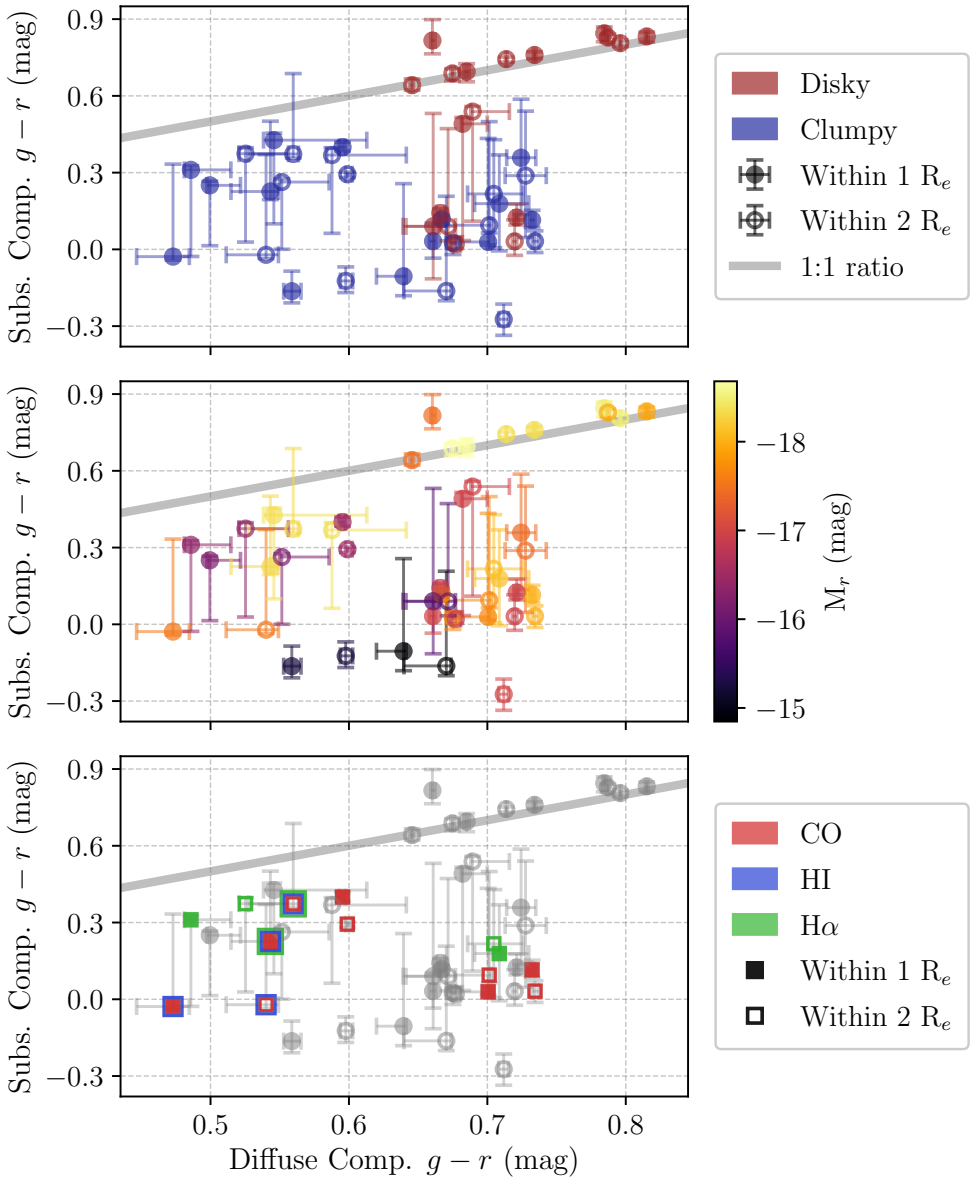

Figure 4.18: Substructure component vs. diffuse component $g-r$ colors of the Fornax dwarf ETG sample. *Top panel:* the galaxies classified as disky are shown as red points, while galaxies classified as clumpy are shown as blue points. *Middle panel:* the galaxies are color coded based on their total r-band absolute magnitude, with lighter colors corresponding to brighter galaxies. *Bottom panel:* the galaxies with CO, HI, and Hα detections are highlighted by red, blue, and green squares, respectively. In all panels, the measurements are performed within one and two effective radii of the galaxies, shown as filled and empty markers, respectively. The error bars are given by the 16th and 84th percentiles of the distributions. The one-to-one relation is shown as a gray line.

and r-band surface brightness profiles and $g-r$ color profiles. For the radial profiles to be comparable on both bands, we sample the model and residual images of a galaxy using a fixed set of isophotes. These isophotes follow the geometry of the diffuse component, in order to minimize any effect that the substructure component may have in driving the galaxy geometry. Specifically, we construct concentric elliptical annuli of a constant 5 pixels (1 arcsec) in width that follow the ellipticity and position angle of the isophotes of the r-band galaxy model image. These annuli are then used to sample the galaxy model and galaxy residual images in both

the g and r bands, extract their light profiles, and construct their surface brightness and color profiles. As an example, we present these radial profiles for the case of dwarf galaxy F02D000 in Figure 4.19, while corresponding Figures for the rest of the dwarf ETG sample are provided in Appendix A.5.

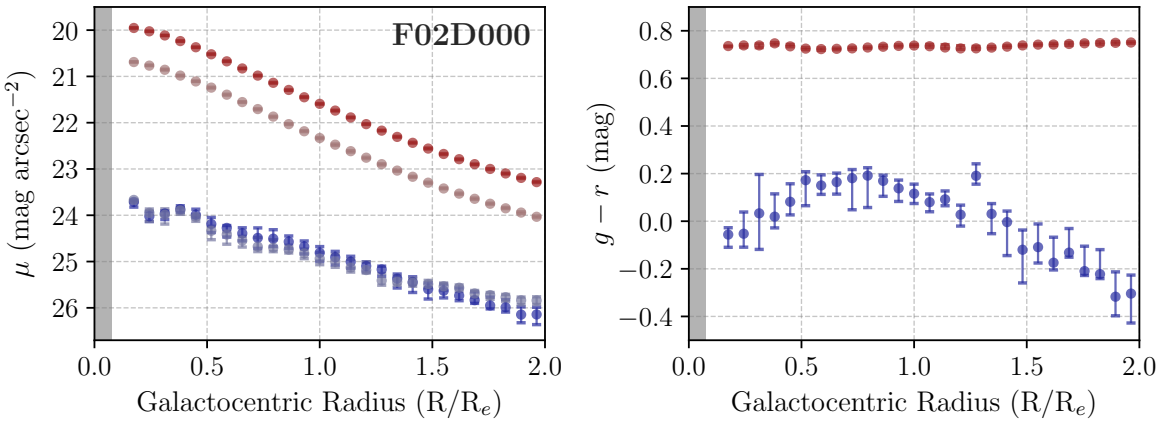

Figure 4.19: Surface brightness and $g-r$ color profiles of the diffuse component (red points) and substructure component (blue points) of Fornax dwarf galaxy F02D000. *Left panel:* surface brightness profiles in the g and r bands. The bright red and bright blue points correspond to the r-band profile, while the faint red and faint blue points correspond to the g-band profile. *Right panel:* $g-r$ color profiles. The measurements are performed in elliptical annuli of constant width that match the geometry of the isophotes of the diffuse component of the galaxy out to two effective radii. The central region is excluded due to the effects of the PSF, and disregard an amount equal to 1.5 times the PSF FWHM. The gray-shaded area indicates the extension of the PSF FWHM. For Figures of the complete sample, see Appendix A.5.

In regards to the surface brightness profiles of our sample, we observe that the diffuse component is brighter than the substructure component at all galactocentric radii. From the galaxy center out to two effective radii, the diffuse component in the g band is on average between $2.0-3.3$ times brighter than the substructure component, with a median of 2.6 times. Similarly, in the r band, it is on average between $2.2-3.5$ times brighter, with a median of 3.0 times. The diffuse component tends to have a smooth profile that becomes steadily fainter with increasing radius, while in contrast the substructure component presents a more irregular profile with fluctuations, which declines less steeply with increasing radius.

To obtain a more quantitative assessment of these observations, we attempt to model the surface brightness profile of the diffuse component, but not of the substructure component. Due to the fluctuating nature of the latter, it would be very difficult to model it properly. Consequently, we choose to only run the 2D fitting algorithm GALFIT (Peng et al. 2002) on the galaxy model images in the r band. As a result, we find that the r-band diffuse components of our dwarf ETG sample appear to be described well by a single Sérsic profile (Sérsic 1968, refer to Equation 3.1) of Sérsic index n ranging between $0.60-2.28$, with a median value of $n=1.33$. Clearly, the diffuse components of our sample are more consistent with being described by an exponential disk profile ($n=1$) than by a de Vaucouleurs profile ($n=4$; de Vaucouleurs 1948). Furthermore, when separated into subsamples, we find that the Sérsic indices of the disky subsample range between $1.04-2.20$, with a median of $n=1.61$; while the Sérsic indices

of the clumpy subsample range between $0.60 - 2.28$, with a median of $n = 1.16$. Therefore, the diffuse component of the disky subsample presents on average larger Sérsic indices than the clumpy subsample. In other words, the disky subsample has a comparatively steeper inner profile with more extended wings on the outer profile. These results are consistent with the work of Su et al. (2021), which perform multi-component decompositions of the FDS galaxies with GALFIT. Interestingly, for our dwarf ETG sample, the Sérsic indices they obtain by modeling the r-band galaxy images are very similar to the ones we obtain by modeling our r-band model images. This serves as an indication that the bright diffuse component is the one in charge: it dominates the galaxy light profile, dictating its overall morphology. In contrast, the substructure component, being several magnitudes fainter, has a more restrictive influence: it can only be properly appreciated once the presence of the diffuse component is removed from the picture.

Finally, in regards to the $g-r$ color profiles of each component, the displayed behavior is a reflection of what is observed in their surface brightness profiles. That is, the color profile of the diffuse component tends to be smooth, while the color profile of the substructure component usually presents strong fluctuations. The results of Figure 4.18 can also be appreciated here and are thus corroborated. For the majority of the galaxies in our sample, their substructure component is bluer than their diffuse component at all galactocentric radii, although there are also cases in which both components have approximately the same radial color. In conclusion, for our sample, their substructure component is always either bluer than or the same color as their diffuse component at all radii within the two effective radii isophote.

4.4.2 Stellar Populations

To go one step further, we will now attempt to use the $g-r$ color information we have extracted to shed some light on the properties of the stellar populations of the diffuse and substructure components of our dwarf ETG sample. However, a single color is usually not enough to break the age-metallicity degeneracy (Worthey 1994). This degeneracy postulates that the age and metallicity of a stellar population are entangled in color space, in the sense that each parameter can independently cause a stellar population to redden.

On the one hand, a young stellar population is dominated by bright massive stars, which have very high effective temperatures and emit in short wavelengths (e.g., in the UV). As a stellar population evolves, short-wavelength radiation gradually diminishes, as massive stars leave the main sequence and arrive to the giant branch, while faint low-mass stars, which have lower effective temperatures and emit on longer wavelengths (e.g., in the IR), become dominant (Schneider 2006). As a result, the observed color of a stellar population reddens with increasing age. On the other hand, the metallicity dictates the stellar opacity and drives effects such as line blanketing on the atmosphere of a star. A metal-rich stellar population has high opacities, so more energy coming from the interior of the star is absorbed, causing the stars to swell up and decrease their effective temperature (Peletier 2013). Similarly, a metal-rich population is more affected by line blanketing, in which short-wavelength radiation is preferentially absorbed on the stellar atmosphere. Together, these effects induce redder colors

with increasing metallicity. As a consequence, a stellar population that appears to be red in color can either be old, metal rich, or (most probably) a certain combination of both.

Taking this degeneracy into account, we will evaluate if the $g-r$ color can still provide some insight on the stellar populations of the diffuse and substructure components. For this purpose, we make use of the stellar population synthesis models provided by the Medium-Resolution Isaac Newton Telescope Library of Empirical Spectra (MILES; Vazdekis et al. 2010), an empirical stellar spectra library. In particular, we use the Extended MILES models (E-MILES; Vazdekis et al. 2012, 2016), which cover stellar Spectral Energy Distributions (SEDs) in a wider spectral range ($168 - 5000$ nm). From the E-MILES SEDs, photometric predictions are derived for a variety of photometric filters, encompassing a large range of ages and metallicities. As the only caveat, these photometric predictions assume Single Stellar Populations (SSPs), meaning that all of the stars are assumed to have formed instantaneously in a single burst of star formation. For the stellar population of a galaxy, this is an extremely simplified view; a galaxy undoubtedly has a multitude of stellar populations, each one with its own complex star formation history. Nonetheless, we use SSPs as a first-order approximation to the problem.

Photometric predictions in the form of AB magnitudes are available in the SDSS g and r bands, allowing us to construct $g - r$ color models that we can directly compare with our observational data. We select SSPs with the following properties:

- **IMF**: the Initial Mass Function (IMF) describes the initial mass distribution of a stellar population. We choose a Kroupa Universal (KU; Kroupa 2001) IMF, which is a multi-part power-law function with a logarithmic slope of 1.30.
- **Isochrones**: by definition, an isochrone describes a stellar population with a given IMF at a specific moment in time (i.e., at the same age). Assuming a range of ages and metallicities, isochrones can be used to construct evolutionary tracks for the stellar populations. We choose the Padova 2000 isochrones (Girardi et al. 2000).
- **Age**: we consider all available ages within the age of the Universe, ranging between $0 - 14$ Gyr.
- **Metallicity**: low-mass galaxies ($M/M_{\odot} \lesssim 10^9$) are expected to have sub-solar metallicities ($\log_{10}(Z/Z_{\odot}) \approx -0.6$; Gallazzi et al. 2005; Toloba et al. 2015). To provide a wider range as a reference, we consider sub-solar to solar metallicities: $\log_{10}(Z/Z_{\odot}) = -1.3$, -0.7, -0.4, and 0.0.

The above setup allows us to construct four $g - r$ color models, each one with a specific metallicity, evolving from 0 to 14 Gyr. In Figure 4.20, we plot these evolutionary tracks and superimpose the $g - r$ colors of the diffuse and substructure components of our sample. If we compare the behavior of the evolutionary tracks, we observe that there are no significant differences in color in the first 1 Gyr. After that, stellar populations that are metal-richer transition into redder colors at a faster rate, and are able to reach redder colors in overall. The age-metallicity degeneracy is evident: a young, metal-rich stellar population can have the same $g - r$ color as a comparatively older, metal-poorer stellar population. Despite this

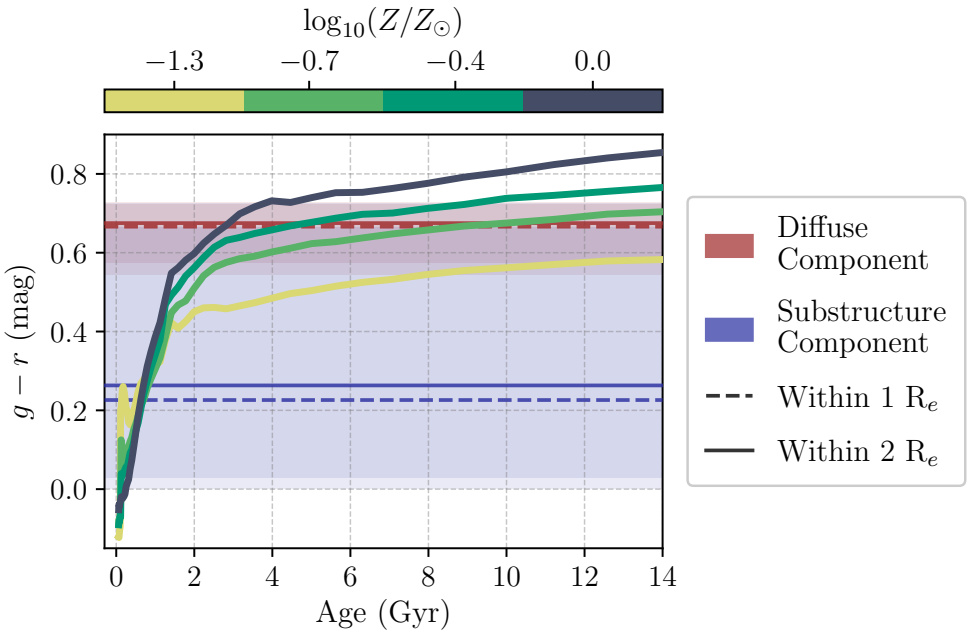

Figure 4.20: Evolution of the $g-r$ color with time, based on the photometric predictions of E-MILES SEDs. The SSP models assume a Kroupa-like IMF and make use of the Padova 2000 isochrones. Four evolutionary tracks with metallicities $\log_{10}(Z/Z_\odot) = -1.3$, -0.7, -0.4, and 0.0 in the age range of 0 to 14 Gyr are shown as thick color-coded lines. We also superimpose the average $g-r$ colors of the diffuse and substructure components of our Fornax dwarf ETG sample in red and blue colors, respectively. The median value of the color measurements within 1 R_e is shown by a dashed line, while the median value within 2 R_e is shown by a continuous line. The shaded regions correspond to the 16th and 84th percentiles of the distributions.

effect, we find that the $g-r$ color of the galaxy components can still give us some insight on their stellar populations. Broadly speaking, we find that the median $g-r$ colors of the diffuse component suggest middle-aged to old stellar populations (> 3 Gyr), while the median colors of the substructure component suggest significantly younger stellar populations (~ 1 Gyr). The diffuse components display a small color scatter, and are consistent with having middle-aged ($2-4$ Gyr), solar-metallicity populations or older ($3-14$ Gyr), sub-solar metallicity populations. In contrast, the substructure components display a very large color scatter, thus encompassing almost the complete range of possible ages and metallicities covered by the evolutionary tracks. This large color diversity (and thus potential age and metallicity diversity) may be a reflection of the different origins and evolutionary histories of the substructure features of our dwarf ETG sample.

Another way to acquire some knowledge on the stellar populations of galaxies is by considering their gas content. The presence of gas serves as an indicator of ongoing star formation, and thus of the existence of a young stellar population. There are several probes that can be used to ascertain the presence of gas, such as the HI, Hα, and CO spectral emission lines:

- **HI**: HI stands for neutral or atomic hydrogen, the most abundant atom in space. HI regions consist of cold interstellar gas that emits in the 21 cm line (i.e., at radio wavelengths).

- **Hα**: Hα is the brightest hydrogen line, corresponding to the H$(3-2)$ transition and emitting at 656 nm (i.e., at the red end of the optical spectrum). It can be used as a tracer to identify ionized hydrogen (HII) regions in the interstellar medium (ISM).
- **CO**: CO stands for carbon monoxide, the most abundant molecule after molecular hydrogen (H_2). Unlike H_2, CO is prone to excitation, with many transitions occurring at low temperatures. The CO$(1-0)$ transition emits at 2.6 mm (i.e., in the radio) and can be used as a tracer for cold molecular gas in the ISM.

In Table 4.7, we present the detections and non-detections of these emission lines in our sample of dwarf ETGs according to different surveys. In total, some kind of ISM is detected in 7 of our dwarf ETGs: there are 5 CO, 2 HI, and 3 Hα detections. In principle, the CO and HI detections are flux limited, while the Hα is not, since only a selected sample of galaxies were observed. First, in regards to the 5 CO detections, the morphology and kinematics of the molecular gas of the galaxies is classified as disturbed, as opposed to regular. In regards to the 2 HI detections, both galaxies appear to be HI deficient (i.e., there is HI, but in low quantities), with one galaxy having a disturbed HI morphology. Finally, in regards to the 3 Hα detections, no additional details are provided. Interestingly, all of the galaxies in our sample with either CO, HI, or Hα detections have been classified in this work as having clump substructures. This means that half of the the galaxies in the clumpy subsample ($7/14$ galaxies) have been confirmed to have an ISM, while in contrast none of the galaxies in the disky subsample ($0/9$ galaxies) have detections.

These results can be visualized in the lower panel of Figure 4.18. We observe that the galaxies with ISM detections have a substructure component that is always bluer than their diffuse component. Therefore, we can hypothesize that their diffuse component is mostly quenched; if there is star formation, then it is happening at some sub-scale. Or, alternatively, their star formation rate is too low to make a difference in the observed $g-r$ color. Given the comparatively bluer color of the substructure component, we would instead expect that the galaxies are forming stars in the ISM of their clumpy substructure regions. This would imply that the bluer colors of their substructures are caused by the presence of young stellar populations.

In conclusion, color information has the potential to provide an in-depth view into the stellar populations of a galaxy. By applying the residual method to our dwarf ETG sample, we have gone one step further, as it has allowed us to derive the colors and characterize the stellar populations of their diffuse and substructure components separately.

Table 4.7: CO, HI, and Hα detections in the Fornax dwarf ETG sample.

Dwarf Galaxy	CO		HI		Hα	
	Targeted?	Detection	Targeted?	Detection	Targeted?	Detection
(1)	(2)	(3)	(4)	(5)	(6)	(7)
F02D000	Yes	Detected, disturbed	Yes	Undetected	No	–
F04D000	Yes	Detected, disturbed	Yes	Undetected	No	–
F04D061	Yes	Detected, disturbed	Yes	Undetected	No	–
F05D000	Yes	Detected, disturbed	Yes	Detected, deficient	Yes	Detected
F07D000	No	–	No	–	Yes	Undetected
F10D189	No	–	No	–	Yes	Undetected
F11D279	No	–	No	–	Yes	Undetected
F15D384	No	–	No	–	Yes	Undetected
F15D417	No	–	No	–	Yes	Undetected
F17D227	Yes	Detected, disturbed	Yes	Detected, deficient, disturbed	No	–
F22D244	No	–	No	–	Yes	Detected
F26D003	No	–	No	–	Yes	Detected

Note. — Col. (1): name of the dwarf galaxy. Cols. (2) and (3): detection of the CO$(1-0)$ line by the ALMA Fornax Cluster Survey (AlFoCS; Zabel et al. 2019). Targeted galaxies by the AlFoCS were previously detected in either HI by the HI Parkes All Sky Survey (HIPASS; Barnes et al. 2001; Waugh et al. 2002) or in the far-infrared by the Hershel Fornax Cluster Survey (HeFoCS; Fuller et al. 2014). The AlFoCS contains five galaxies of our sample. The morphology and kinematics of the molecular gas of our five galaxies is identified as disturbed, as opposed to regular. Cols. (4) and (5): detection of the HI line by the ATCA HI Survey (Loni et al. 2021), which covers an area that goes slightly beyond the Virial radius of the Fornax cluster ($R_{vir} = 0.7$ Mpc; Drinkwater et al. 2001). Two out of our five galaxies also contained in AlFoCS have detections in HI, while the remaining three have non-detections. The two detections are deficient in HI, with one of them also having a disturbed HI morphology. Cols. (6) and (7): detection of the Hα line by the SAMI-Fornax Dwarfs Survey (SAMI-FDS; Scott et al. 2020), to be published in Peletier et al. (in prep.). The SAMI-FDS targeted eight galaxies of our sample, of which only three have detections in Hα (R. Peletier, private communications).

5

Discussion: From Virgo to Fornax

In this Chapter, we provide an in-depth discussion of our results and their implications. To be able to properly compare all that we have learned from our samples of Virgo and Fornax dwarf ETGs with substructure features (refer to Chapters 3 and 4), there are several factors that must be taken carefully into account. First, in Section 5.1, we consider the properties of the Virgo and Fornax galaxy clusters, and address how each cluster environment may have played a role in shaping the properties of their dwarf galaxy populations. Then, in Section 5.2, we consider the properties of the data, and evaluate if the differences in data quality, such as the imaging resolution and depth, may have biased the results obtained for our two samples. Finally, in Section 5.3, we consider the properties of the dwarf ETGs constituting our Virgo and Fornax samples, and perform a direct comparison while keeping in mind the differences between the clusters they inhabit and the differences in the data quality. In particular, we examine the results obtained through the application of the residual method, and address how they can be used to constrain the possible formation and evolution scenarios of dwarf ETGs that have embedded substructure features.

5.1 Galaxy Cluster Properties

To begin with, we analyze the context in which our dwarf ETG samples are found in: the Virgo and Fornax galaxy clusters. First, in Section 5.1.1, we describe and compare the properties of the clusters. Then, in Section 5.1.2, we consider the environmental processes that can be driven by the cluster environment, evaluate their relative importance in the Virgo and Fornax clusters, and weigh in how they could have influenced the population of dwarf ETGs with substructure features.

5.1.1 Virgo vs. Fornax

To introduce the Virgo and Fornax galaxy clusters, let us first consider their spatial distribution and overall appearance. On the one hand, the Virgo cluster is found on the northern sky, and at a galactic latitude of about 74.5 deg. It is constituted by an aggregate of several galaxy subsystems (or subclumps). The main subclump (Virgo A) is centered around the brightest cluster galaxy (BCG), the cD-type galaxy M87 (located at R.A. $= 12^{\rm h}30^{\rm m}49.4^{\rm s}$, Decl. $= +12°23'28.0''$ in J2000.0, according to the NASA/IPAC Extragalactic Database; NED). At least two more subclumps can be easily identified: the Virgo B subclump, located towards the south of the cluster and centered around the early-type galaxy M49, and another subclump towards the north-west and centered around the early-type galaxy M86. On the other hand, the Fornax cluster is found on the southern sky, and at a galactic latitude of about -53.6 deg. With a comparatively more regular appearance, it is centered around the cD-type galaxy NGC 1399 (located at R.A. $= 03^{\rm h}38^{\rm m}29.0^{\rm s}$, Decl. $= -35°27'02.4''$ in J2000.0, according to NED). Additionally, towards the south-west of the cluster, there is an infalling subgroup by the name of Fornax A, centered on the lenticular (S0) galaxy NGC 1316, which constitutes the actual BGC of Fornax.

We now consider the properties of the Virgo and Fornax galaxy clusters. In Table 5.1, we summarize their main attributes. Both clusters are located in the nearby Universe (< 20 Mpc) and at comparable distances from us, with the Fornax cluster being about 1.2 times further away than the Virgo cluster (the exact distance ratio being $\mathrm{d}_F/\mathrm{d}_V = 1.214 \pm 0.017$; Blakeslee et al. 2009). However, despite their closeness to us, we will see that they have very different properties, and thus constitute two distinct environments for their galaxies to evolve in.

The Virgo cluster is comparatively larger in size and significantly more massive, having approximately 2 times the virial radius and 6 times the virial mass of the Fornax galaxy cluster. Specifically, the Virgo cluster has a virial radius of 1.5 Mpc and a virial mass of 4×10^{14} $\mathrm{M}_\odot$, while the Fornax cluster has a virial radius of 0.7 Mpc and a virial mass of 6×10^{13} $\mathrm{M}_\odot$ (McLaughlin 1999; Drinkwater et al. 2001; Weinmann et al. 2011). These values, of course, assume that both clusters are virialized (i.e., that their kinetic and potential energy have reached equilibrium), which may not necessarily be true. Nonetheless, they can still be used as a guideline. These differences in size and mass are directly reflected on the velocity distribution of their galaxies, with the Virgo cluster members presenting more than 2 times the velocity dispersion of the Fornax cluster members; about 890 km s^{-1} against 370 km s^{-1}, respectively. The radial velocities of their members also behave as expected: the Virgo cluster, being closer to us, has a mean radial velocity of 950 km s^{-1}; while the Fornax cluster, being comparatively farther away, has a larger mean radial velocity of 1490 km s^{-1} (Binggeli et al. 1993; Drinkwater et al. 2001; Boselli & Gavazzi 2006; Janz et al. 2021).

The more massive Virgo cluster is as a consequence also richer, in the sense that it hosts a considerably larger number of galaxies. Within the same multiple of their core radius R_c (King 1962) length ($3.5 \times \mathrm{R}_c$) and the same magnitude cut ($\mathrm{m}_B \lesssim 18$ mag), the Virgo cluster hosts 1170 galaxies while the Fornax cluster hosts only 235, a difference in a factor of 5 (Ferguson

Table 5.1: Comparison of the properties of the Virgo and Fornax galaxy clusters.

Cluster Properties (1)	Virgo Cluster (2)	Fornax Cluster (3)
Distance modulus (mag)	31.09 ± 0.15	31.51 ± 0.15
Physical distance (Mpc)	16.5 ± 1.1	20.0 ± 1.4
Virial radius (Mpc)	1.5	0.7
Virial mass ($M_\odot$)	4×10^{14}	6×10^{13}
Mean radial velocity (km s^{-1})	951	1493 ± 36
Velocity dispersion (km s^{-1})	886	374 ± 26
Velocity dispersion of ETGs (km s^{-1})	753	356 ± 31
Velocity dispersion of LTGs (km s^{-1})	1340	405 ± 45
King profile core radius, R_c (Mpc)	0.63	0.25
Number of galaxies (within $3.5 \times R_c$)	1170	235
Fraction of dwarf ETGs (within $3.5 \times R_c$)	0.76	0.77
Fraction of ETGs (within $3.5 \times R_c$)	0.82	0.87
Fraction of LTGs (within $3.5 \times R_c$)	0.18	0.13
Central galaxy number density (Mpc^{-3})	250	500
Relative gas density of IGM	1	1/4
Average temperature of IGM (keV)	2.58 ± 0.03	1.20 ± 0.04
Average temperature of IGM (K)	$\sim 3.0 \times 10^7$	$\sim 1.4 \times 10^7$
Average Fe abundance of IGM ($[Fe/H]_\odot$)	0.34 ± 0.02	0.23 ± 0.03

Note. — Col. (1): cluster properties, with the units given in parenthesis. Col. (2): values for the Virgo galaxy cluster. Col (3): values for the Fornax galaxy cluster. The distance moduli and physical distances are taken from Blakeslee et al. (2009). The cluster virial radii and virial masses are taken from Weinmann et al. (2011) and references therein (McLaughlin 1999; Drinkwater et al. 2001). The mean radial velocities and velocity dispersions, including the velocity dispersion of the early-type galaxies (ETGs) and late-type galaxies (LTGs), are taken from Janz et al. (2021) and references therein (Binggeli et al. 1993; Drinkwater et al. 2001; Boselli & Gavazzi 2006). The King profile (King 1962) core radii R_c, and the number of galaxies within $3.5 \times R_c$ that have apparent magnitudes $m_B \lesssim 18$ mag, are taken from Jordán et al. (2007) and references therein (Ferguson 1989a). Within the same clustercentric radii and magnitude range, we derive galaxy population fractions relative to the total number of cluster members from Ferguson (1989a). The morphological types considered encompass elliptical (E), lenticular (S0), dwarf elliptical (dE), dwarf spheroidal (dS0), spiral (Sp) and irregular (Irr) galaxies. Thus, dwarf ETGs are dE+dS0, ETGs are E+S0+dE+dS0, and LTGs are Sp+Irr. The central galaxy number densities are taken from Janz et al. (2021) and references therein (Ferguson 1989a). The relative gas densities of the intracluster or intergalactic medium (IGM) are taken from Janz et al. (2021) and references therein (Jones et al. 1997; Schindler et al. 1999; Paolillo et al. 2002). Derived from X-ray observations that exclude the innermost cluster regions, the average temperature of the IGM, and the average Fe abundance of the IGM as compared to solar, are taken from Jordán et al. (2007) and references therein (Fukazawa et al. 1998).

1989a; Jordán et al. 2007). Despite this fact, the Virgo cluster is half as dense as the Fornax cluster: the former has a central number density of 250 galaxies per Mpc^3, while the latter has a central number density of 500 galaxies per Mpc^3 (Ferguson 1989a; Janz et al. 2021). So, although the Virgo cluster is more massive and rich, the Fornax cluster is comparatively more compact and dense.

The properties of their intracluster or intergalactic medium (IGM), as expected, also correlate with the mass of the clusters. The gas that constitutes the IGM is 4 times denser in the Virgo cluster than in the Fornax cluster (Jones et al. 1997; Schindler et al. 1999; Paolillo et al. 2002; Janz et al. 2021). As a result, the average temperature of the IGM in the Virgo cluster is approximately 2 times higher than in the Fornax cluster, adopting temperatures of about 3.0×10^7 K and 1.4×10^7 K, respectively. The average Fe abundance, which works as a proxy of the metallicity of the IGM, is also higher in Virgo compared to Fornax, approximately by a factor of 1.5. While the Fe abundance of the Virgo IGM is about 0.34 [Fe/H]$_\odot$, the Fornax IGM has an abundance of about 0.23 [Fe/H]$_\odot$ (Fukazawa et al. 1998; Jordán et al. 2007).

The most interesting differences between the two clusters, and also the most relevant for this work, concern their galaxy populations. When dividing the cluster members into early-type galaxies (ETGs) and late-type galaxies (LTGs), we find that they have different relative fractions and velocity distributions. First, let us consider the population numbers based on the work of Ferguson (1989a). The Virgo cluster has a lower early-type fraction compared to the Fornax cluster, with ETGs constituting 82% of the population in Virgo and 87% of the population in Fornax. Conversely, Virgo has a higher late-type fraction compared to Fornax, with LTGs constituting 18% of the population in Virgo and 13% in Fornax. However, no significant differences are found in the relative fractions of their dwarf ETGs, which comprise 76% of the population in Virgo and 77% in Fornax. Therefore, dwarf ETGs, our objects of interest, are by far the most abundant type of galaxy in these clusters, comprising around $3/4$ of their total galaxy population.

Second, let us consider the velocity distributions of their galaxy populations. In both clusters, we find that their ETGs present a lower velocity dispersion than their LTGs, which is an indication that velocity segregation exists between the two populations. On the one hand, the Virgo ETGs have a velocity dispersion of about 750 km s^{-1}, while the LTGs have a velocity dispersion of about 1340 km s^{-1} (Boselli & Gavazzi 2006; Janz et al. 2021). On the other hand, the Fornax ETGs have a velocity dispersion of about 360 km s^{-1}, while the LTGs have a velocity dispersion of about 410 km s^{-1} (Drinkwater et al. 2001; Janz et al. 2021). Therefore, it is evident that each cluster displays very different levels of velocity segregation. The velocity dispersion of the late-type population compared to the early-type population is larger by a factor of 1.8 in the Virgo cluster, but only by a factor of 1.1 in the Fornax cluster. Thus, the velocity segregation in the Virgo cluster is significant, while it is quite negligible in the Fornax cluster.

Together, the different properties of the two clusters help us construct the following comparative picture:

- **Virgo cluster**: a massive, loosely concentrated cluster. It is constituted by several galaxy subclumps. It is both rich in galaxy numbers and IGM content. It has a comparatively larger fraction of star-forming (SF) galaxies (LTGs), which present a higher velocity dispersion than their non-SF counterparts (ETGs). Therefore, it is a dynamically "younger" cluster, in the sense that it is experiencing an ongoing assembly process, in which infalling field galaxies and galaxy groups are gradually becoming part of the cluster (Lisker et al. 2018).
- **Fornax cluster**: a less massive, more compact cluster. It is constituted by one main galaxy clump, with a galaxy subgroup (Fornax A) currently infalling. It has lower galaxy numbers and a poorer IGM but, at the same time, it is much denser. It contains a comparatively higher fraction of non-SF galaxies (ETGs). Both the SF and non-SF galaxies (LTGs and ETGs) present similar velocity distributions. Therefore, it is a dynamically "older" cluster, in the sense that it is more virialized and evolved; i.e., more close to equilibrium or relaxation and with a larger passive galaxy population (Raj et al. 2019).

In conclusion, the Virgo and Fornax galaxy clusters appear to be at different evolutionary stages, and thus constitute two distinct environments. It is to be expected, therefore, that their properties influenced the evolution of their galaxy populations in different ways and in different relative strengths. We expect these environmental differences to be particularly imprinted on their dwarf galaxy populations, which are very susceptible to the environment due to their overall low masses and shallow potential wells.

5.1.2 Environmental Processes

We now consider the environmentally-driven processes that were introduced and thoroughly described in Section 1.2.2. We address their relative importance in the Virgo and Fornax galaxy clusters, and how they could have influenced their respective populations of dwarf ETGs with substructure features. For clarity, we divide the environmental processes into four categories: small-scale gravitational processes, large-scale gravitational processes, short-timescale hydrodynamical processes, and long-timescale hydrodynamical processes.

- **Small-scale gravitational processes:** galaxy-galaxy harassment, galaxy mergers.

The efficiency of small-scale gravitational processes is strongly correlated with the relative velocity of the interacting systems. "Galaxy-galaxy harassment" and "galaxy mergers" are interactions that are more efficient in low density regions, such as in galaxy groups and in the outskirts of galaxy clusters, where the relative velocity between the galaxies is smaller. In this situation, galaxies are more likely to gravitationally interact and even merge, as the duration of the interaction is longer and thus more impactful overall. As seen in the previous Section 5.1.1, the Virgo cluster is significantly more massive than the Fornax cluster, to the point that the velocity dispersion of its galaxies is 2 times larger than in Fornax. As a result, we expect that galaxy-galaxy harassment and galaxy mergers are more likely to occur in the Fornax cluster outskirts than in the Virgo cluster outskirts. We should also acknowledge that there is a group of galaxies, known as the Fornax A subgroup, currently falling into the Fornax cluster. In

such a low-velocity-dispersion environment, galaxy-galaxy interactions are expected to leave a more lasting impact on the galaxies involved.

Overall, small-scale gravitational processes should be more predominant in the Fornax cluster than in the Virgo cluster. Dwarf ETGs with substructure features should be specially susceptible to these gravitational processes, due to their shallow potential wells. On the one hand, galaxy-galaxy harassment may induce the gradual morphological transformation of dwarf spiral galaxies into dwarf ETGs with disk substructures, and dwarf irregular galaxies into dwarf ETGs with clump substructures. Conversely, tidal harassment may instead trigger the formation of disk substructures, such as bars and spiral arms, on some of the dwarf ETGs. On the other hand, galaxy mergers usually also lead to morphological transformations. A merger involving a dwarf spiral galaxy may transform most of its disk features into diffuse light, while a merger involving a dwarf irregular galaxy may transform most of its clump features into diffuse light. This way, the resulting merger may adopt the general appearance of a dwarf ETG, with some of the defining features of the progenitor galaxy still surviving in the form of faint substructures.

► **Large-scale gravitational processes:** galaxy-cluster harassment.

The efficiency of large-scale gravitational processes is strongly correlated with the gravitational potential of the environment. "Galaxy-cluster harassment" is an interaction that is more efficient in high density regions, such as the core of galaxy clusters. In this case, the larger the gravitational potential of the environment, the larger the gravitational disruption that can be induced in the galaxy. As seen in the previous Section 5.1.1, the Virgo cluster is 6 times more massive than the Fornax cluster, and consequently has a much deeper potential well. As a result, the Virgo cluster members can potentially experience stronger galaxy-cluster harassment than members of the Fornax cluster, where tidal forces should be comparatively weaker.

Overall, large-scale gravitational processes should be more predominant in the Virgo cluster than in the Fornax cluster. Like in the case of galaxy-galaxy harassment, dwarf ETGs with substructure features should also be very susceptible to galaxy-cluster harassment, due to their shallow potential wells. Therefore, it is probable that these galaxies may have experienced (or may be currently experiencing) tidally-induced transformations. Through the gravitational interaction with the cluster potential, dwarf spirals and dwarf irregulars may be perturbed and transformed into dwarf ETGs with embedded substructure features. As an opposite possibility, the tidal force of the cluster potential may perturb dwarf ETGs that are seemingly featureless, and trigger the formation of disk substructures.

► **Short-timescale hydrodynamical processes:** ram-pressure stripping, turbulent viscous stripping, thermal evaporation.

The efficiency of short-timescale hydrodynamical processes is mainly correlated with the density, temperature, and velocity differences between the interstellar medium (ISM) of a galaxy and its surrounding intracluster or intergalactic medium (IGM). The interaction between the

cold ISM and hot IGM results in the partial, and sometimes even total, removal of the ISM of a galaxy. These processes dominate in the core of galaxy clusters, which tend to have a very dense and hot IGM. As seen in the previous Section 5.1.1, the IGM of the Virgo cluster is 4 times as dense and 2 times as hot than the IGM of the Fornax cluster. As a result, gas-stripping processes (such as "ram-pressure stripping" and "turbulent viscous stripping") and heat-transfer processes (such as "thermal evaporation") are significantly more efficient and also more likely to happen in the Virgo cluster (Davies et al. 2013).

Overall, short-timescale hydrodynamical processes should be more predominant in the Virgo cluster than in the Fornax cluster. The dense and hot IGM can effectively strip away or evaporate the gas content of dwarf ETGs with substructure features, given their shallow potential wells and thus low binding energy of their gaseous component. Any remaining gas is likely kept in the disk and clump substructures, where star formation may continue at a slow rate, making these features bluer in comparison to the main body of their galaxy. As another option, their gaseous component may have already been completely removed through the interaction with the IGM in a not-so-distant past. As such, their disk and clump features may be in the process of slowly fading away, given that there is no more ongoing star formation. Therefore, gas-stripping and gas-evaporation processes constitute a possible explanation as to why we find dwarf ETGs that have substructure features that are just as "red and dead" as the main body of their galaxy, while at the same time being considerably fainter than the main body.

► **Long-timescale hydrodynamical processes:** starvation or strangulation.

As their name implies, the efficiency of long-timescale hydrodynamical processes are mainly dependent on the amount of time a galaxy has been immersed in a particular environment, be it a galaxy group or cluster. These processes (such as gas "starvation" or "strangulation") are ubiquitous once a galaxy leaves the field and becomes part of a group or cluster, already coming into effect when the galaxy is still lingering on the outskirts and experiencing its first infall. Starvation acts by halting the supply of cold gas infalling into the galaxy, which continues to form stars until its gas reservoir is eventually depleted. As seen in the previous Section 5.1.1, the Virgo and Fornax galaxy clusters are among the most massive and galaxy-rich locations in the nearby (< 20 Mpc) Universe, and as such, their formation began long time ago. Thus, the slow-paced process of starvation must have affected their first galaxy members for several gigayears already, and is undoubtedly affecting their new galaxy members that are currently infalling.

Overall, long-timescale hydrodynamical processes should be predominant in both the Virgo and Fornax galaxy clusters. Due to the low binding energy of dwarf systems, they should be specially susceptible to gas starvation induced the environment. In particular, starvation accelerates the transition of dwarf star-forming galaxies into dwarf non-star-forming galaxies. If a cluster dwarf ETG with substructure features still contains some gas on its disk or clump substructures, then we can surely expect that it is currently experiencing this slow (but unavoidable) environmental process. If, instead, the dwarf ETG is devoid of gas and its substruc-

Table 5.2: Comparison of the data properties of the Virgo and Fornax samples.

Data Properties (1)	Virgo Sample (2)	Fornax Sample (3)
Observation filters	White ($\rightarrow r$)	g, r
Angular pixel size (arcsec)	0.71	0.20
Physical pixel size (pc)	57.18	19.39
Median angular PSF FWHM, r band (arcsec)	1.27	0.95
Median physical PSF FWHM, r band (pc)	101.92	92.11
Median depth, r band (mag arcsec^{-2})	27.79	26.01

Note. — Col. (1): data properties, with the units given in parenthesis. Col. (2): values for the Virgo dwarf ETG data (presented in Section 3.1). Col. (3): values for the Fornax dwarf ETG data (presented in Section 4.2). When transforming angular to linear physical lengths, we adopt a Virgo cluster distance of 16.5 Mpc and a Fornax cluster distance of 20.0 Mpc (Blakeslee et al. 2009). All photometric measurements in the white band are eventually transformed into their r-band equivalent.

ture features appear as red as the main body, we can assume that this process (in conjunction with other gas-stripping processes) may have already acted in the past.

5.2 Data Properties

Let us now consider the properties of the data. On the one hand, the 9 dwarf ETGs that constitute our Virgo sample (described in Section 3.1) were specifically selected due to the presence of embedded disk substructures, which were originally detected in SDSS images of the galaxies (Lisker et al. 2006c). Our Virgo sample was then observed with the ESO 2.2m/WFI in the white filter (i.e., no filter) in order to maximize the signal. All photometric measurements were then translated into the r band. On the other hand, the 23 dwarf ETGs that constitute our Fornax sample (described in Section 4.2) fall on the footprint of the Fornax Deep Survey (FDS; Iodice et al. 2016) and are part of the FDS dwarf galaxy catalog (FDSDC; Venhola et al. 2018). The FDS data was observed with VST/OmegaCAM in the u, g, r, and i filters. Out of the 564 dwarf galaxies that are part of the FDSDC, we constructed our Fornax sample of 23 dwarf ETGs based on the presence of either embedded disk or clump substructures. We also exclusively use the g and r-band FDS data (for reasons explained in Section 4.2.2).

A comparison of the main data properties is provided in Table 5.2. There are two fundamental differences: the image resolution and the image depth, which we respectively address in the following Sections 5.2.1 and 5.2.2. Overall, while the Fornax data is better resolved, the Virgo data is deeper.

5.2.1 Imaging Resolution

First, we address the difference in imaging resolution. By taking into account the distance to each galaxy cluster, we translate the angular scale of the data into a physical scale. Thus,

we find that the physical size of one pixel corresponds to 57.2 pc in the Virgo data, while it corresponds to 19.4 pc in the Fornax data. In other words, the Fornax data has about 3 times better resolution than the Virgo data (the actual factor being 2.9 times). Similarly, by translating the angular PSF FWHM into a physical measurement, we find that the Fornax data has a physical PSF FWHM that is about 10% narrower than the Virgo data. Consequently, in terms of the quality of the data, the Fornax data is superior to the Virgo data.

To assess if the better resolution of the Fornax data is playing a role in our capability to detect faint substructure features, we worsen it to match the resolution of the Virgo data. For this purpose, we use the IRAF `magnify` task to re-bin the PSF-matched $g+r$ image cutouts of the FDSDC galaxies (see Section 4.2.3) in order to degrade their resolution by a factor of 2.9. We then create unsharp mask images in the same way we did for the original galaxy image cutouts (refer to Section 4.2.4). By comparing the original images with the binned images, and their respective unsharp masks, we can conclude that binning does not fundamentally contribute in revealing new substructure features. While substructure features that were already present become brighter and clearer in appearance, no new substructures pop-up in galaxies that had non-detections in the first place. For our sample of 23 dwarf ETGs, we confirm that we do not observe any new features after binning.

As a test, we also tried increasing more drastically the amount of binning, and degraded the resolution of the Fornax sample by a factor of 3, 6, and 9. On the one hand, we find that binning increases the brightness of faint, embedded substructure features, making them easier to identify. On the other hand, the details of the substructure features are progressively lost by decreasing the image resolution. For example, binning by a factor of 9 makes the substructure features completely unrecognizable. Therefore, the binning technique embodies a delicate balance between improving the detectability of faint features and sacrificing their individuality and characteristics.

In summary, binning high-resolution images by a small, reasonable amount can help in the detection process of substructure features. However, binned images will never reveal features that were not, at the very least, already hinted at in the original galaxy images (and their associated unsharp masks). Thus, in the case of our Fornax dwarf ETG sample, we do not find any new substructure features after degrading its imaging resolution to match the one of the Virgo sample. In conclusion, the comparatively higher resolution of the Fornax sample is not detrimental for substructure detection purposes.

5.2.2 Imaging Depth

The second important difference between the data is in regards to the imaging depth. We find that the Virgo data reaches a median depth of 27.8 mag arcsec^{-2} in the r band at a S/N $= 1$; in contrast, the Fornax data is only able to reach up to 26.0 mag arcsec^{-2} in the same band and at the same S/N. This means that the Virgo data is about 2 magnitudes deeper than the Fornax data in the r band (the actual difference being 1.8 magnitudes). Therefore, it is possible that extremely faint substructure features found in the Virgo data would actually be undetectable in the comparatively shallower Fornax data.

In order to increase the S/N and thus the depth of the Fornax data, the g and r-band galaxy images were coadded into a single $g + r$ image (see Section 4.2.3). These coadded images (and their unsharp masks) were then individually inspected and used to detect any embedded substructure features. Nonetheless, this coaddition is still not enough to match the greater depth of the Virgo data. As further increasing the depth of the Fornax data is not possible, we instead consider if the substructure features of our Virgo dwarf ETG sample would be detectable (or not) if the data had a much shallower depth.

To answer this question, we refer to the work of Lisker et al. (2006c), in which SDSS Data Release 4 (DR4; Adelman-McCarthy et al. 2006) images were used to originally detect the substructure features of our Virgo sample. These SDSS images reach a median depth of 24.4 mag arcsec^{-2} in the r band at a S/N $= 1$: more than 3 magnitudes shallower than our Virgo data (the actual number being 3.4 magnitudes). For detection, Lisker et al. (2006c) used optimized $g + r + i$ coadded galaxy images, but they do not state the increase in depth. We therefore consider the SDSS DR4 r-band images on their own, as we know how their depth compares to the depth of our Virgo data. By creating unsharp mask images from the SDSS DR4 r-band images of our 9 Virgo dwarf ETGs, we can confirm that their substructure features are still detectable. The bar substructures, which tend to be bright, are clearly there; while the spiral arm substructures, which are comparatively fainter, are at the very least hinted at.

We would like to highlight that these r-band SDSS data are more than 1.5 magnitudes shallower than our FDS r-band data (the actual number being 1.6 magnitudes). Despite the gain in depth of the FDS data compared to the SDSS data, we are still unable to detect, for example, any spiral arm substructures in the dwarf ETGs of the FDSDC. The Fornax dwarf ETGs in our disky subsample display edge-on disks and rings, but definitely no spiral arms. This leads us to conclude that not finding embedded spiral arms in the dwarf ETGs of the Fornax cluster must have an underlying physical reason, and is not tied to possible limitations regarding the depth of the data —at least, when talking about spiral arms of equivalent surface brightness as the ones found in the dwarf ETGs of the Virgo cluster. It would appear, therefore, that the shallower depth of our Fornax data compared to our Virgo data is not significantly hindering our ability to detect substructure features.

5.3 Dwarf ETG Sample Properties

At last, we have established the necessary background to be able to properly compare our results and findings regarding the Virgo and Fornax dwarf ETGs samples (see Chapters 3 and 4) that we analyzed in this work. First, in Section 5.3.1, we characterize each sample and compare them based on the properties of their dwarf ETGs and the results we obtained through the application of the residual method. Then, in Section 5.3.2, we briefly introduce the high-resolution numerical simulations we carried out in Smith et al. (2021), which were used to test if tidal harassment by the cluster environment can serve as a possible explanation for the presence of disk substructures in dwarf galaxies. Finally, in Section 5.3.3, we attempt to tie everything together: how our results can either help to support or reject formation

and evolution scenarios of dwarf ETGs with substructure features, given the particular cluster environment that serves as the global context of their existence.

5.3.1 Results Comparison

To begin with, we define our two dwarf ETG samples. On the one hand, we have the Virgo sample, which is constituted by 9 dwarf ETGs. All of them have been classified as having disk substructures. To construct the sample, the dwarf ETGs were hand-picked based on the presence of disk substructures from a series of other candidates that also showed substructures (Lisker et al. 2006c). As such, this sample constitutes only a partial selection of the whole population of dwarf ETGs with substructure features that are found in the Virgo cluster. On the other hand, we have the Fornax sample, constituted by 23 dwarf ETGs. We have classified 9 of them as having disk substructures, and the remaining 14 of them as having clump substructures. To construct the sample, we included all of the dwarf ETGs in which we could detect some kind of substructures, by taking into consideration the complete dwarf population (564 dwarfs, according to the FDSDC; Venhola et al. 2018) of the Fornax cluster. Therefore, this sample aims to be a more complete selection of all the dwarf ETGs with substructure features that are part of the Fornax cluster.

For comparison purposes, we further divide our two samples into three subsamples: the disky dwarf ETGs of Virgo, the disky dwarf ETGs of Fornax, and the clumpy dwarf ETGs of Fornax. We will refer to them as the disky-Virgo, disky-Fornax, and clumpy-Fornax subsamples, respectively. In Table 5.3, we provide the main photometric and structural properties of the two dwarf ETG samples, separated by cluster environment (Virgo or Fornax) and then further separated by substructure category (disky or clumpy). This Table also summarizes the results obtained through the residual method.

► Photometric properties.

Let us first compare the photometric properties of the two dwarf ETG samples. Overall, the Virgo sample is in average brighter than the Fornax sample, but only by a fraction of a magnitude. The disky-Virgo subsample has a median r-band absolute magnitude of about -17.6 mag, while both the disky-Fornax and clumpy-Fornax subsamples have a median value of about -17.5 mag. Despite this similarity, the Fornax sample encompasses a wider range of magnitudes, both towards the bright end and the faint end; however, this is specially notorious on the faint end, with the faintest Fornax dwarf ETG being almost 2 whole magnitudes fainter than the faintest Virgo dwarf ETG (the actual number being 1.8 magnitudes). Within the Fornax sample, the clumpy-Fornax subsample reaches fainter magnitudes than the disky-Fornax subsample.

In terms of surface brightness, the disky dwarf ETGs have significantly brighter centers than the clumpy dwarf ETGs. The disky-Virgo and disky-Fornax subsamples have a median central r-band surface brightness of about 19.3 and 18.7 mag arcsec^{-2}, respectively. In contrast, the clumpy-Fornax subsample has a fainter median value of 20.1 mag arcsec^{-2}. However,

Table 5.3: Comparison of the dwarf ETG properties of the Virgo and Fornax samples.

Dwarf ETG Properties	Virgo Sample	Fornax Sample	
	Disky	Disky	Clumpy
(1)	(2)	(3)	(4)
Absolute magnitude, r band (mag)	-17.62 $[-16.67, -18.34]$	-17.45 $[-15.77, -18.68]$	-17.47 $[-14.85, -18.35]$
Central surface brightness, r band (mag arcsec^{-2})	19.28 [19.85, 18.77]	18.69 [20.69, 17.56]	20.06 [22.27, 18.43]
Effective surface brightness, r band (mag arcsec^{-2})	22.36 [23.22, 21.81]	21.64 [22.84, 20.08]	22.18 [23.90, 21.16]
$g - r$ color (mag)	0.62 [0.58, 0.69]	0.64 [0.60, 0.76]	0.57 [0.51, 0.66]
Angular effective radius (arcsec)	20.99 [12.93, 30.13]	14.64 [7.60, 17.03]	14.59 [6.75, 24.30]
Physical effective radius (kpc)	1.68 [1.04, 2.41]	1.42 [0.74, 1.65]	1.41 [0.65, 2.36]
Axis ratio at 1 R_e isophote	0.76 [0.59, 0.93]	0.52 [0.29, 0.94]	0.65 [0.30, 0.89]
Axis ratio at 2 R_e isophote	0.88 [0.61, 0.94]	0.49 [0.30, 1.00]	0.64 [0.26, 0.92]
Residual light fraction within 1 R_e (%)	3.1 [1.7, 6.8]	3.7 [2.9, 5.7]	5.7 [3.7, 20.8]
Residual light fraction within 2 R_e (%)	3.5 [2.2, 6.4]	5.1 [4.5, 6.3]	6.0 [4.5, 16.9]
Sérsic index n of diffuse component	1.43 [1.15, 2.02]	1.61 [1.04, 2.20]	1.16 [0.60, 2.28]

Note. — Col. (1): properties of the dwarf ETG samples, with the units given in parenthesis. In the following columns, we provide the median value, with the range given in square brackets. Col. (2): values for the Virgo dwarf ETG sample (presented in Chapter 3). The substructures of the whole sample have been classified as disky. The residual light fraction measurements and all of the structural parameters are derived from white-band imaging. We assume $g - r$ colors integrated within two effective radii by Janz & Lisker (2008, 2009). When required, we adopt a Virgo cluster distance of 16.5 Mpc (Blakeslee et al. 2009). Cols. (3) and (4): values for the Fornax dwarf ETG sample (presented in Chapter 4). The substructures of the sample have been classified either as disky or clumpy. The residual light fraction measurements and all of the structural parameters are derived from r-band imaging. The angular effective radii and total apparent magnitudes (used to derive the total absolute magnitudes and total $g - r$ colors) are taken from the FDSDC (Venhola et al. 2018). When required, we adopt a Fornax cluster distance of 20.0 Mpc (Blakeslee et al. 2009).

their effective measurements are much more comparable than their central measurements, with the three subsamples having a median effective r-band surface brightness in the order of 22 mag arcsec^{-2}.

In regards to color, the Virgo and Fornax dwarf ETG samples are, by construction, red in global color ($g - r \geq 0.5$ mag). We observe that the disky dwarf ETGs have slightly redder average colors than the clumpy dwarf ETGs. The disky-Virgo and disky-Fornax subsamples have a median $g - r$ color of 0.62 and 0.64 mag, respectively. Meanwhile, the clumpy-Fornax subsample has a bluer median value of 0.57 mag. Additionally, the reddest dwarf ETGs are part of the disky subsamples, while the bluest dwarf ETGs are found in the clumpy subsample.

In summary, the main differences in terms of photometry are not found by comparing the dwarf ETGs of the Virgo and Fornax clusters, but instead by comparing their disky and clumpy populations. In general, the disky dwarf ETGs encompass a brighter magnitude range, have a brighter central surface brightness, and display redder colors. In contrast, the clumpy dwarf ETGs can reach fainter magnitudes, have a fainter central surface brightness, and display comparatively bluer colors. We note that the fact that the Fornax sample is able to reach fainter magnitudes than the Virgo sample may be simply due to a selection bias of the latter. As mentioned earlier, the Virgo sample was built by choosing only 9 particular dwarf ETGs in which the substructure features appeared clear and bright, while the Fornax sample was built by selecting all of the dwarf ETGs with substructures we found in the Fornax cluster, including even the least impressive and faint cases.

► Structural properties.

We now address the structural properties of the two dwarf ETG samples. We first consider the effective radius, which can be used as a proxy of the galaxy size. For a fair comparison, we translate the angular measurements into physical (or linear) measurements, by assuming a Virgo cluster distance of 16.5 Mpc and a Fornax cluster distance of 20.0 Mpc (Blakeslee et al. 2009). Overall, we find that the Virgo dwarf ETGs have larger physical sizes than the Fornax dwarf ETGs. While the disky-Virgo subsample has a median effective radius of about 1.7 kpc, both the disky-Fornax and clumpy-Fornax subsamples have a smaller median value of about 1.4 kpc. This can be understood by the fact that the Fornax sample includes dwarf ETGs that have effective radii as small as 0.7 kpc, while in contrast the smallest dwarf ETG in the Virgo sample has an effective radius of about 1.0 kpc.

In regards to the shape of the dwarf ETGs, we use the axis ratio as a proxy. An axis ratio of 1 means that the galaxy is perfectly circular in projection, while an axis ratio $\ll 1$ indicates that the galaxy is highly elliptical. On a first instance, we find that within a given subsample, the median axis ratio does not significantly change if measured at either the isophote at one or two effective radii (R_e). The main differences, instead, are found when we compare the subsamples against each other. The disky-Virgo subsample is by far the roundest in appearance, with a median axis ratio of about 0.8 at 1 R_e and 0.9 at 2 R_e. In contrast, the disky-Fornax subsample is highly elliptical, with a median axis ratio of about 0.5 both at 1 and 2 R_e. The clumpy-Fornax subsample is in between these two, with a median axis ratio of 0.7 at 1 R_e and

0.6 at 2 R_e.

In summary, the structural differences we find are in part due to the selection bias that is also affecting some of the photometric properties (see previous Section). On the one hand, the dwarf ETGs of the Virgo sample were selected in particular for displaying clear and bright disk substructures. As such, they are in average larger in size and rounder in projected appearance, as the face-on orientation is ideal for recognizing spiral arm features. On the other hand, the Fornax sample encompasses all possible Fornax dwarf ETGs with substructure features. As such, we were able to include the smaller and less spectacular dwarf ETGs that still showed some substructures. As a result, the Fornax sample presents more diverse structural properties, covering a wider range of sizes and axis ratios than the Virgo sample. Interestingly, within the Fornax sample, the disky subsample is on average more elliptical (i.e., has a smaller axis ratio) than the clumpy subsample. This is a reflection of the fact that the disky-Fornax subsample is mainly constituted by edge-on disks, giving the galaxies a highly elongated appearance. No spiral arm features were observed, an important fact that we will explore later in Section 5.3.3.

► Residual properties.

The main result obtained through the application of the residual method is the measurement of the residual light fraction (RLF), which represents the relative contribution of the substructure light to the total light of a galaxy. For the disky-Virgo subsample, we measure a median RLF of 3.1% within 1 R_e and 3.5% within 2 R_e. Then, for the disky-Fornax subsample, we measure a median RLF of 3.7% within 1 R_e and 5.1% within 2 R_e. Finally, for the clumpy-Fornax subsample, we measure a median RLF of 5.7% within 1 R_e and 6.0% within 2 R_e. We note that the aforementioned measurements were performed in the white band for the Virgo sample, and in the r band for the Fornax sample[1]. As such, they may not be completely comparable. Thus, we cautiously carry out the following three main observations: *(1)* the median relative contribution of the substructures to the total galaxy light is always larger within 2 R_e than within 1 R_e; *(2)* the clump substructures are brighter than the disk substructures; and *(3)* the disk substructures in Fornax are comparatively brighter than the disk substructures in Virgo. Overall, one thing is clear: both the disk and clump substructures embedded in dwarf ETGs are extremely faint features, and contribute a very small fraction of the total galaxy light (typically less than 10%).

Once we isolated the substructure component from the diffuse component of the dwarf ETGs by using the residual method, we characterized their diffuse galaxy light by fitting it with a Sérsic profile (Sérsic 1968). We find that the average Sérsic index n of the diffuse component is mostly consistent with the one of an exponential disk profile ($n = 1$). The disky-Virgo subsample has a median Sérsic index n of about 1.4. Similarly, the disky-Fornax and clumpy-Fornax subsamples have a median n of about 1.6 and 1.2, respectively. Although it is

[1]RLF measurements for the Fornax sample were carried out in the g and r bands (see Section 4.3.2). However, as the g band is particularly sensitive to young stellar populations, we believe that the r-band measurements of the Fornax sample provide a fairer comparison to the bolometric white-band measurements of the Virgo sample.

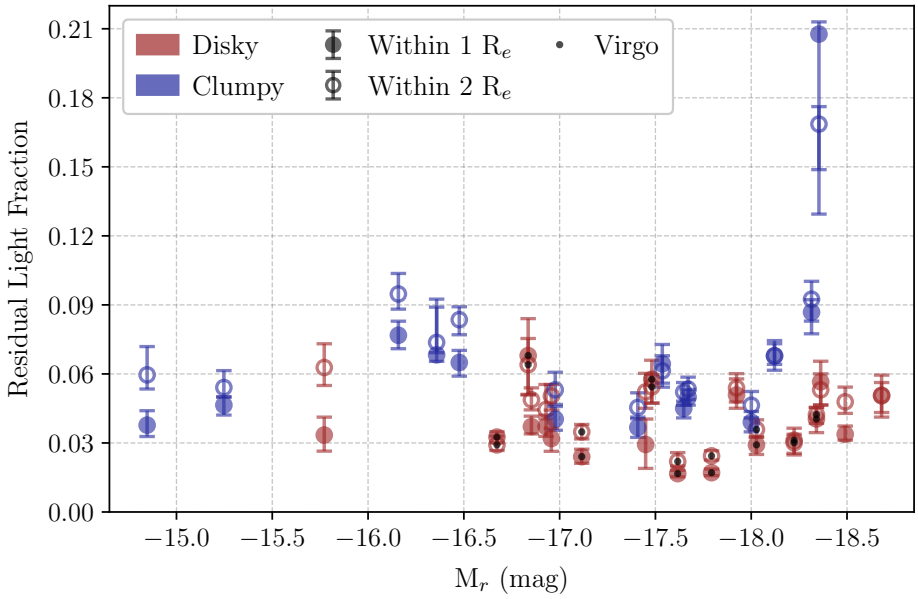

Figure 5.1: Residual light fractions as a function of the total r-band absolute magnitude of the Virgo and Fornax dwarf ETG samples. Galaxies classified as disky are shown as red points, while galaxies classified as clumpy are shown as blue points. The Virgo sample has been classified as disky, and is highlighted by small black points. The measurements are performed within one and two effective radii of the galaxies, represented by filled and empty circles, respectively. The error bars are given by the 16th and 84th percentiles of the distributions. The residual light fractions of the Virgo and Fornax samples are derived from white-band and r-band imaging, respectively.

not a significant difference, the diffuse light of the disky dwarf ETGs tends to have slightly larger Sérsic indices compared to the clumpy dwarf ETGs.

As a way to visualize our main results, in Figure 5.1 we plot the residual light fraction versus the total r-band absolute magnitude of the dwarf ETGs in the Virgo and Fornax samples. We highlight our main result: the clump substructures tend to contribute more to the total galaxy light than the disk substructures; i.e., the former are, in relative terms, brighter than the latter. Therefore, on the plot, the blue data points are on average further up on the y-axis than the red data points. This behavior is observed across the whole brightness range covered by our samples. However, even though our dwarf ETGs span a range of almost four magnitudes in brightness, we find no significant trends between their residual light fraction and their total absolute magnitude, with the relation being mostly flat (excluding the outlier galaxy D26D000, located at the top right of the plot). In other words, independent of how bright a galaxy is, the substructure features tend to contribute about the same fractional amount to the total galaxy brightness, typically between $2 - 10\%$ —at least, in the dwarf ETG regime that we have studied.

Our main results can be seen under a different perspective in Figure 5.2, where we plot the residual light fraction versus the total $g-r$ color of the dwarf ETGs in the Virgo and Fornax samples. We can clearly appreciate that disk substructures are found in dwarf ETGs that tend to have redder colors, while clump substructures are found in dwarf ETGs that tend to have comparatively bluer colors (or, better put, "less red" colors, as they still have a $g - r \geq 0.5$

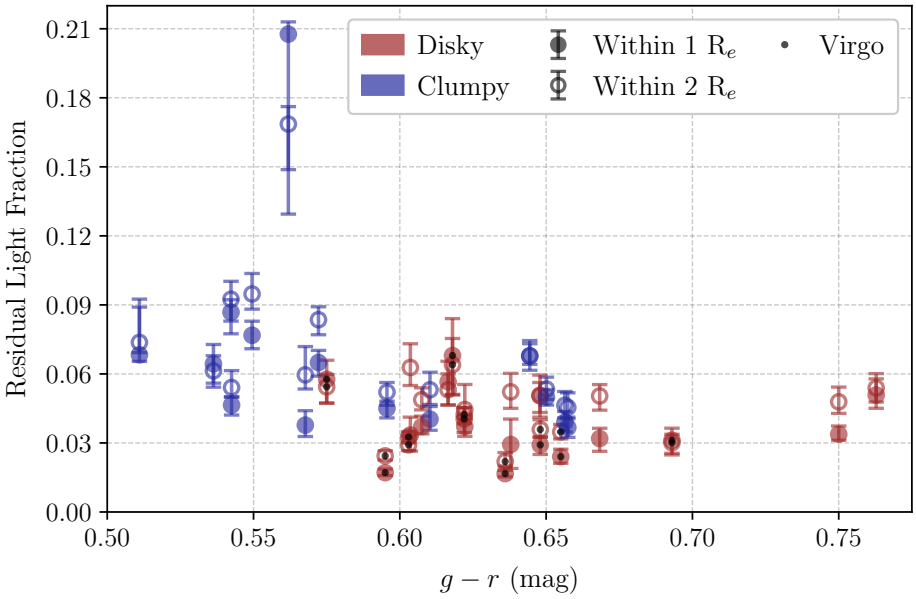

Figure 5.2: Residual light fractions as a function of the total $g-r$ color of the Virgo and Fornax dwarf ETG samples. Galaxies classified as disky are shown as red points, while galaxies classified as clumpy are shown as blue points. The Virgo sample has been classified as disky, and is highlighted by small black points. The measurements are performed within one and two effective radii of the galaxies, represented by filled and empty circles, respectively. The error bars are given by the 16th and 84th percentiles of the distributions. The residual light fractions of the Virgo and Fornax samples are derived from white-band and r-band imaging, respectively. For the Virgo sample, we assume $g-r$ colors integrated within two effective radii by Janz & Lisker (2008, 2009).

mag). There appears to be a weak correlation between the residual light fraction and the $g-r$ color of the host galaxy, with the RLF tending to increase with smaller (i.e. bluer) $g-r$ colors. Considering all dwarf ETGs together, we find a Pearson correlation coefficient of $r=-0.38$ ($r=-0.44$) and a p-value $=3\times10^{-2}$ (p-value $=1\times10^{-2}$) for the one and two effective radii measurements, respectively. However, things change if we consider the disky and clumpy subsamples separately. The disky subsample (red data points) shows no meaningful correlations. In contrast, the clumpy subsample (blue data points) shows a weak correlation, with a Pearson correlation coefficient of $r=-0.44$ ($r=-0.53$) and a p-value $=4\times10^{-2}$ (p-value $=1\times10^{-2}$) for the one and two effective radii measurements, respectively. This leads us to conclude that the bluer ("less red") the host galaxy is, then the larger the fraction that their clump substructures will contribute to the total galaxy light, thus increasing the relative brightness of their clumps (i.e., the RLF). In contrast, the relative amount of light contributed by disk substructures is mostly insensitive to the color of their host galaxy. The implications of these differences between the disk and clump substructures are addressed in the upcoming Section 5.3.3.

5.3.2 Link to Simulations

As follows, we briefly introduce the work we carried out in Smith et al. (2021). We aimed to answer the following question: can tidal harassment induced by the cluster environment trigger the formation of disk substructures (such as bars and spiral arms) in dwarf galaxies?

For this purpose, in Smith et al. (2021) we present high-resolution numerical simulations of dwarf systems that are being subjected to tidal harassment by a galaxy cluster potential. On the one hand, the galaxy cluster corresponds to a Virgo-like, time-evolving analytical model, in which the tidal fields of the main cluster halo and of the individual galaxy halos have been extracted from a cosmological simulation and replaced by analytical potentials. On the other hand, the model galaxies being thrown into the cluster potential are constituted by particles that inhabit a Navarro-Frenk-White (NFW; Navarro et al. 1996) dark matter halo and a stellar exponential disk (i.e., there are stellar particles and there are dark matter particles).

This study focuses on the conditions under which disk features are triggered in the stellar disk of the model galaxies. We conclude that two main factors influence the formation and evolution of disk features: *(1)* how plunging the orbit is in which the model galaxy falls into the cluster, and *(2)* the level of rotational support of the stellar disk. As the main result, we find that disk features form in galaxies that experience close pericenter passages to the cluster core and that have a component of their stellar disk that is highly rotationally supported. Notably, the wide range of disk features exhibited by these simulated galaxies closely resemble the appearance of the disk features we detect in our observational dwarf ETG sample (which corresponds to our Virgo sample, see Chapter 3). Thus, we formulate the hypothesis that the disk substructures present in our dwarf ETG sample could have been tidally triggered by the Virgo cluster potential.

While it has been found that dwarf ETGs can indeed be rotationally supported (Toloba et al. 2009), they usually have low to medium rotational support, which contradicts the high rotational support demanded by our simulations. Therefore, for the tidal triggering of disk features to be possible, at least a fraction of the light of the galaxy is required to be in the form of a thin, dynamically cold stellar disk, while the remaining light can be in the form of a thick, dynamically hot stellar disk. To test this conjecture, in Smith et al. (2021) we constructed a mixed galaxy model, in which 20% of the stellar mass is in a thin disk component and 80% is in a thick disk component. We find that, while the thick disk component remains featureless, the thin disk component is still sensitive to the cluster potential and reacts to it by forming disk features. Consequently, it is plausible that our observed Virgo dwarf ETGs could have a faint, thin disk component embedded in a much brighter, thick disk component. If the two components were to share similar properties, such as their overall color, then they would be mostly indistinguishable under normal, non-harassment circumstances, as both would be smooth in appearance. Therefore, we propose that the thin disk component could reveal itself through the formation of disk features, such as bars and spiral arms, that are triggered when the galaxy is subjected to harassment along a plunging orbit.

Taking into consideration the color-magnitude, spatial, and phase-space distribution of our Virgo dwarf ETG sample (refer to Figure 3.3), the aforementioned hypothesis is plausible. Our dwarf ETGs have red optical colors and color gradients, and lie on the red sequence of the Virgo cluster. Thus, they show no evidence of recent star formation, at least based on their shallow SDSS colors. The projected spatial distribution of our dwarf ETGs shows that they are spread across the cluster, while their phase-space distribution shows that they have low velocities

relative to the cluster, with most of them being consistent with having passed through the cluster core at least once. Together, this sustains a picture in which these galaxies could have been heavily transformed by the environment: first through pre-processing in galaxy groups and then through their infall into the Virgo cluster, their star formation was quenched and their morphology was altered, leaving them with red colors, most of their thin disk converted into a thick disk, and possibly triggering disk features in their remaining thin disk.

In conclusion, there are two main formation scenarios that could explain the presence of faint disk substructures embedded in our Virgo dwarf ETGs: *(1)* their disk substructures are remnants of a previous life away from the cluster environment, or *(2)* they are instead the signatures of a new life given by the cluster environment. In the first scenario, these dwarf ETGs may have been dwarf LTGs (e.g., dwarf spiral galaxies) in the past, and environmentally-driven processes (see Section 1.2.2) induced by the cluster environment quenched their star formation and caused most of their disk features to fade and redden with time. In the second scenario, these dwarf ETGs may have been initially featureless, but with a part of their stellar component contained in the form of a thin and highly rotationally supported disk. Upon falling into the Virgo cluster, the tidal force of the cluster potential may have triggered the formation of disk features, such as bars and spiral arms, on their rotation-supported component. While our work in Smith et al. (2021) investigates and supports this second formation scenario, it certainly does not exclude the possibility of the first scenario having taken place.

5.3.3 Formation and Evolution Scenarios

Finally, we attempt to constrain the possible formation and evolution scenarios of the dwarf ETG population with embedded substructure features. For this purpose, we consider the results obtained for our two dwarf ETG samples, separated by cluster environment (Virgo or Fornax) and by substructure category (disky or clumpy). First, we consider the different cluster environments, so we compare the disky-Virgo subsample with the disky-Fornax subsample. Then, we consider the different substructure types, so we compare the disky-Virgo and disky-Fornax subsamples with the clumpy-Fornax subsample. In both cases, we aim to answer the question: how can the observed differences explain the formation and evolution of substructure features?

► **Environmental differences: Virgo cluster vs. Fornax cluster.**
(disky-Virgo vs. disky-Fornax subsamples).

We begin by stating the fact that the fraction of dwarf ETGs that have disk substructures is moderately larger in the Virgo cluster than in the Fornax cluster. As part of the analysis of our Fornax dwarf ETG sample (see Section 4.3.2), we showed how the "disk fraction" is dependent on the galaxy brightness, steeply decreasing as the dwarf ETGs become fainter. As illustrated in the bottom panel of Figure 4.16, we find that the disk fraction of the Fornax dwarf ETGs can be as high as 40% $(2/5)$ on the bright galaxy end, dropping to a low 5% on the faint galaxy end; where we define the location of the faint end as three magnitudes away from the bright end. In comparison, while Lisker et al. (2006c) observe that the same overall behavior

is followed by the disky dwarf ETGs of the Virgo cluster, they find a comparatively higher disk fraction. As shown in the top panel of Figure 12 of Lisker et al. (2006c), the disk fraction of the Virgo dwarf ETGs corresponds to about 60% $(3/5)$ on the bright end, dropping to 5% once reaching the faint end (which we again define to be three magnitudes away). This means that dwarf ETGs with disk substructures are in relative terms more numerous in Virgo compared to Fornax.

The second important fact is that while spiral arms are a common sight among the types of disk substructures found in the dwarf ETGs of the Virgo cluster, we fail to find any clear spiral arms in the disky dwarf ETGs of the Fornax cluster. Out of the 564 Fornax dwarf galaxies catalogued by the FDSDC (Venhola et al. 2018), we find 23 dwarf ETGs with substructure features (our Fornax sample), of which we classify 9 as having disk substructures. However, all of them appear to be edge-on disks (see Figures 4.6 and 4.12); some unperturbed, and some a bit warped, with only one case showing a ring-like feature (dwarf galaxy F19D001). We can firmly confirm that we do not find any spiral arm features within our disky-Fornax dwarf ETGs. Interestingly, there are two clumpy-Fornax dwarf ETGs that do show subtle hints of very broad spiral arms (dwarf galaxies F04D053 and F26D000, see Figure 4.7). However, their spiral arms are so wide and faint that they do not show up in our residual analysis. In any case, these clumpy-Fornax cases fall out of the scope of the comparison we are trying to make with the disky-Virgo sample. In stark contrast, all 9 disky dwarf ETGs that constitute our Virgo sample show spiral features in some form, while several more cases have been reported to exist in the Virgo cluster (Lisker et al. 2006c).

Could this difference between the two clusters be a simple matter of bad luck, where all of the disky-Fornax dwarf ETGs with spiral arms are orientated edge-on along our line of sight, effectively hiding their spiral arms from us and adopting the appearance of elongated disks? We believe this would be too much of a coincidence to be a reasonable explanation. We also dismiss the possibility that this difference is an artificial by-product of the different data quality of our Virgo and Fornax samples. As we carefully addressed in Section 5.2, the better resolution and shallower depth of the Fornax data compared to the Virgo data is not fundamentally hindering our ability to detect substructure features of any kind, including spiral-like features. Based on our tests and calculations, we should be able to detect substructures of similar brightness and appearance as the ones observed in our Virgo sample.

These fundamental differences between the disky dwarf ETG populations of the Virgo and Fornax clusters can help us constrain the origins of their disk substructures. To begin with, the Virgo cluster is very massive ($\sim 10^{14}$ $M_{\odot}$), so large-scale gravitational processes such as galaxy-cluster harassment should be very efficient[2]. Therefore, it is plausible that a fraction of the disk features found in the Virgo dwarf ETGs, like bars and spiral arms, had their formation triggered by the tidal interaction with the deep cluster potential. This scenario is explored and supported by the simulations of Smith et al. (2021), which we introduced in Section 5.3.2. In comparison, the Fornax cluster is less massive ($\sim 10^{13}$ $M_{\odot}$), so its shallower cluster potential is

[2]For a refresh on environmentally-driven processes, refer to Sections 1.2.2 and 5.1.2. We described and compared the properties of the Virgo and Fornax clusters in Section 5.1.

only able to exert a comparatively weaker tidal force. As a consequence, while the formation of disk features in dwarf ETGs triggered by galaxy-cluster harassment can still occur in Fornax, it is far less likely to happen than in Virgo. This can help to explain the lack of spiral arm substructures in the disky-Fornax dwarf ETGs.

In addition, the Virgo cluster has a dense and hot intergalactic medium (IGM), making short-timescale hydrodynamical processes such as ram-pressure stripping and thermal evaporation very efficient. It is possible, therefore, that a fraction of the disky-Virgo dwarf ETGs constitute a transition population, caught in the transformation from star-forming dwarf LTGs to non-star-forming dwarf ETGs. As such, some of the faint disk substructures that we observe in the Virgo dwarf ETGs could be remnants of their previous life as dwarf spiral galaxies. With the quenching of star formation, the bars and spiral arms have become red in color and are slowly fading away. In comparison, the Fornax cluster has a comparatively sparser and colder IGM, thus making it less capable of inducing gas-stripping processes in an efficient way. While these processes can still happen in Fornax, we would expect to observe the transitional stage of dwarf LTGs into dwarf ETGs more frequently in Virgo. This can help to explain the larger ratio of disky-Virgo to disky-Fornax dwarf ETGs.

Being dynamically young, the Virgo cluster is in the process of assembly, containing a larger fraction of star-forming LTGs compared to the Fornax cluster. This means that many of the dwarf LTGs in Virgo should be currently experiencing environmentally-driven processes, which are accelerating their transition into dwarf ETGs. Consequently, we should be more likely to catch them in the process of transition, which can help to explain the large population of dwarf ETGs with embedded disk substructures found in Virgo. In contrast, the Fornax cluster is dynamically older, being more relaxed and containing a larger fraction of non-star-forming ETGs compared to the Virgo cluster. Therefore, we can assume that most of its dwarf LTGs have already transitioned into dwarf ETGs. As such, this should make it harder (and thus less probable) for us to catch the dwarf LTG to dwarf ETG transformation process in action in the Fornax cluster compared to Virgo.

In summary, we have found that the Virgo cluster has a larger fraction of dwarf ETGs with disk substructures, with an abundance of embedded spiral arm features. In contrast, the Fornax cluster has a smaller fraction of dwarf ETGs with disk substructures, with a complete absence of embedded spiral arm features. As addressed, we believe that these findings are a reflection of the environmental differences between the Virgo and Fornax clusters, which can convincingly explain the origin of the observed differences between their respective disky dwarf ETG populations.

► **Substructural differences: disk substructures vs. clump substructures.**
(disky-Virgo and disky-Fornax vs. clumpy-Fornax subsamples).

We now address the differences that distinguish disk substructures from clump substructures in dwarf ETGs as a way to constrain their origins. First, we confront the fact that disky and clumpy dwarf ETGs have different photometric and structural properties (see previous Section 5.3.1). By carefully taking into consideration possible biases introduced by the different con-

struction of our Virgo and Fornax samples, we can state with certainty the following. Disky dwarf ETGs tend to encompass a brighter magnitude range, have a brighter central surface brightness, have redder global $g-r$ colors, and can span a wide range of axis ratios (from circular face-on spiral galaxies to highly elliptical edge-on disks). In comparison, clumpy dwarf ETG tend to encompass a wider magnitude range that can reach fainter magnitudes, have a fainter central surface brightness, have bluer ("less red") global $g-r$ colors, and appear to span a smaller range of axis ratios.

The second fact is that disky and clumpy dwarf ETGs also have different residual properties (again addressed in Section 5.3.1, and illustrated in Figures 5.1 and 5.2). Disk substructures tend to contribute a smaller fraction of the total galaxy light (i.e., have smaller RLFs), their relative contribution is independent from the $g-r$ color of their host galaxy (i.e., flat distribution), and are found in galaxies with redder global $g-r$ colors. In comparison, clump substructures tend to contribute a larger fraction of the total galaxy light (i.e., have larger RLFs), their relative contribution increases with bluer ("less red") $g-r$ colors of their host galaxy (i.e., negative correlation with color), and are found in galaxies with bluer ("less red") global $g-r$ colors.

It seems that many of the characteristics that distinguish disky from clumpy dwarf ETGs involve the color parameter. Therefore, we propose that these color-driven differences could be a reflection of the different star formation histories of the disky and clumpy dwarf ETGs. On the one hand, the clump substructures in dwarf ETGs are revealed as irregular light overdensities that have the appearance of star forming regions (refer to Figures 4.6 and 4.12). As supported by the results of our color analysis in Section 4.4, the clump substructures are in average bluer, and therefore they also are probably younger than the rest of the main body of their host galaxy (refer to Figures 4.17 and 4.20). As such, these clumpy regions could still be forming stars at a very low rate (low enough as to maintain an overall red $g-r$ galaxy color), or alternatively they could have ceased forming stars not that long ago. We believe that this may be the reason why the clump substructures appear in relative terms brighter (i.e., larger RLF) as the global galaxy color becomes bluer, as younger stellar populations are more luminous than older ones. On the other hand, the disk substructures in dwarf ETGs display in general (although not always) a $g-r$ color that is as red as the diffuse light of the galaxy (refer to the upper panel of Figure 4.18). Having a similar color may be an indication that some disk substructures could be as old as the main body of their host galaxy. Consequently, a considerable fraction of disky dwarf ETGs must have ceased forming stars long ago, while a small remaining fraction may be still forming stars in their disk features at a very low rate, or ceased to do so only recently.

Despite this hypothesized difference in their star formation histories, the formation of both disky and clumpy dwarf ETGs can be easily explained through the environmental transformation scenario (refer to Section 1.3.2). In this scenario, these galaxies were originally star-forming dwarf LTGs. Upon their first infall into their host cluster, they began to experience a gradual environmentally-induced transformation into non-star-forming dwarf ETGs. As such, dwarf spiral galaxies could be the progenitors of dwarf ETGs with disk substructures, and likewise dwarf irregular galaxies could be the progenitors of dwarf ETGs with clump

substructures. However, we believe that their transformation is not yet complete, which is why we can still observe faint substructure features embedded in them. Therefore, the dwarf ETG population with substructure features can be understood as a transition population (i.e., transition-type dwarf galaxies), caught in the late-to-early-type transformation: while some of their properties associate them with LTGs (e.g., their substructures features, sometimes bluer than the main body of their galaxy and possibly still forming some stars), other properties associate them with ETGs (e.g., their global red colors and overall diffuse appearance).

The different star formation histories of disky and clumpy dwarf ETGs could then be an indication that they are currently at different stages of their transition process. Disky dwarf ETGs, which tend to have redder $g-r$ colors and smaller RLFs, could be first place in the race of becoming early-types. In contrast, clumpy dwarf ETGs, which tend to have comparatively bluer $g-r$ colors and larger RLFs, could be lagging behind, being instead closer to their late-type progenitors. The projected spatial distribution of the disky and clumpy dwarf ETGs of the Fornax cluster supports this conjecture (see Figure 4.11). While most of the disky dwarf ETGs are found within the projected virial radius of Fornax, most of the clumpy dwarf ETGs are instead notoriously found outside this radius. Although this is just a projected view, it can still serve as an indication that the disky dwarf ETGs have been part of the Fornax cluster for a longer time in average than their clumpy counterparts. As a result, the cluster environment and its environmentally-induced processes have had more time to impact and transform the properties of the disky population compared to the clumpy population of dwarf ETGs.

We would like to note that while it appears that most of the disky and clumpy dwarf ETGs are at different evolutionary stages, there is still some overlap. As shown in Sections 4.3 and 4.4, we find disky and clumpy cases that have comparable properties, such as their RLFs and colors. Therefore, the two substructure categories are not divided by a razor-sharp boundary; instead, there is a region in parameter space that they share. This may be an indication that some disky and clumpy dwarf ETGs may have experienced similar evolutionary histories. In these cases, the rest of the properties that still differentiate them (e.g., the fact that they have either disk or clump features, or a certain axis ratio, or a certain luminosity) have more to do with nature than with nurture. In other words, with what they were in the past, before becoming part of the cluster environment. If disky dwarf ETGs originate from dwarf spirals, and clumpy dwarf ETGs from dwarf irregulars, then it is to be expected for them to fundamentally differ in some of their photometric and structural parameters.

As a closing remark, there is an additional scenario that can explain the origin of disky dwarf ETGs, but not of clumpy dwarf ETGs. It is possible that through the tidal interaction between a dwarf galaxy and the potential well of its host cluster, disk features are tidally triggered. Based on the simulations described in Section 5.3.2, initially featureless dwarf ETGs could potentially form disk features as long as they have a small fraction of their stars in the form of a thin and highly-rotationally supported disk, and follow a plunging orbit that passes near to the cluster core. This formation scenario could help to explain why we find many disk features in dwarf ETGs that are the same color as the main body of their galaxy. In this case, their disk features are not remnants of a star-forming past, where they are fading to

red from bluer colors, but instead they are already as red as the thin stellar disk from which they originated. However, while high-resolution numerical simulations show that the tidal harassment scenario can explain the formation of disk features such as bars, spiral arms, and rings, it cannot induce the formation of clump features (Kwak et al. 2019; Smith et al. 2021). As such, this scenario is limited to explain the existence of a part of the disky dwarf ETG population, but not of the clumpy dwarf ETG population.

In summary, we believe that the origin of the dwarf ETG population with substructure features found in galaxy clusters, such as Virgo or Fornax, can be satisfactorily explained through environmentally-induced processes. As our main hypothesis, we propose that dwarf ETGs with disk or clump substructures could constitute a transition population (i.e., transition-type dwarf galaxies), caught in the environmentally-driven transformation from star-forming dwarf LTGs to non-star-forming dwarf ETGs. The characteristic properties that distinguish the disky population from the clumpy population could be a reflection of their different evolutionary histories, suggesting that they are at different stages in their late-to-early-type transition process. Complementary to this transformation scenario, a fraction of dwarf ETGs with disk substructures could have already been ETGs, and the cluster environment, instead of contributing to the gradual erasure of these features, could have tidally triggered their formation. In conclusion, through our study of the different substructure features embedded in dwarf ETGs, we have been able to establish that the cluster environment must play a major role in shaping and transforming the dwarf galaxy population in galaxy clusters.

6

Conclusions

In this Thesis work, we have studied the population of dwarf early-type galaxies (ETGs) with embedded substructure features. We have considered two different environments, the Virgo and Fornax galaxy clusters; and two types of substructure features, disk-like and clump-like substructures. As follows, we provide a summary of the contents of each Chapter and their main findings and results in Section 6.1, and draw our main conclusions in Section 6.2.

6.1 Summary

► Chapter 1: "Introduction: Dwarf Early-Type Galaxies".

In the introductory Chapter, we introduced our objects of study, dwarf ETGs. To characterize them, we began by presenting their main photometric, structural, and dynamical properties.

Photometrically, dwarf ETGs have a faint luminosity and low surface brightness, with a general lack of star formation, and a low gas and dust content. As such, they typically have red global colors and belong to the red sequence of galaxies. They can have radial color gradients, reddening outwards, and sometimes even have blue cores, suggesting that some could be still forming stars at their central regions. They can also span a wide range of ages and metallicities.

Structurally, dwarf ETGs have small intrinsic sizes. They can host nuclei at their centers, with the nucleation fraction increasing with galaxy brightness. They tend to have featureless and smooth surface brightness profiles, which can be typically characterized by a single Sérsic function with a small Sérsic index. However, they can also be structurally more complex, requiring more than one function to describe them, and can even present embedded

substructure features, like the ones we study in this work.

Dynamically, dwarf ETGs tend to be dispersion supported, although they can also show various degrees of rotational support. They have low stellar masses. Their dynamical masses suggest that a large fraction of their mass is constituted by dark matter.

We then described the variety of environments dwarf ETGs can be found in, including the field, galaxy groups, and galaxy clusters. While they are extremely rare in low-density environments, they are by far the most common type of galaxy in high-density environments. They can experience a wide range of environmentally-driven processes, which we described and categorized into small-scale gravitational processes (galaxy-galaxy harassment, galaxy mergers), large-scale gravitational processes (galaxy-cluster harassment), short-timescale hydrodynamical processes (ram-pressure stripping, turbulent viscous stripping, thermal evaporation), and long-timescale hydrodynamical processes (starvation or strangulation). Due to their shallow potential wells, dwarf ETGs can be strongly influenced by these environmental processes during their lifetime.

We proceeded to address the possible formation scenarios of dwarf ETGs. The hierarchical structure formation scenario proposes that they were formed by gradual accretion events, while the environmental transformation scenario proposes that the environment has shaped them into what they are today. These scenarios are not mutually exclusive, and are probably required to work in unison in order to be able to explain the complete population of dwarf ETGs.

We then focused on the sub-population of dwarf ETGs with embedded substructure features, which we study in this work. We categorized their substructures into two types: disk-like features, such as bars, spiral arms, and edge-on disks; and clump-like features, such as irregular light overdensities, star forming regions, and dust lanes. We reported the findings in the literature, and the approaches that have been taken in order to detect and quantify these substructures. We described these different approaches, which included the unsharp masking, galaxy modeling, and Fourier analysis techniques. We used aspects of these three techniques in the course of this work.

► **Chapter 2: "Residual Method for the Extraction of Substructures".**

This Chapter described the "residual method", a new procedure that we developed in this work that aims to robustly identify and extract the substructure features embedded in a galaxy image. We began by introducing the concept behind it. The method consists in an iterative procedure that gradually separates a galaxy image into two components: the bright, dominant, diffuse component, and the much fainter, underlying substructure component. We then provided a detailed step-by-step description of the method. We specified the software used, and the particular tasks that are needed to be run in each step.

We then explained the parameter configuration of the residual method. First, we described the basic parameters, which can be expected to work well independently from the science case the method is being applied to. We then addressed the more complex parameters, which

need to be configured based on the particular science case and the properties of the data. There are two important parameters to be set: the smoothing kernel size, which dictates the amount of smoothing the galaxy image is subjected to; and the sampling step size, which dictates the frequency with which the galaxy image is radially sampled. In order to obtain a robust result when running the method, we suggested that the user should adopt a range of smoothing kernel sizes and sampling step sizes that are appropriate for their science case, effectively constructing a parameter configuration grid. This way, the residual method is run several times on each galaxy image with a slightly different parameter configuration, allowing to assign uncertainties to any measurements.

Next, as a means to quantify the substructure features extracted by the method, we introduced the concept of a "residual light fraction", which measures the relative contribution of the substructure component to the total light of the galaxy. We also investigated how the results change throughout the parameter configuration grid, including: the number of iterations needed in the residual method, the measured residual light fraction, and the brightness and appearance of the substructure features. Overall, we found that larger smoothing kernel sizes and sampling step sizes tend to result in less iterations being needed, larger residual light fractions, and brighter substructure features.

We then proceeded by describing the main strengths of the residual method and its improvements on previous approaches, which are mainly related to two main factors: accuracy and adaptability. The method is accurate, as it allows to reliably extract both the actual geometry and the light content of the substructure features that are underlying in a galaxy image. The method is also adaptable, as its iterative aspect and the setup of its configuration parameters allows it to be tuned on a case-by-case basis.

Finally, we discussed the potential of the method, and the kind of analyses that could be carried out on the extracted substructure features. We gave as examples a Fourier analysis, which we performed on our Virgo dwarf ETG sample in Chapter 3; and a color analysis, which we performed on our Fornax dwarf ETG sample in Chapter 4. We also stated that to take maximum advantage of the residual method, the data set being analyzed should ideally be a large-enough galaxy sample consisting of deep multi-band imaging.

► Chapter 3: "Substructures in Dwarf ETGs of the Virgo Cluster".

In this Chapter, we analyzed a white-band imaging sample of 9 dwarf ETGs with disk substructure features that are part of the Virgo galaxy cluster. We began by describing the observations and the data reduction, and how we processed the data to prepare it for analysis. This included measuring the noise level and PSF FWHM of each galaxy image, and creating bad pixel mask images by masking out any interloping sources.

To characterize the dwarf ETGs of the sample, we derived and presented their main photometric and structural properties. Their photometric properties are given in the r-band, and include: the central and effective surface brightness, the total apparent and total absolute magnitudes, and the $g-r$ color within two effective radii. Their structural properties include:

the effective radius, the ellipticity at one and two effective radii, and the position angle at one and two effective radii. We also derived and presented radial parameter profiles of their surface brightness, ellipticity, and position angle. To visualize their substructure features, we created and showed unsharp mask images of the galaxies. We observed a variety of disk substructures, such as bars, spiral arms, rings, and dumbbells. We also presented their distribution in projected space, color-magnitude space, and phase space.

The residual method was then applied to the dwarf ETG sample. We specified the adopted parameter configuration. As a result, we obtained that the relative contribution of the substructure features to the total galaxy light (i.e., the residual light fraction) ranges between $1.7 - 6.8\%$ within one effective radius, and between $2.2 - 6.4\%$ within two effective radii. We showed the appearance of the extracted substructure components (i.e., the residual images), and confirmed that the residual method was able to effectively capture the substructure features originally observed in the unsharp mask images. We also derived the surface brightness profiles of the diffuse and substructure components separately, demonstrating that the diffuse components tend to be significantly brighter and smoother than the substructure components.

As a means of assessing the robustness of the residual method, we constructed a mock galaxy sample and subjected it to a variety of tests. We compared the residual method to alternative approaches, such as a simplified version of the method where there is no iterative procedure, and to the unsharp masking and galaxy modeling techniques. Essentially, we tested the efficiency with which each method is able to recover the residual light fractions that have been manually introduced into the mock galaxy images. Our results indicated that only the complete, iterative version of the residual method is successful in recovering the introduced fractions, and does so with great accuracy.

To showcase a potential application of the method, we performed a Fourier analysis on the extracted substructure features of the dwarf ETG sample. We began by explaining the concept behind the Fourier decomposition, and how it can be used to identify and characterize bar features and spiral arm features. Then, we demonstrated that by performing a Fourier decomposition directly on the residual images instead of the galaxy images, it is possible to easily decompose the very faint substructure features that normally lie hidden in the bright diffuse light of the galaxies. As a result of the Fourier analysis on the residual images, we were able to cleanly distinguish and separate the bar and spiral arm regions of the dwarf ETGs. Finally, we reported our Fourier measurements of the orientation, length, and strength of the bar features; and the pitch angle and strength of the spiral arm features.

► Chapter 4: "Substructures in Dwarf ETGs of the Fornax Cluster".

In this Chapter, we analyzed a g and r-band imaging sample of 23 dwarf ETGs with disk and clump substructure features that are part of the Fornax galaxy cluster. We began by introducing the data. The imaging data consists in a deep, multi-band (u, g, r, and i) survey centered on the Fornax cluster and out to the virial radius, which additionally includes the Fornax A infalling subgroup. We also had access to a dwarf galaxy catalog of the Fornax cluster, comprised by 564 dwarf galaxies that were identified as cluster members, and which

provides some basic photometric and structural properties of the galaxies.

Next, we described how we processed and prepared the g and r-band imaging data of all the dwarf galaxies in the catalog. We first built g and r-band image cutouts of each dwarf galaxy. We then constructed PSF models of each field in the survey, and matched the PSFs of the g and r-band galaxy cutouts. We proceeded by coadding the PSF-matched g and r-band galaxy cutouts, in order to increase the S/N and thus the depth of the images. Then, we created several unsharp mask images of each $g+r$ galaxy cutout. Finally, we jointly inspected the $g + r$ galaxy images and their unsharp mask images in order to identify and select the dwarf ETGs with substructure features.

This way, we constructed our sample of 23 dwarf ETGs, where 9 have disk substructures and 14 have clump substructures. We then prepared the sample for analysis, which included correcting for galactic extinction, and creating bad pixel mask images by masking out any interloping sources.

To characterize the dwarf ETGs of the sample, we derived and presented their main photometric and structural properties. Their photometric properties are given in the g and r bands, and include: the central and effective surface brightness, the total apparent and total absolute magnitudes, and the total $g-r$ color. Their structural properties are based on the r-band images, and include: the effective radius, the ellipticity at one and two effective radii, and the position angle at one and two effective radii. We also derived and presented radial parameter profiles of their g and r-band surface brightness, r-band ellipticity, r-band position angle, and $g - r$ color. To visualize their substructure features, we created and showed unsharp mask images of the galaxies. We also presented their distribution in projected space and in color-magnitude space.

The residual method was then applied to the dwarf ETG sample. We explained how we adapted the method for the application in two different bands (the g and r bands), and specified the adopted parameter configuration. As a result, we obtained that the g-band residual light fraction has a median value of 6.7% and 8.7% within one and two effective radii, respectively. In contrast, the r-band residual light fraction is comparatively smaller, with a median value of 4.6% and 5.3% within one and two effective radii, respectively. We found that the g and r-band residual light fractions of a galaxy strongly correlate with each other. We also observed a different behavior between the disky and clumpy sub-classes: disk substructures tend to be fainter, and are found in galaxies with redder $g - r$ global colors; while clump substructures tend to be brighter, and are found in galaxies with bluer $g - r$ global colors. We proceeded by showing the r-band residual images, and confirmed that the residual method was able to effectively capture the substructure features originally observed in the unsharp mask images. Finally, we found that the fraction of Fornax dwarf ETGs that have substructures can be as high as 80% on the bright galaxy end, steeply dropping to 5% on the faint end, located only three magnitudes away.

To showcase a potential application of the method, we performed a color analysis on the dwarf ETG sample, in which we considered their diffuse and substructure components sepa-

rately. We computed both integrated $g-r$ colors and radial $g-r$ color profiles. We found that the diffuse component tends to have significantly redder $g-r$ colors than the substructure component. In particular, disky dwarf ETGs have overall redder diffuse components, and their two components tend to have similar colors. Clumpy dwarf ETGs have overall bluer diffuse components, and their substructure component tends to be bluer than their diffuse component. Finally, we carried out a basic stellar population analysis of the two components. We found that the median $g-r$ colors of the diffuse component suggest the dominance of middle-aged to old stellar populations (> 3 Gyr), while for the substructure component they suggest significantly younger stellar populations (~ 1 Gyr).

► **Chapter 5: "Discussion: From Virgo to Fornax".**

In this Chapter, we provided an in-depth discussion of our results and their implications. We began by addressing the multiple factors that may be influencing and/or biasing our Virgo and Fornax dwarf ETG samples.

First, our two samples are in different cluster environments, so we described and compared the properties of the Virgo and Fornax galaxy clusters. We found that Virgo is a dynamically younger cluster, experiencing an ongoing assembly process; while Fornax is a dynamically older cluster, being more virialized and evolved. We then evaluated the relative importance of various environmentally-driven processes in the Virgo and Fornax cluster environments, and weighed in how they could have influenced their respective dwarf galaxy populations.

Second, our two samples have different data sources, so we described and compared the properties of the imaging data. In particular, we addressed the differences in data quality, such as the imaging resolution and depth. While the Fornax data is better resolved, the Virgo data is deeper. However, after various checks and tests, we confirmed that the better resolution and shallower depth of the Fornax data is not significantly hindering our ability to detect substructure features.

Taking these factors into account, we proceeded to describe and compare the photometric properties, structural properties, and the results obtained through the residual method for our two samples. In general, we found that disky dwarf ETGs encompass a brighter magnitude range, display redder global $g-r$ colors, and tend to have smaller residual light fractions than their clumpy counterparts. Overall, we concluded that all types of substructure features embedded in dwarf ETGs are indeed very faint: they typically contribute only between $2-10\%$ of the total galaxy light.

We followed by making a brief link to simulations, as a means to evaluate if tidal harassment by the cluster environment can serve as a possible explanation for the presence of disk substructures in dwarf galaxies. The simulations showed that disk features form in dwarf galaxies that experience close pericenter passages to the cluster core and that have a component of their stellar disk that is highly rotationally supported. Consequently, we formulated the hypothesis that the disk substructures present in some of our dwarf ETGs could have been tidally triggered by the cluster potential.

Finally, we attempted to constrain the possible formation and evolution scenarios of the dwarf ETG population with embedded substructure features. Our results indicate that the Virgo cluster has a larger fraction of dwarf ETGs with disk substructures compared to the Fornax cluster, and that embedded spiral arm features are common in disky dwarf ETGs in Virgo but completely absent in Fornax. We believe that these findings are a reflection of the environmental differences between the Virgo and Fornax clusters.

As our main hypothesis, we proposed that dwarf ETGs with disk or clump substructures found in clusters could constitute a transition population (i.e., transition-type dwarf galaxies), caught in the environmentally-driven transformation from dwarf LTGs to dwarf ETGs. The characteristic properties that distinguish the disky and clumpy populations could be a reflection of their different evolutionary histories, suggesting that they are at different stages in their late-to-early-type transition process. Complementary to this transformation scenario, it is plausible that a fraction of disky dwarf ETGs could have already been ETGs, and the cluster environment is tidally triggering the formation of disk features.

6.2 Final Remarks

To close, we would like to highlight two main conclusions that can be drawn from this Thesis work: *(1)* the importance of having the right tools and techniques to extract the substructure features embedded in dwarf galaxies, and *(2)* the importance that the environment has in shaping these substructure features.

On the one hand, we have concluded that the substructure features that can be found embedded in the dwarf ETG population are extremely faint. Independent from their cluster environment (Virgo or Fornax) and independent from their substructure category (disky or clumpy), the substructure features typically contribute only between $2 - 10\%$ of the total galaxy light. Therefore, in order to be able to accurately isolate and extract them, there is a fundamental need of using imaging techniques, such as the residual method we have developed in this work for this exact purpose. Without the residual method, we would have been unable to carry out all the subsequent analyses that we performed on the substructure features —i.e., the bulk of this Thesis work.

On the other hand, our results make very clear that the cluster environment plays a fundamental role in shaping and transforming the dwarf galaxy populations in galaxy clusters. The environment is so important, that the existence of the population of dwarf ETGs with substructure features that we have studied can be consistently explained by taking environmentally-driven processes into account. Furthermore, the various differences observed between our Virgo and Fornax data sets suggest that the particular characteristics of a given cluster environment are strongly imprinted on the properties of the most vulnerable systems that they host: dwarf galaxies.

A

Additional Figures

A.1 Virgo: Parameter Profiles and Isophote Overlays

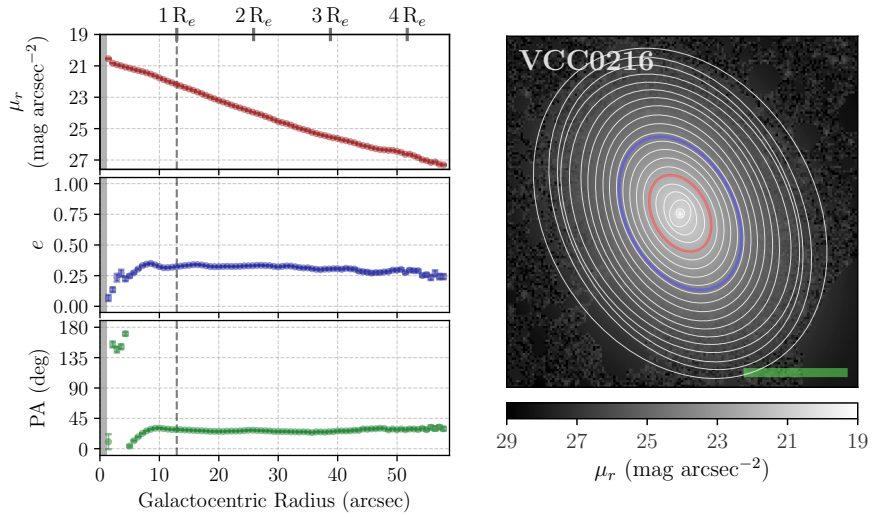

Figure A.1: Radial parameter profiles and isophote overlays of Virgo dwarf galaxy VCC0216. *Left panels:* from top to bottom, radial profiles of the surface brightness in the r-band, the ellipticity, and the position angle. The position angle is measured counterclockwise from the $+y$-axis (north towards east of the images). The gray-shaded area indicates the extension of the PSF FWHM. The vertical dashed line marks the position of the one effective radius. The radial profiles are shown out to the last valid isophote, whose intensity is 2σ above the background noise level. *Right panel*: galaxy image with isophote overlays. The isophotes at one and two effective radii are shown as red and blue ellipses, respectively. The last ellipse shown corresponds to the last valid galaxy isophote. The image scale is shown as a green line, and corresponds to 30 arcsec. North is up, east is to the left.

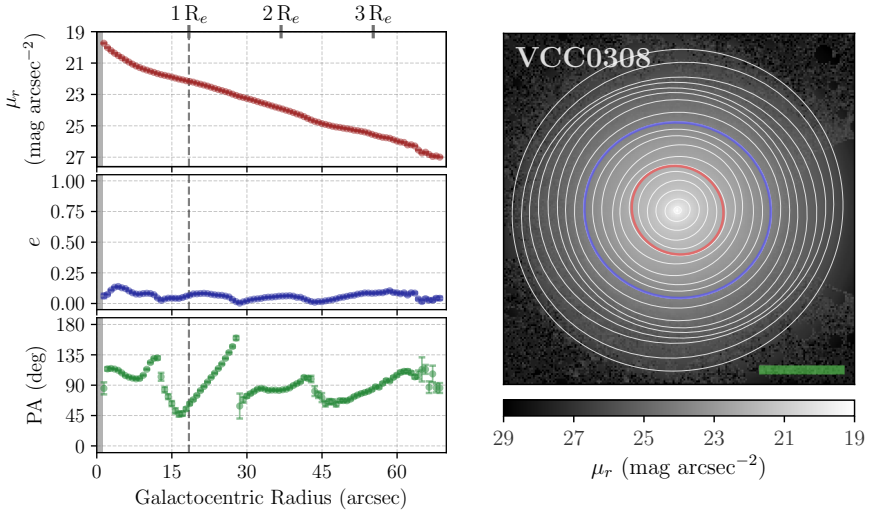

Figure A.2: Same as the caption of Figure A.1, but for Virgo dwarf galaxy VCC0308.

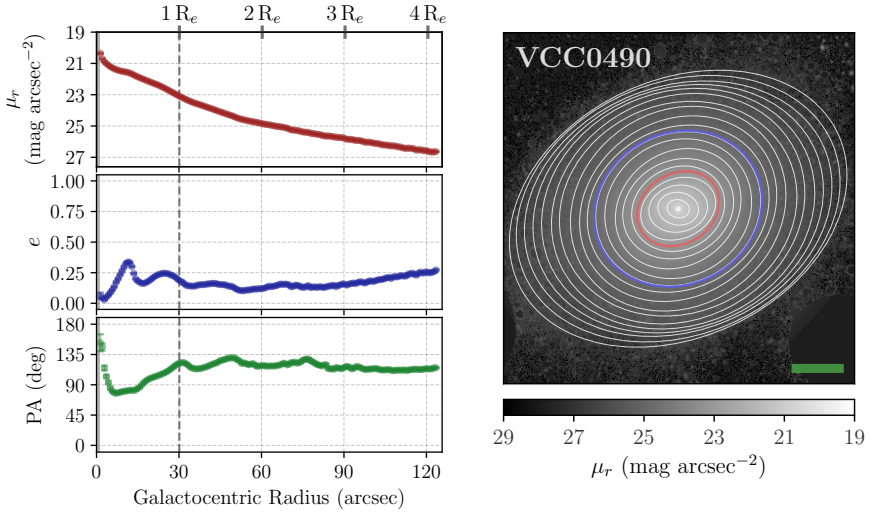

Figure A.3: Same as the caption of Figure A.1, but for Virgo dwarf galaxy VCC0490.

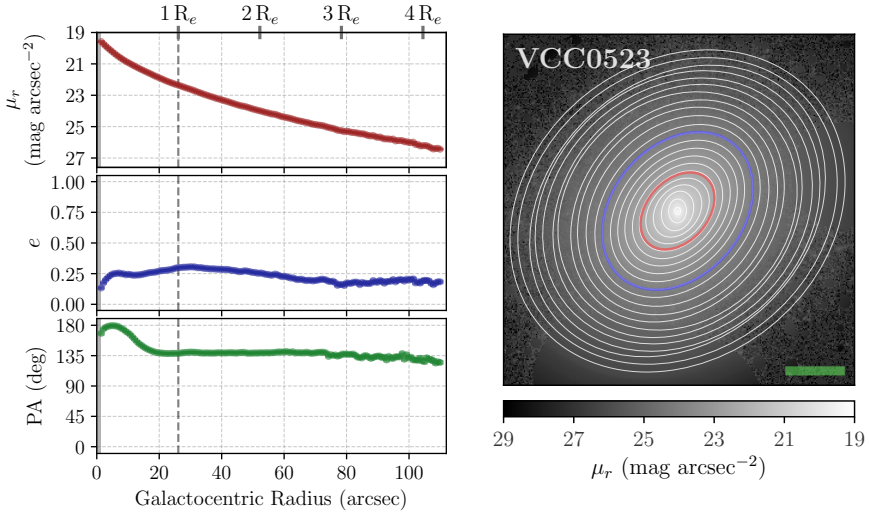

Figure A.4: Same as the caption of Figure A.1, but for Virgo dwarf galaxy VCC0523.

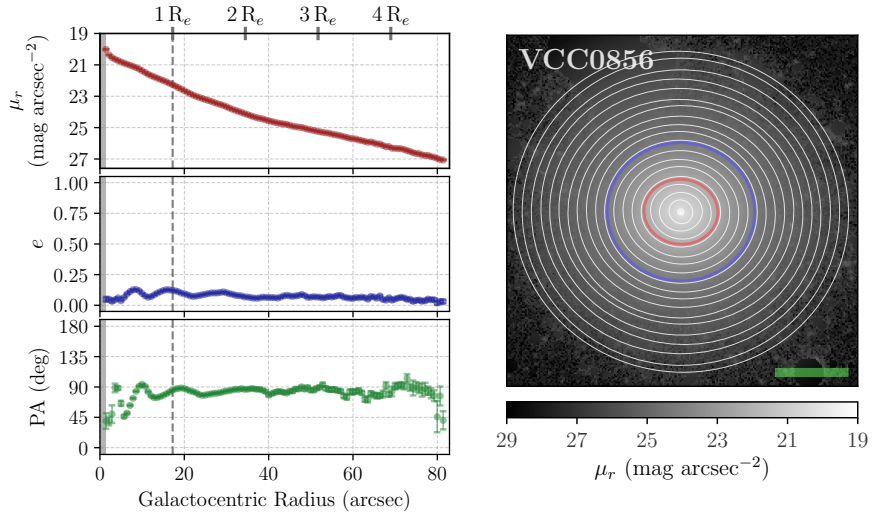

Figure A.5: Same as the caption of Figure A.1, but for Virgo dwarf galaxy VCC0856.

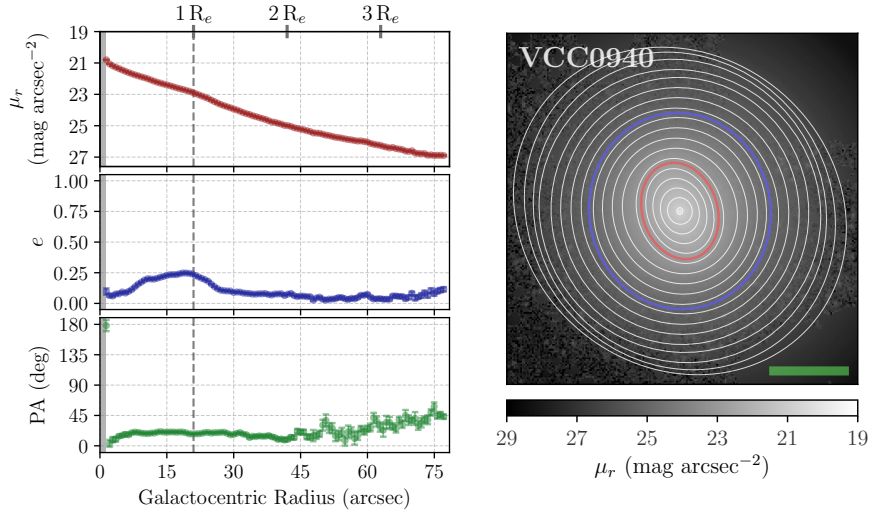

Figure A.6: Same as the caption of Figure A.1, but for Virgo dwarf galaxy VCC0940.

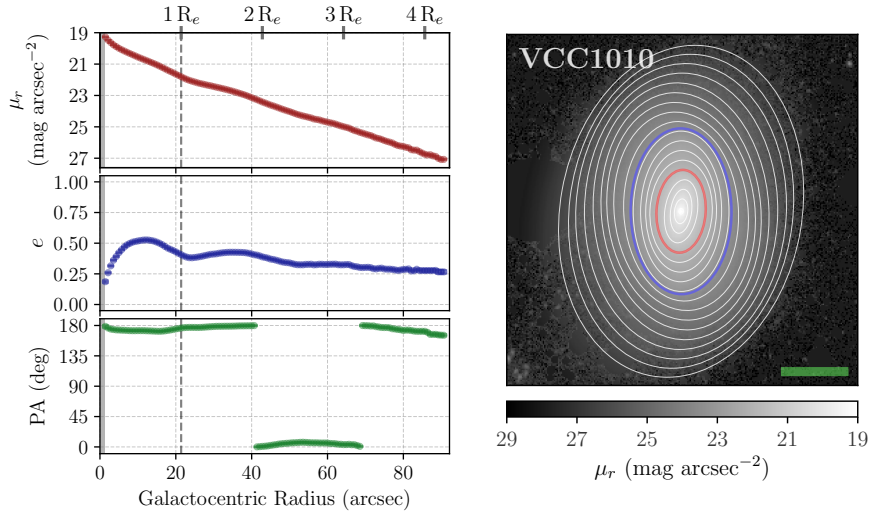

Figure A.7: Same as the caption of Figure A.1, but for Virgo dwarf galaxy VCC1010.

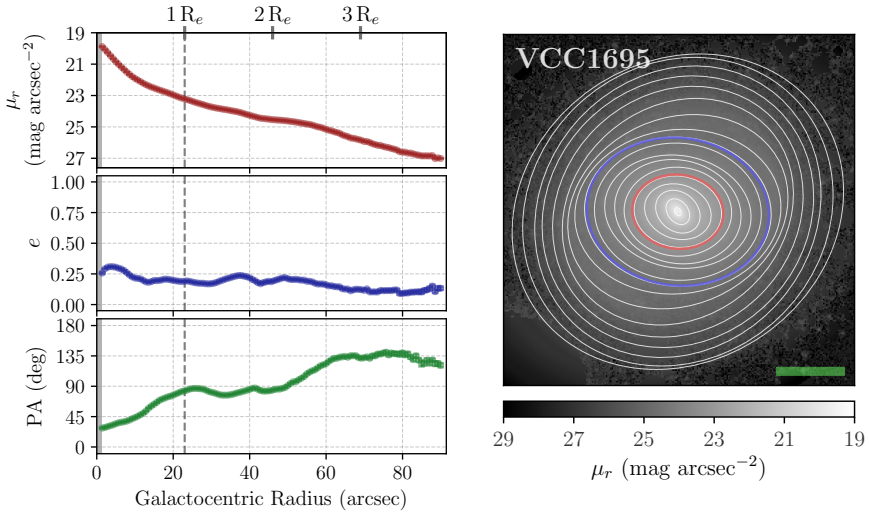

Figure A.8: Same as the caption of Figure A.1, but for Virgo dwarf galaxy VCC1695.

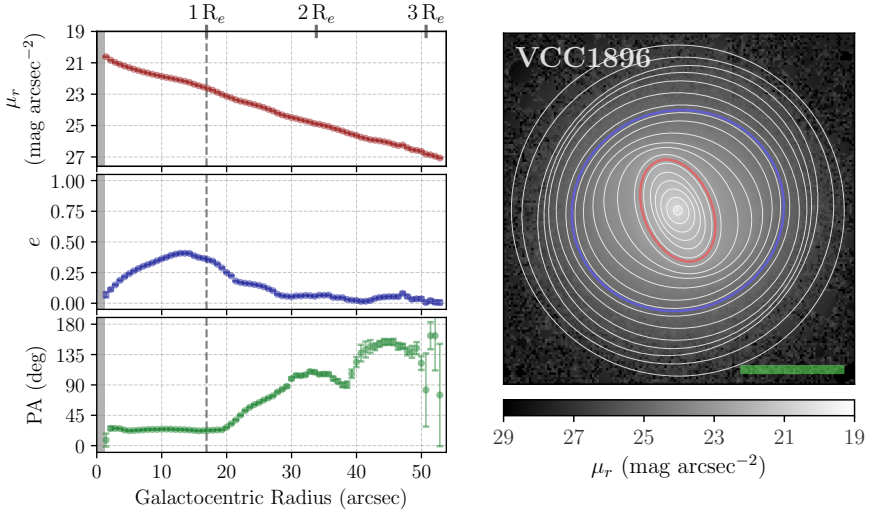

Figure A.9: Same as the caption of Figure A.1, but for Virgo dwarf galaxy VCC1896.

A.2 Virgo: Fourier Maps and Parameter Profiles

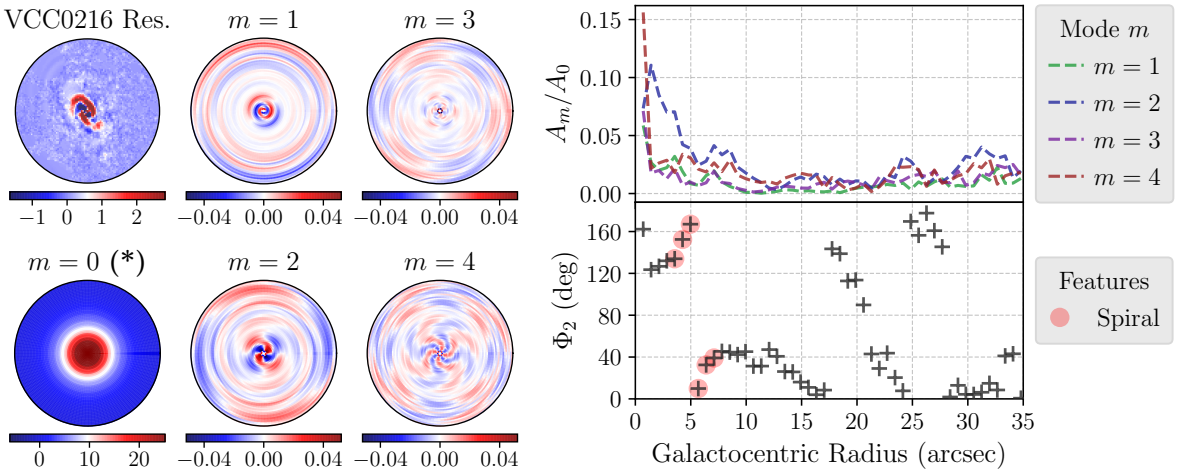

Figure A.10: Fourier mode maps and Fourier parameters corresponding to the galaxy residual image of Virgo dwarf galaxy VCC0216. *Left circular panels*: the galaxy residual image and maps of Fourier modes $m = 0$ through $m = 4$ are shown. The Fourier maps of modes $m = 1$ through $m = 4$ have been normalized by the map of mode $m = 0$ of the original galaxy image, which is displayed here and marked with an asterisk (*). Each image has its own color bar; the residual image and the map of mode $m = 0$ are in units of counts s^{-1}, while the maps of modes $m = 1$ through $m = 4$ are unitless. If a bar was identified, the dashed circle in the $m = 2$ map marks the detected end radius of the bar. The images display a circular area of 35 arcsec in radius. North is up, east is to the left. *Right rectangular panels*: the Fourier parameters, amplitude and phase, are shown as a function of galactocentric radius. On the top panel, we show the amplitude of modes $m = 1$ through $m = 4$, which have been normalized by the amplitude of mode $m = 0$ of the original galaxy image. On the bottom panel, we show the phase of mode $m = 2$, measured counterclockwise from the $+y$-axis. The data points associated with spiral-like substructure are highlighted by red circles, while points associated with bar-like substructure are highlighted by a blue rectangle. In this case, only spiral-like substructure is detected.

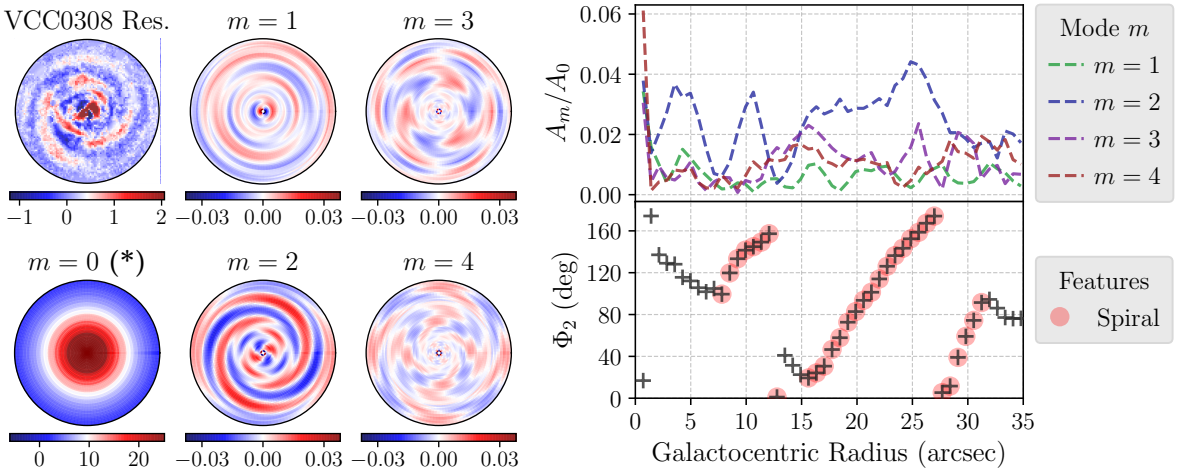

Figure A.11: Same as the caption of Figure A.10, but for Virgo dwarf galaxy VCC0308.

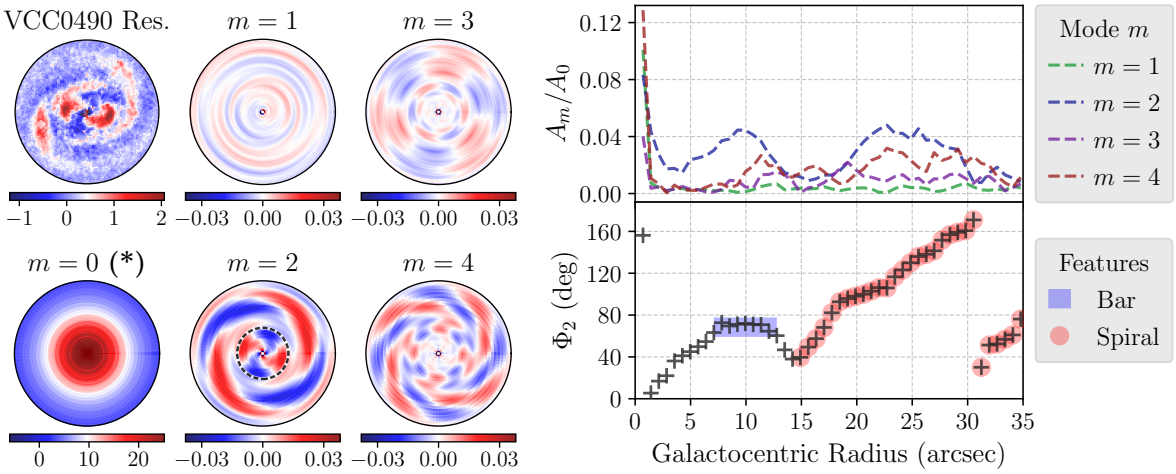

Figure A.12: Same as the caption of Figure A.10, but for Virgo dwarf galaxy VCC0490.

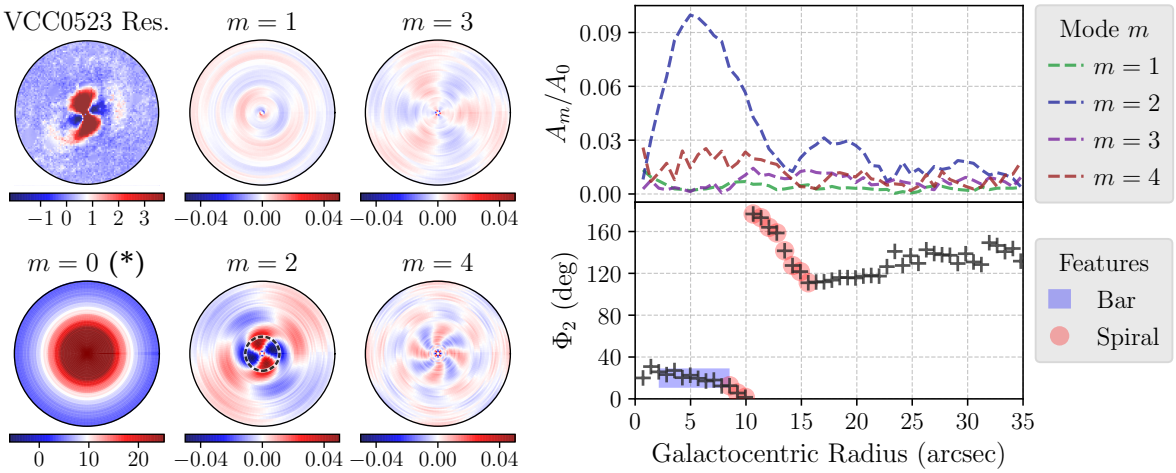

Figure A.13: Same as the caption of Figure A.10, but for Virgo dwarf galaxy VCC0523.

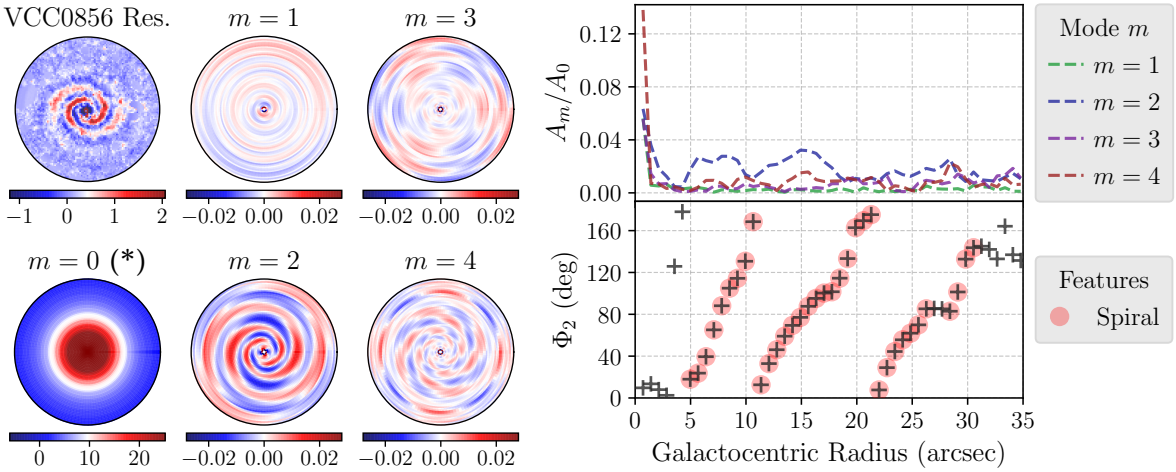

Figure A.14: Same as the caption of Figure A.10, but for Virgo dwarf galaxy VCC0856.

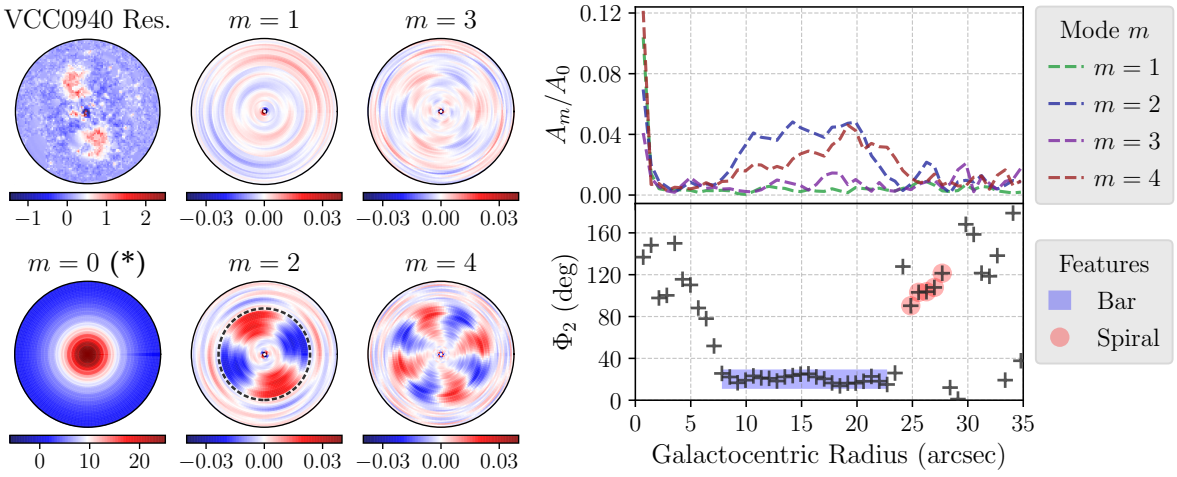

Figure A.15: Same as the caption of Figure A.10, but for Virgo dwarf galaxy VCC0940.

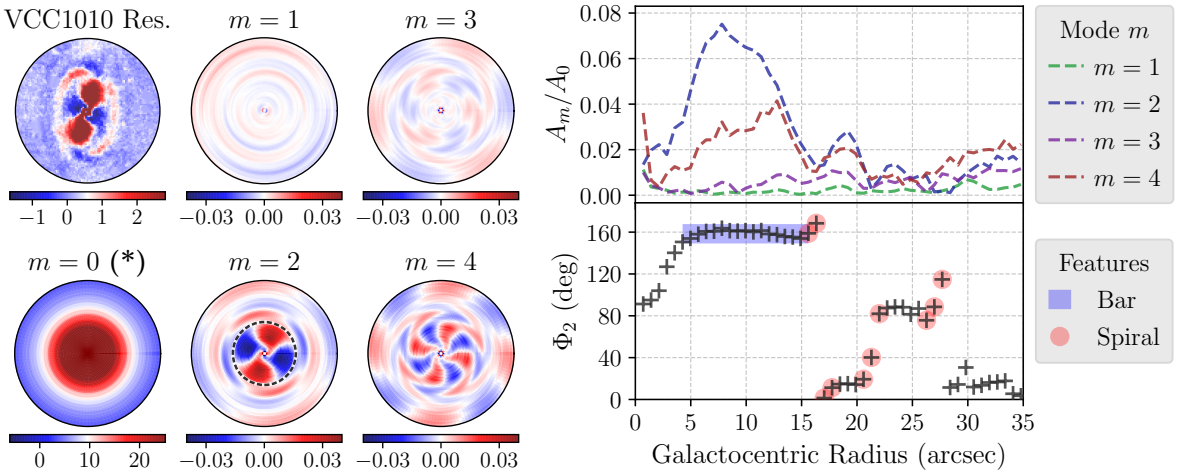

Figure A.16: Same as the caption of Figure A.10, but for Virgo dwarf galaxy VCC1010.

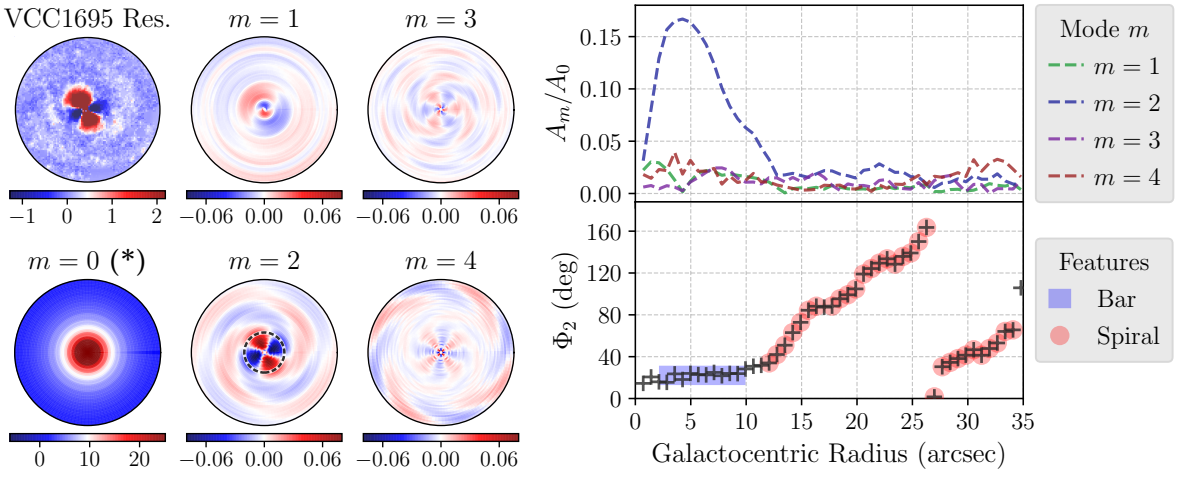

Figure A.17: Same as the caption of Figure A.10, but for Virgo dwarf galaxy VCC1695.

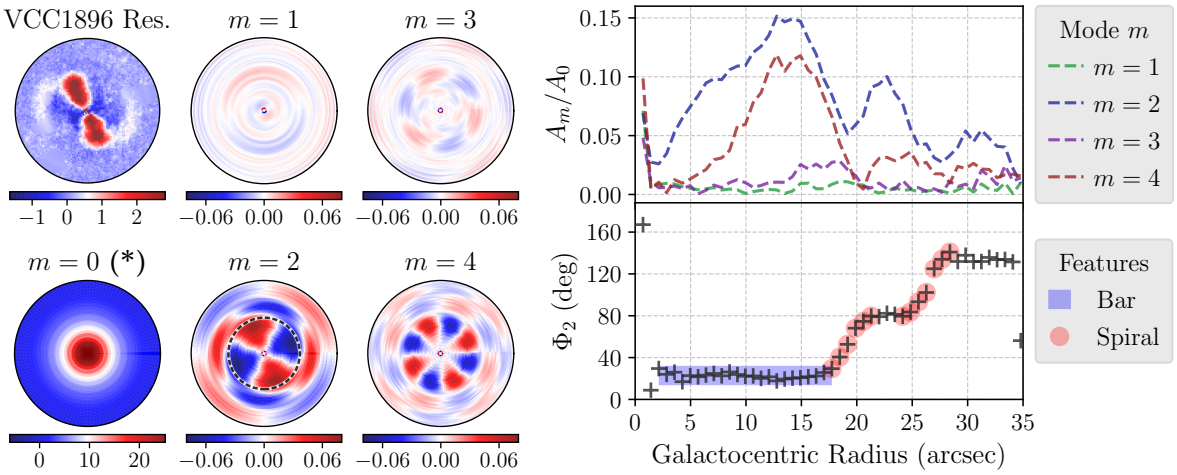

Figure A.18: Same as the caption of Figure A.10, but for Virgo dwarf galaxy VCC1896.

A.3 Fornax: Parameter Profiles and Isophote Overlays

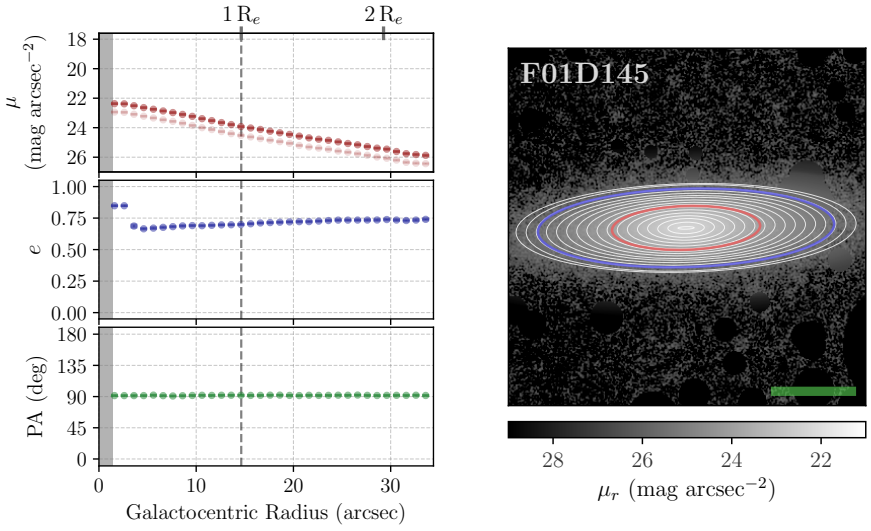

Figure A.19: Radial parameter profiles and isophote overlays of Fornax dwarf galaxy F01D145. *Left panels:* from top to bottom, r-band radial profiles of the surface brightness, the ellipticity, and the position angle. On the top panel, the g-band surface brightness profile is also plotted in a fainter red color. The position angle is measured counterclockwise from the $+y$-axis (north towards east of the images). The gray-shaded area indicates the extension of the PSF FWHM. The vertical dashed line marks the position of the one effective radius. The radial profiles are shown out to a maximum of three effective radii. In cases such as this one, the background surface brightness level is reached before three effective radii, so the profiles are instead shown out to the last valid galaxy isophote. *Right panel*: r-band galaxy image with isophote overlays. The isophotes at one and two effective radii are shown as red and blue ellipses, respectively. The last ellipse shown corresponds either to the isophote at three effective radii, or to the last valid galaxy isophote, such as in this case. The image scale is shown as a green line, and corresponds to 15 arcsec. North is up, east is to the left.

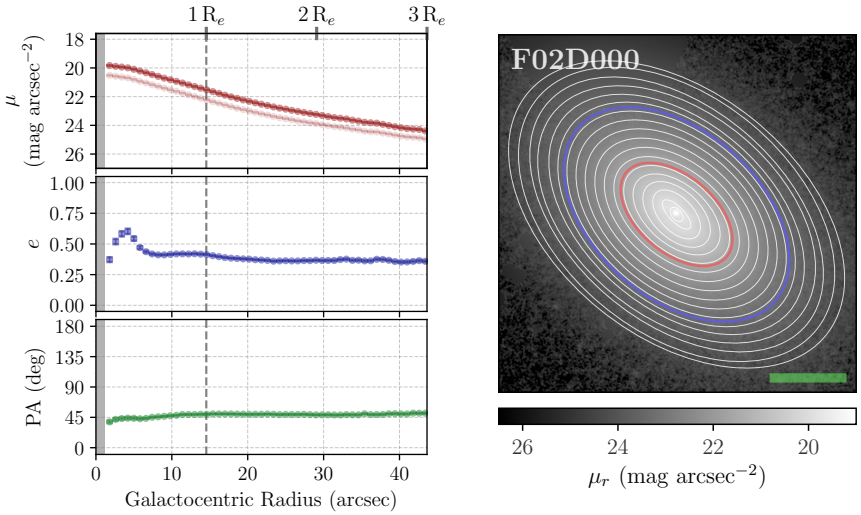

Figure A.20: Same as the caption of Figure A.19, but for Fornax dwarf galaxy F02D000.

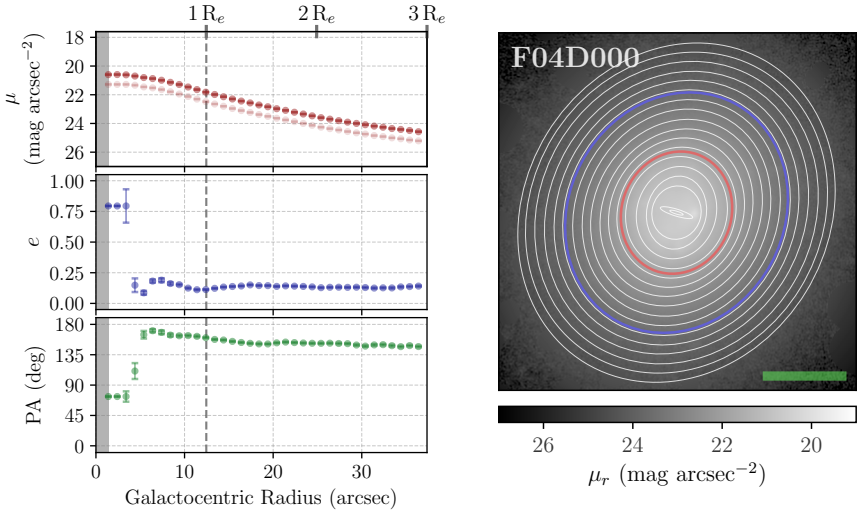

Figure A.21: Same as the caption of Figure A.19, but for Fornax dwarf galaxy F04D000.

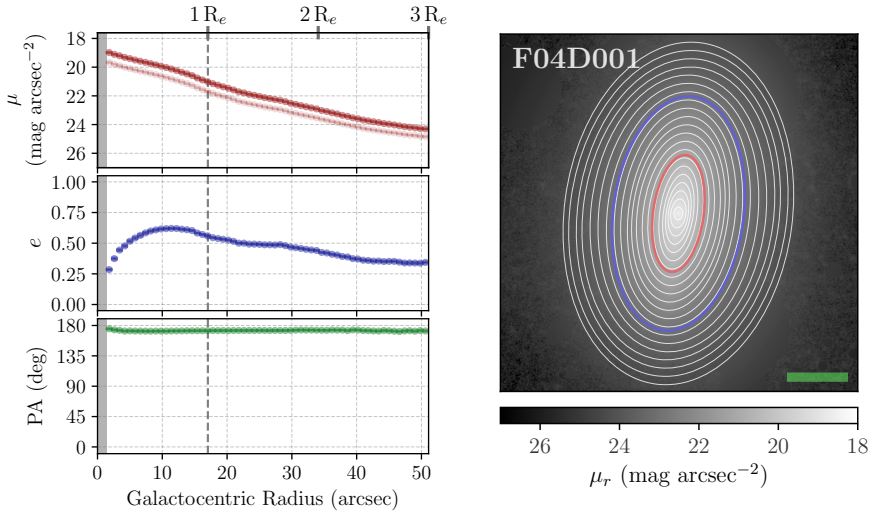

Figure A.22: Same as the caption of Figure A.19, but for Fornax dwarf galaxy F04D001.

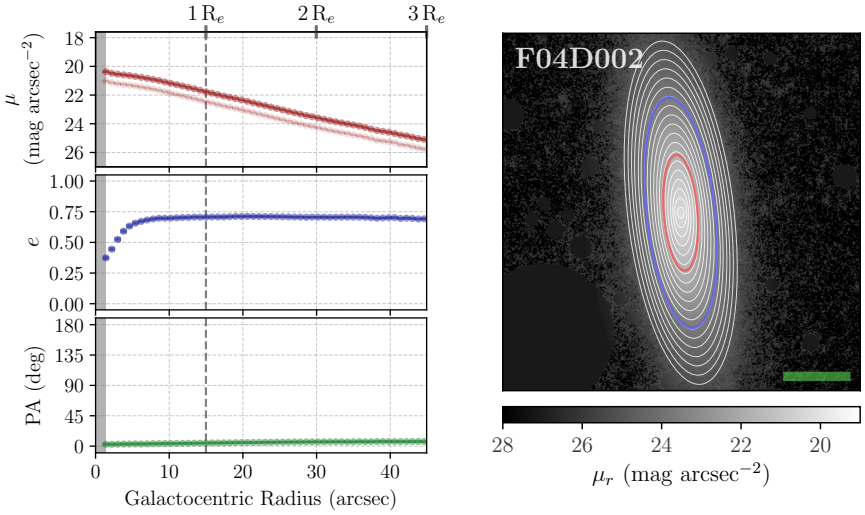

Figure A.23: Same as the caption of Figure A.19, but for Fornax dwarf galaxy F04D002.

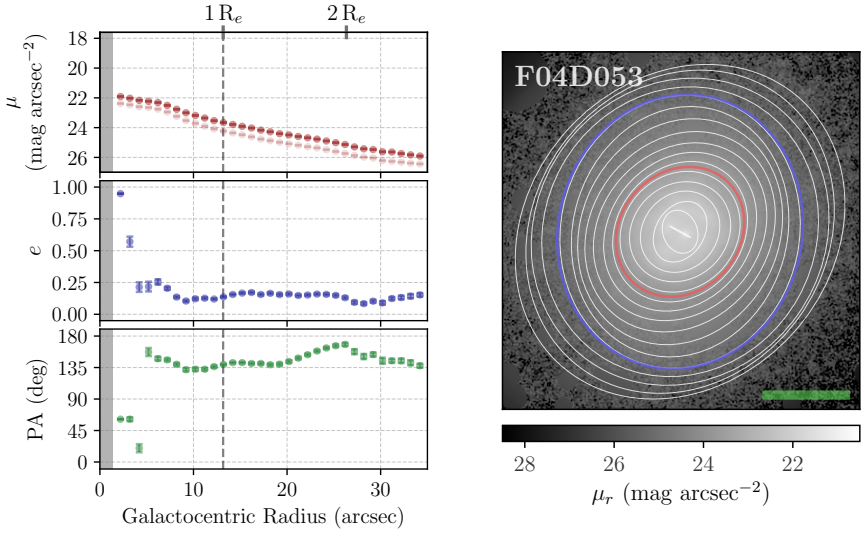

Figure A.24: Same as the caption of Figure A.19, but for Fornax dwarf galaxy F04D053.

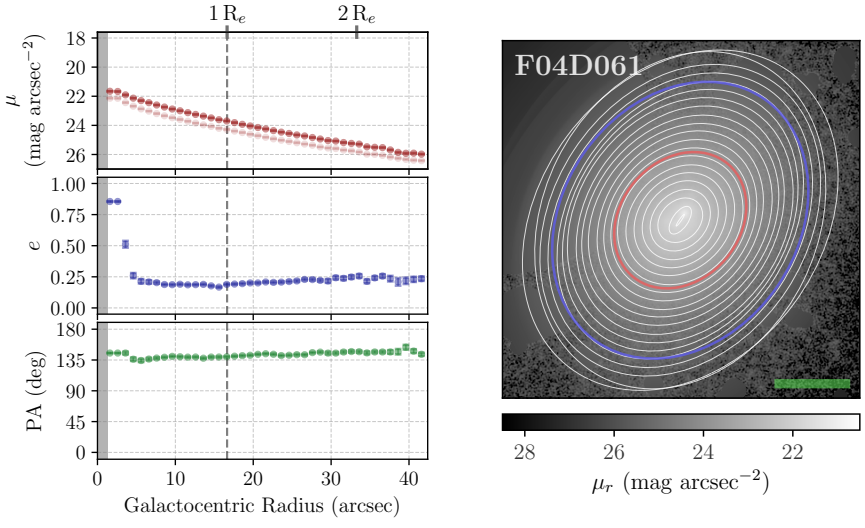

Figure A.25: Same as the caption of Figure A.19, but for Fornax dwarf galaxy F04D061.

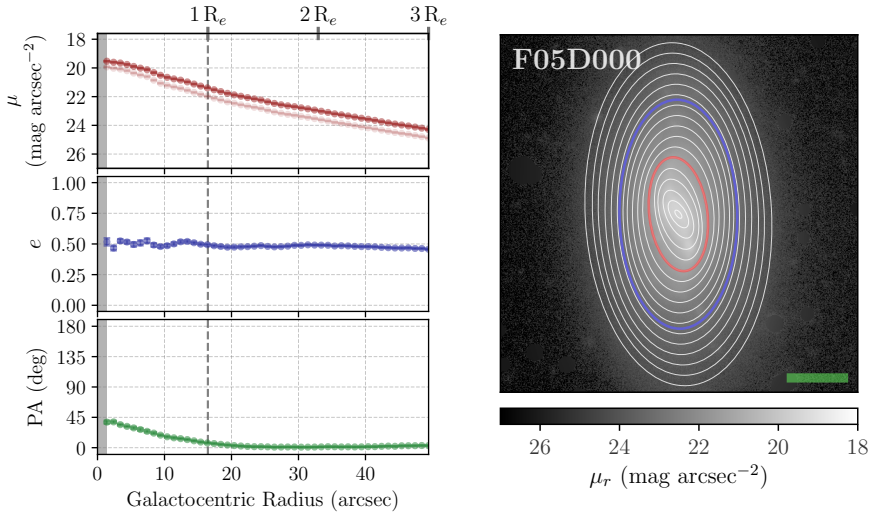

Figure A.26: Same as the caption of Figure A.19, but for Fornax dwarf galaxy F05D000.

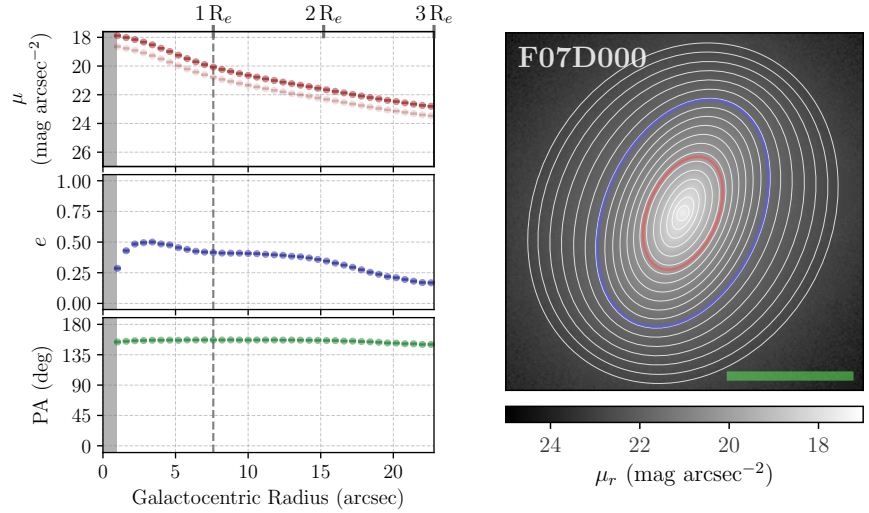

Figure A.27: Same as the caption of Figure A.19, but for Fornax dwarf galaxy F07D000.

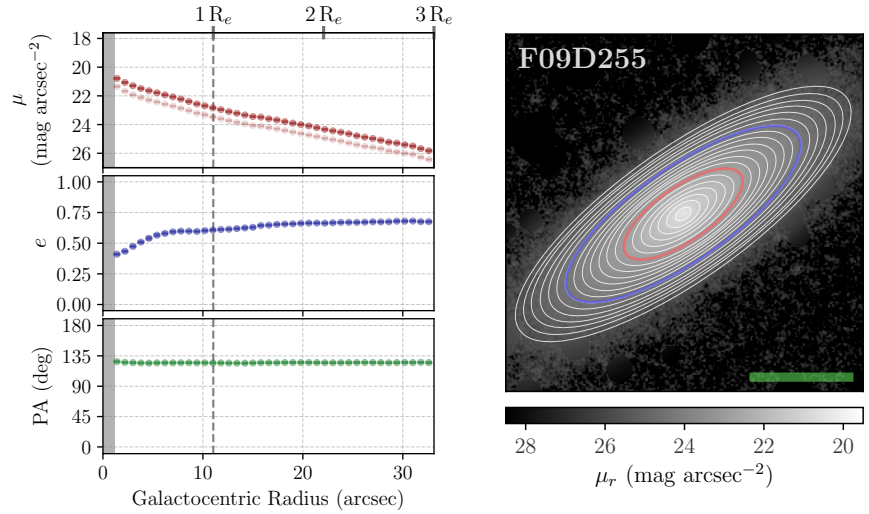

Figure A.28: Same as the caption of Figure A.19, but for Fornax dwarf galaxy F09D255.

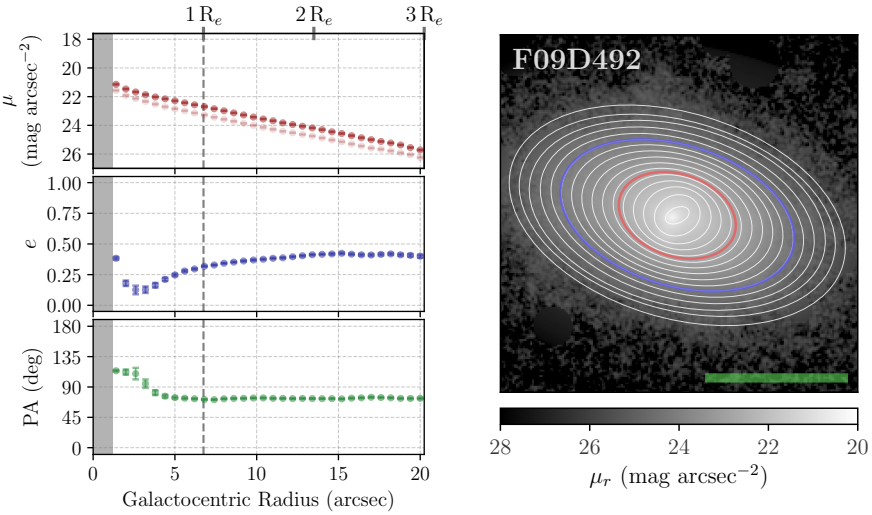

Figure A.29: Same as the caption of Figure A.19, but for Fornax dwarf galaxy F09D492.

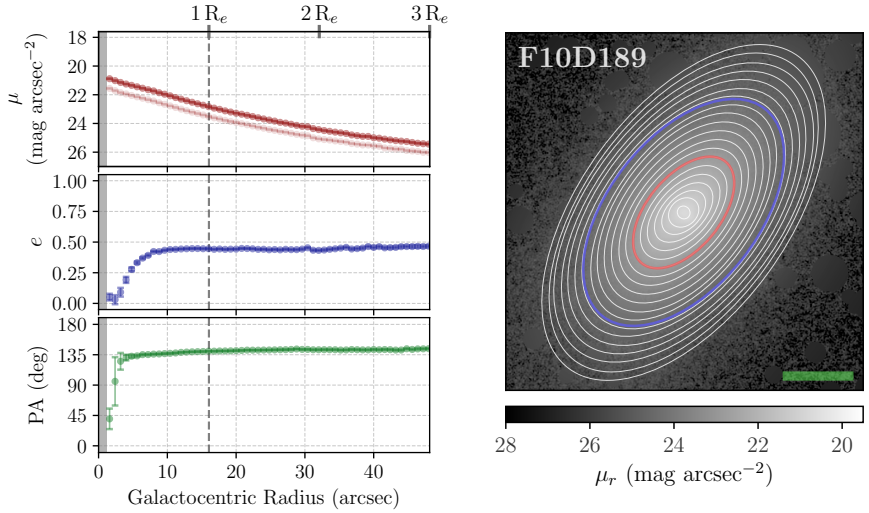

Figure A.30: Same as the caption of Figure A.19, but for Fornax dwarf galaxy F10D189.

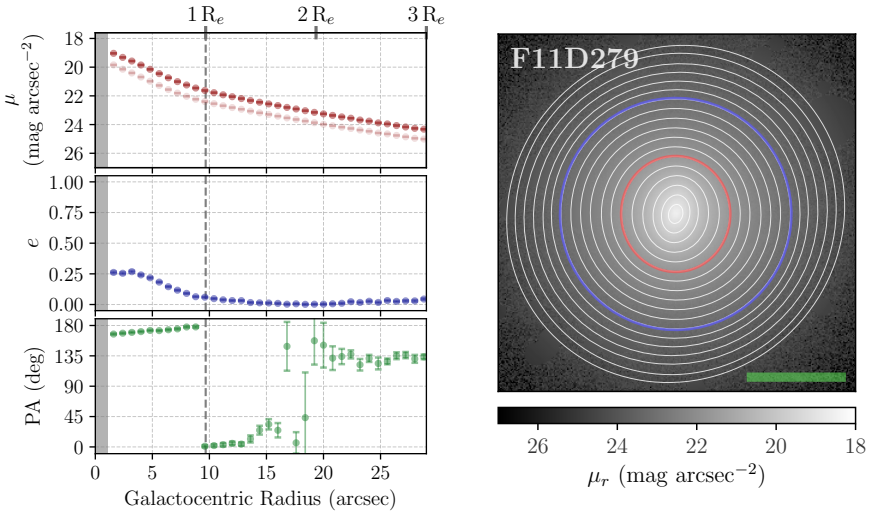

Figure A.31: Same as the caption of Figure A.19, but for Fornax dwarf galaxy F11D279.

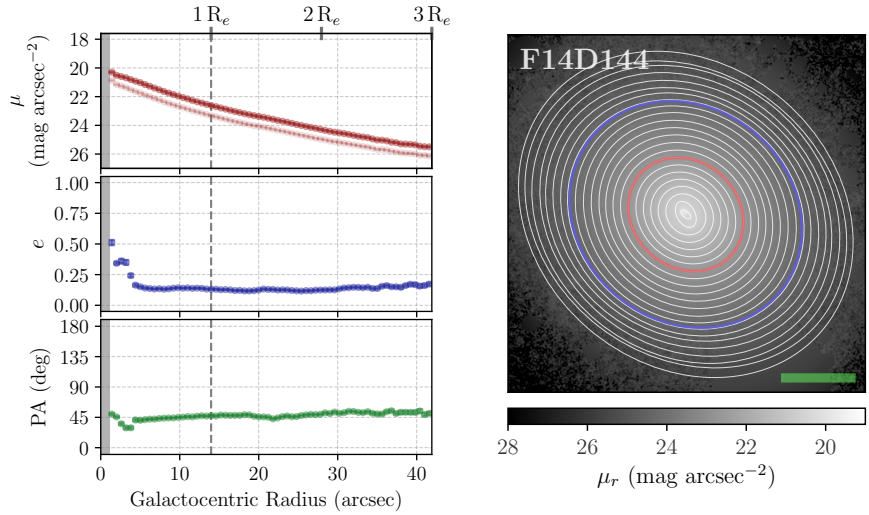

Figure A.32: Same as the caption of Figure A.19, but for Fornax dwarf galaxy F14D144.

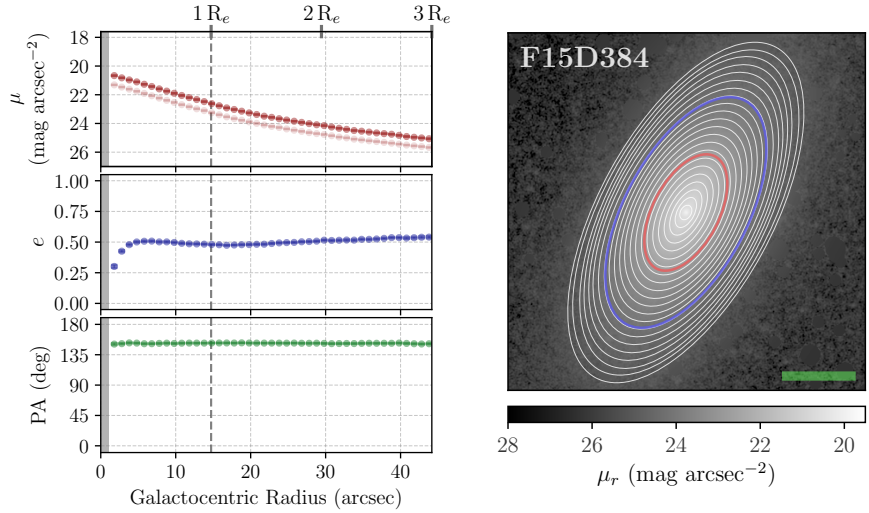

Figure A.33: Same as the caption of Figure A.19, but for Fornax dwarf galaxy F15D384.

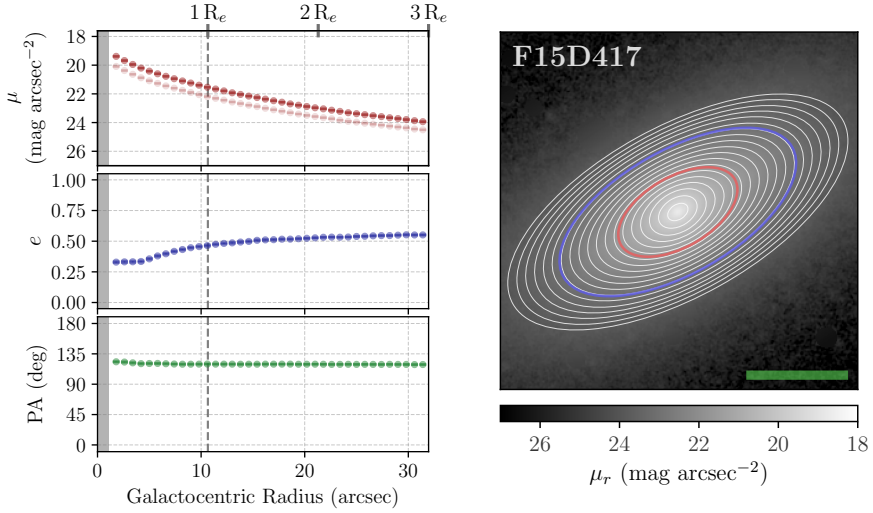

Figure A.34: Same as the caption of Figure A.19, but for Fornax dwarf galaxy F15D417.

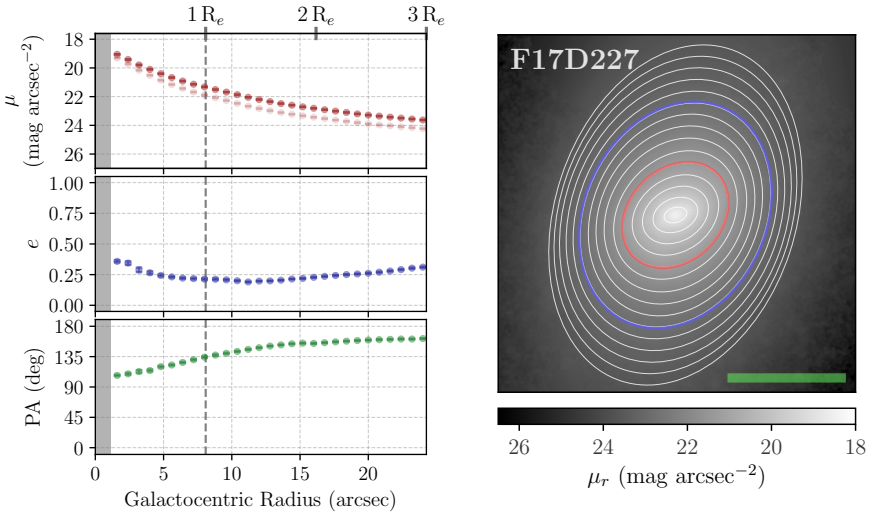

Figure A.35: Same as the caption of Figure A.19, but for Fornax dwarf galaxy F17D227.

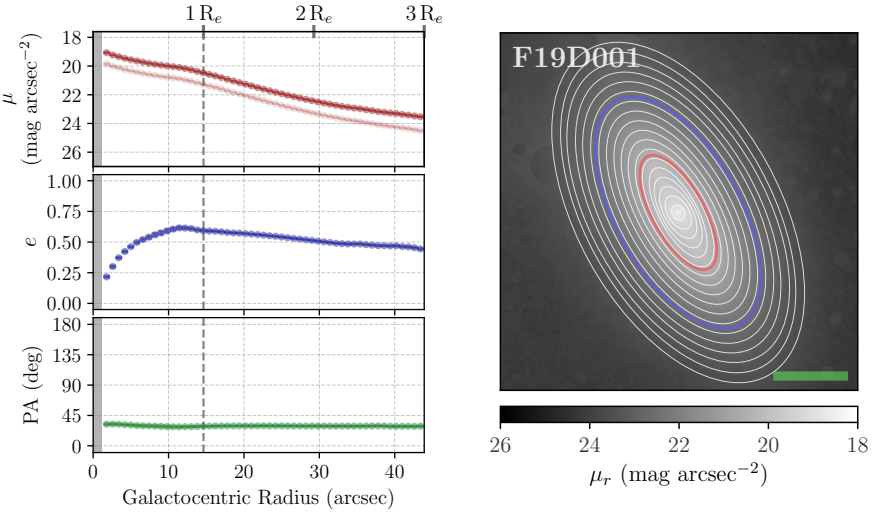

Figure A.36: Same as the caption of Figure A.19, but for Fornax dwarf galaxy F19D001.

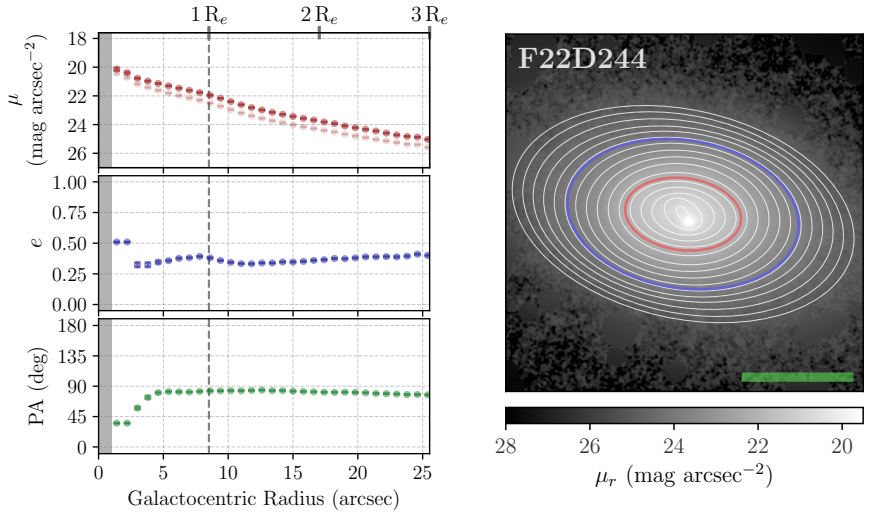

Figure A.37: Same as the caption of Figure A.19, but for Fornax dwarf galaxy F22D244.

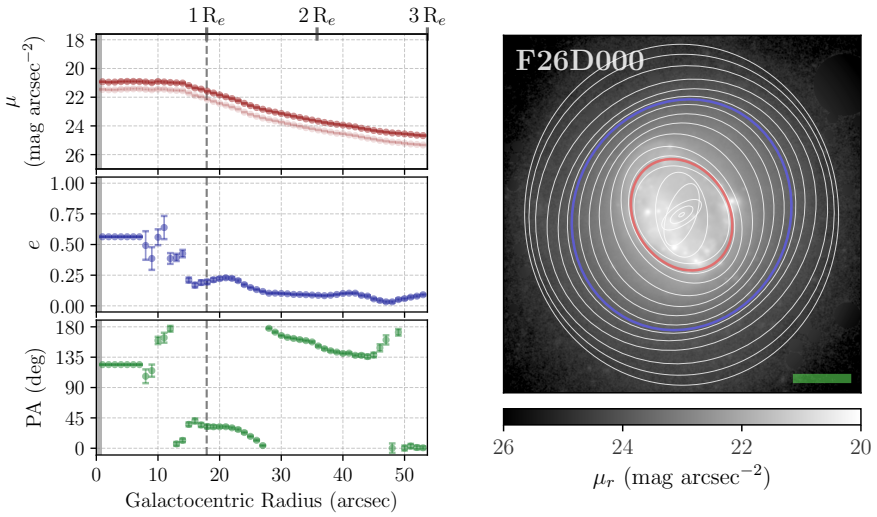

Figure A.38: Same as the caption of Figure A.19, but for Fornax dwarf galaxy F26D000.

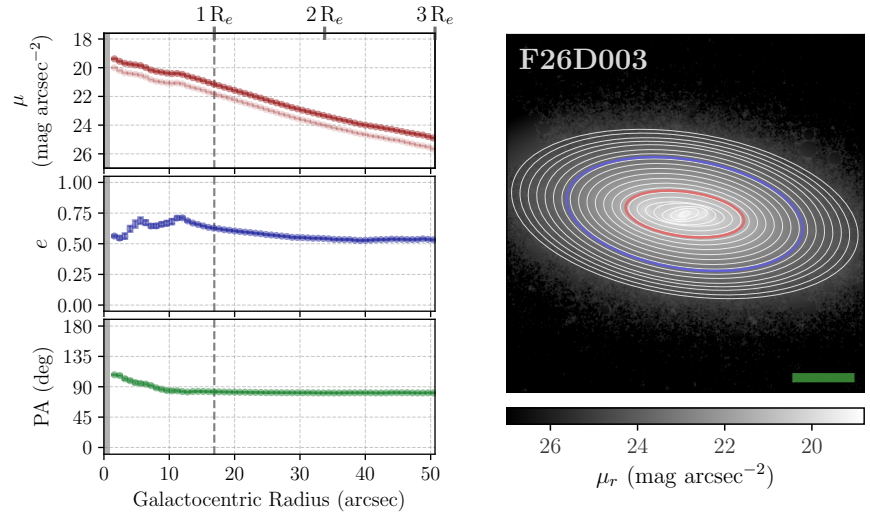

Figure A.39: Same as the caption of Figure A.19, but for Fornax dwarf galaxy F26D003.

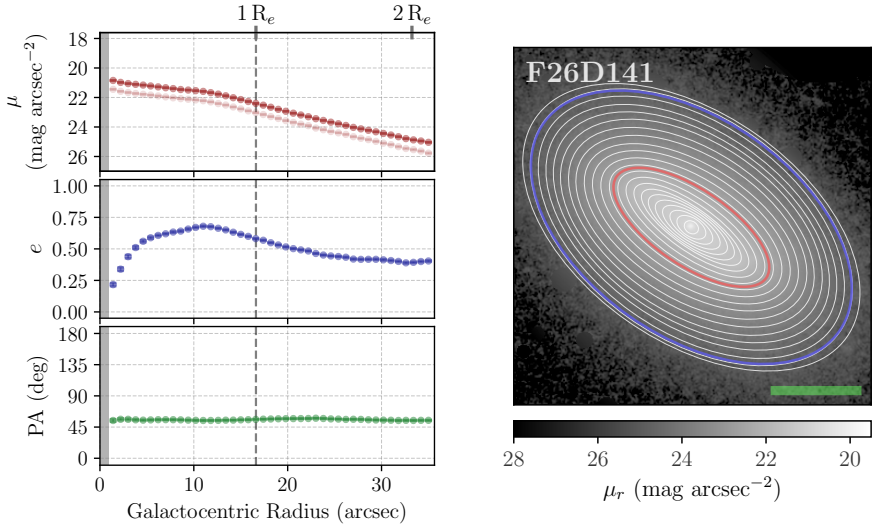

Figure A.40: Same as the caption of Figure A.19, but for Fornax dwarf galaxy F26D141.

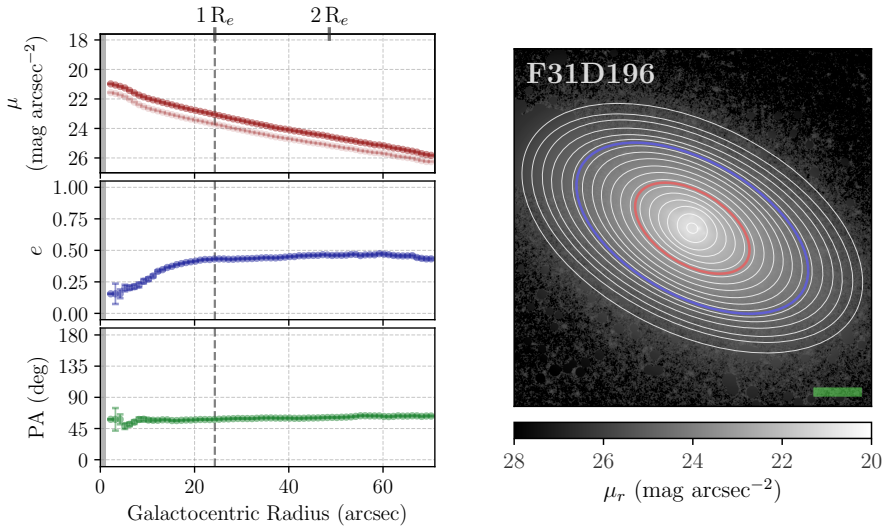

Figure A.41: Same as the caption of Figure A.19, but for Fornax dwarf galaxy F31D196.

A.4 Fornax: $g - r$ Color Profiles

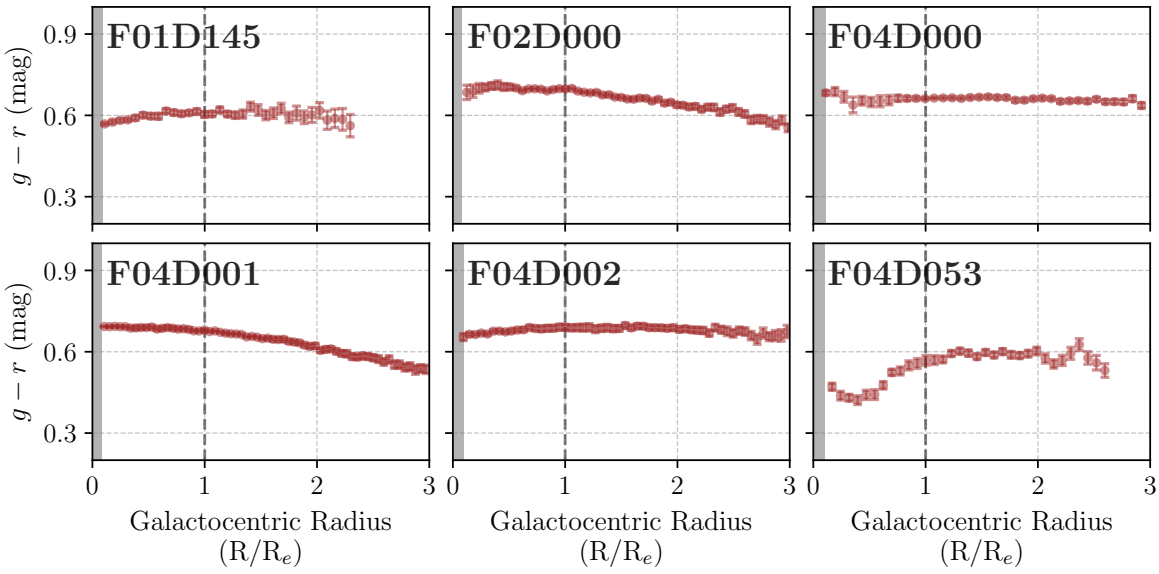

Figure A.42: $g - r$ color profiles of the Fornax dwarf ETG sample. The gray-shaded area indicates the extension of the PSF FWHM. The vertical dashed line marks the position of the one effective radius. The color profiles are shown out to a maximum of three effective radii. In cases where the background surface brightness level is reached before three effective radii, the profiles are instead shown out to the last valid galaxy isophote.

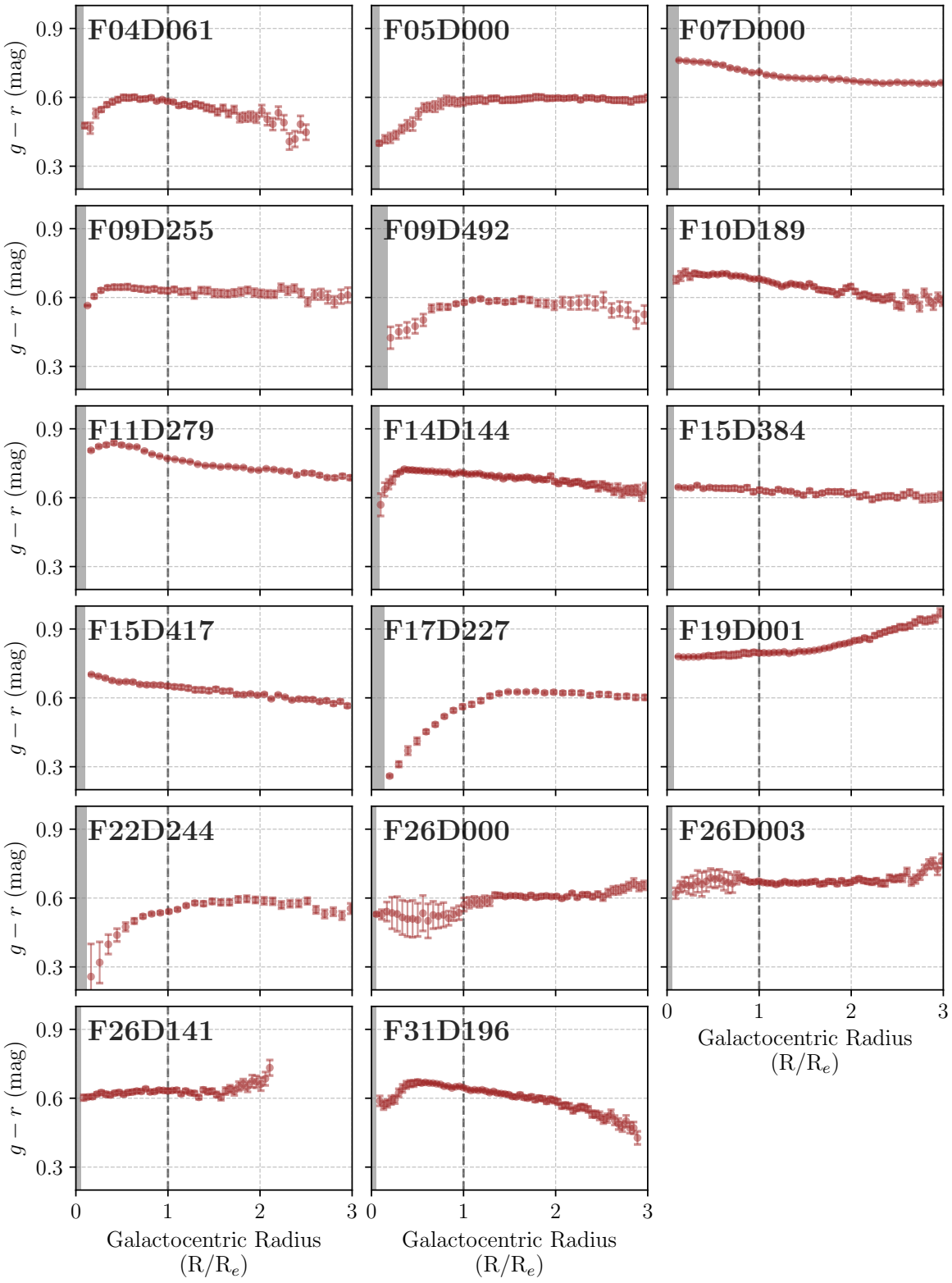

Figure A.42: $g - r$ color profiles of the Fornax dwarf ETG sample *(cont.)*.

A.5 Fornax: Profiles of the Diffuse and Substructure Components

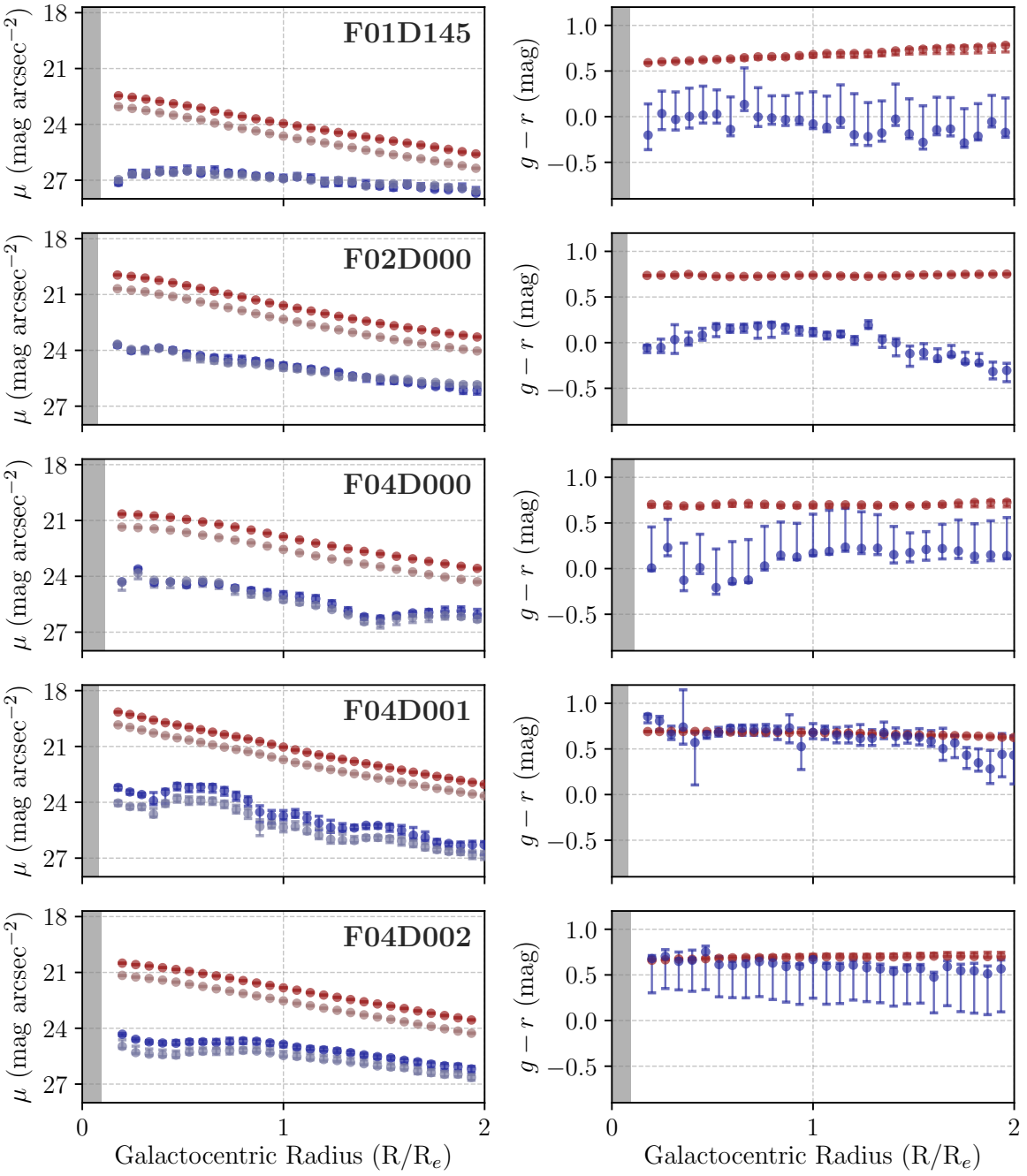

Figure A.43: Surface brightness and $g-r$ color profiles of the diffuse component (red points) and substructure component (blue points) of the Fornax dwarf ETG sample. *Left panels:* surface brightness profiles in the g and r bands. The bright red and bright blue points correspond to the r-band profile, while the faint red and faint blue points correspond to the g-band profile. *Right panels:* $g-r$ color profiles. The measurements are performed in elliptical annuli of constant width that match the geometry of the isophotes of the diffuse component of the galaxies out to two effective radii. The central region is excluded due to the effects of the PSF, and disregard an amount equal to 1.5 times the PSF FWHM. The gray-shaded area indicates the extension of the PSF FWHM.

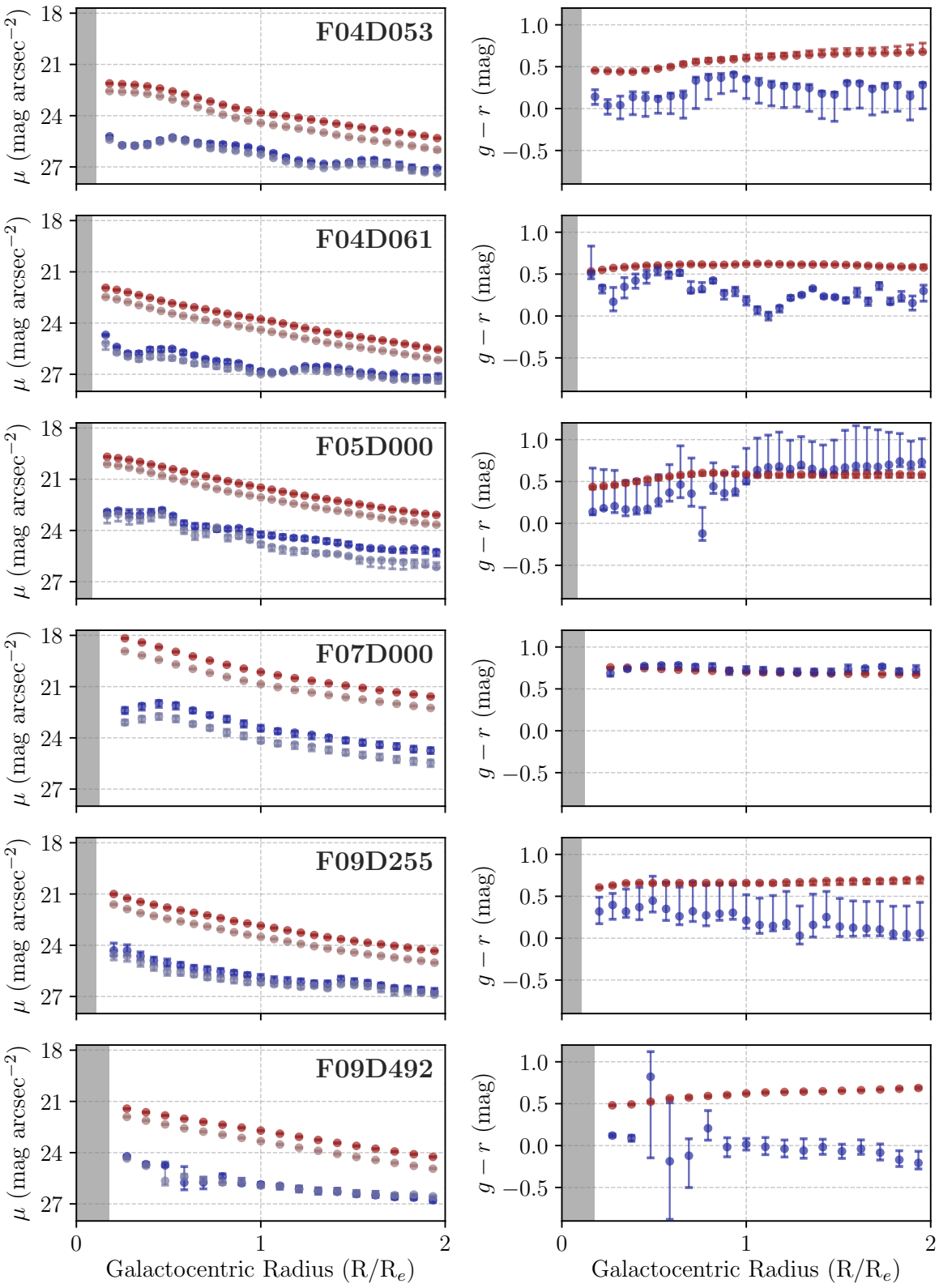

Figure A.43: Surface brightness and $g-r$ color profiles of the diffuse and substructure components of the Fornax dwarf ETG sample *(cont.)*.

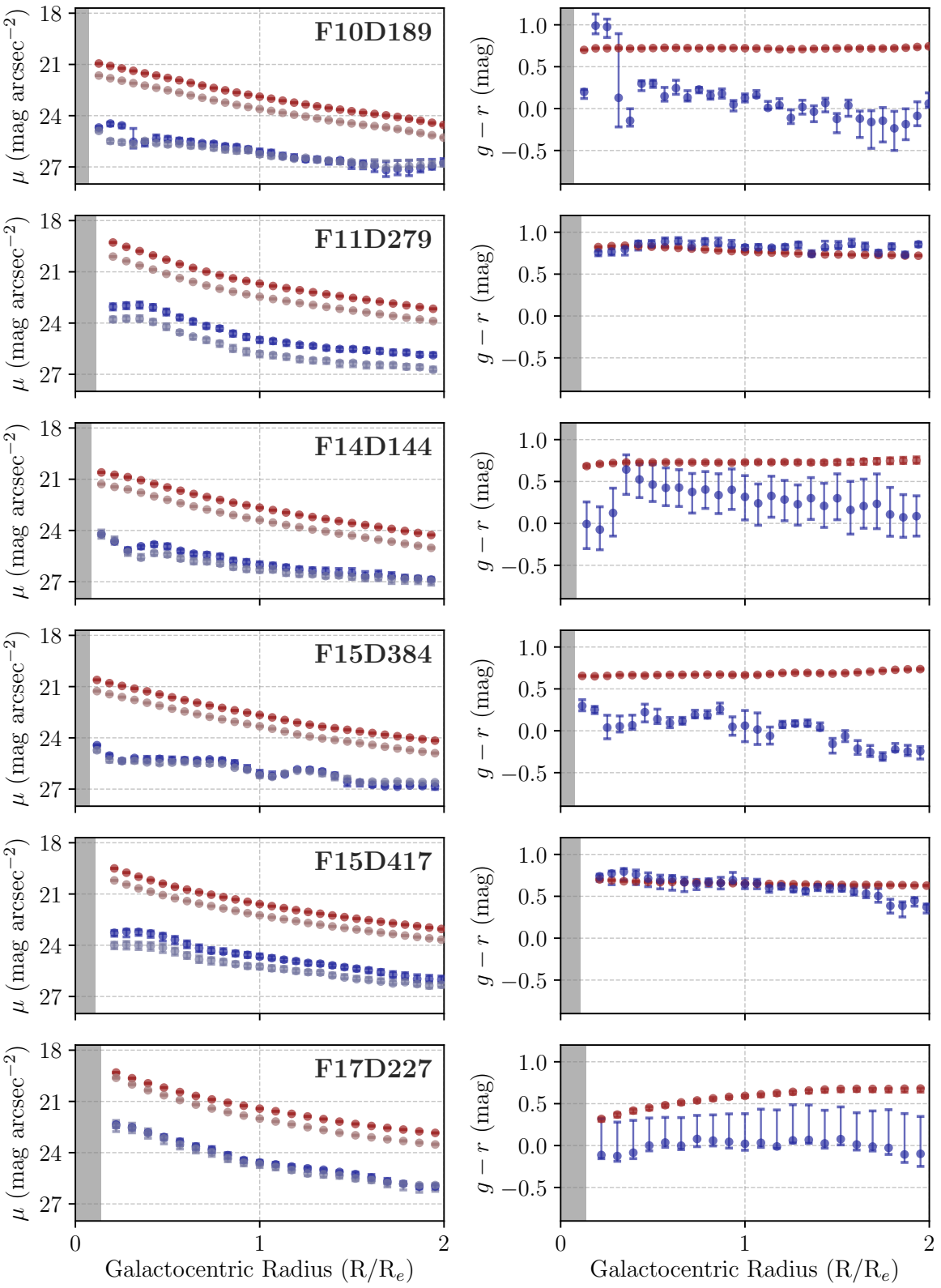

Figure A.43: Surface brightness and $g-r$ color profiles of the diffuse and substructure components of the Fornax dwarf ETG sample *(cont.)*.

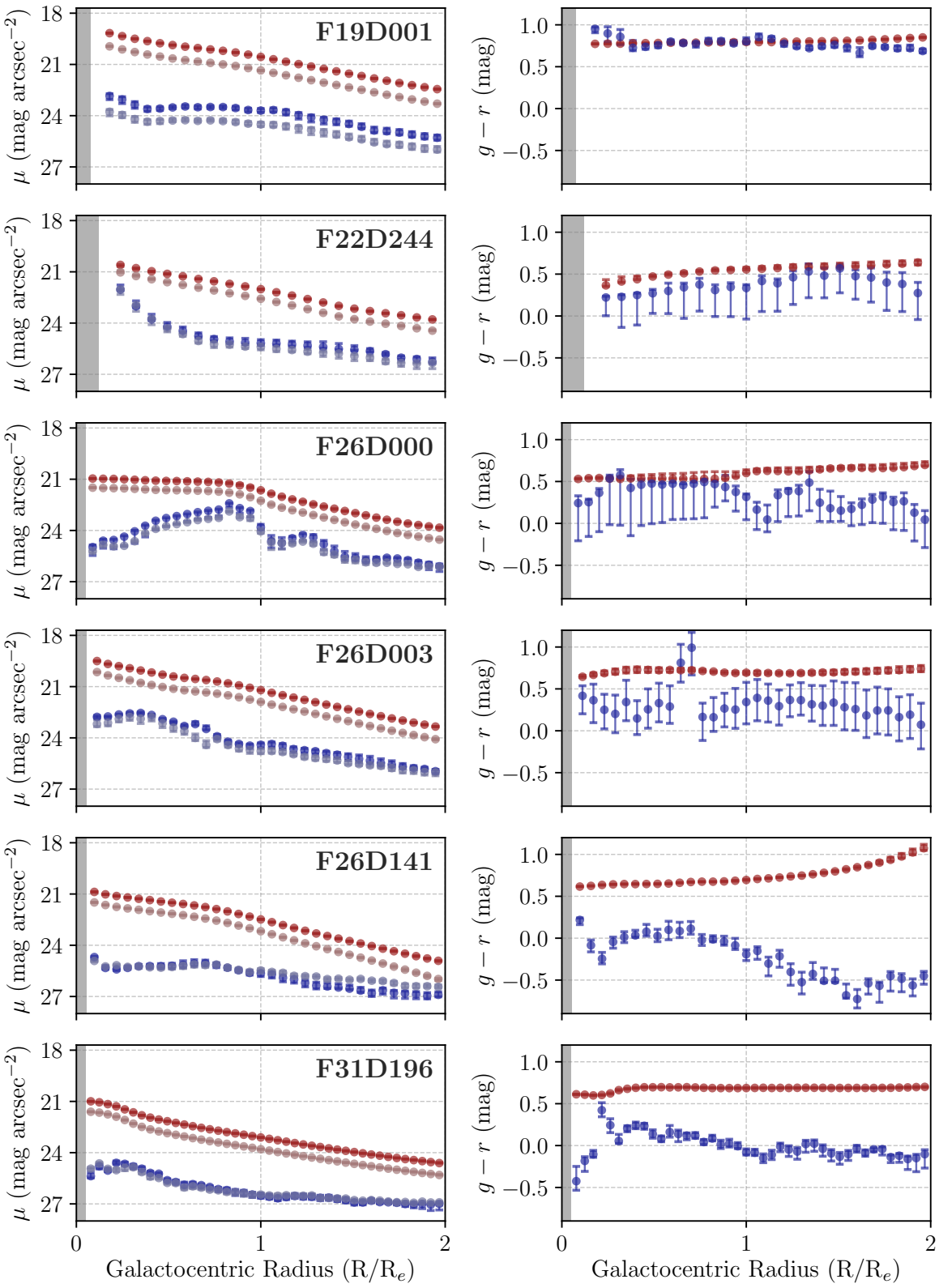

Figure A.43: Surface brightness and $g - r$ color profiles of the diffuse and substructure components of the Fornax dwarf ETG sample *(cont.)*.

B

Additional Tables

B.1 Description of IRAF Parameters

Table B.1: Parameter description of the IRAF `gauss` and `bmodel` tasks.

Task	Parameter	Description
(1)	(2)	(3)
`gauss`	`sigma`	Standard deviation of the Gaussian function used as a smoothing kernel, defined along the direction `theta` of the major axis of the function (pixels).
	`ratio`	Ratio of the standard deviation of the Gaussian function in the minor axis direction to the major axis direction (b/a). If equal to 1, the function is circular.
	`theta`	Position angle of the major axis of the Gaussian function, measured counterclockwise from the $+x$-axis (degrees). Must be between 0 and 180 degrees.
	`nsigma`	Extent of the major axis of the Gaussian function, given as a multiple of `sigma` pixels. The function is truncated beyond this value.
	`bilinear`	Use a bilinear approximation of the Gaussian function when possible, in in order to compute the 2D convolution more efficiently?
	`boundary`	Algorithm used to compute the values of out-of-bounds pixels. Options: nearest (default), constant, reflect, wrap.
`bmodel`	`fulltab`	Use full range of semi-major axis lengths from the input `ellipse` table to construct the 2D model?
	`backgr`	Background value to assign to the pixels outside the maximum semi-major axis length.
	`interp`	Algorithm used to interpolate between successive isophotes. Options: spline (default), poly3, linear, nearest.
	`highar`	Use the 3rd and 4th harmonics when constructing the 2D model?

Note. — Col. (1): IRAF task name. Col. (2): parameter name. Col. (3): parameter description, based on the official IRAF and STSDAS documentation of the `gauss` and `bmodel` tasks. When applicable, the parameter units are provided in parenthesis.

Table B.2: Parameter description of the IRAF `ellipse` task.

Configuration Task (1)	Parameter (2)	Description (3)
Ellipse	`dqf`	Data quality file associated with the input image. In a bad pixel mask image, pixels with a value of zero represent good pixels, while non-zero pixels represent bad pixels that should be rejected by the fitting algorithm.
	`inellip`	Input table in `ellipse` format, containing the information of the isophotal geometry to be used in no-fit photometry-only mode. In this mode, the light distribution is not fit, but only measured at the given isophotes.
Sampling	`integrmode`	Method used to sample the image along an elliptical path. Options: median, mean, bi-linear (default).
	`usclip`	K-sigma clipping criterion applied to deviant points above the average along an elliptical isophote.
	`lsclip`	K-sigma clipping criterion applied to deviant points below the average along an elliptical isophote.
	`nclip`	Number of iterations of the k-sigma clipping algorithm.
	`fflag`	Maximum fraction of flagged pixels that are acceptable along an elliptical isophote. If exceeded, the fitting algorithm stops increasing the semi-major axis.
	`harmonics`	List of optional upper harmonics to be used by the fitting algorithm. By default, only the 1st and 2nd harmonics are fit.
Control	`conver`	Convergency criterion for stopping iterations in the fitting algorithm. Iterations stop when the largest harmonic amplitude is less than `conver` times the rms residual of the fit.
	`minit`	Minimum number of iterations when fitting an isophote.
	`maxit`	Maximum number of iterations when fitting an isophote.
	`hcenter`	Hold the central coordinates of the isophote fixed during the fit?
	`hellip`	Hold the ellipticity of the isophote fixed during the fit?
	`hpa`	Hold the position angle of the isophote fixed during the fit?
	`wander`	Maximum distance that the central coordinates are allowed to wander between successive isophote fits (pixels).
	`maxgerr`	Main criterion for stopping the growth of the semi-major axis length in the fitting algorithm, which prevents the growth of the isophotes to regions of too low S/N. The growth stops when the maximum acceptable relative error in the local intensity gradient `maxgerr` is exceeded.
	`olthresh`	Threshold for the object locator algorithm. By lowering this value the object locator becomes less strict, accepting lower S/N data. If set to zero, the central coordinates (`x0`,`y0`) are used without questioning.
	`soft`	Soft stop of the fitting algorithm? If yes, the `maxgerr` criterion has to be reached by two consecutive isophotes in order to be triggered.

Note. — Col. (1): IRAF `ellipse` configuration tasks: ellipse parameters, image sampling parameters (`samplepar`), algorithm control parameters (`controlpar`), and geometrical parameters (`geopar`). Col. (2): parameter name. Col. (3): parameter description, based on the official STSDAS documentation of the `ellipse` task. When applicable, the parameter units are provided in parenthesis.

Table B.2: Parameter description of the IRAF `ellipse` task *(cont.)*.

Configuration Task (1)	Parameter (2)	Description (3)
Geometrical	`x0`	Initial guess for the central x coordinate of the first isophote fit (pixels).
	`y0`	Initial guess for the central y coordinate of the first isophote fit (pixels).
	`ellip0`	Initial guess for the ellipticity of the first isophote fit. The ellipticity is defined as $e = 1 - ba^{-1}$, where a and b are the semi-major and semi-minor axis lengths, respectively. The algorithm diverges at zero ellipticity (a circle).
	`pa0`	Initial guess for the position angle of the first isophote fit (degrees). The position angle is measured counterclockwise from the $+y$-axis, and must be between -90 and 90 degrees.
	`sma0`	Semi-major axis length that is used during the first isophote fit (pixels).
	`minsma`	Minimum semi-major axis length to be measured (pixels). If set to zero, the central pixel intensity is measured.
	`maxsma`	Maximum semi-major axis length to be measured (pixels).
	`step`	Step in semi-major axis length between successive isophotes If geometric steps, the semi-major axis length of the next isophote is increased by either a factor of $(1 + \texttt{step})$ or $(1/(1 + \texttt{step}))$, depending on the sense of growing (outwards or inwards, respectively).
	`linear`	Increase/decrease of the semi-major axis length by linear steps, as opposed to geometric?
	`maxrit`	Maximum semi-major axis length for iterative mode. If INDEF, no limit is imposed.
	`recenter`	Allow the finding routine to re-center the central coordinates (`x0`,`y0`) after a successful object detection?
	`xylearn`	Update the parameter set with new values of the central coordinates (`x0`,`y0`), either from the first isophote fit or the finding routine?
	`physical`	Use a physical coordinate system, as opposed to relative coordinates of an input image section?

Note. — Table B.2 continued.

Acknowledgements

To my supervisor, Eva Grebel. You have only shown me genuine kindness and a caring patience throughout all these years. Your continuous support has meant the world to me, and motivated me to keep fighting and striving forward. Thank you for your scientific guidance, all your caring messages, the lovely pictures — for everything.

To my advisor, Anna Pasquali. You have been a constant source of inspiration and encouragement. Without your careful guidance, this work would not have been possible. Thank you for always having such a kindhearted disposition to discuss all matter of things.

To my collaborators: Rory Smith, Paula Calderón-Castillo, and Katarina Kraljic. Your collaboration has been fundamental to my growth as a researcher. Thank you for all the fruitful discussions.

To the members of my examination committee: Jochen Heidt, Björn Schäfer, and Joachim Wambsganß. Thank you for kindly agreeing to be part of my defense. Special thanks to Jochen, for additionally acting as a referee and also for having been a member of my thesis committee.

On a more personal note, to my doctor, Mónica Bruzzone. You believed from day one that I could get better, and I trusted you. We have worked relentlessly, breaking old foundations and slowly establishing new ones. What I am today is thanks to you — to both of us. From the bottom of my heart, thank you.

To my mother. You have always been there for me, and I can now say with certainty that I will always be there for you. To my father. You have taught me the meaning of resilience, and to try not to take life too seriously. Thank you both for your unconditional love.

To my friends, Francisco Aros and Gergely Hajdu. Thank you for your friendship and all the good times throughout so many years, and here's to many more to follow.

Last, but certainly not least, to Ilja Moderau. Thank you for all your love.

I would also like to acknowledge the financial support I received throughout my PhD studies. The Deutscher Akademischer Austauschdienst (DAAD) provided me with a doctoral scholarship, while the Max-Planck-Institut für Astronomie (MPIA) and Universität Heidelberg provided additional funding. I also acknowledge support from the European Union's Horizon 2020 research and innovation program under the Marie Sklodowska-Curie grant agreement no. 721463 to the SUNDIAL ITN network.

Author's Publications

The publications by the author are listed as follows.

- Brought to Light. I. Quantification of Disk Substructure in Dwarf Early-type Galaxies. **Michea, J.**, Pasquali, A., Smith, R., et al. 2021, AJ, 161, 268, doi: 10.3847/1538-3881/abf24b
- Brought to Light. II. Revealing the Origins of Cloaked Spiral Features in Cluster Passive Dwarf Galaxies.
  Smith, R., **Michea, J.**, Pasquali, A., et al. 2021, ApJ, 912, 149, doi: 10.3847/1538-4357/abe1b1

In this thesis, Chapters 2 and 3 are mainly based on the work by Michea et al. (2021). In Chapter 5, Section 5.3.2, we address parts of the work by Smith et al. (2021).

References

Abazajian, K. N., Adelman-McCarthy, J. K., Agüeros, M. A., et al. 2009, ApJS, 182, 543, doi: 10.1088/0067-0049/182/2/543

Adelman-McCarthy, J. K., Agüeros, M. A., Allam, S. S., et al. 2006, ApJS, 162, 38, doi: 10.1086/497917

—. 2007, ApJS, 172, 634, doi: 10.1086/518864

Aguerri, J. A. L., Beckman, J. E., & Prieto, M. 1998, AJ, 116, 2136, doi: 10.1086/300615

Aguerri, J. A. L., & González-García, A. C. 2009, A&A, 494, 891, doi: 10.1051/0004-6361:200810339

Ann, H. B., Seo, M., & Ha, D. K. 2015, ApJS, 217, 27, doi: 10.1088/0067-0049/217/2/27

Arnaboldi, M., Capaccioli, M., Mancini, D., et al. 1998, The Messenger, 93, 30

Astropy Collaboration, Robitaille, T. P., Tollerud, E. J., et al. 2013, A&A, 558, A33, doi: 10.1051/0004-6361/201322068

Astropy Collaboration, Price-Whelan, A. M., Sipőcz, B. M., et al. 2018, AJ, 156, 123, doi: 10.3847/1538-3881/aabc4f

Athanassoula, E., & Misiriotis, A. 2002, MNRAS, 330, 35, doi: 10.1046/j.1365-8711.2002.05028.x

Baade, D., Meisenheimer, K., Iwert, O., et al. 1999, The Messenger, 95, 15

Balogh, M. L., Navarro, J. F., & Morris, S. L. 2000, ApJ, 540, 113, doi: 10.1086/309323

Barazza, F. D., Binggeli, B., & Jerjen, H. 2002, A&A, 391, 823, doi: 10.1051/0004-6361:20020875

Barnes, D. G., Staveley-Smith, L., de Blok, W. J. G., et al. 2001, MNRAS, 322, 486, doi: 10.1046/j.1365-8711.2001.04102.x

Bechtol, K., Drlica-Wagner, A., Balbinot, E., et al. 2015, ApJ, 807, 50, doi: 10.1088/0004-637X/807/1/50

Bekki, K., Couch, W. J., & Shioya, Y. 2002, ApJ, 577, 651, doi: 10.1086/342221

Bialas, D., Lisker, T., Olczak, C., Spurzem, R., & Kotulla, R. 2015, A&A, 576, A103, doi: 10.1051/0004-6361/201425235

Bidaran, B., Pasquali, A., Lisker, T., et al. 2020, MNRAS, 497, 1904, doi: 10.1093/mnras/staa2097

Binggeli, B., & Cameron, L. M. 1991, A&A, 252, 27

Binggeli, B., Popescu, C. C., & Tammann, G. A. 1993, A&AS, 98, 275

Binggeli, B., Sandage, A., & Tammann, G. A. 1985, AJ, 90, 1681, doi: 10.1086/113874

Binney, J., & Tremaine, S. 2008, Galactic Dynamics: Second Edition (Princeton, NJ USA: Princeton University Press)

Blakeslee, J. P., Jordán, A., Mei, S., et al. 2009, ApJ, 694, 556, doi: 10.1088/0004-637X/694/1/556

Boselli, A., Boissier, S., Cortese, L., & Gavazzi, G. 2008, ApJ, 674, 742, doi: 10.1086/525513

Boselli, A., & Gavazzi, G. 2006, PASP, 118, 517, doi: 10.1086/500691

—. 2014, A&A Rv, 22, 74, doi: 10.1007/s00159-014-0074-y

Bradley, L., Sipőcz, B., Robitaille, T., et al. 2021, astropy/photutils, 1.1.0, Zenodo, doi: 10.5281/zenodo.4624996

Capaccioli, M., Spavone, M., Grado, A., et al. 2015, A&A, 581, A10, doi: 10.1051/0004-6361/201526252

Cappellari, M., Scott, N., Alatalo, K., et al. 2013, MNRAS, 432, 1709, doi: 10.1093/mnras/stt562

Carignan, C., & Beaulieu, S. 1989, ApJ, 347, 760, doi: 10.1086/168167

Chilingarian, I. V. 2009, MNRAS, 394, 1229, doi: 10.1111/j.1365-2966.2009.14450.x

Cole, S., Lacey, C. G., Baugh, C. M., & Frenk, C. S. 2000, MNRAS, 319, 168, doi: 10.1046/j.1365-8711.2000.03879.x

Conselice, C. J. 2003, ApJS, 147, 1, doi: 10.1086/375001

Conselice, C. J., O'Neil, K., Gallagher, J. S., & Wyse, R. F. G. 2003, ApJ, 591, 167, doi: 10.1086/375216

Cortese, L., Fogarty, L. M. R., Ho, I. T., et al. 2014, ApJL, 795, L37, doi: 10.1088/2041-8205/795/2/L37

Côté, P., Piatek, S., Ferrarese, L., et al. 2006, ApJS, 165, 57, doi: 10.1086/504042
Cowie, L. L., & McKee, C. F. 1977, ApJ, 211, 135, doi: 10.1086/154911
Cowie, L. L., & Songaila, A. 1977, Nature, 266, 501, doi: 10.1038/266501a0
Davies, J. I., Bianchi, S., Baes, M., et al. 2013, MNRAS, 428, 834, doi: 10.1093/mnras/sts082
Davis, M., Efstathiou, G., Frenk, C. S., & White, S. D. M. 1985, ApJ, 292, 371, doi: 10.1086/163168
De Rijcke, S., Buyle, P., & Koleva, M. 2013, ApJL, 770, L26, doi: 10.1088/2041-8205/770/2/L26
De Rijcke, S., Dejonghe, H., Zeilinger, W. W., & Hau, G. K. T. 2003, A&A, 400, 119, doi: 10.1051/0004-6361:20021866
De Rijcke, S., Van Hese, E., & Buyle, P. 2010, ApJL, 724, L171, doi: 10.1088/2041-8205/724/2/L171
de Vaucouleurs, G. 1948, Annales d'Astrophysique, 11, 247
Dressler, A. 1980, ApJ, 236, 351, doi: 10.1086/157753
Drinkwater, M. J., Gregg, M. D., & Colless, M. 2001, ApJL, 548, L139, doi: 10.1086/319113
Drinkwater, M. J., Jones, J. B., Gregg, M. D., & Phillipps, S. 2000, PASA, 17, 227, doi: 10.1071/AS00034
Eggen, O. J., Lynden-Bell, D., & Sandage, A. R. 1962, ApJ, 136, 748, doi: 10.1086/147433
Eigenthaler, P., Puzia, T. H., Taylor, M. A., et al. 2018, ApJ, 855, 142, doi: 10.3847/1538-4357/aaab60
Elmegreen, B. G., Elmegreen, D. M., & Seiden, P. E. 1989, ApJ, 343, 602, doi: 10.1086/167733
Erben, T., Schirmer, M., Dietrich, J. P., et al. 2005, Astronomische Nachrichten, 326, 432, doi: 10.1002/asna.200510396
Erwin, P. 2004, A&A, 415, 941, doi: 10.1051/0004-6361:20034408
Faber, S. M., & Jackson, R. E. 1976, ApJ, 204, 668, doi: 10.1086/154215
Ferguson, H. C. 1989a, Ap&SS, 157, 227, doi: 10.1007/BF00637334
—. 1989b, AJ, 98, 367, doi: 10.1086/115152
Ferguson, H. C., & Binggeli, B. 1994, A&A Rv, 6, 67, doi: 10.1007/BF01208252
Ferrarese, L., Côté, P., Jordán, A., et al. 2006, ApJS, 164, 334, doi: 10.1086/501350
Ferrarese, L., Côté, P., Cuilland re, J.-C., et al. 2012, ApJS, 200, 4, doi: 10.1088/0067-0049/200/1/4
Fillingham, S. P., Cooper, M. C., Pace, A. B., et al. 2016, MNRAS, 463, 1916, doi: 10.1093/mnras/stw2131
Fujita, Y. 2004, PASJ, 56, 29, doi: 10.1093/pasj/56.1.29
Fukazawa, Y., Makishima, K., Tamura, T., et al. 1998, PASJ, 50, 187, doi: 10.1093/pasj/50.1.187
Fuller, C., Davies, J. I., Auld, R., et al. 2014, Monthly Notices of the Royal Astronomical Society, 440, 1571, doi: 10.1093/mnras/stu369
Gallazzi, A., Charlot, S., Brinchmann, J., White, S. D. M., & Tremonti, C. A. 2005, MNRAS, 362, 41, doi: 10.1111/j.1365-2966.2005.09321.x
Geha, M., Blanton, M. R., Yan, R., & Tinker, J. L. 2012, ApJ, 757, 85, doi: 10.1088/0004-637X/757/1/85
Geha, M., Guhathakurta, P., & van der Marel, R. P. 2003, AJ, 126, 1794, doi: 10.1086/377624
Girardi, L., Bressan, A., Bertelli, G., & Chiosi, C. 2000, A&AS, 141, 371, doi: 10.1051/aas:2000126
Graham, A. W. 2019, PASA, 36, e035, doi: 10.1017/pasa.2019.23
Graham, A. W., & Guzmán, R. 2003, AJ, 125, 2936, doi: 10.1086/374992
Graham, A. W., Janz, J., Penny, S. J., et al. 2017, ApJ, 840, 68, doi: 10.3847/1538-4357/aa6e56
Graham, A. W., Jerjen, H., & Guzmán, R. 2003, AJ, 126, 1787, doi: 10.1086/378166
Grebel, E. K. 2001, Astrophysics and Space Science Supplement, 277, 231, doi: 10.1023/A:1012742903265
Grebel, E. K., Gallagher, John S., I., & Harbeck, D. 2003, AJ, 125, 1926, doi: 10.1086/368363
Gu, Q., Zhao, Y., Shi, L., Peng, Z., & Luo, X. 2006, AJ, 131, 806, doi: 10.1086/498891
Gunn, J. E., & Gott, J. Richard, I. 1972, ApJ, 176, 1, doi: 10.1086/151605
Haines, C. P., Gargiulo, A., La Barbera, F., et al. 2007, MNRAS, 381, 7, doi: 10.1111/j.1365-2966.2007.12189.x
Hamraz, E., Peletier, R. F., Khosroshahi, H. G., et al. 2019, A&A, 625, A94, doi: 10.1051/0004-6361/201935076
Harbeck, D., Grebel, E. K., Holtzman, J., et al. 2001, AJ, 122, 3092, doi: 10.1086/324232
Hickson, P. 1982, ApJ, 255, 382, doi: 10.1086/159838
Hilker, M., Infante, L., Vieira, G., Kissler-Patig, M., & Richtler, T. 1999, A&AS, 134, 75, doi: 10.1051/aas:1999434
Hodge, P. W. 1973, ApJ, 182, 671, doi: 10.1086/152176

Impey, C., Bothun, G., & Malin, D. 1988, ApJ, 330, 634, doi: 10.1086/166500
Iodice, E., Capaccioli, M., Grado, A., et al. 2016, ApJ, 820, 42, doi: 10.3847/0004-637X/820/1/42
Ivezić, Ž., Kahn, S. M., Tyson, J. A., et al. 2019, ApJ, 873, 111, doi: 10.3847/1538-4357/ab042c
Janz, J., Laurikainen, E., Laine, J., Salo, H., & Lisker, T. 2016, MNRAS, 461, L82, doi: 10.1093/mnrasl/slw104
Janz, J., & Lisker, T. 2008, ApJL, 689, L25, doi: 10.1086/595720
—. 2009, ApJL, 696, L102, doi: 10.1088/0004-637X/696/1/L102
Janz, J., Penny, S. J., Graham, A. W., Forbes, D. A., & Davies, R. L. 2017, MNRAS, 468, 2850, doi: 10.1093/mnras/stx634
Janz, J., Salo, H., Su, A. H., & Venhola, A. 2021, A&A, 647, A80, doi: 10.1051/0004-6361/202039408
Janz, J., Laurikainen, E., Lisker, T., et al. 2012, ApJL, 745, L24, doi: 10.1088/2041-8205/745/2/L24
—. 2014, ApJ, 786, 105, doi: 10.1088/0004-637X/786/2/105
Jedrzejewski, R. I. 1987, MNRAS, 226, 747, doi: 10.1093/mnras/226.4.747
Jerjen, H., Binggeli, B., & Barazza, F. D. 2004, AJ, 127, 771, doi: 10.1086/381065
Jerjen, H., Binggeli, B., & Freeman, K. C. 2000a, AJ, 119, 593, doi: 10.1086/301216
Jerjen, H., Freeman, K. C., & Binggeli, B. 1998, AJ, 116, 2873, doi: 10.1086/300635
Jerjen, H., Kalnajs, A., & Binggeli, B. 2000b, A&A, 358, 845. https://arxiv.org/abs/astro-ph/0004248
Jerjen, H., Kalnajs, A., & Binggeli, B. 2001, in Astronomical Society of the Pacific Conference Series, Vol. 230, Galaxy Disks and Disk Galaxies, ed. J. G. Funes & E. M. Corsini, 239–240
Jones, C., Stern, C., Forman, W., et al. 1997, ApJ, 482, 143, doi: 10.1086/304104
Jordán, A., Blakeslee, J. P., Côté, P., et al. 2007, ApJS, 169, 213, doi: 10.1086/512778
Joye, W. 2019, SAOImageDS9/SAOImageDS9, v8.0.1, Zenodo, doi: 10.5281/zenodo.2530958
Joye, W. A., & Mandel, E. 2003, in Astronomical Society of the Pacific Conference Series, Vol. 295, Astronomical Data Analysis Software and Systems XII, ed. H. E. Payne, R. I. Jedrzejewski, & R. N. Hook, 489
Karachentsev, I. D., Makarova, L. N., Makarov, D. I., Tully, R. B., & Rizzi, L. 2015, MNRAS, 447, L85, doi: 10.1093/mnrasl/slu181
King, I. 1962, AJ, 67, 471, doi: 10.1086/108756
Koleva, M., Prugniel, P., De Rijcke, S., & Zeilinger, W. W. 2011, MNRAS, 417, 1643, doi: 10.1111/j.1365-2966.2011.19057.x
Kormendy, J. 1985, ApJ, 295, 73, doi: 10.1086/163350
Kraljic, K., Bournaud, F., & Martig, M. 2012, ApJ, 757, 60, doi: 10.1088/0004-637X/757/1/60
Kroupa, P. 2001, MNRAS, 322, 231, doi: 10.1046/j.1365-8711.2001.04022.x
Kuijken, K. 2011, The Messenger, 146, 8
Kuijken, K., Bender, R., Cappellaro, E., et al. 2002, The Messenger, 110, 15
Kwak, S., Kim, W.-T., Rey, S.-C., & Quinn, T. R. 2019, ApJ, 887, 139, doi: 10.3847/1538-4357/ab5716
Larson, R. B., Tinsley, B. M., & Caldwell, C. N. 1980, ApJ, 237, 692, doi: 10.1086/157917
Laurikainen, E., Salo, H., Athanassoula, E., Bosma, A., & Herrera-Endoqui, M. 2014, MNRAS, 444, L80, doi: 10.1093/mnrasl/slu118
Lisker, T. 2009, Astronomische Nachrichten, 330, 1043, doi: 10.1002/asna.200911291
—. 2012, Astronomische Nachrichten, 333, 405, doi: 10.1002/asna.201211691
Lisker, T., Brunngräber, R., & Grebel, E. K. 2009, Astronomische Nachrichten, 330, 966, doi: 10.1002/asna.200911271
Lisker, T., Debattista, V. P., Ferreras, I., & Erwin, P. 2006a, MNRAS, 370, 477, doi: 10.1111/j.1365-2966.2006.10493.x
Lisker, T., & Fuchs, B. 2009, A&A, 501, 429, doi: 10.1051/0004-6361/200811331
Lisker, T., Glatt, K., Westera, P., & Grebel, E. K. 2006b, AJ, 132, 2432, doi: 10.1086/508414
Lisker, T., Grebel, E. K., & Binggeli, B. 2006c, AJ, 132, 497, doi: 10.1086/505045
—. 2008, AJ, 135, 380, doi: 10.1088/0004-6256/135/1/380
Lisker, T., Grebel, E. K., Binggeli, B., & Glatt, K. 2007, ApJ, 660, 1186, doi: 10.1086/513090
Lisker, T., Vijayaraghavan, R., Janz, J., et al. 2018, ApJ, 865, 40, doi: 10.3847/1538-4357/aadae1
Loni, A., Serra, P., Kleiner, D., et al. 2021, A&A, 648, A31, doi: 10.1051/0004-6361/202039803
Ma, J., Zhao, J. L., Shu, C. G., & Peng, Q. H. 1999, A&A, 350, 31. https://arxiv.org/abs/astro-ph/0002476

Makarov, D., Makarova, L., Sharina, M., et al. 2012, MNRAS, 425, 709, doi: 10.1111/j.1365-2966.2012.21581.x
Makino, J., & Hut, P. 1997, ApJ, 481, 83, doi: 10.1086/304013
Malin, D. F. 1977, AAS Photo Bulletin, 16, 10
Marcolini, A., Brighenti, F., & D'Ercole, A. 2003, MNRAS, 345, 1329, doi: 10.1046/j.1365-2966.2003.07054.x
McConnachie, A. W. 2012, AJ, 144, 4, doi: 10.1088/0004-6256/144/1/4
McGaugh, S. S., & Bothun, G. D. 1990, AJ, 100, 1073, doi: 10.1086/115580
McLaughlin, D. E. 1999, ApJL, 512, L9, doi: 10.1086/311860
Michea, J., Pasquali, A., Smith, R., et al. 2021, AJ, 161, 268, doi: 10.3847/1538-3881/abf24b
Michielsen, D., Boselli, A., Conselice, C. J., et al. 2008, MNRAS, 385, 1374, doi: 10.1111/j.1365-2966.2008.12846.x
Mihos, J. C. 2004, in Clusters of Galaxies: Probes of Cosmological Structure and Galaxy Evolution, ed. J. S. Mulchaey, A. Dressler, & A. Oemler, 277
Moore, B., Katz, N., Lake, G., Dressler, A., & Oemler, A. 1996, Nature, 379, 613, doi: 10.1038/379613a0
Moore, B., Lake, G., & Katz, N. 1998, ApJ, 495, 139, doi: 10.1086/305264
Moore, B., Lake, G., Quinn, T., & Stadel, J. 1999, MNRAS, 304, 465, doi: 10.1046/j.1365-8711.1999.02345.x
Mori, M., & Burkert, A. 2000, ApJ, 538, 559, doi: 10.1086/309140
Muñoz, R. P., Eigenthaler, P., Puzia, T. H., et al. 2015, ApJL, 813, L15, doi: 10.1088/2041-8205/813/1/L15
Navarro, J. F., Frenk, C. S., & White, S. D. M. 1996, ApJ, 462, 563, doi: 10.1086/177173
Nulsen, P. E. J. 1982, MNRAS, 198, 1007, doi: 10.1093/mnras/198.4.1007
Ordenes-Briceño, Y., Eigenthaler, P., Taylor, M. A., et al. 2018a, ApJ, 859, 52, doi: 10.3847/1538-4357/aaba70
Ordenes-Briceño, Y., Puzia, T. H., Eigenthaler, P., et al. 2018b, ApJ, 860, 4, doi: 10.3847/1538-4357/aac1b8
Pak, M., Rey, S.-C., Lisker, T., et al. 2014, MNRAS, 445, 630, doi: 10.1093/mnras/stu1722
Paolillo, M., Fabbiano, G., Peres, G., & Kim, D. W. 2002, ApJ, 565, 883, doi: 10.1086/337919
Pasquali, A., Larsen, S., Ferreras, I., et al. 2005, AJ, 129, 148, doi: 10.1086/426319
Pasquali, A., Smith, R., Gallazzi, A., et al. 2019, MNRAS, 484, 1702, doi: 10.1093/mnras/sty3530
Paudel, S., Lisker, T., Kuntschner, H., Grebel, E. K., & Glatt, K. 2010, MNRAS, 405, 800, doi: 10.1111/j.1365-2966.2010.16507.x
Paudel, S., Smith, R., Yoon, S. J., Calderón-Castillo, P., & Duc, P.-A. 2018, ApJS, 237, 36, doi: 10.3847/1538-4365/aad555
Peletier, R. F. 1993, A&A, 271, 51
—. 2013, Stellar Populations, ed. J. Falcón-Barroso & J. H. Knapen, 353
Peng, C. Y., Ho, L. C., Impey, C. D., & Rix, H.-W. 2002, AJ, 124, 266, doi: 10.1086/340952
Penny, S. J., Forbes, D. A., Pimbblet, K. A., & Floyd, D. J. E. 2014, MNRAS, 443, 3381, doi: 10.1093/mnras/stu1397
Planck Collaboration, Aghanim, N., Akrami, Y., et al. 2020, A&A, 641, A6, doi: 10.1051/0004-6361/201833910
Polzin, A., van Dokkum, P., Danieli, S., Greco, J. P., & Romanowsky, A. J. 2021, ApJL, 914, L23, doi: 10.3847/2041-8213/ac024f
Raj, M. A., Iodice, E., Napolitano, N. R., et al. 2019, A&A, 628, A4, doi: 10.1051/0004-6361/201935433
Rix, H.-W., & Zaritsky, D. 1995, ApJ, 447, 82, doi: 10.1086/175858
Roediger, E., Bruggen, M., Owers, M. S., Ebeling, H., & Sun, M. 2014, MNRAS, 443, L114, doi: 10.1093/mnrasl/slu087
Ryś, A., Falcón-Barroso, J., & van de Ven, G. 2013, MNRAS, 428, 2980, doi: 10.1093/mnras/sts245
Ryś, A., Koleva, M., Falcón-Barroso, J., et al. 2015, MNRAS, 452, 1888, doi: 10.1093/mnras/stv1364
Ryś, A., van de Ven, G., & Falcón-Barroso, J. 2014, MNRAS, 439, 284, doi: 10.1093/mnras/stt2417
Sánchez-Janssen, R., Côté, P., Ferrarese, L., et al. 2019, ApJ, 878, 18, doi: 10.3847/1538-4357/aaf4fd
Sandage, A., & Binggeli, B. 1984, AJ, 89, 919, doi: 10.1086/113588

Schindler, S., Binggeli, B., & Böhringer, H. 1999, A&A, 343, 420. https://arxiv.org/abs/astro-ph/9811464
Schirmer, M. 2013, ApJS, 209, 21, doi: 10.1088/0067-0049/209/2/21
Schlafly, E. F., & Finkbeiner, D. P. 2011, ApJ, 737, 103, doi: 10.1088/0004-637X/737/2/103
Schneider, P. 2006, Extragalactic Astronomy and Cosmology (Springer Berlin Heidelberg), doi: 10.1007/978-3-540-33175-9
Scott, N., Eftekhari, F. S., Peletier, R. F., et al. 2020, MNRAS, 497, 1571, doi: 10.1093/mnras/staa2042
Sérsic, J. L. 1968, Atlas de Galaxias Australes (Córdoba: Observatorio Astronómico, Universidad Nacional de Córdoba)
Shipp, N., Drlica-Wagner, A., Balbinot, E., et al. 2018, ApJ, 862, 114, doi: 10.3847/1538-4357/aacdab
Skillman, E. D., Kennicutt, R. C., & Hodge, P. W. 1989, ApJ, 347, 875, doi: 10.1086/168178
Smith, R., Davies, J. I., & Nelson, A. H. 2010, MNRAS, 405, 1723, doi: 10.1111/j.1365-2966.2010.16545.x
Smith, R., Duc, P. A., Candlish, G. N., et al. 2013, MNRAS, 436, 839, doi: 10.1093/mnras/stt1619
Smith, R., Sánchez-Janssen, R., Beasley, M. A., et al. 2015, MNRAS, 454, 2502, doi: 10.1093/mnras/stv2082
Smith, R., Michea, J., Pasquali, A., et al. 2021, ApJ, 912, 149, doi: 10.3847/1538-4357/abe1b1
Steyrleithner, P., Hensler, G., & Boselli, A. 2020, MNRAS, 494, 1114, doi: 10.1093/mnras/staa775
STSDAS Group. 1994, STSDAS User's Guide (Baltimore, MD: Space Telescope Science Institute)
Su, A. H., Salo, H., Janz, J., et al. 2021, A&A, 647, A100, doi: 10.1051/0004-6361/202039633
Swaters, R. A., Sancisi, R., van Albada, T. S., & van der Hulst, J. M. 2009, A&A, 493, 871, doi: 10.1051/0004-6361:200810516
Swaters, R. A., van Albada, T. S., van der Hulst, J. M., & Sancisi, R. 2002, A&A, 390, 829, doi: 10.1051/0004-6361:20011755
Sybilska, A., Lisker, T., Kuntschner, H., et al. 2017, MNRAS, 470, 815, doi: 10.1093/mnras/stx1138
Tody, D. 1986, in Society of Photo-Optical Instrumentation Engineers (SPIE) Conference Series, Vol. 627, Proc. SPIE, ed. D. L. Crawford, 733, doi: 10.1117/12.968154
Tody, D. 1993, in Astronomical Society of the Pacific Conference Series, Vol. 52, Astronomical Data Analysis Software and Systems II, ed. R. J. Hanisch, R. J. V. Brissenden, & J. Barnes, 173
Toloba, E., Boselli, A., Cenarro, A. J., et al. 2011, A&A, 526, A114, doi: 10.1051/0004-6361/201015344
Toloba, E., Boselli, A., Peletier, R. F., et al. 2012, A&A, 548, A78, doi: 10.1051/0004-6361/201218944
Toloba, E., Boselli, A., Gorgas, J., et al. 2009, ApJL, 707, L17, doi: 10.1088/0004-637X/707/1/L17
Toloba, E., Guhathakurta, P., Peletier, R. F., et al. 2014, ApJS, 215, 17, doi: 10.1088/0067-0049/215/2/17
Toloba, E., Guhathakurta, P., Boselli, A., et al. 2015, ApJ, 799, 172, doi: 10.1088/0004-637X/799/2/172
Treu, T., Ellis, R. S., Kneib, J.-P., et al. 2003, ApJ, 591, 53, doi: 10.1086/375314
Tully, R. B., & Fisher, J. R. 1977, A&A, 500, 105
Urich, L., Lisker, T., Janz, J., et al. 2017, A&A, 606, A135, doi: 10.1051/0004-6361/201730897
van Dokkum, P. G., Abraham, R., Merritt, A., et al. 2015, ApJL, 798, L45, doi: 10.1088/2041-8205/798/2/L45
van Zee, L., Barton, E. J., & Skillman, E. D. 2004a, AJ, 128, 2797, doi: 10.1086/425530
van Zee, L., Skillman, E. D., & Haynes, M. P. 2004b, AJ, 128, 121, doi: 10.1086/421368
Vazdekis, A., Koleva, M., Ricciardelli, E., Röck, B., & Falcón-Barroso, J. 2016, MNRAS, 463, 3409, doi: 10.1093/mnras/stw2231
Vazdekis, A., Ricciardelli, E., Cenarro, A. J., et al. 2012, MNRAS, 424, 157, doi: 10.1111/j.1365-2966.2012.21179.x
Vazdekis, A., Sánchez-Blázquez, P., Falcón-Barroso, J., et al. 2010, MNRAS, 404, 1639, doi: 10.1111/j.1365-2966.2010.16407.x
Venhola, A., Peletier, R., Laurikainen, E., et al. 2018, A&A, 620, A165, doi: 10.1051/0004-6361/201833933
—. 2019, A&A, 625, A143, doi: 10.1051/0004-6361/201935231
Vigroux, L., Souviron, J., & Vader, J. P. 1984, A&A, 139, L9
Waugh, M., Drinkwater, M. J., Webster, R. L., et al. 2002, Monthly Notices of the Royal Astronomical

Society, 337, 641, doi: 10.1046/j.1365-8711.2002.05942.x
Weinmann, S. M., Lisker, T., Guo, Q., Meyer, H. T., & Janz, J. 2011, MNRAS, 416, 1197, doi: 10.1111/j.1365-2966.2011.19118.x
White, S. D. M., & Rees, M. J. 1978, MNRAS, 183, 341, doi: 10.1093/mnras/183.3.341
Worthey, G. 1994, ApJS, 95, 107, doi: 10.1086/192096
Zabel, N., Davis, T. A., Smith, M. W. L., et al. 2019, MNRAS, 483, 2251, doi: 10.1093/mnras/sty3234
Zaritsky, D., Zabludoff, A. I., & Gonzalez, A. H. 2008, ApJ, 682, 68, doi: 10.1086/529577